Department of Environment, Land and Infrastructure Engineering (DIATI)
Master of Science in Environmental and Land Engineering

Geological Hazard Current And Future Scenarios Due to Climate Change In Western Italian Alps

By

Monireh Karimian Mobarakeh

Supervisor:
Professor Chiara Deangeli

Co-supervisors:
Dr. Elisa Brussolo
Dr. Davide Tiranti

Politecnico di Torino
July 2025

Declaration

I hereby declare that, except where specific reference is made to the work of others, the contents and organization of this dissertation constitute my own original work and does not compromise in any way the rights of third parties, including those relating to the security of personal data. This dissertation is entirely the result of my own work and includes nothing which is the outcome of work done in collaboration.

Monireh Karimian Mobarakeh

I would like to dedicate this thesis to my father, for being my calm in the storm, and to my mother, whose quiet strength taught me how to rise with grace.
And to every woman who has ever carried a dream close to her heart and followed it, even when the path was uncertain.

تقدیم به

پدرم،

برای آن‌که همیشه آرامش من در میان طوفان‌ها بود،

و به مادرم،

که با قدرتی آرام، به من آموخت چگونه با وقار برخیزم

و به تمام زنانی

که رویایی را در دل نگه داشتند و آن را دنبال کردند، حتی وقتی مسیر پیش رو روشن نبود...

Acknowledgment

First and foremost, I would like to express my heartfelt gratitude to my supervisor, Professor Chiara Deangeli. Her expert guidance and constant support greatly enriched this thesis and deepened my understanding of geo-structures under climate change. Beyond her academic mentorship, she represented an exemplary model of a strong woman in the field of engineering: resilient, principled.

I would also like to express my sincere appreciation to Dr. Davide Tiranti, who was consistently available throughout all stages of this thesis. His generosity in sharing his knowledge, along with his openness and dedication, had a meaningful impact on the development of this work. His clear and insightful responses guided me through key decisions, while his mentorship fostered critical thinking and encouraged intellectual independence.

I am deeply grateful to Dr. Elisa Brussolo for her sharp scientific insight and continued support. Her expertise was instrumental in refining the analytical framework of this study. Working with her was both stimulating and rewarding, and I truly value the time and thoughtful feedback she provided at every step.

Last but certainly not least, I would like to express my deepest gratitude to my kind and supportive family. Though far away, their affection has never failed to reach me, and their unwavering belief in me has been my strongest encouragement throughout this path. I am sincerely thankful to dear Nima, whose love has been a steady source of inspiration, and peace throughout this entire journey. My heartfelt thanks also go to my dear friends, who over the years have truly become a second family to me and whose presence has been an irreplaceable part of my life.

Abstract

This thesis investigates how climate change affects geohazards, specifically rockfalls, debris flows, and shallow landslides in the Susa Valley, a high relief Alpine region in northwest Italy. The study combines analysis of historical climate data (1957–2024) and predictions of the future (2025–2100) under two greenhouse gas scenarios: RCP 4.5 (moderate emissions) and RCP 8.5 (high emissions). Multi-hazard susceptibility maps, gridded temperature and precipitation datasets, and high-resolution Digital Elevation Models (DEMs) were used in a thorough spatial analysis. The study region was divided into five altitudinal zones with elevation-based classification, which made the ability to assess climate-hazard interactions at different terrain levels.

Historical temperature analysis revealed a consistent upward trend in both maximum and minimum temperatures, with *ΔT* (temperature range between maximum and minimum values) showing a slight narrowing over time. A critical elevation threshold of ~795 m was identified, above which freezing maximum temperatures are more frequent. Precipitation analysis showed rare but significant 24-hour and 48-hour rainfall extremes, especially during late spring and early winter. The study found that these climatic factors significantly influence hazard distribution: Rockfall susceptibility increases with *ΔT* values above 8°C in mid-to-high elevation zones; debris flows occur most often in ECM-class catchments, characterized by high clay-weathering lithology (CWI) in elevation zones where summer rainfall intensity exceeds 20 mm/h; and shallow landslides are concentrated in Elevation Class 3 (1000–2000 m), mainly under Susceptibility Class 4, triggered by exceeding the rainfall threshold of 120 mm (24 h) or 170 mm (48 h).

All elevation zones continue to warm, according to future climate projections (2025–2100) under both RCP 4.5 and RCP 8.5 scenarios. It is anticipated that *Tmin* will rise faster than *Tmax*, particularly in regions with high elevation. A significant retreat of periglacial conditions is indicated by the critical freezing elevation shifting further upward to nearly 1550 m under RCP 8.5 and rising to about 1427 m under RCP 4.5. Under RCP 4.5, the temperature range (*ΔT*) stays largely constant, but under RCP 8.5, especially in Elevation Classes 1 to 3, there is a slight summer increase. These thermal changes are expected to amplify rockfall risk, as *ΔT* values above 8 °C become more frequent in lower and mid-elevation zones under RCP 4.5 and expand to higher susceptibility classes under RCP 8.5. Rainfall projections indicate a slight increase in short-duration extremes during late spring and autumn, with May and November exhibiting the steepest upward trends. Under RCP 4.5, several 24-hour rainfall events are projected to surpass the 120 mm threshold, especially in Elevation Classes 3 and 4. In the RCP 8.5 scenario, although average daily rainfall

may decline slightly, intense events persist and occasionally exceed 170 mm in 48-hour windows, posing continued shallow landslide risk in Susceptibility Classes. Debris flows are projected to become more frequent in ECM zones under both scenarios, driven by projected intensification of summer rainfall. The convergence of rising temperatures, shifting thermal thresholds, and localized hydrological intensification suggests that mid- to high-elevation areas will remain the most vulnerable to compound climate-driven geo-hazards throughout the 21st century.

Table of Contents

Chapter 1

Introduction

1.1 Background and Motivation

Climate change describes the long-term shifts in precipitation and temperature patterns which human-produced greenhouse gas emissions tend to intensify. The changes in geotechnical conditions result from modifications to soil behavior as well as hydrology and slope stability. The evaluation of climate-related geohazards depends on knowledge about how slopes react to climatic factors especially in vulnerable regions (Psarropoulos et al., 2024).

Climate fluctuations including drought and warmth and heavy rainfall affect key geotechnical parameters such as pore-water pressure, matric suction and shear strength. The changes in these parameters can lead to erosion, cracking and slope failures in unsaturated and fine-grained soils. It is important to understand these impacts in order to plan and preserve geostructures in the face of changing climate conditions(Kandalai et al., 2023).

Research indicates that heavy rainfall triggers shallow landslides primarily in regions with brittle rock and soil structures. The statistical analysis revealed that northwest Italy experienced more landslide events when climate factors such as the Montana Coefficient and mean annual precipitation were considered instead of topography features. These results highlight how crucial it is to include climate data in early warning systems (Tiranti et al., 2019).

Climate change affects debris flow activity through the combined effects of rising temperatures and modified precipitation patterns and changing sediment availability. Heavy rainfall at high elevations leads to increased slope failure risk because freeze-thaw cycles occur less frequently. The northward movement of debris flow beginning zones requires evaluating hydrometeorological and sediment supply parameters to assess climate vulnerability (Jomelli et al., 2004).

The protective function of mountain forests against rockfalls will decrease because climate change causes forest density and structure to decline and species richness to decrease especially in mid-elevation areas that experience drought.

The high-emission RCP8.5 scenario predicts a significant increase in rockfall frequency and without forest management intervention the damage risk will exceed triple by 2100 (Moos et al., 2021).

The rising occurrence of climate-related geohazards demands integrated assessments which link climatic indicators to geomorphological susceptibility for specific regions. The Susa Valley represents an area of high risk because it features steep terrain and high sediment mobility together with expanding infrastructure in an alpine region. The current research lacks sufficient studies that analyze historical climate patterns in relation to hazard occurrences and project future climate changes under various emission scenarios. The research aims to address the immediate need for better understanding climate variability effects on hazard susceptibility because it will help create more effective risk management and adaptation strategies.

1.2 Problem Statement

The scientific community now acknowledges the link between climate change and geomorphological hazards but most research either studies broad climatic patterns or creates local hazard maps without uniting these perspectives. The Susa Valley's Alpine region demonstrates how steep terrain and climate fluctuations interact yet current research separates these elements which hinders our ability to understand hazard development across time and space.

The majority of hazard assessments depend on fixed topographical characteristics yet fail to consider how shifting climate patterns affect vulnerability levels. The integration of historical hazard data with climate projections remains limited because researchers lack a single framework which can analyze past behavior alongside future risk development.

The research fills this knowledge gap through its multi-hazard analysis which evaluates rockfalls and debris flows and shallow landslides based on their historical and projected susceptibility levels. The research method differs from previous studies because it incorporates elevation classes into its susceptibility framework to enhance topographic control representation. The study incorporates delta temperature (ΔT) as an additional thermal indicator together with daily minimum and maximum temperatures. The research investigates how

thermal patterns interact with precipitation trends to understand their combined impact on hazard behavior which current literature tends to ignore.

1.3 Objectives of the Study

This study aims to investigate the impacts of climate change on geomorphological hazard susceptibility in the Susa Valley by analyzing both historical patterns and future projections. The specific objectives are:

- ✓ To assess long-term trends in temperature (Tmax, Tmin, and ΔT) and precipitation from 1957 to 2024 across different elevation bands;
- ✓ To classify and evaluate the spatial distribution of rockfalls, debris flows, and shallow landslides using susceptibility maps and threshold models;
- ✓ To explore how susceptibility patterns for each hazard type may shift under RCP 4.5 and RCP 8.5 climate scenarios;
- ✓ To incorporate elevation as a spatial conditioning factor in both historical and projected hazard assessments;
- ✓ To examine the combined effects of temperature variation and precipitation intensity on hazard triggering mechanisms;
- ✓ To compare spatiotemporal overlaps and possible hazard cascades across scenarios for better risk understanding.

Chapter 2

Climate Change and Geo Structures

The following sections analyze how climate change affects specific geohazards by focusing on environmental and physical slope instability factors. The sections examine the challenges of predicting future hazard patterns under different climatic scenarios while discussing uncertainties and geographical variations and modeling difficulties.

2.2 Natural Slopes

Multiple elements including slope geometry and vegetation cover and soil and rock types and hydrological conditions and climate affect the natural formation of slopes. The slopes receive special attention in geotechnical research because they directly relate to landslide and rockfall hazards. The natural equilibrium between these factors will be disrupted by climate change which will result in higher slope instability according to Figure 1 (Bračko et al., 2025).

Figure 1 Landslides After Temporary Roadway Intervention, Source: Bračko et al. (2025)

The main reason for slope instability in Alpine regions stems from the breakdown of cryospheric elements including glaciers and permafrost. The removal of mechanical support through glacial retreat and the weakening of slope integrity due to thawing permafrost primarily affects granite terrains at high elevations. The combination of increasing summer temperatures with unpredictable hydrological patterns makes these changes worse while producing more frequent rockfalls and geomorphic adjustments (Castellazzi & Previtali, 2024).

Slope instability results from multiple factors which include geometry and soil composition and vegetation loss and extreme weather events. The strength of saturated clays decreases when heated while slopes with angles between 30 and 40

degrees have the highest risk of failure. The loss of vegetation through wildfire or land use changes or climate stress leads to increased surface erosion and instability. Heavy rainfall near old infrastructure causes pore-water pressure to rise which results in landslides. Post-glacial terrains experience destabilization through the mobilization of debris and collapses which permafrost and glacier changes trigger. The end tipping construction method used in British railway projects serves as an example of infrastructure-induced instability as shown in Figure 2. The embankment instability under wet conditions was frequently caused by this technique (Walker et al., 2022).

Figure 2 Image Showing End Tipping Construction Method Used in British Railway, Source: Walker et al. (2022)

The stability of natural slopes faces negative impacts from climate change because of rising temperatures and modified precipitation patterns and stronger weather events. The strength of clay soils decreases when exposed to warm humid conditions yet sand soils maintain their stability. The comparison shows that fine-textured terrains with moisture-retaining properties are more susceptible to slope (Yavari et al., 2016).

Natural slopes present dangers but specific elements enhance their stability. The binding of soil and reduction of erosion through dense vegetation makes wooded regions more resistant to climatic stress. The stability of slopes depends on permafrost stability until it is disrupted by prolonged warming but slopes with gentle inclines and compacted coarse soils tend to be less prone to failure (Magnin et al., n.d.).

The recent developments in slope stability modeling demonstrate that climate-related factors especially heavy rainfall should be taken into account. The simulation of a failed slope in Slovenia demonstrated that heavy rainfall elevated pore-water pressure and decreased the factor of safety beyond the effects of soil strength modifications. The results demonstrate that hydrological stress plays the most significant role in climate-induced slope failures as shown in Figure 3 which displays

the modeled pore-water pressure distribution throughout the slope after three days of rainfall (Bračko et al., 2022).

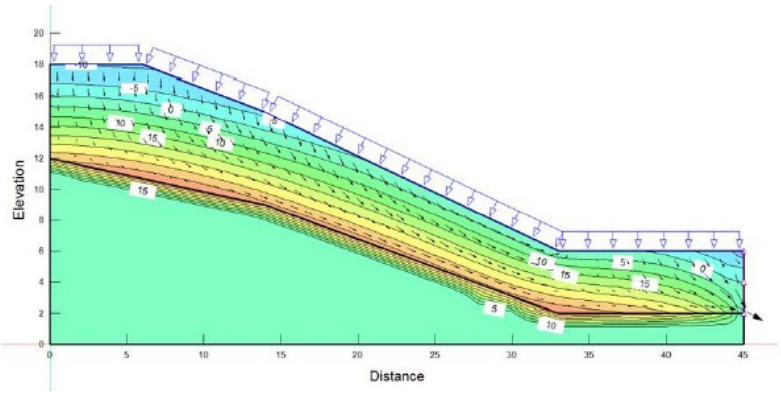

Figure 3 Computed Poor Water Pressure Within the Slope After 3 Days of Rainfall, Source: Bračko et al. (2022)

Experimental flume research has demonstrated the transition from slope failure to granular flow. The research used sand-water mixtures to model slope collapse events. The experimental results demonstrated a sequential transition from retrogressive sliding to unstable flow which produced three distinct layers consisting of a flowing surface and a sliding center and a static foundation. The sand particles in lower strata took longer to settle than water while pore pressure remained slightly above hydrostatic levels. The Cellular Automata model together with other simplified models successfully replicated essential features including runout and deposition (Deangeli, 2008).

2.3 Shallow Landslides

Geotechnical engineering has faced landslides as a significant problem throughout many years. Varnes (1978) developed a complete classification system based on material types (rock, debris, earth) and movement mechanisms (fall, topple, slide, spread, flow, complicated). The framework demonstrates mechanical diversity in slope failures through its emphasis on slow creep to rapid debris flows which enables consistent analysis between different examples. The Yungay landslide of 1970 serves as a notable example of these complex events according to Varnes (1978) (Varnes, 1978).

The study of shallow landslides under changing climate conditions has utilized physically based models together with empirical data. The models show that pyroclastic soils in Italy will have more winter and spring events instead of the previous fall peaks. The Chinese study showed that land use changes had a smaller effect than rainfall intensity did and the future projections indicated a more stable situation. The

research demonstrates that rainfall patterns need to be considered in landslide predictions for climate adaptation (Rianna et al., 2017 ;Guo et al., 2023).

A multidisciplinary study of the 2013 Montescaglioso landslide in southern Italy found that bedrock fractures and saturated zones below the surface were crucial to the collapse. When surface data was scarce, geophysical technologies offered crucial information (Figure 4), highlighting the importance of subsurface imaging for hazard assessment(Calamita et al., 2023).

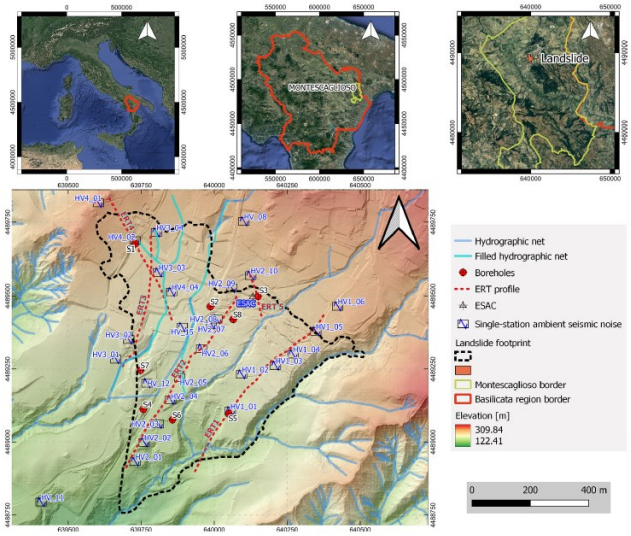

Figure 4 Landslide area and survey locations, Source: Calamita et al. (2023)

According to research on Holocene landslides in Iceland, a large number of them happened right below the old permafrost barrier during the Holocene Thermal Maximum. The work highlights the long-term climatic influence on slope stability by indicating that delayed permafrost thaw may cause deep-seated slope failures even long after glacial retreat (Figure 5). A full landscape view of the Öxnadalur valley with mapped landslide deposits may be found in Figure 6 (Booth & Pétursson, 2025).

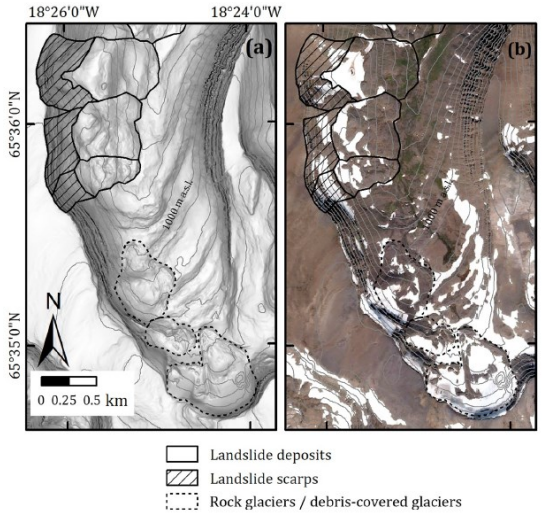

Figure 5 Examples of distinguishing features of bedrock landslides and icy features, Source: Booth & Pétursson. (2025)

The Piemonte region demonstrated the effectiveness of radar-based rainfall monitoring for predicting shallow landslides. Radar data provided better spatial resolution and earlier detection of critical rainfall thresholds than traditional rain gauge networks. The research findings validate the implementation of radar technology in real-time early warning systems for landslide risk management. Figure 6, shows radar rainfall intensity overlays with landslide initiation points during the November 2016 storm event (Cremonini & Tiranti, 2018).

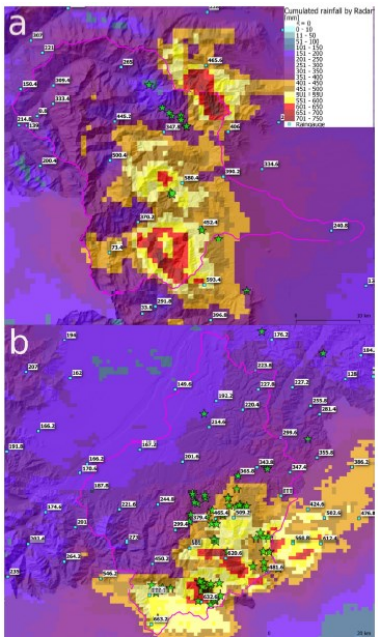

Figure 6 Total rainfall accumulation, estimated by weather radar (grid) and observed by rain gages (values) from 21st to 26th November 2016 in the study areas, Source: Cremonini & Tiranti. (2018)

2.4 Debris flow

The fast-moving mixture of water and sediment in debris flows depends on slope conditions and rainfall patterns and pore pressure levels. The research established water content and slope angle and solid–fluid interactions as fundamental elements which led to contemporary runout modeling and rheological classification (Tiranti & Deangeli, 2015).

The abrupt release of glacial water pockets and buried ice within moraines have been demonstrated to be significant triggers for several debris flow occurrences in the Western Alps' glacial catchments. Notably, some flows happened without any prior precipitation, suggesting that internal glacier dynamics, including ice melt and moraine saturation, are important contributors to the start of debris movement. As a result of the melting of the ice-cored moraine, 15,000 m^3 of debris were mobilized in Forno Alpi Graie. This event is visually documented in Figure 7, showing the coarse debris accumulation in the village of Forno Alpi Graie after the 24 September 1993 debris flow (Chiarle et al., 2007).

Figure 7 Coarse debris accumulation in the village of Forno Alpi Graie, Source: Chiarle et al. (2007)

Alpine basins damaged by wildfires exhibit increased susceptibility to debris flows as a result of hydrological changes and vegetation loss. Within a year following fire incidents, floods in the Western Italian Alps have been caused by rainfall as little as 15 to 30 mm/h. This emphasizes how important early warning systems are in the post-fire environment. Figure 8, illustrates the geological context of one such basin, showing an interpolated lithological map of the Rio Casella area based on Piemonte's regional geological map(Tiranti et al., 2021).

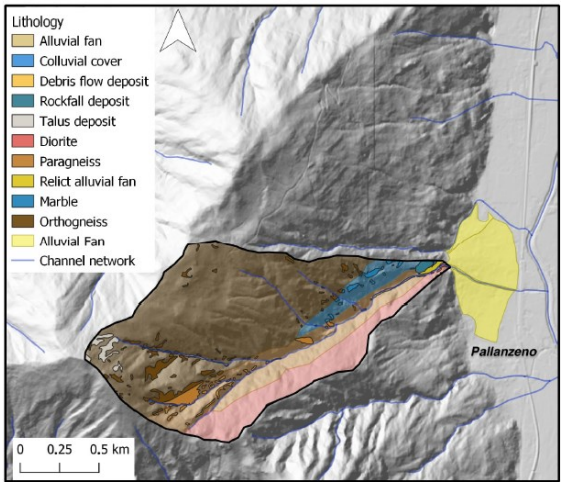

Figure 8 Geological interpolated map of Rio, Source: Tiranti et al. (2021)

Pudasaini (2012) developed an extensive model to simulate the complex two-phase behavior of debris flows. The model distinguishes itself from previous models by modeling solid-fluid phase interactions through interfacial momentum exchange and includes non-Newtonian viscous stress and virtual mass effects and generalized drag. The generalized expression for interfacial force density (Ms) represents the relative motion and acceleration between phases which stands as a major advancement. The model achieves enhanced capability to simulate realistic debris flow dynamics through this advanced formulation.

$$\mathbf{M}_s = \mathbf{M}_D + \mathbf{M}_{VM} = C_{DG}(\mathbf{u}_f - \mathbf{u}_s)|\mathbf{u}_f - \mathbf{u}_s| + C_{VMG}\frac{d}{dt}(\mathbf{u}_f - \mathbf{u}_s),$$

Where CDG is the generalized drag coefficient and, CVMG is the generalized virtual mass coefficient. Generalized drag force. The viscous drag, MD, can be written as M_D = asFD/Bd, where FD is the drag force (Bd is the particle volume), which in classical form reads (Pudasaini, 2012).

The hydrodynamic model provided by Hübl et al. (2009) incorporates both flow height and velocity through the Froude number to calculate impact forces on protective barriers, hence improving debris flow mitigation design. The model is more accurate than conventional hydrostatic methods and offers scale-independent estimations of impact pressure, particularly under dynamic flow settings. It has been validated by field observations and laboratory tests (Hübl et al., n.d.).

As climate change continues, Stoffel et al. (2014) predict that debris-flow activity in the Alps will change dramatically. One important finding is that future occurrences are probably going to be more common in the spring and fall, while summer events might become less frequent. This is because of both snowmelt contributions and an

increase in heavy precipitation during the shoulder seasons. Destabilized permafrost bodies, increased sediment availability, and more frequent extreme precipitation events are also predicted to increase the size of debris flows (Stoffel et al., 2014).

2.5 Rockfall

A higher likelihood of large-volume occurrences is implied by the power-law volume-frequency distribution of rockfalls, which has lower b-values (0.4–0.6) than landslides (~1.2). This recurring pattern is found when inventories from worldwide, Yosemite, and Grenoble databases are analyzed. The behavior of rockfall is significantly influenced by the mechanical characteristics of the rock mass, especially cohesiveness and friction (Dussauge et al., 2003).

To map rockfall susceptibility in the Alpine region, Tiranti et al. (2023) created a GIS-based model that included topography and climatic factors such as slope, elevation, mean annual precipitation (MAP), daily thermal excursion (ATE), and simplified lithology. They discovered that regions with slopes between 30° and 70°, ATE temperatures between 5 and 8 °C, and MAP measurements between 1100 and 1700 mm accounted for almost 70% of rockfalls. As a mitigating factor, forest cover was incorporated, especially for exposed road networks. The most susceptible areas are indicated in dark red, as seen in Figure 9. This study's consideration of forest cover as a mitigating factor, particularly when assessing the exposure of road networks, is one of its important features (Tiranti et al., 2023).

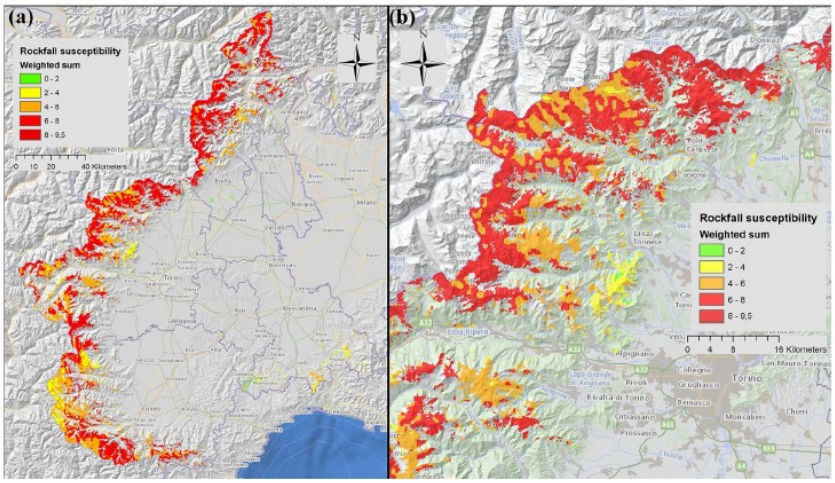

Figure 9 Rockfall susceptibility map of Piemonte weighted sum of all parameters), Source: Tiranti et al. (2023)

Using 30 years of historical and predicted climate data (1990–2100), Mirhadi et al. (2023) examined 14 years of rockfall data along a British Columbian railway. Using von Mises circular distributions, they found that 78% of rockfall episodes were strongly

correlated with precipitation (r = 0.975). There would be a noticeable seasonal shift, with rockfalls predicted to increase 9–19% in the winter and decrease 24% in the spring under RCP 4.5 (Mirhadi & Macciotta, 2023).

A GIS-based application called Rockfall Analyst (RA) combines raster modeling and 3D rockfall trajectory simulation to evaluate hazards in mountainous regions. RA, which is built into ArcGIS, simulates rolling, bouncing, and sliding rocks using a lumped-mass method based on surface and topography data. The tool demonstrated notable frequency and energy reductions behind a 5-meter virtual barrier in a case study along the Canadian Pacific Railway by simulating over 1000 trajectories from four source zones. As shown in Figure 10, the spatial reduction in rockfall activity confirms the tool's value in engineering design and hazard mitigation planning (Lan et al., 2007).

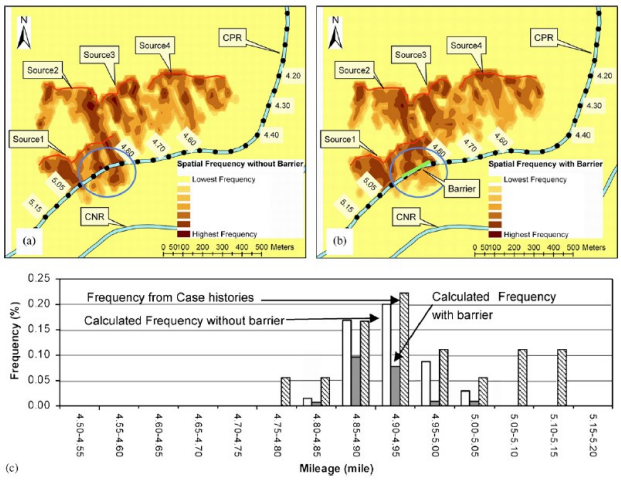

Figure 10 Distribution of rockfalls Spatial Frequency. A 5m high barrier is set near the region, Source: Lan et al. (2007)

The impact of historical changes in land use and land cover (LULC) on the risk of rockfall close to Crolles, Grenoble, was investigated by Lopez-Saez et al. (2016). They discovered that afforestation significantly extended return durations for smaller blocks using RockyFor3D modeling and reconstructed LULC maps from 1850 to 2013. For example, the return period for 1.2 m^3 blocks increased from 143 years in 1850 to 5000 years in 2013, demonstrating the forest cover's long-term protective function (Lopez-Saez et al., 2016).

By Eurocode 7, Marchelli and Deangeli (2022) presented an analytical design approach for reinforced earth embankments. Their methodology computes kinetic energy absorption through compaction and interface friction and estimates the minimal embankment height. According to sensitivity analysis, friction can waste up to 25% of energy, allowing for effective designs that don't entirely depend on numerical simulation (Marchelli & Deangeli, 2022).

2.6 Climate Drivers

The analysis of this section focuses on climatic drivers through temperature and precipitation patterns. The two elements play a major role in different geo-hazards so they need thorough examination.

2.6.1 Temperature:

The Rochers de Valabres study in France demonstrated that daily heat cycling with ±8 °C sinusoidal changes could produce rock displacements of 1.5 mm over days. The field monitoring data showed that micro-movements occurred three hours after temperature peaks thus indicating thermal fluctuations play a vital role in long-term slope degradation(Gunzburger et al., 2005).

According to Shibasaki et al. (2016), declining ground temperatures caused shallow landslides in Japan to accelerate in the fall and winter. Cooling to 9 °C decreased shear strength and produced creep under continuous load, according to lab tests conducted on smectite-rich soils. This highlights the importance of temperature in stability evaluations by offering experimental proof that thermal changes alone can cause slope displacement (Shibasaki et al., 2016).

Rockfalls in Switzerland, Mont Blanc, and New Zealand were studied by Allen et al. (2013). They discovered that most Swiss incidents occurred during periods of intense summer heat. Trends of long-term warming were also noted at high-altitude locations such as Jungfraujoch. According to these findings, rockfalls may be directly caused by thermal extremes, especially in Alpine areas that are influenced by permafrost. As shown in Figure 11, the frequency of warm days before rockfall events in the Swiss Alps greatly exceeds climatological expectations (Allen & Huggel, 2013).

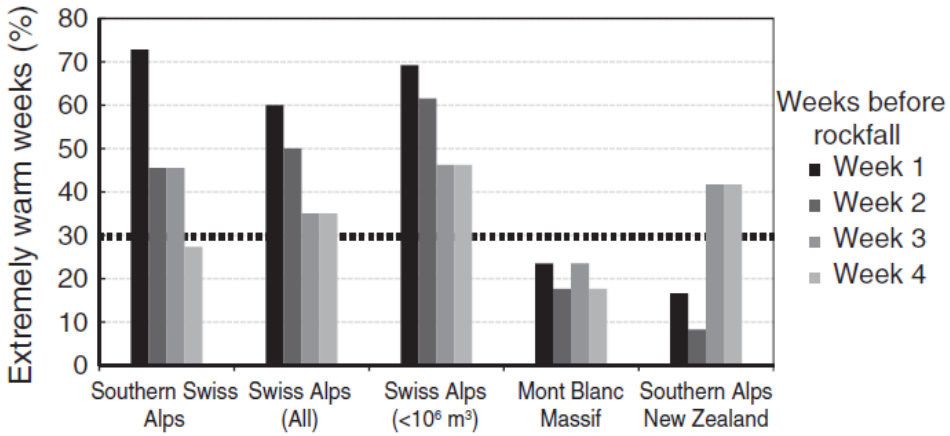

Figure 11 For the four successive 7-day periods leading up to each rockfall, the observed, Source: Allen & Huggel. (2013)

Loche and Scaringi (2025) used national landslide inventories and MODIS satellite data to predict landslide susceptibility in more than 100,000 slope units in Italy. The GAM model showed that there was a clear correlation between enhanced instability and higher land surface temperatures, especially in smectite-rich terrains. Temperature plays a crucial role in climate-related slope failures, since field validation verified that warming reactivated previous landslides (Loche & Scaringi, 2025).

By combining rainfall and freezing level height, Ponziani et al. (2020) developed the Debris Flow Indicator (DFI) to enhance early warnings for summer debris flows. The combined indicator greatly increased accuracy, but rainfall alone lacked predictive value, according to an analysis of 18 incidents in the Aosta Valley. The importance of incorporating temperature-related factors is demonstrated by the DFI's current inclusion in the region's operational warning system (Ponziani et al., 2020).

2.6.2 Precipitation:

According to Chien-Yuan et al.'s (2005) analysis of 61 debris flows in Taiwan, 60% of them happened within an hour of the hourly rainfall peak. They distinguished between two forms of rainfall, each with a distinct threshold: intermittent and continuous. Slopes were more vulnerable after the Chi-Chi earthquake in 1999. They used these insights to create empirical rainfall thresholds that can be monitored in real time using common rain gauges (Chien-Yuan et al., 2005).

Using high-resolution rainfall data, Iadanza et al. (2016) investigated more than 260 landslides in Trento, Italy. To further characterize triggering events, they established the Critical Dry Period. They also presented two models: a unique IRP–DRP model and the traditional Intensity–Duration (I–D) model. The latter offered more accuracy for brief, powerful storms that are typical in Alpine regions by concentrating on event-critical rainfall and its return duration. As shown in Figure 12, it better identifies triggering rainfall and reduces false alarms compared to the I–D model (Iadanza et al., 2016).

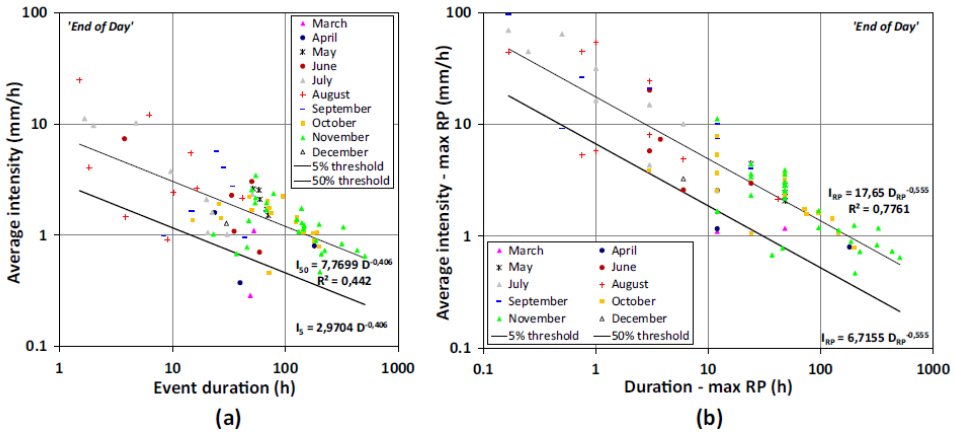

Figure 12 (a) Intensity–duration thresholds (b) IRP–DRP thresholds, Sources: Iadanza et al. (2016)

Over 8,000 rockfalls and daily rainfall in Tenerife and Gran Canaria from 2010 to 2016 were examined by Melillo et al. (2020). They determined empirical ED thresholds by bootstrapping and the CTRL-T approach. The findings demonstrated seasonal clustering (October–March) and different island responses, with Tenerife requiring more severe rainfall and Gran Canaria experiencing rockfalls after shorter storms, indicating varying climatic sensitivities (Melillo et al., 2020).

Using 12 trap nets, Krautblatter and Moser (2009) tracked rockfalls in the Reintal Valley, Germany, over a four-year period. They discovered that when 30-minute rainfall surpassed 9–13 mm, rockfall rates sharply increased. The abrupt, explosive nature of rain-induced rockfalls was highlighted by their three logistic models (r1–r3), which represented nonlinear responses with R2 up to 0.99. The explosive nature of rain-triggered rockfall occurrences is captured in Figure 13, which shows that rockfall intensity stays low until a crucial rainfall threshold is achieved, at which point the response curve jumps abruptly (Krautblatter & Moser, 2009)

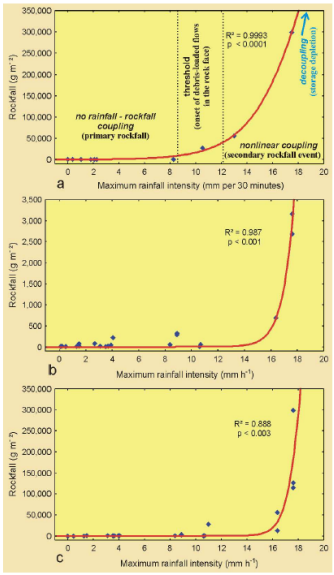

Figure 13 Rockfall response function of a single net, Sources: Krautblatter & Moser. (2009)

Using quantile regression and Mann-Kendall tests, Mazzoglio et al. (2025) evaluated changes in short-duration rainfall extremes throughout Italy. One-hour high-intensity rainfall increased significantly in upper quantiles (0.95–0.99) between 1960 and 2022, especially in Sardinia and the north. 24-hour trends, on the other hand, were less reliable. These results highlight the necessity of taking upper extremes into account when planning for climate risk. Six national maps are used in Figure 14, to illustrate these tendencies. It draws attention to the fact that short-duration, high-intensity rainfall is increasing dramatically, particularly in the north and some parts of the south, indicating a higher danger of hydrogeology in these regions (Mazzoglio et al., 2025).

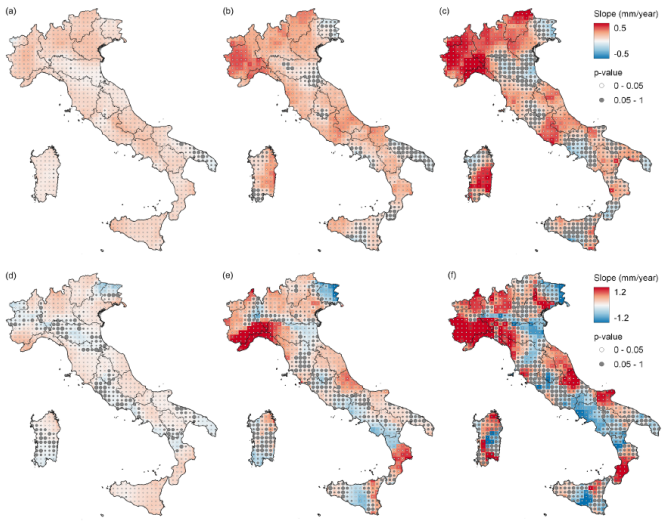

Figure 14 The basemap of the quantile regressi, Sources: Mazzoglio et al. (2025)

Chapter 3

Presentation Of Case Study

3.1 Description of Study Area

One of Italy's most geologically and geomorphologically complicated mountainous areas is the Susa Valley, which is situated in the Piedmont Region in northwest Italy, in the western sector of the Alps. The valley has long been a natural and physical link between Italy and continental Europe because of its advantageous location along the French border, which creates a significant trans-Alpine corridor. As a left tributary of the Po River, the Dora Riparia River runs parallel to the valley's main axis and is essential to its depositional and erosional processes.

3.1.1 Geology and Metamorphism:

The Susa Valley runs through the Western Alpine band's inner sector where it passes through both oceanic and continental metamorphic strata according to geotectonic (Figure 15). The Penninic Domain contains the Dora-Maira Massif together with the Internal and External Piedmont Zones which have experienced metamorphism. The lithology contains numerous minerals which have undergone high-pressure (HP) or ultra-high-pressure (UHP) metamorphism including carbonate-rich calcschists, marbles, serpentinites, orthogneiss and micaschists. The P-T evolution of these rocks provides essential information about slope material thermal-mechanical responses to climatic stress through exhumation and subduction processes (Cadoppi et al., 2007).

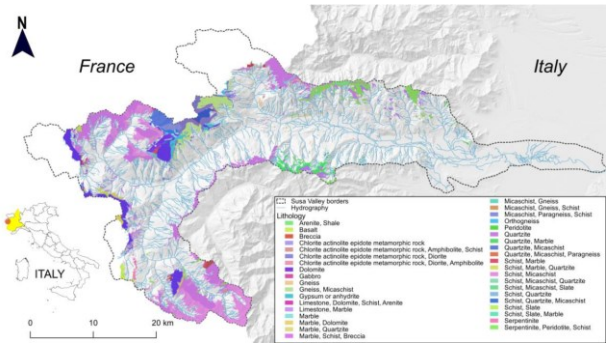

Figure 15 Lithological map of the Susa Valley showing major metamorphic rock units within the study area Source: Tiranti (2024)

3.1.2 Tectonic Structure and Shear Zones:

A polyphase tectonic border between the Internal and External Piedmont Zones, the Susa Shear Zone (SSZ) is a significant structural feature of the region. This shear zone has a block-in-matrix structure and widespread mylonitic foliations, which are signs of several stages of deformation. The SSZ may be important in directing the geographical distribution of cracks and discontinuities, which in turn affect water penetration and the precipitation of rockfall events, according to structural mapping (Ghignone et al., 2024).

3.1.3 Geomorphology and Surficial Deposits:

The Susa Valley shows complex geomorphological features because of tectonostratigraphic variations and Quaternary glacial activities. The southern part of the valley consists of calcschists and oceanic metabasites from the Piemontese region whereas the northern part consists of gneisses, micaschists and metabasites of polymetamorphic origin. The Pleistocene glaciers shaped the valley landscape through their erosive and depositional activities which produced U-shaped valleys and glacial confluences and morainic accumulations. The glacial processes created slope dynamic changes through the unloading effects which occurred during glacier retreat. The valley floor together with its slopes contains Quaternary deposits that consist of talus and landslide debris and lacustrine sediments which were formed by past landslide dams (Borgogno Mondino et al., 2009).

3.1.4 Climate Conditions:

The Susa Valley's orographic location largely determines its climate, which is Mediterranean-subcoastal with autumnal peak precipitation and spring secondary

maximums and comparatively dry summers. Snowfall averages 144 cm per year, mostly in the winter, and precipitation averages about 800 mm. The amount of rainfall that occurs each day is usually moderate, seldom going above 20 mm. Due to less influence from both oceanic and Mediterranean air masses, the Susa Valley is more xeric than other regions of the Piedmont Alps, particularly in its inner axial portion (Fratianni et al., 2009).

3.1.5 Geohazards and Historical Events:

Many geo-hydrological hazards, especially debris flows and shallow landslides, which are frequently brought on by heavy precipitation events, have occurred in the Susa Valley. On August 13, 2023, a localized convective storm in the upper Frejus basin caused a colata detritica (debris flow) that affected the alluvial fan area in Bardonecchia. This was one of the most recent and noteworthy debris-flow events, according to ARPA Piemonte. Based on historical reconstructions of torrential activity and sediment connectivity analyses, this event is consistent with the valley's high susceptibility to mass movement processes. In particular, ARPA's assessments classify sub-basins based on debris-flow susceptibility (ECM, BCM, GCM), using morphometric and hydrological indicators, as well as thresholds of critical rainfall (e.g., ECM: 20 mm/h on clay-producing rocks like phyllatic schists; GCM: 30 mm/h in limestone-rich basins; BCM: 50 mm/h in resistant lithologies such as gneisses and granitoids;(Tiranti et al., 2014)), using morphometric and hydrological indicators, as well as thresholds of critical rainfall (Cremonini, 2023).

3.2 Climatic Characteristics

The assessment of climatic conditions on slope instability in the Susa Valley used multiple long-term meteorological datasets. The datasets contain historical observations together with projected future values of climate variables that affect hydrological and geomorphological processes.

- The **historical precipitation data** were acquired as high-resolution gridded time-series in NetCDF format, spanning from 1957 to 2024. Each grid cell contains daily cumulative precipitation values for northwestern Italy, which allows for consistent spatial and temporal comparisons throughout the study area. These data were obtained from regional environmental agencies and are frequently employed in climatological and hydrological analyses.

- The **historical temperature data** contains daily maximum and minimum values which are available in NetCDF format from 1957 to 2024. The datasets contain daily temperature values spread across space which enables the computation of derived indices including the diurnal temperature range (ΔT) that serves as an essential indicator for thermal stress and frost-related weathering processes.
- **Future climate projections** from 2025 to 2100 and include three essential climate variables: monthly total precipitation and monthly average maximum temperature and monthly average minimum temperature. The datasets originate from global climate models (GCMs) that use two greenhouse gas emission scenarios: RCP 4.5 (moderate emissions) and RCP 8.5 (high emissions). The future data exist as GeoTIFF raster layers which present annual stacks of monthly values thus enabling integration into geospatial workflows.

The evaluation of past and future climatic influences on slope stability becomes possible through the analysis of historical and projected datasets. Daily-resolution records help identify short-term triggers and thresholds (e.g., extreme rainfall or ΔT anomalies) but monthly future projections reveal long-term trends and climate-driven risk shifts.

3.3 Source of data

The research data originated from dependable open-access repositories and official institutions which maintained scientific credibility and spatial consistency. The data consist of three primary categories.

- **Climatic data** were sourced from regional environmental agencies for historical observations, including daily precipitation and temperature records over northwestern Italy. Future climate projections were acquired from the **Coupled Model Intercomparison Project Phase 6 (CMIP6)** under two greenhouse gas emission scenarios: **RCP 4.5** and **RCP 8.5**. These datasets serve as the basis for analyzing both short-term variability and long-term climatic trends affecting slope stability.
- **Topographic and geospatial data** included high-resolution digital elevation models (DEM) and administrative boundary shapefiles. These were obtained from national geospatial portals and used to define the study area, derive terrain parameters (e.g., slope, aspect), and standardize the spatial extent of the analysis.

- **Susceptibility maps** for different slope failure types including rockfall, shallow landslides and debris flows were obtained from regional hazard zoning projects and previous academic studies. The classified raster layers allowed for spatial correlation between hazard-prone areas and climate-related indices.

The datasets required necessary preprocessing to achieve format conversion and coordinate system unification and resolution harmonization before they could be analyzed together in a single geospatial framework.

3.4 Spatial data overview

The spatial analysis of rockfall, shallow landslide, and debris flow susceptibility in the Susa Valley required the use of raster and vector geospatial datasets. The datasets offer fundamental topographic information which helps identify spatial patterns of hazard susceptibility for different slope failure types.

- **Digital Elevation Model (DEM):** A high-resolution (10-meter) raster elevation model was employed to derive slope, aspect, and elevation classes. These terrain variables are among the primary conditioning factors influencing slope instability and were used for zonal classification across the study area.
- **Study Area Boundary:** The Susa Valley was defined by a vector shapefile that served as the geographic boundary. The boundary functioned as a spatial mask to clip all climatic and hazard-related layers which maintained analytical consistency within the region of interest.
- **Susceptibility Maps**
  A set of three classified raster maps was used to represent terrain susceptibility to distinct types of slope failures within the Susa Valley. Each map was developed based on different physical criteria and classification systems adapted to the nature of the corresponding phenomenon.
  - ✓ **Rockfall Susceptibility Map:** The study area receives classification through an ordinal susceptibility map which ranges from very low (1) to very high (5). The classification process relies on topographic and structural features including slope angle and lithology and fracture intensity. The susceptibility map received spatial correlation with climatic triggers through the addition of rainfall exceedance data and thermal indices. The analysis

revealed areas where high rockfall sensitivity meets essential environmental thresholds(Tiranti et al., 2023).

- ✓ **Shallow Landslide Susceptibility Map**: The shallow landslide map uses a three-class system (*low*, *moderate*, and *high* susceptibility) based on surface processes, soil depth, slope gradient, and vegetation cover. It supports comparative analysis of slope responses to rainfall intensity and seasonal conditions, particularly in colluvial and soil-mantled hillslopes (Tiranti et al., 2019)
- ✓ **Debris Flow Susceptibility Map:** This map categorizes catchments into three susceptibility classes according to the clay-generating potential of the dominant lithologies in each catchment, following the methodology developed by (Tiranti et al., 2014), The three classes include:

  ECM (Excellent Clay-Maker): susceptible at 20 mm/h rainfall thresholds; composed of easily weatherable rocks such as phylladic calc-schists, black shales, and phyllades.

  GCM (Good Clay-Maker): with a 30 mm/h threshold; predominantly limestone and dolostone catchments.

  BCM (Bad Clay-Maker): requiring 50 mm/h rainfall to trigger events; composed of resistant lithologies such as granitoids, quartzites, gneisses, mica-schists, and ophiolites (Tiranti et al., 2014).

The susceptibility layers in Figure16 received spatial alignment with climatic datasets and topographic parameters to determine the potential overlap between hazard-prone zones and climate-induced triggers. The analysis of multiple maps enabled researchers to understand how different slope instability types would react to present and future environmental conditions.

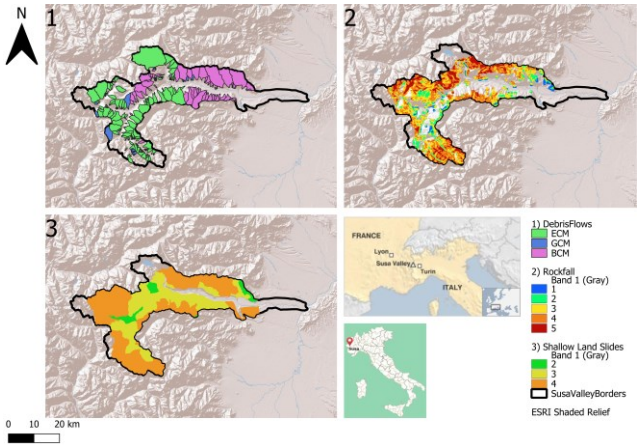

Figure 16 Susceptibility maps for debris flows (ECM, GCM, BCM), rockfalls (five-class scale), and shallow landslides (three classes) in the Susa Valley. All layers are displayed over a shaded relief base map, with study area boundaries outlined in black. Inset maps show the regional location within Italy

Chapter 4

Data, Processing, Results

4.1 Introduction

In this chapter, the data processing methods and analytical results from past and future climate datasets, with a focus on temperature and precipitation variables, are described. The research aims to study how climate factors affect the risk of geo-hazards including shallow landslides, rockfalls and debris flows across elevation zones in the Susa Valley while assessing future risk changes.

The analysis consists of two primary sections.

1) **Historical climate analysis**, covering the period from 1957 to 2024,
2) **Future climate projections**, based on CMIP6 models under RCP 4.5 and RCP 8.5 scenarios from 2025 to 2100.

For temperature, the following metrics were computed and analyzed:

- **Monthly and daily average delta temperatures** were calculated and compared.
- **Monthly delta temperature (ΔT)** was extracted.
- **Monthly maximum and minimum temperatures** were also derived.

With a focus on rockfall sensitivity, these temperature indicators were examined across various elevation bands in order to identify critical thresholds and areas that are especially vulnerable to thermally induced slope instability.

The following analyses were carried out for precipitation:

- **24-hour and 48-hour cumulative rainfall** was calculated monthly.
- **Return period analysis** was conducted for June, July, and August to identify critical rainfall events.
- **Hourly rainfall intensity** was estimated in order to assess **debris flow susceptibility**.
- The effects of 24/48-hour cumulative rainfall on **shallow landslides** and **rockfalls** were evaluated.

Finally, these climatic variables were integrated with slope failure susceptibility maps using zonal statistics. This approach enabled the spatial correlation analysis between extreme temperature and precipitation events and areas characterized by high slope failure susceptibility. The resulting analysis provides a comprehensive understanding of both current and projected hazard exposure within the study area.

4.2 Historical Temperature Analysis

4.2.1 Monthly and Daily Average Delta Temperatures

In the initial stage of the temperature analysis, daily maximum (Tmax) and minimum (Tmin) temperature values were extracted for the period from December 1, 1957, to December 1, 2024. These datasets were then used to calculate two key indicators:

- Daily average delta temperature (ΔT = Tmax − Tmin for each day)
- Monthly average delta temperature (the mean ΔT over each month)

In order to reduce data volume and improve computational efficiency, the initial daily ΔT values were spatially averaged throughout the study area (Susa Valley) due to the NetCDF files' large size and high spatial resolution. A representative and well-structured dataset was produced, and it was then exported to Excel for efficient analysis and visualization. Plotting and comparing daily and monthly average ΔT trends improved the evaluation of long-term thermal dynamics (Figures 17 and 18).

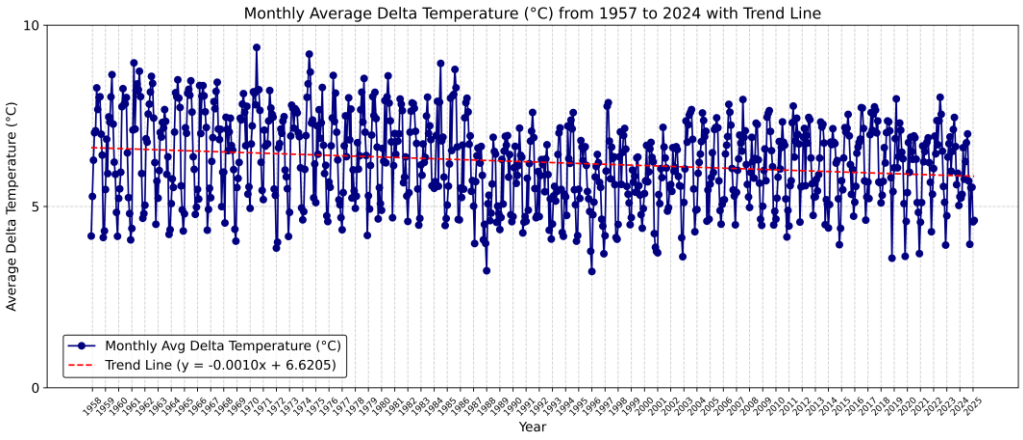

Figure 17_Monthly Average Delta Temperature (°C) from 1957 to 2024 with Trend Line

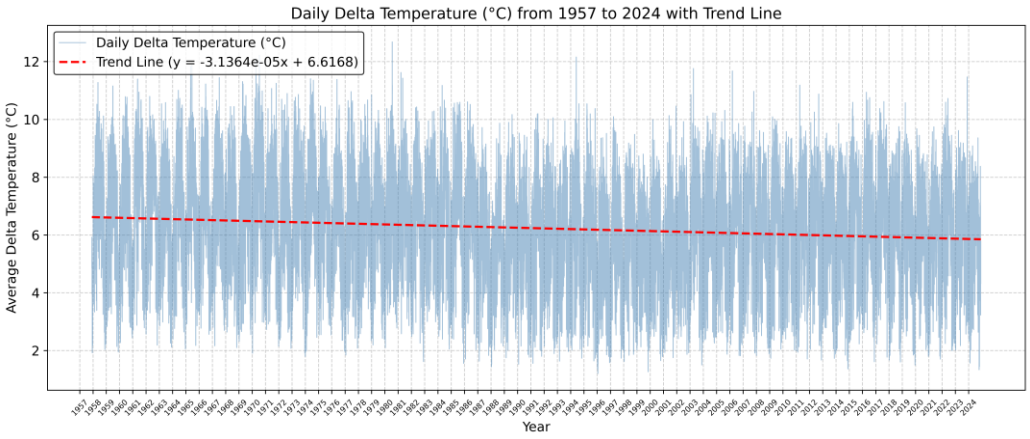

Figure 18_Daily Delta Temperature (°C) from 1957 to 2024 with Trend Line

The difference between maximum and minimum temperatures gradually decreases over time, according to trend analyses of daily and monthly average ΔT from 1957 to 2024 (Figures 17 and 18). The overall pattern indicates a consistent narrowing of ΔT over the recorded period, despite short-term fluctuations.

The following charts (Figures 19, 20, and 21) show monthly trend analyses in addition to the aggregated daily data to provide a more thorough understanding of average temperature variations.

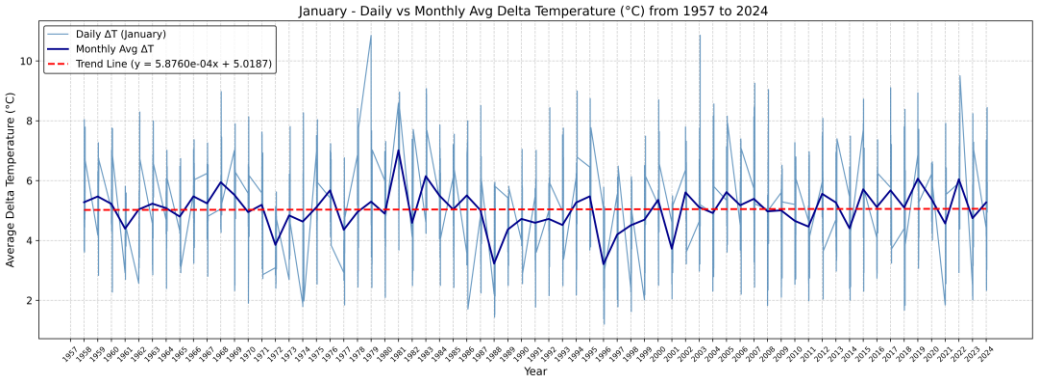

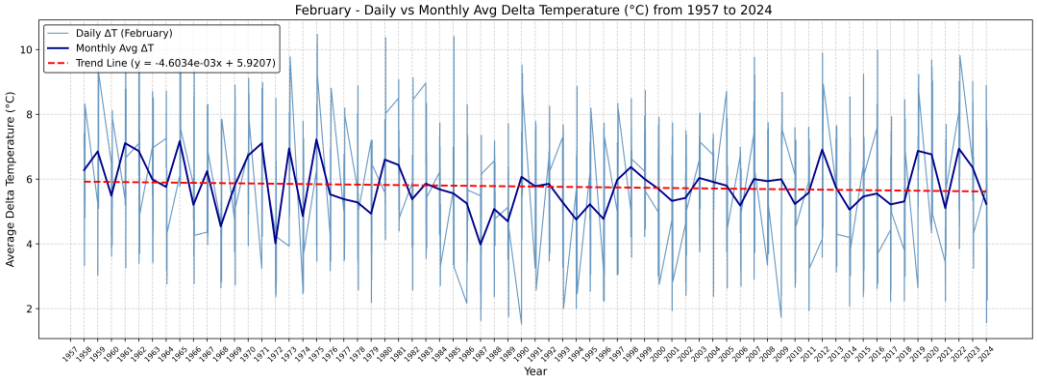

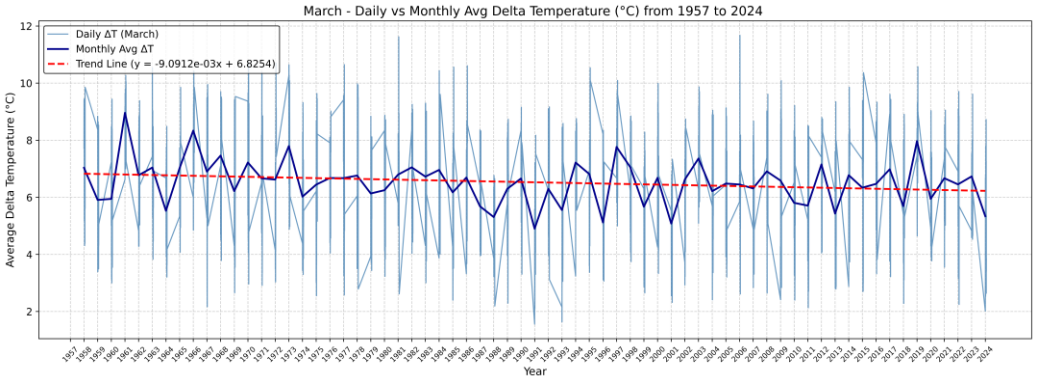

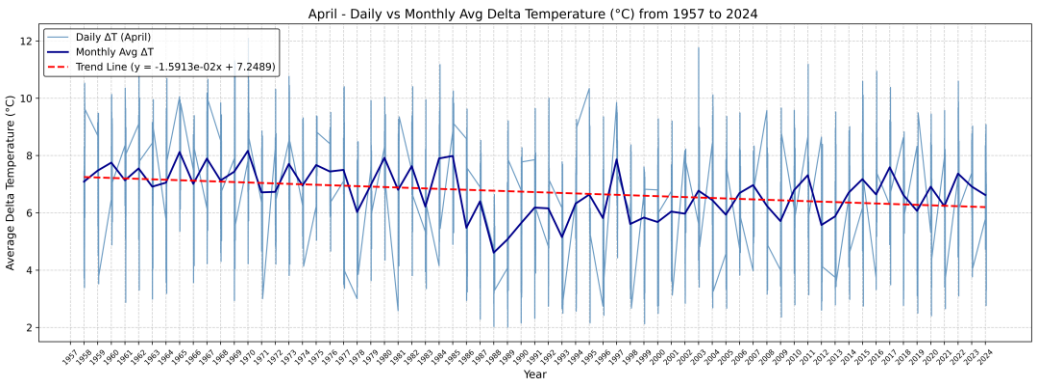

Figure 19_Monthly Average Delta Temperature (°C) from 1957 to 2024 with Trend Line_ Jan to Apr

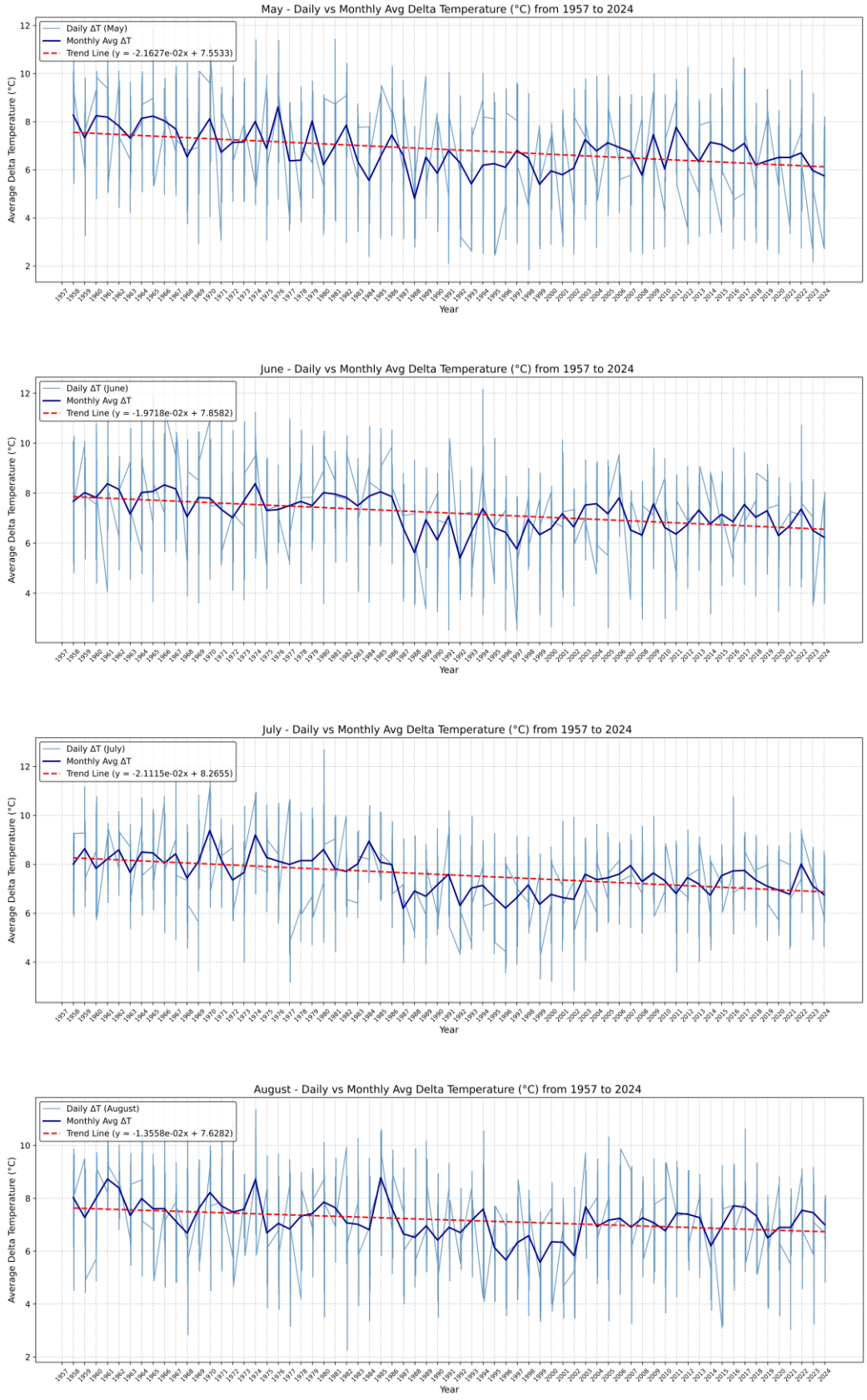

Figure 20_Monthly Average Delta Temperature (°C) from 1957 to 2024 with Trend Line_ May to Aug

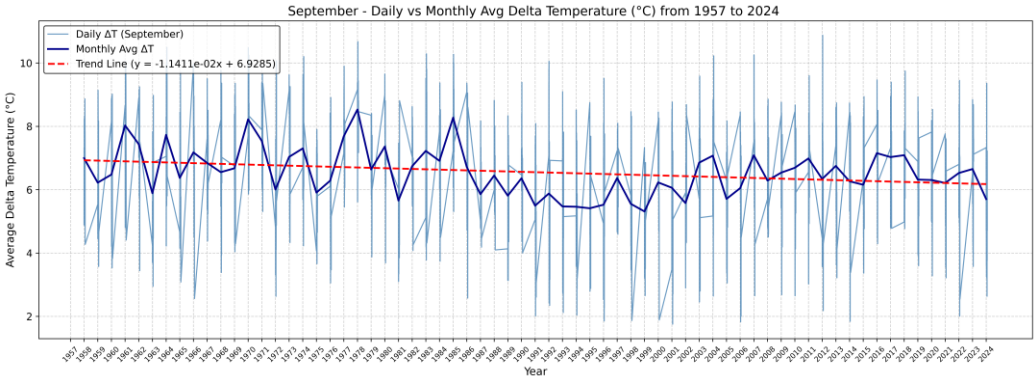

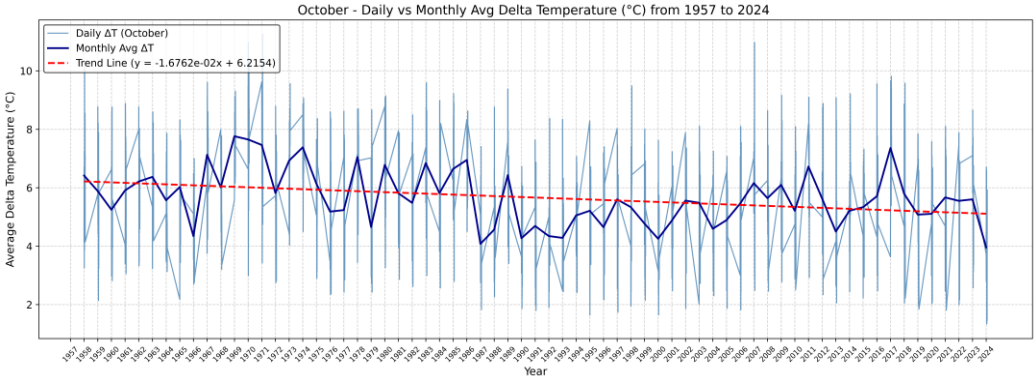

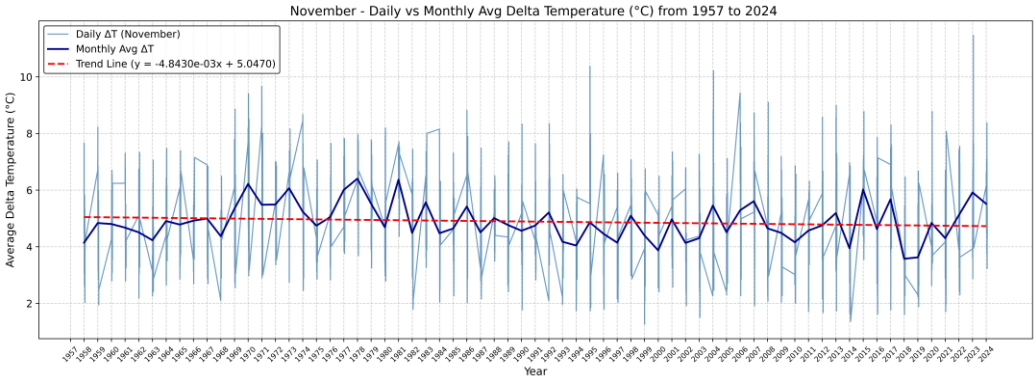

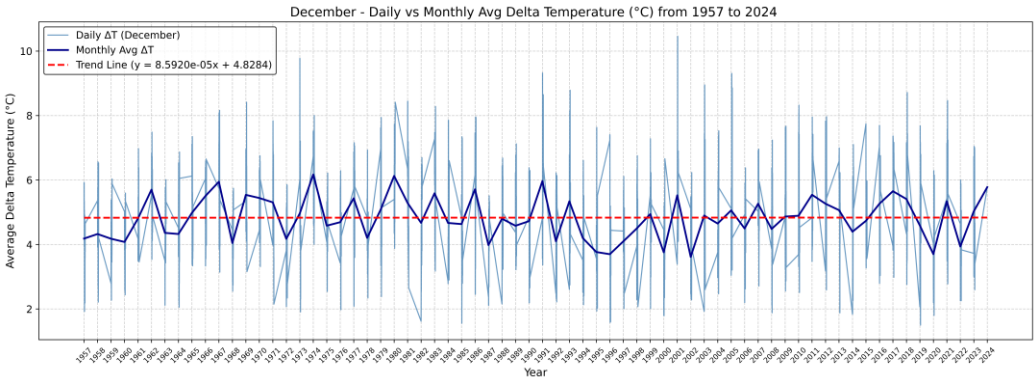

Figure 21_Monthly Average Delta Temperature (°C) from 1957 to 2024 with Trend Line_ Sep to Dec

The monthly average delta temperature (ΔT) trends from 1957 to 2024 indicate a downward trend in the most of the months, as shown in Figures 19, 20, and 21. However, January and December exhibit positive slopes, indicating a minor rise in ΔT throughout the winter.

4.2.2 Monthly Delta Temperature (ΔT)

A Python script that obtained monthly maximum and minimum temperatures from 1957 to 2024 was used to construct the dataset. Long-term changes in monthly thermal variability were assessed using the Delta Temperature (ΔT), which is the difference between these two values. ΔT, as compared with absolute temperature trends, shows how the difference between monthly maximum and minimum temperatures has changed over time as opposed to reflecting absolute warming or cooling trends. On the other hand, an increasing ΔT may indicate drier conditions, stronger solar input, or less cloud cover, all of which increase temperature contrasts. A declining ΔT indicates faster increases in minimum temperatures, a recognized signal of ongoing climatic shifts. Figure 22 illustrates a slight increase in the ΔT trend from 1957 to 2024.

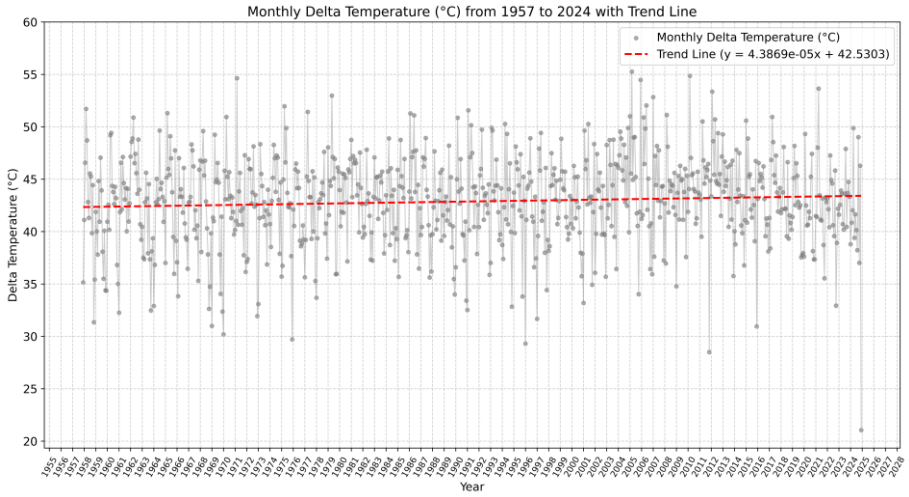

Figure 22_Monthly Delta Temperature (°C) from 1957 to 2024 with Trend Line

Monthly delta temperature (ΔT) values from 1957 to 2024 are shown in Figure 22, alongside a linear trend line. during the period, the data points show significant short-term fluctuations, which are indicative of the monthly thermal amplitude's associated variability. However, a minor rise in ΔT over time is apparent by the trend line's slight positive slope. The slight positive slope of the trend line reflects a small but measurable change in ΔT throughout the study period. Figures 23 to 26 show the results of a separate analysis of the ΔT values for each month over several years in order to better examine these conditions.

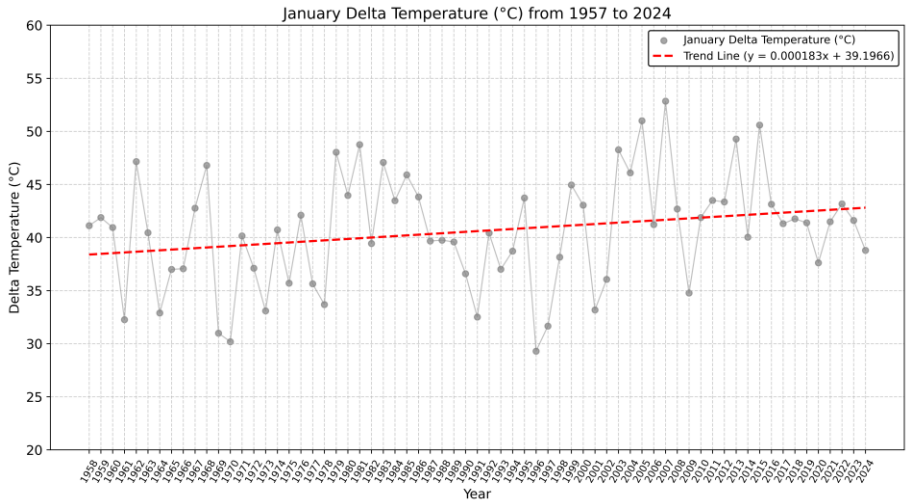

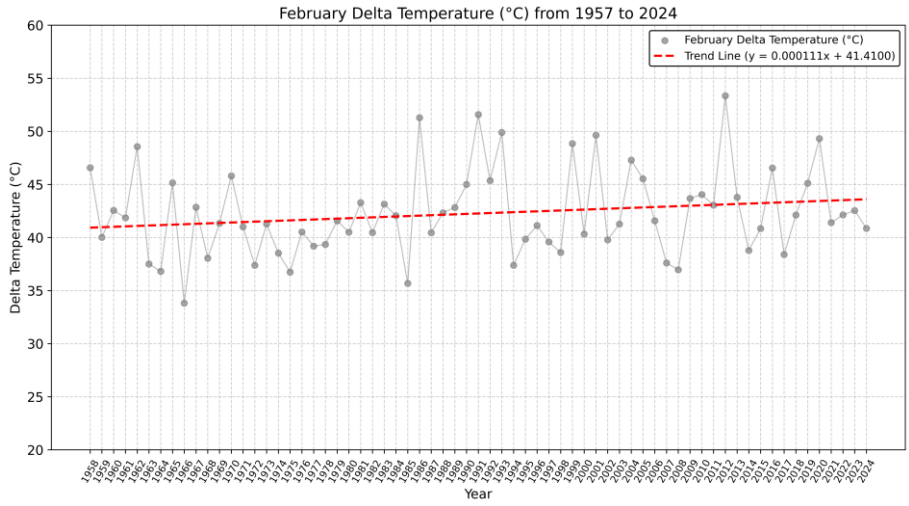

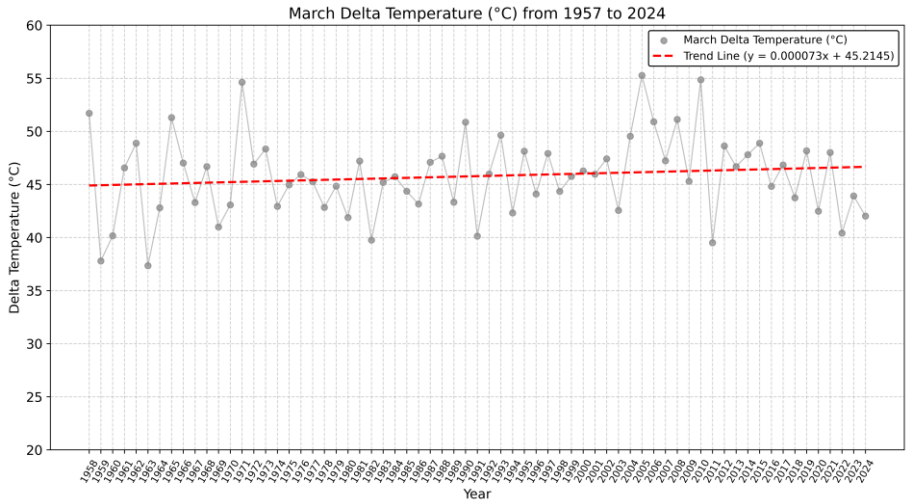

Figure 23_Monthly Delta Temperature (°C) from 1957 to 2024 with Trend Line_ Jan to Mar

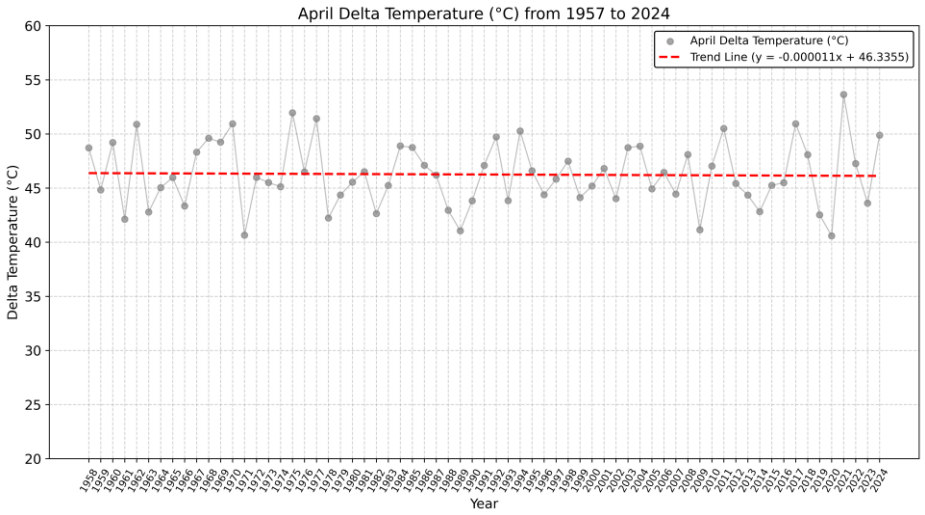

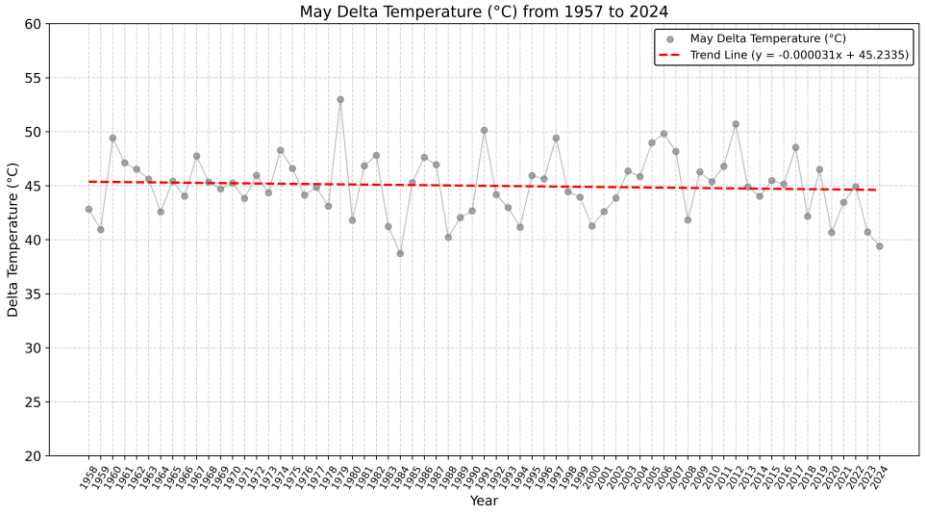

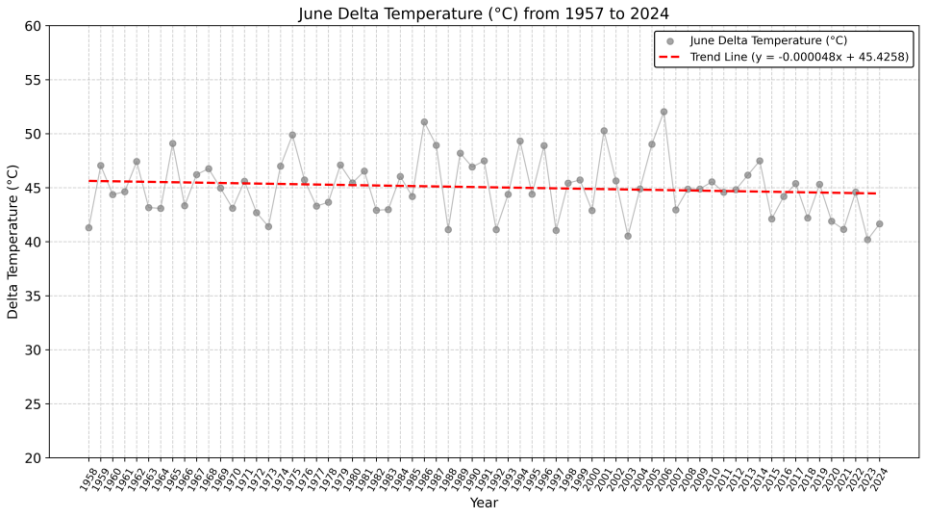

Figure 24_Monthly Delta Temperature (°C) from 1957 to 2024 with Trend Line_ Apr to Jun

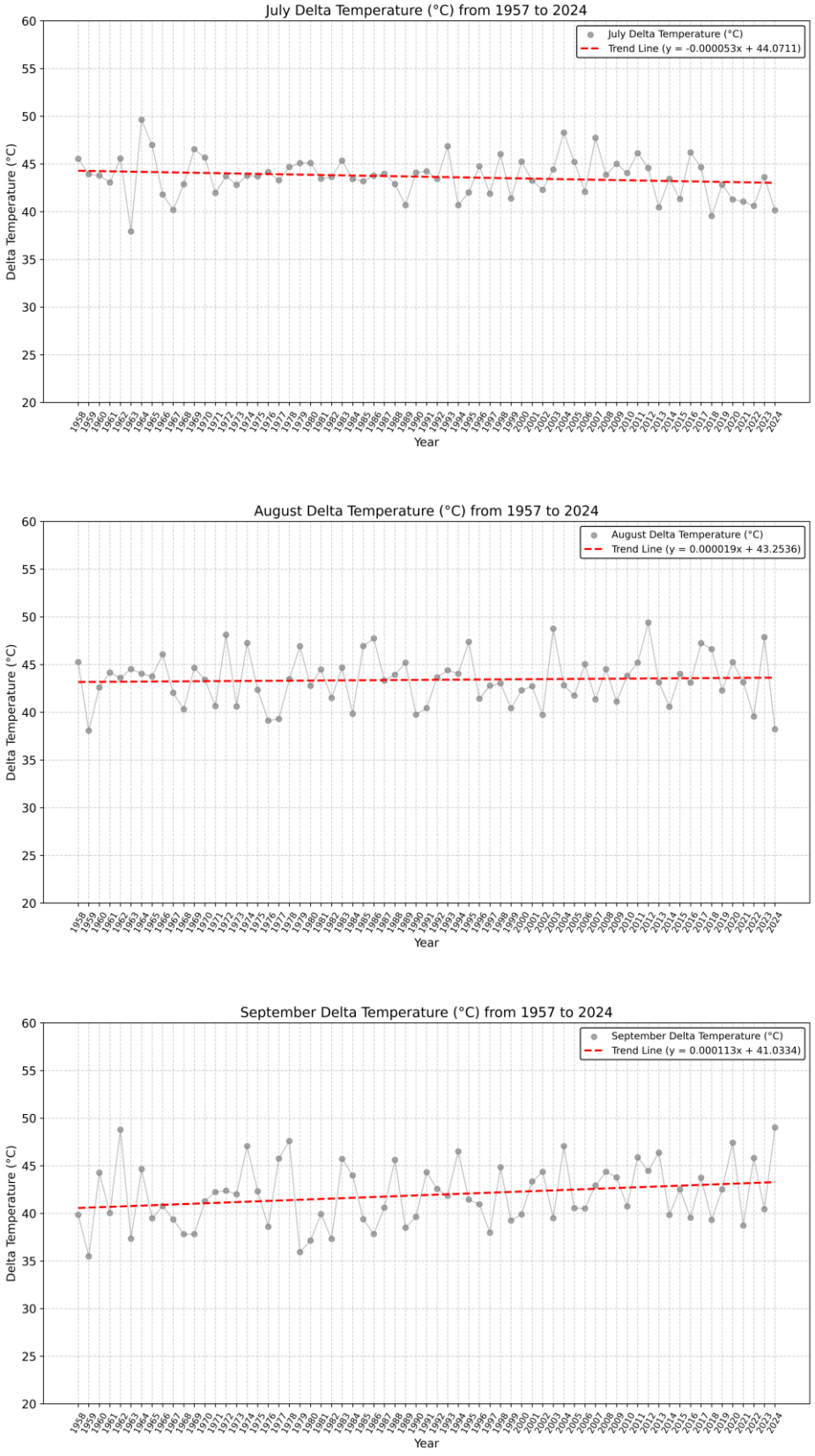

Figure 25_Monthly Delta Temperature (°C) from 1957 to 2024 with Trend Line_ Jul to Sep

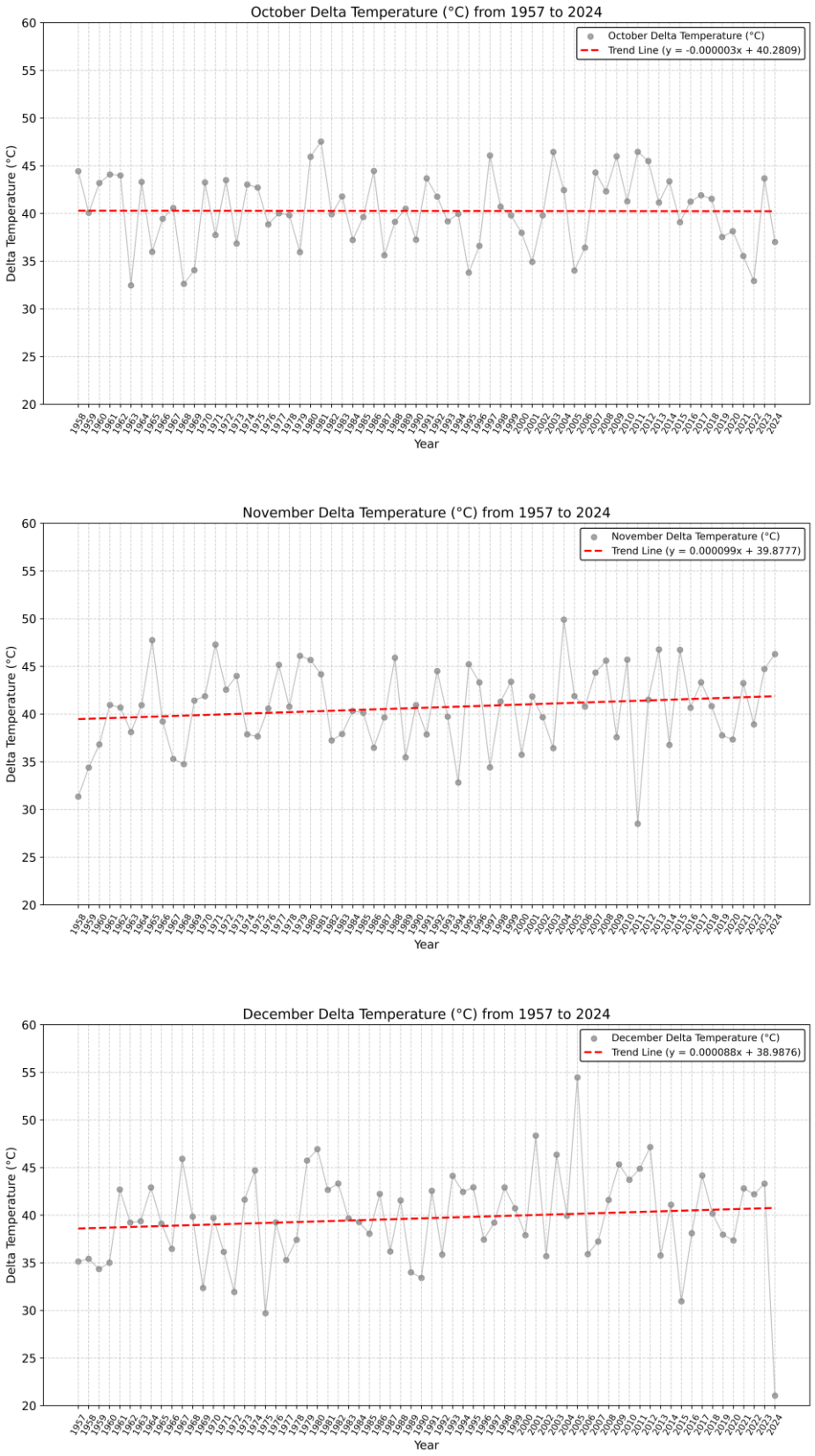

Figure 26_Monthly Delta Temperature (°C) from 1957 to 2024 with Trend Line_ Oct to Dec

Most months have a positive trend, according to monthly temperature data from 1957 to 2024, however, a few months have slightly negative slopes. As shown by the trend lines in the corresponding figures, this variation is noticeable over the years. Across the twelve months, the trend lines predominantly suggest increasing temperatures, although the steepness varies from one month to another.

4.2.3 Monthly Maximum and Minimum Temperatures

The monthly maximum (Tmax) and minimum (Tmin) temperatures for the years 1957–2024 were examined in this section. Assessing long-term patterns in temperature extremes and spotting seasonal fluctuations that might indicate elevated thermal risk or climate-related shifts in the Susa Valley were the objectives.

The historical NetCDF dataset was used to extract daily Tmax and Tmin values for each month of the year, which were then combined using Python to create monthly averages. The data were then exported into Excel for visualization and trend analysis. To identify gradual changes over the decades, trend lines were fitted. An overview of the rising and falling temperature trends from 1957 to 2024 is first shown in the section that follows (Figure 27). These patterns are then analyzed for every month during the previous 60 years.

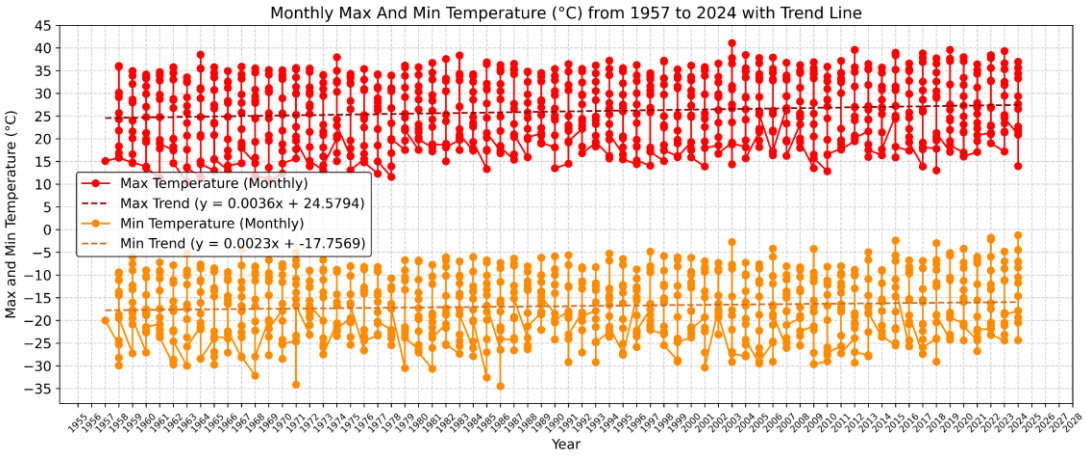

Figure 27_Monthly Max and Min Temperature (°C) from 1957 to 2024 with Trend Line

The analysis of monthly maximum and minimum temperatures from 1957 to 2024 revealed positive linear trends for both variables (Figure 27). The slope for maximum temperature (Tmax) was approximately +0.0036°C per year, while minimum temperature (Tmin) increased at a slightly lower rate of +0.0023°C per year, indicating a consistent yet uneven warming pattern over the study period. To investigate this further, monthly Tmax and Tmin values were calculated and analyzed separately for each month over the past six decades (Figures 28, 29, and 30).

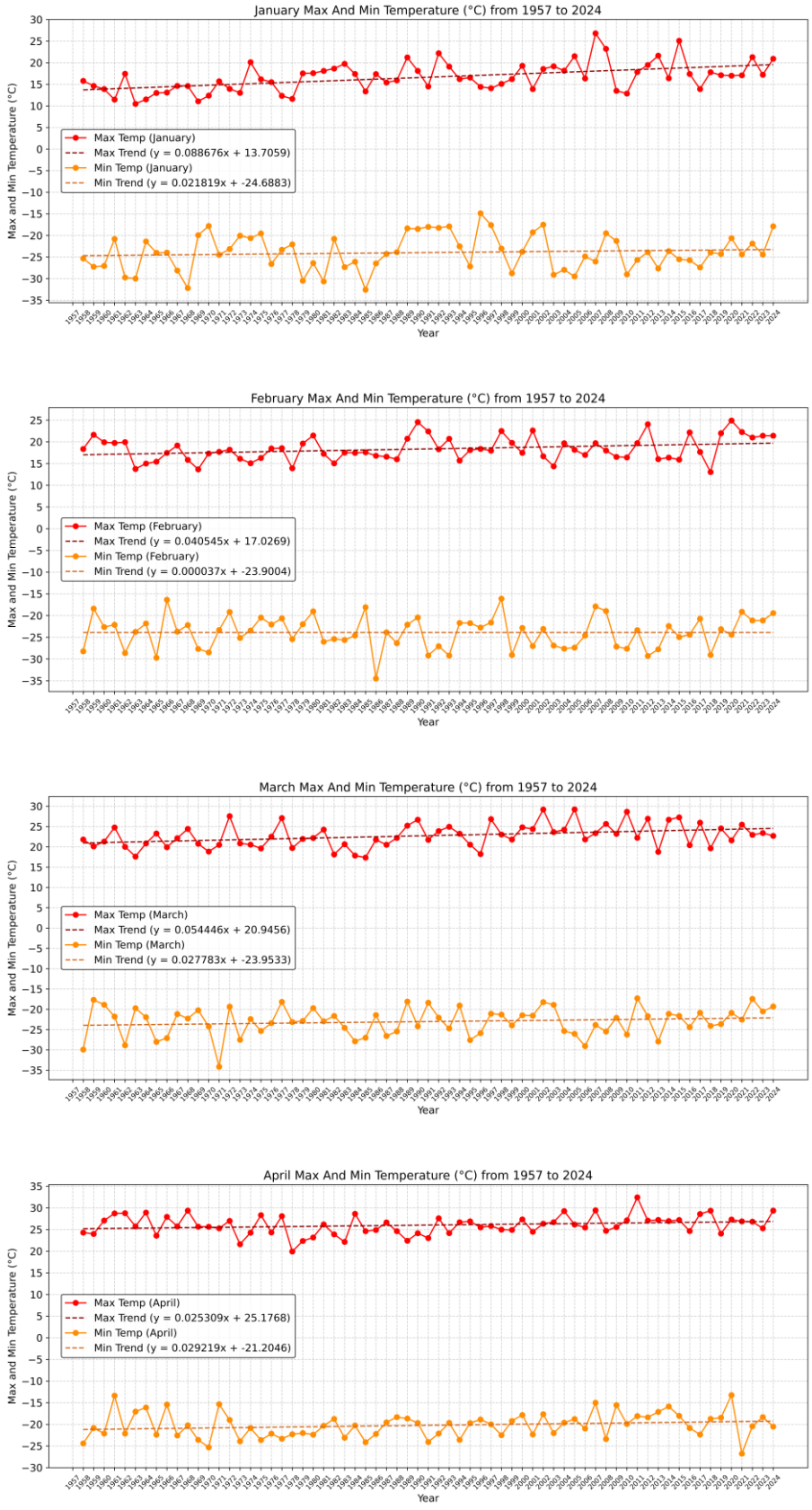

Figure 28 _Monthly Max and Min Temperature (°C) from 1957 to 2024 with Trend Line_ Jan to Apr

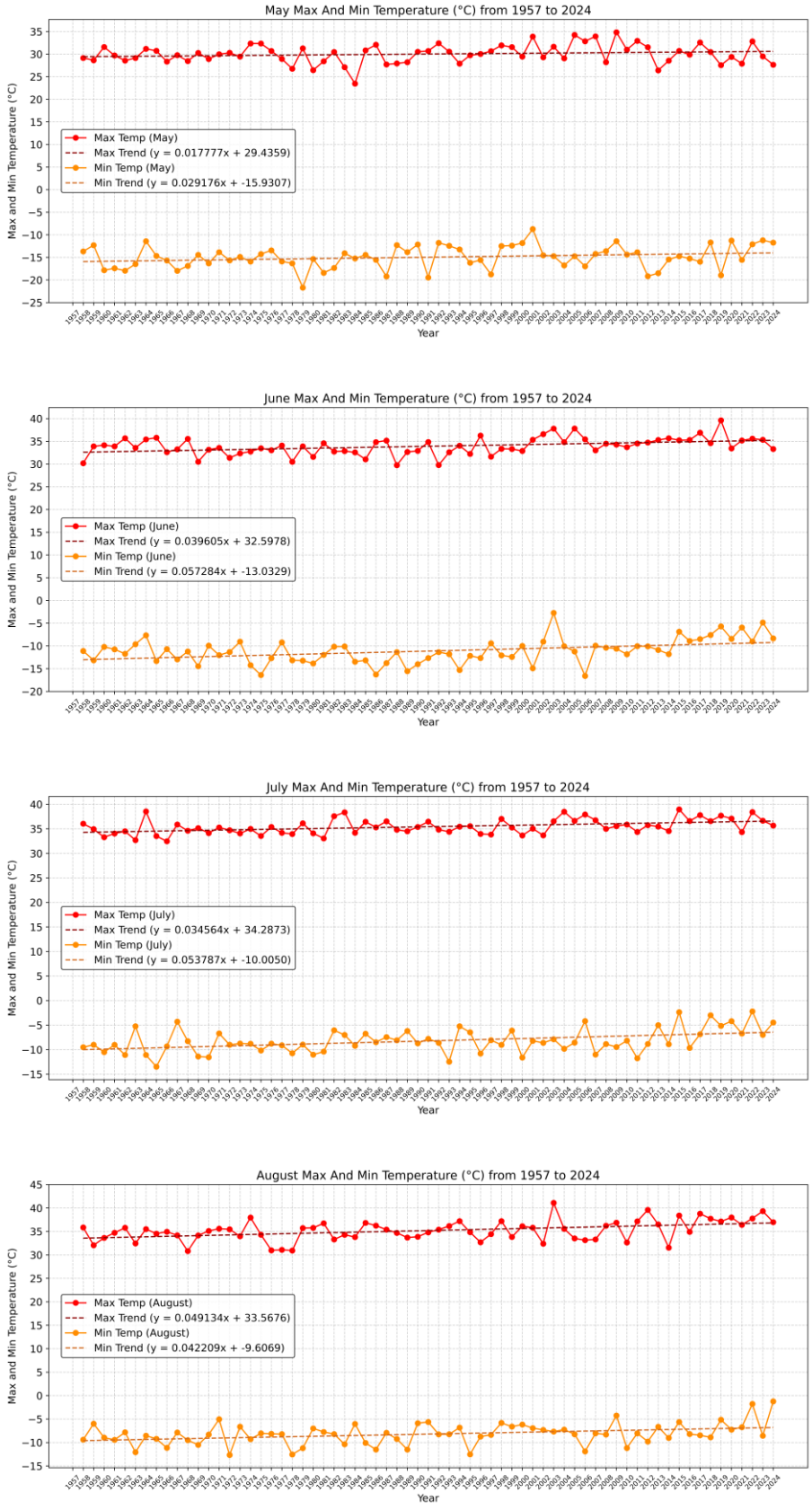

Figure 29_Monthly Max and Min Temperature (°C) from 1957 to 2024 with Trend Line_ May to Aug

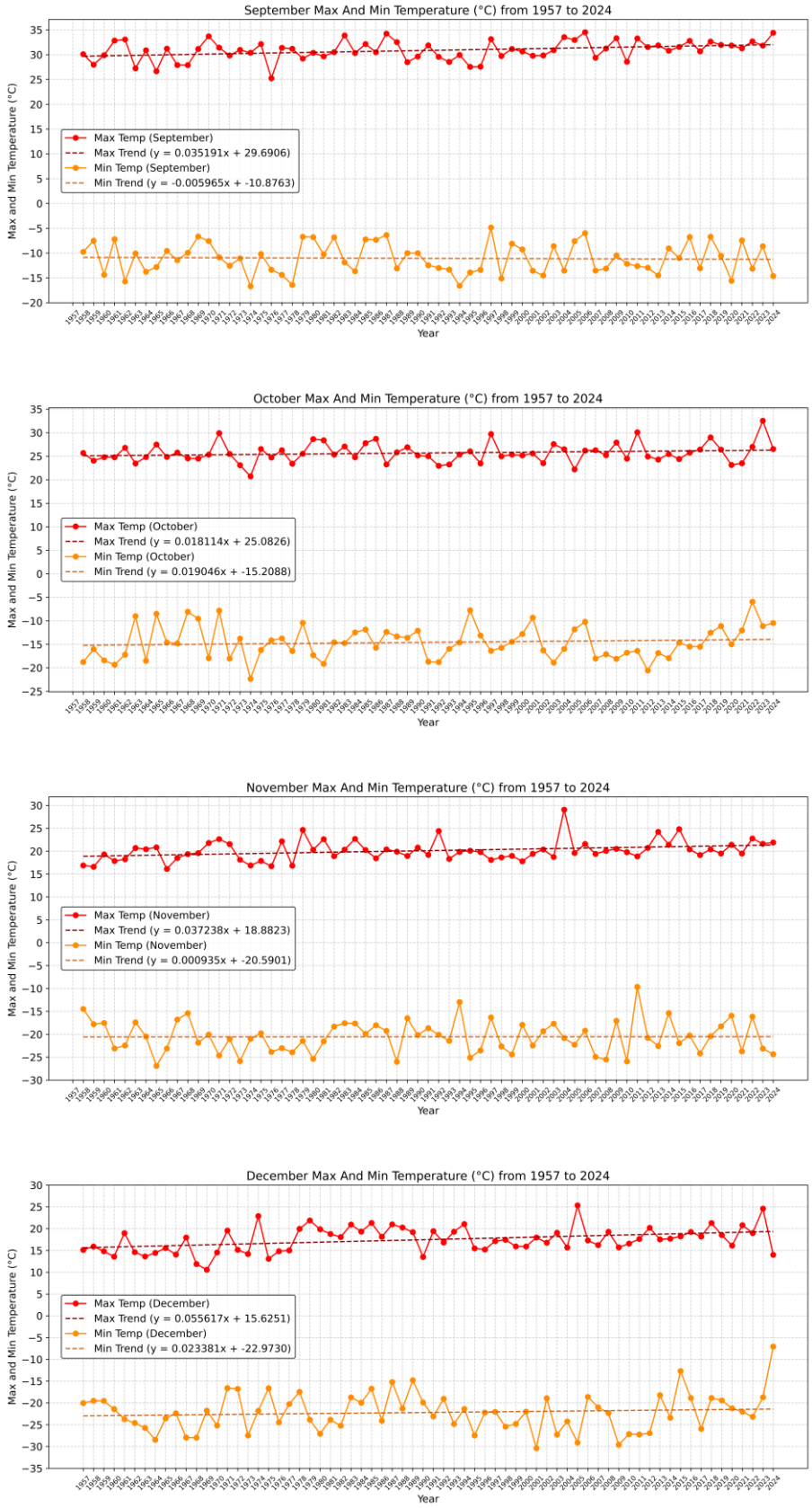

Figure 30_Monthly Max and Min Temperature (°C) from 1957 to 2024 with Trend Line_ Sep to Dec

The monthly trend analysis of maximum and minimum temperatures from 1957 to 2024 reveals distinct seasonal variations throughout the year. All months exhibit a positive linear trend in maximum temperature (Tmax), whereas trends in minimum temperature (Tmin) are more heterogeneous. While most months show an upward trend in Tmin, September stands out as the only month with a negative Tmin slope. The steepest increases in Tmax occur in January, February, and December, accompanied by comparatively slower increases in Tmin. Conversely, June and July display higher slope values for Tmin than for Tmax. In October, the trends for both Tmax and Tmin are nearly identical. These seasonal differences are illustrated in the corresponding monthly charts.

4.2.4 Elevation-Based Temperature Analysis

According to the classification suggested by Tiranti et al. (2023) for the Western Alps, the Susa Valley was divided into five major altitudinal classes in order to examine the relationship between temperature behavior and elevation. In addition to elevation range, this division considered climatic zoning and aspects into account (Tiranti et al., 2023).

- **Class 1**: 400–700 m a.s.l. (foothills, transition to plains)
- **Class 2**: 700–1000 m a.s.l. (low-altitude Alpine zone)
- **Class 3**: 1000–2000 m a.s.l. (mid-altitude Alpine environment)
- **Class 4**: 2000–3000 m a.s.l. (high-altitude zone with significant slope exposure)
- **Class 5**: >3000 m a.s.l. (very high-altitude, often vegetation-free)

This classification served as the spatial framework for extracting temperature trends and conducting further statistical analyses related to geomorphological processes. Using the regional digital elevation model (DEM) provided by ARPA Piemonte, along with masked NetCDF files for Tmin and Tmax, average values and linear trend slopes were calculated for each elevation class through Python-based geoprocessing.

The monthly maximum and minimum temperature trends for each elevation band from 1957 to 2024 are shown in Figures 31 and 32. The findings show significant differences in warming rates between various altitudinal zones. A detailed overview of these trends, categorized by elevation class, is presented in the following sections.

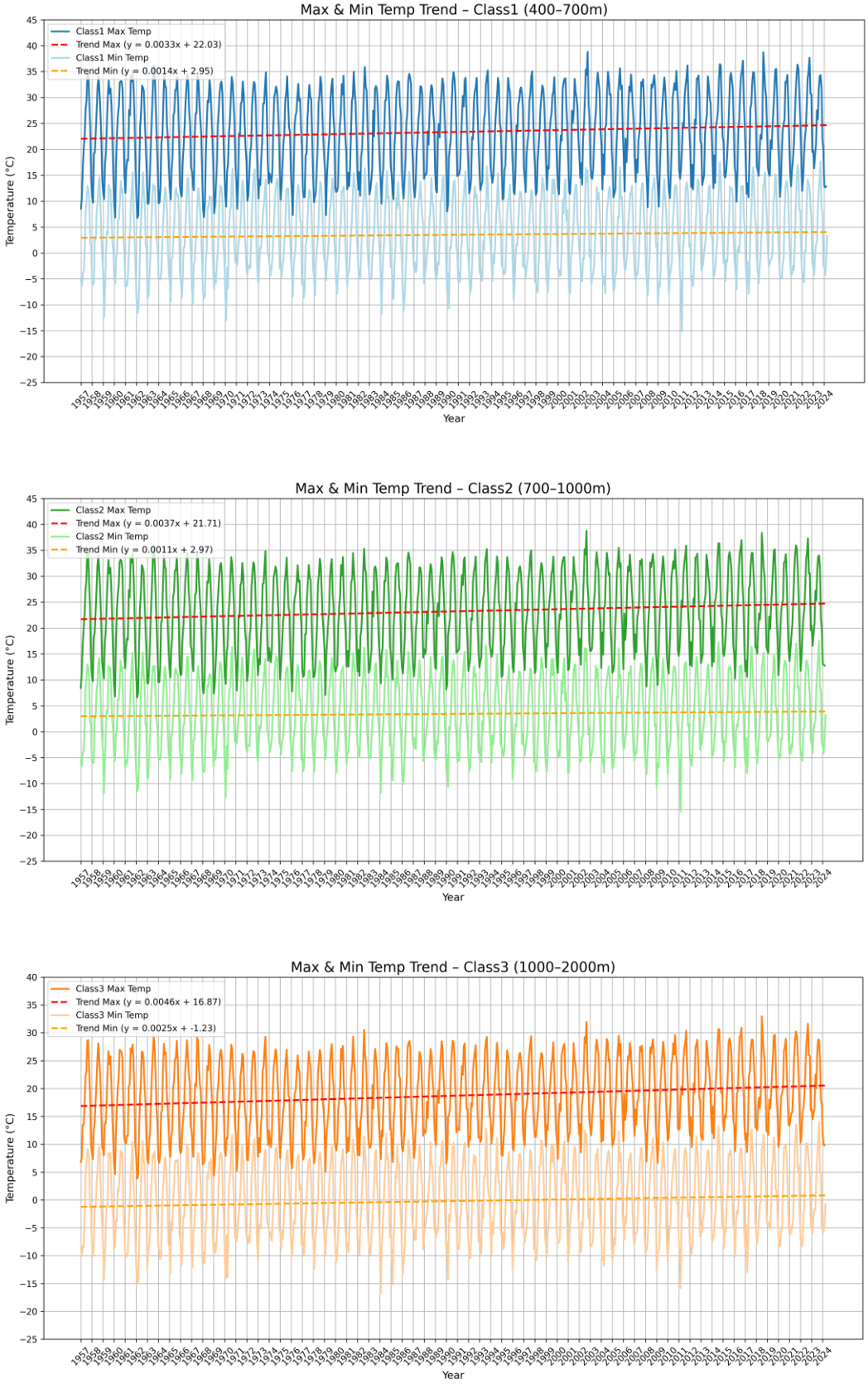

Figure 31_Max and Min Temperature Trend with Elevation Classes 1,2,3

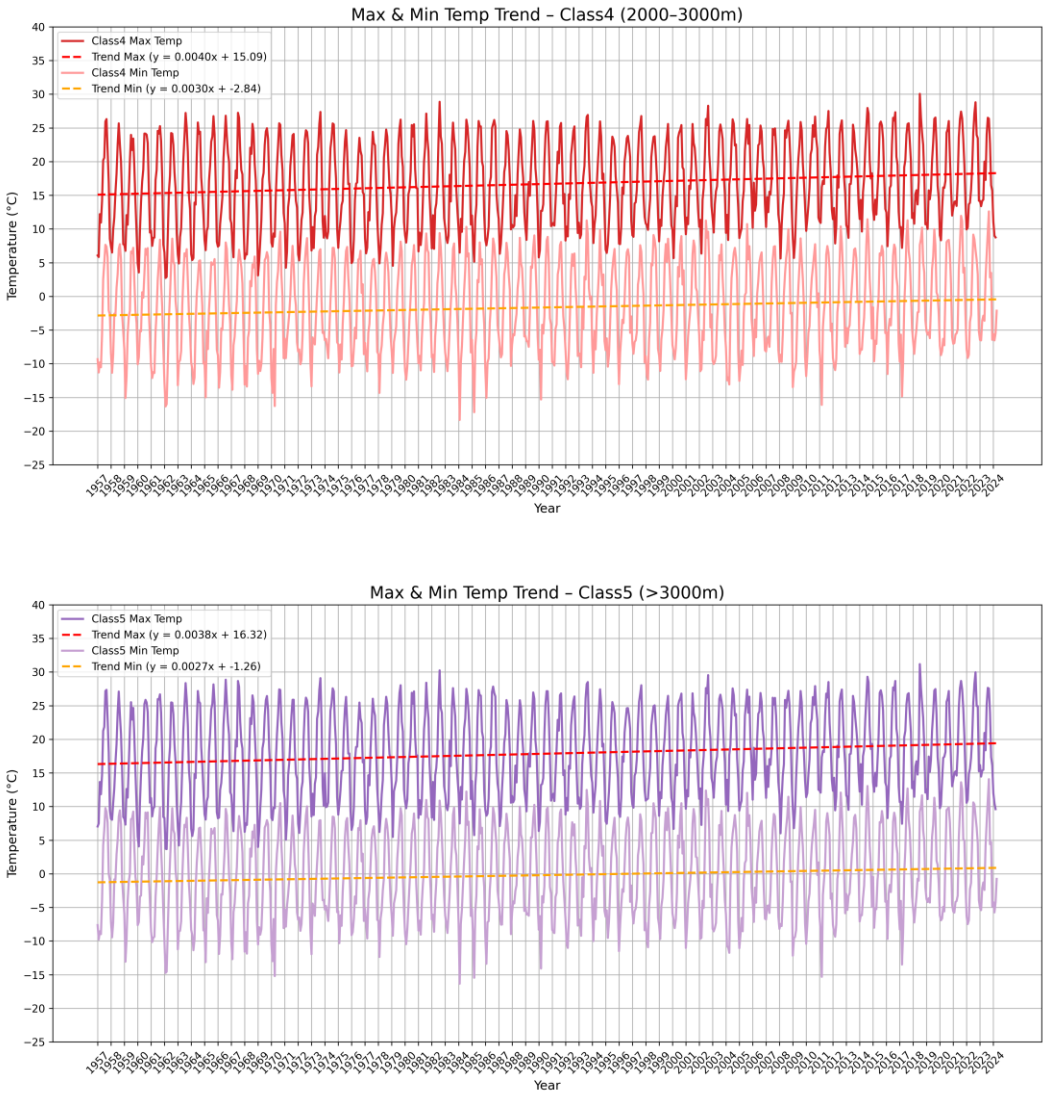

Figure 32_Max and Min Temperature Trend with Elevation Classes 4,5

Temperature trends differ among the five elevation classes, as shown in Figures 31 and 32. Significant variations in the slope of Tmax and Tmin are observed along the altitudinal gradient. Temperature trends exhibit variability throughout the altitudinal gradient, with variations in the slope magnitude between Tmax and Tmin observed across all classes.

Class 1 (400–700 m) shows an increasing trend in Tmax of +0.0033°C per year, corresponding to an approximate total rise of +2.2°C over the study period, while Tmin increases at a rate of +0.0014°C per year (approximately +1.0°C). Class 2 (700–1000 m) exhibits a Tmax trend of +0.0037°C per year (about +2.6°C) and a Tmin trend of +0.0011°C per year (near +0.75°C). Class 3 (1000–2000 m) displays the steepest Tmax increase among all classes, with a rate of +0.0046°C per year (+3.2°C), while Tmin rises at +0.0025°C per year (around +1.7°C). Class 4 (2000–

3000 m) records a Tmax increase of +0.0040°C per year (approximately +2.7°C) and a Tmin increase of +0.0030°C per year (estimated +2.0°C). Finally, Class 5 (>3000 m) shows a Tmax trend of +0.0038°C per year (approximately +2.6°C), with Tmin increasing at +0.0027°C per year (+1.5°C).

Class 4 shows relatively balanced trends between Tmax and Tmin, while Class 3 shows the highest Tmax increase. These trends show that warming rates vary across elevation bands.

To enable a more precise analysis and comparison of maximum and minimum temperature trends across the elevation classes, the data are presented in the form of bar charts and histograms. To enhance the accuracy and clarity of the comparison, the average values of maximum and minimum temperatures for each elevation class were calculated and are displayed in Figure 33.

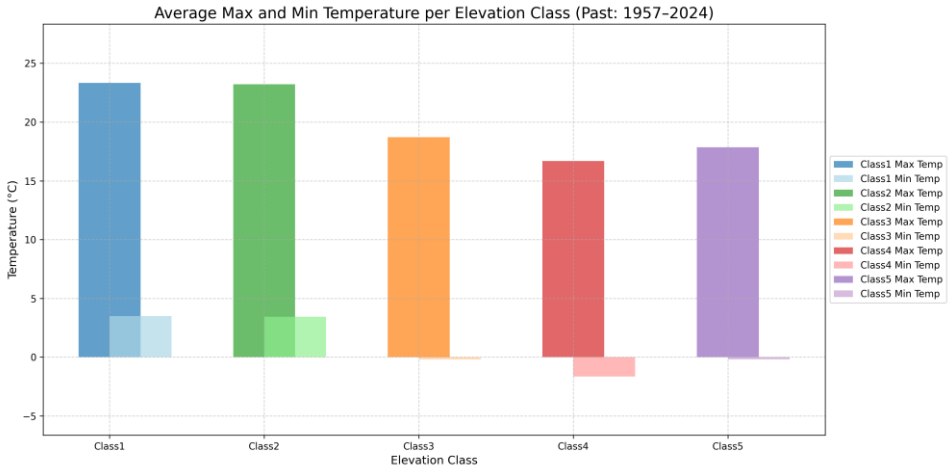

Figure 33_Average Max and Min Temperature per Elevation Class from 1957 to 2024

The data in Figure 33 shows a clear change in thermal behavior with altitude, which means that temperature changes in a systematic way as elevation rises. The highest average maximum temperatures, between roughly 23.2°C and 23.4°C, are found in Class 1 (400–700 m) and Class 2 (700–1000 m), with corresponding minimum temperatures of about 3.4°C. There is a clear thermal transition zone in Class 3 (1000–2000 m), where the average maximum temperature drops to roughly 19°C and the minimum temperature gets close to 0°C. The lowest average maximum temperature (~17°C) is found in Class 4 (2000 3000 m), while the lowest values fall below –1.5°C. Class 5 (>3000 m) has a slightly higher average maximum temperature than Class 4, at around 18°C, while the minimum temperature rises to about 0°C.

The results show a clear temperature gradient across elevation bands, which is in line with the spatial patterns seen in the analysis of temporal trends.

4.2.5 Critical Elevation Identification

To identify the elevation threshold above which maximum temperatures rarely exceed the freezing point, a spatial analysis was conducted using historical Tmax data from 1957 to 2024. The original NetCDF files were first converted to GeoTIFF format and spatially masked to the extent of the Susa Valley. Elevation-specific temperature values were then extracted using QGIS and organized into tabular format. These data were subsequently analyzed in Python to assess the frequency of above-freezing Tmax values across elevation bands.

The resulting dataset was used to generate a scatter plot showing the relationship between elevation and average Tmax (Figure 34).

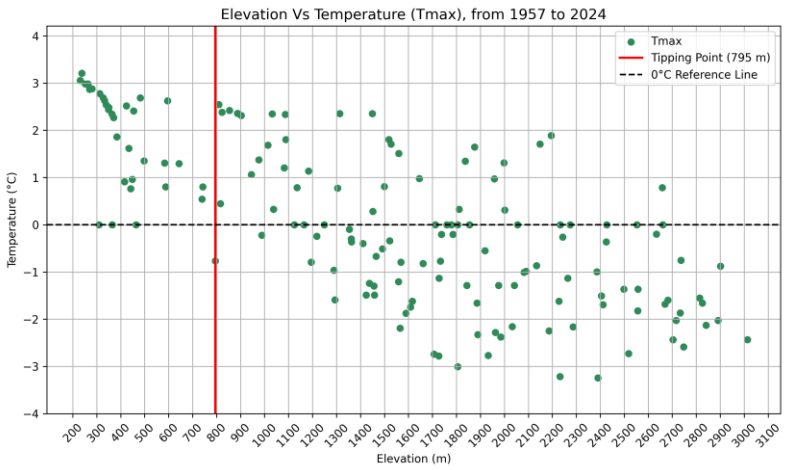

Figure 34_Elevation Vs Max Temperature, from 1957 to 2024

Figure 34, displays a clear inverse relationship—Tmax values decrease as elevation increases. Based on the distribution of values, a notable shift is observed around 795 meters, above which many Tmax points fall below 0°C. This observation provides a measurable reference point to distinguish between areas where freezing conditions are likely and those where they are less frequent. The elevation of ~795 m is therefore noted as a potential thermal threshold based solely on historical maximum temperature data.

4.3 Historical Precipitation Analysis

The Susa Valley's historical precipitation patterns are examined in detail in this section using cumulative rainfall data taken from NetCDF datasets between December 1, 1957, and December 1, 2024. Using Python, the study area was selected through spatial filtering, and the 24- and 48-hour rainfall totals were

analyzed in the same way as the temperature data. The calculated cumulative rainfall values were systematically compared against the established thresholds of 120 mm for 24-hour cumulative rainfall and 170 mm for 48-hour cumulative rainfall, which are frequently linked to the beginning of shallow landslides and rockfalls. The results indicate that these thresholds were rarely exceeded during the 1957–2024 period. Furthermore, the trend lines for both datasets show a slightly negative slope, suggesting no significant long-term increase in extreme precipitation events.

4.3.1 Cumulative 24-Hour Rainfall

This section mainly focuses on the 24-hour cumulative rainfall values to evaluate the short-duration precipitation patterns that may cause localized geohazards. Figure 35 displays the overall trend of cumulative 24-hour rainfall over the course of the study, based on daily precipitation measurements extracted from the historical dataset filtered for the Susa Valley. This broad view makes it easier to identify long-term variations in rainfall frequency and intensity.

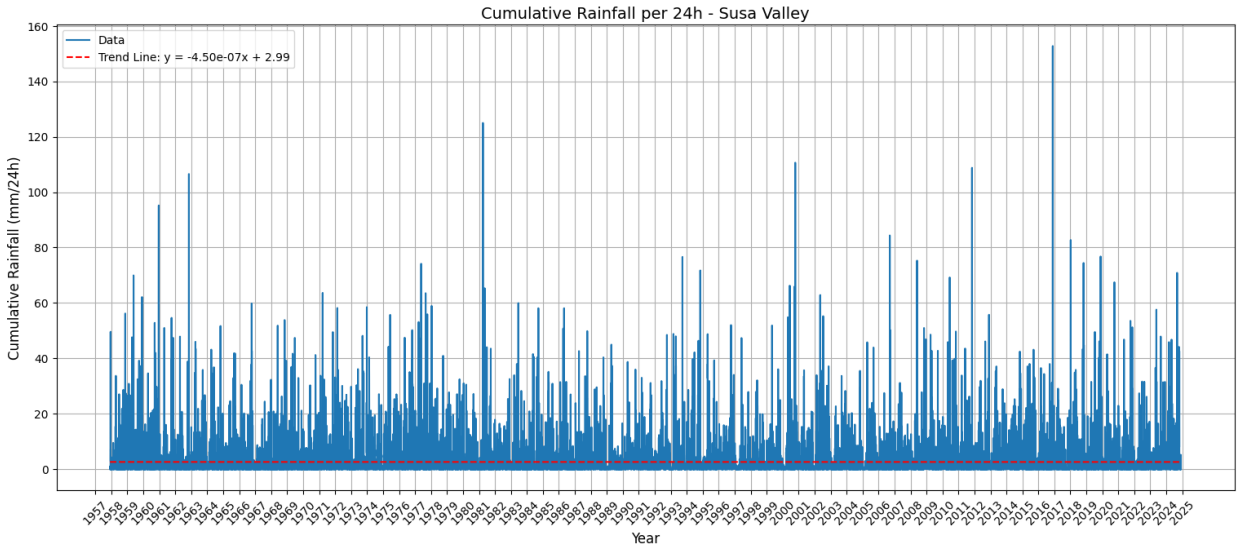

Figure 35_Cumulative Rainfall per 24 hour from 1957 to 2025

Although most values fall within a moderate range, as illustrated in Figure 35, several notable spikes represent exceptional events that are sporadically distributed across the decades. Plotting the trend line, which shows a slight downward trend, provides a visual representation of the long-term variation in daily rainfall extremes without suggesting sudden shifts or persistent abnormalities. Monthly trends of 24-hour cumulative rainfall were examined to find seasonal peaks, changes in the distribution of rainfall, and times when the probability of intense events was higher in order to improve comprehension. This

method enhances the assessment of seasonal hazards and draws attention to climate-driven changes (Figures 36, 37, 38).

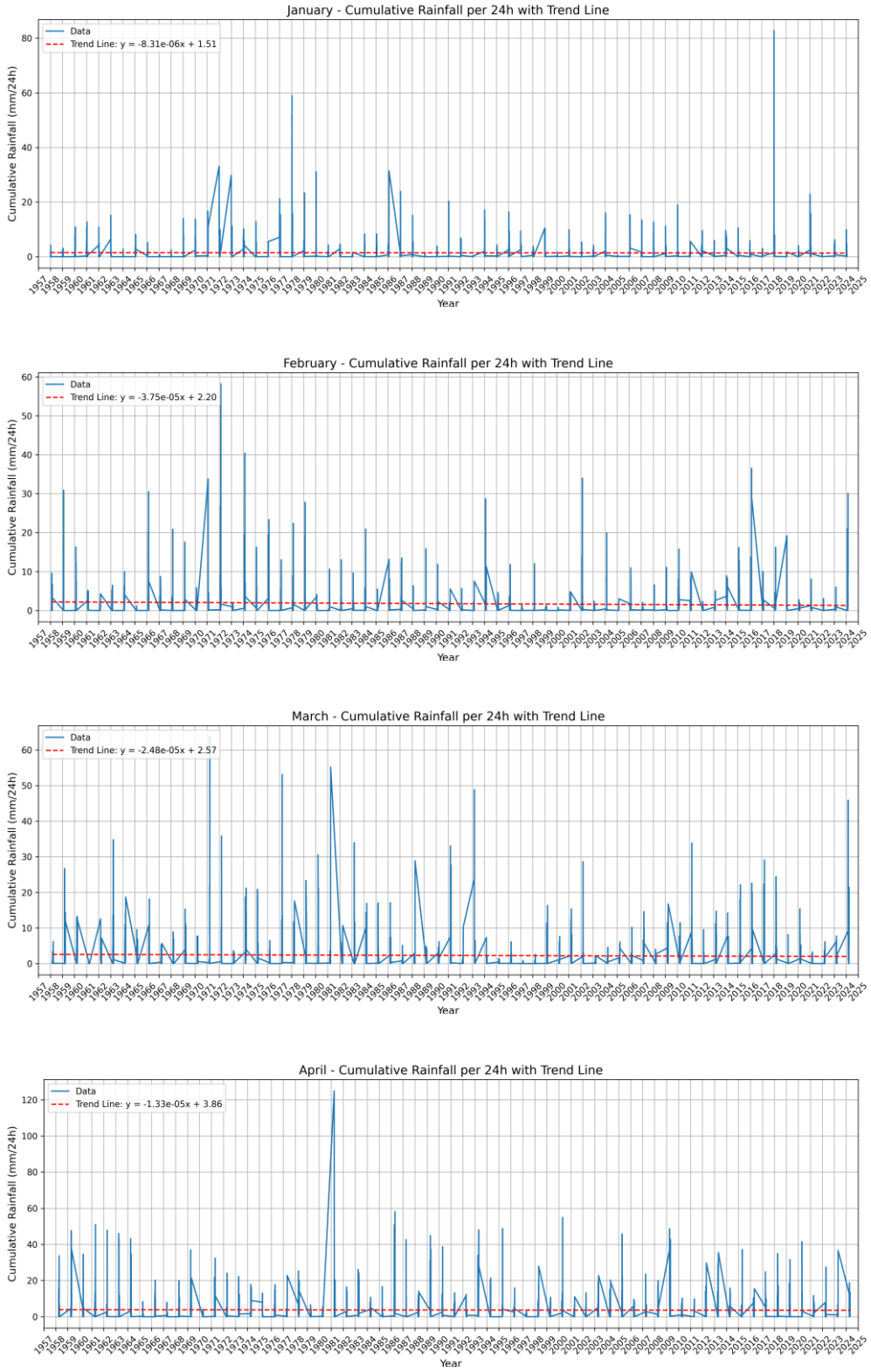

Figure 36_Cumulative Rainfall per 24 hours from 1957 to 2024_ Jan to Apr

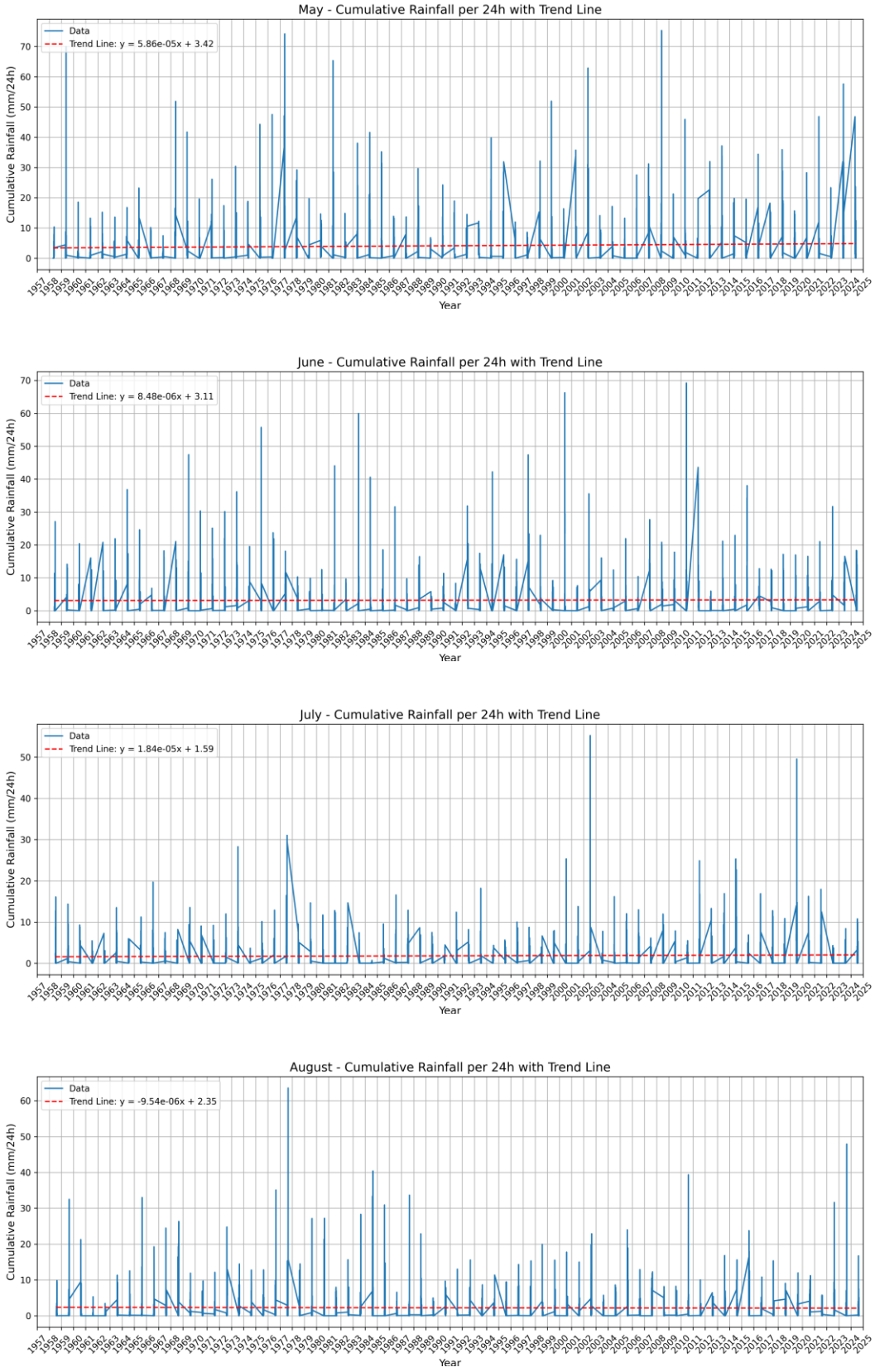

Figure 37_Cumulative Rainfall per 24 hours from 1957 to 2024_ May to Aug

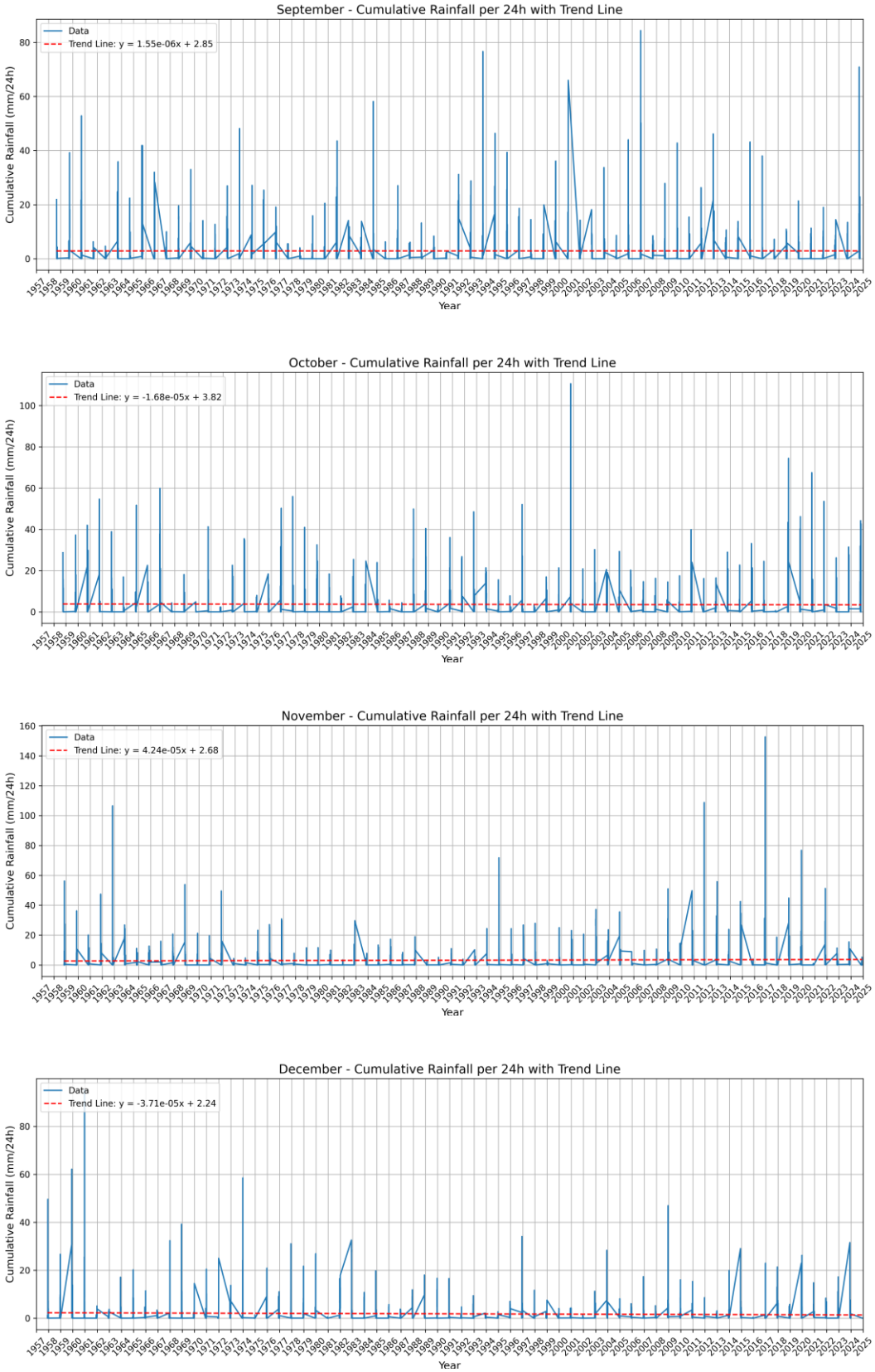

Figure 38_Cumulative Rainfall per 24 hours from 1957 to 2024_ Sep to Dec

There are clear seasonal patterns throughout the year, according to the monthly trend analysis of 24-hour cumulative rainfall from 1957 to 2025 (Figure 36,37,38). The majority of the months exhibit trends that are either comparatively stable or slightly declining, with winter months like January, February, and December showing particularly noticeable negative slopes. May is notable for showing a definite upward trend, indicating a rise in late-spring short-duration rainfall. March and April, on the other hand, exhibit patterns that are either almost flat or slightly negative. While August seems to be fairly stable, the summer months—especially June and July—show modest upward trends. While September and October exhibit minimal or mixed trend behaviors, November is marked by the most noticeable increase. These month-specific differences are illustrated in the corresponding graphs and reflect how the temporal distribution of intense daily rainfall has shifted over time.

4.3.2 Cumulative 48-Hour Rainfall

The analysis of 48-hour cumulative rainfall values is presented to evaluate medium-duration precipitation patterns that may contribute to rainfall-induced geohazards. The overall trend for the entire study period is shown in Figure 39, based on data filtered for the Susa Valley. This overview allows the identification of long-term variations in rainfall intensity across 48-hour windows.

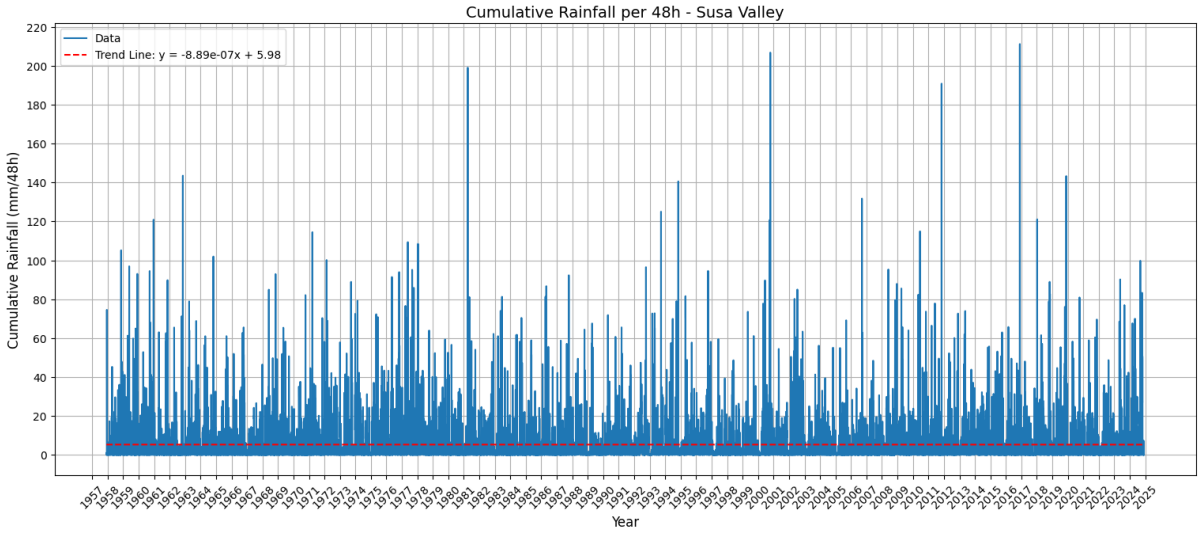

Figure 39_Cumulative Rainfall per 48 hours from 1957 to 2025

The distribution of extreme 48-hour cumulative rainfall events is displayed in Figure 39, where each bar denotes the highest annual total value. The overall trend line indicates a slight long-term decrease, but a number of sharp peaks indicate sporadic intense multi-day rainfall. The fluctuation is indicative of the

erratic character of precipitation extremes with a medium duration. In order to identify seasonal patterns and assist with hazard assessment, monthly trends of 48-hour rainfall were analyzed (Figures 40, 41, 42).

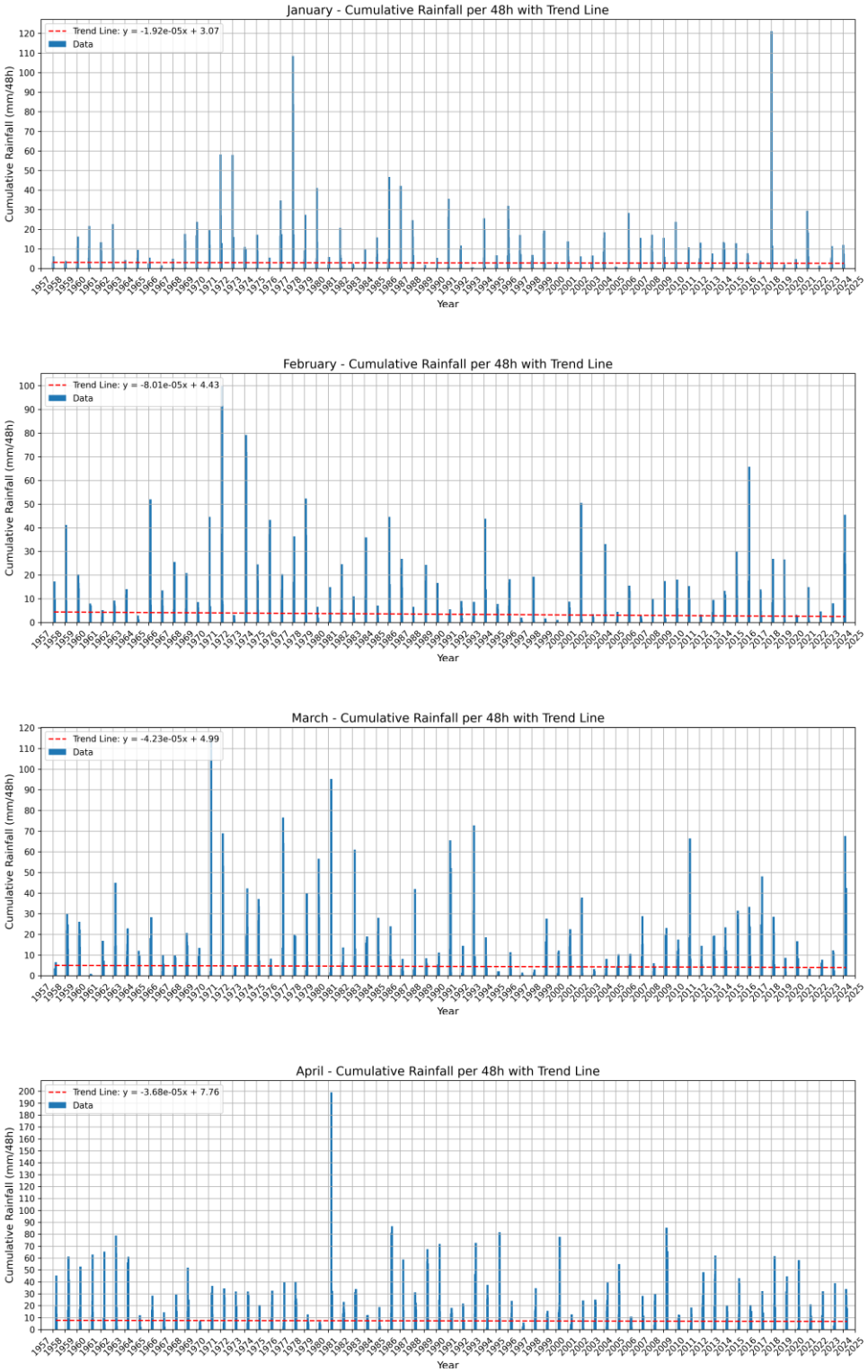

Figure 40_Cumulative Rainfall per 48 hours from 1957 to 2024_ Jan to Apr

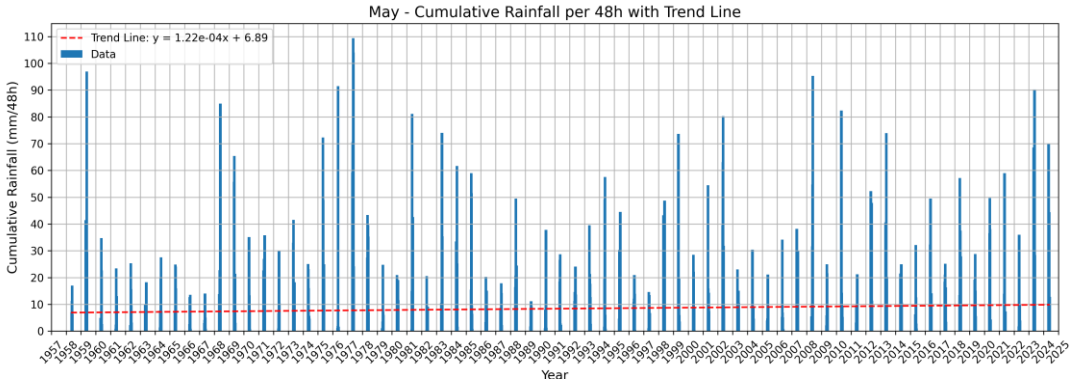

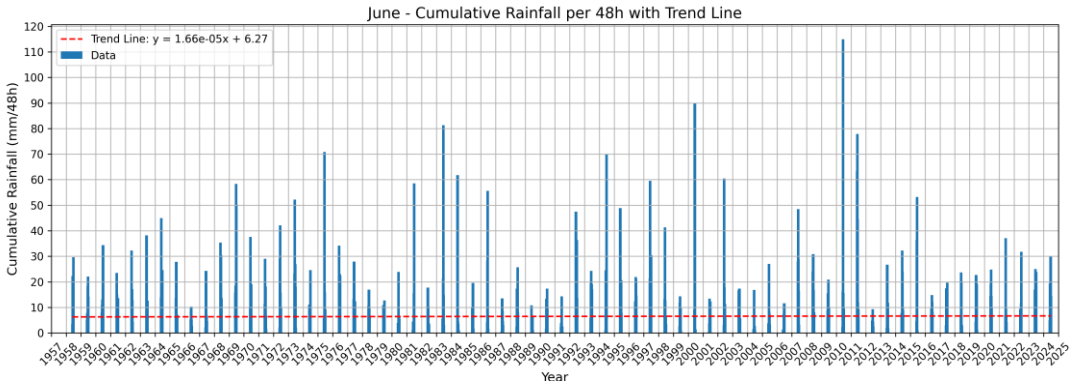

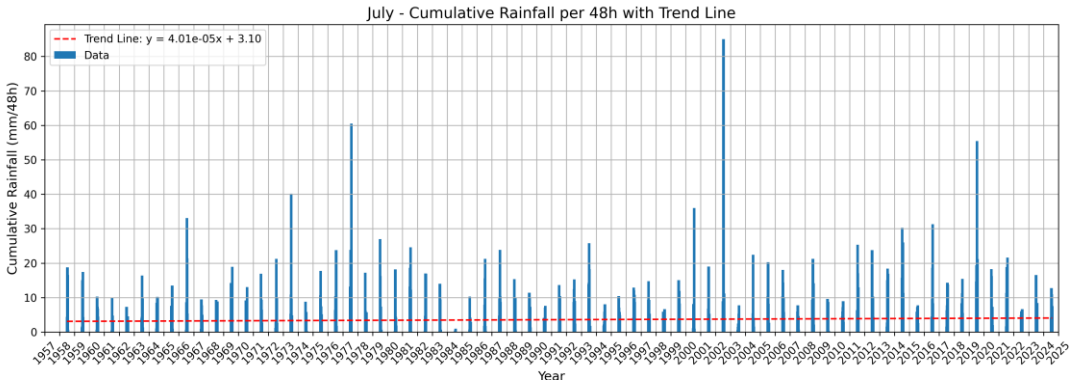

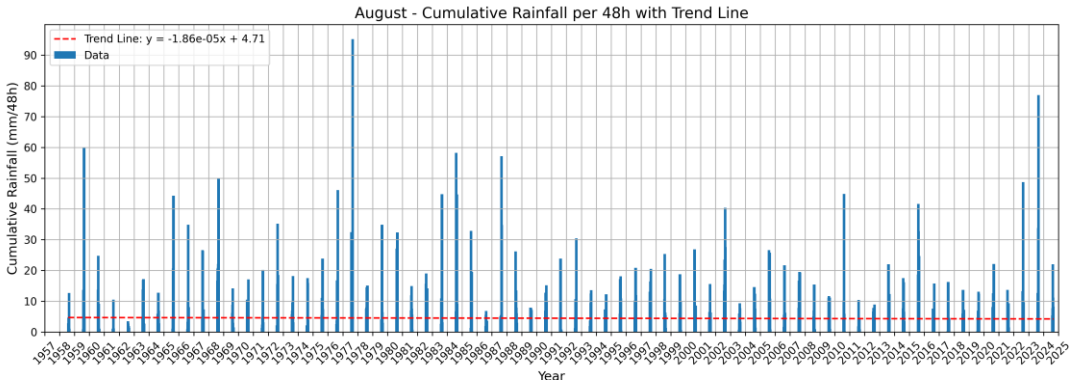

Figure 41_Cumulative Rainfall per 48 hours from 1957 to 2024_ May to Aug

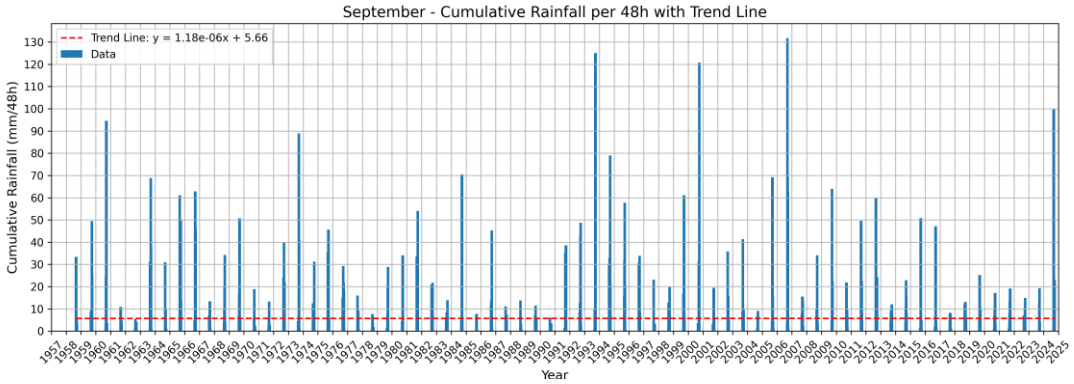

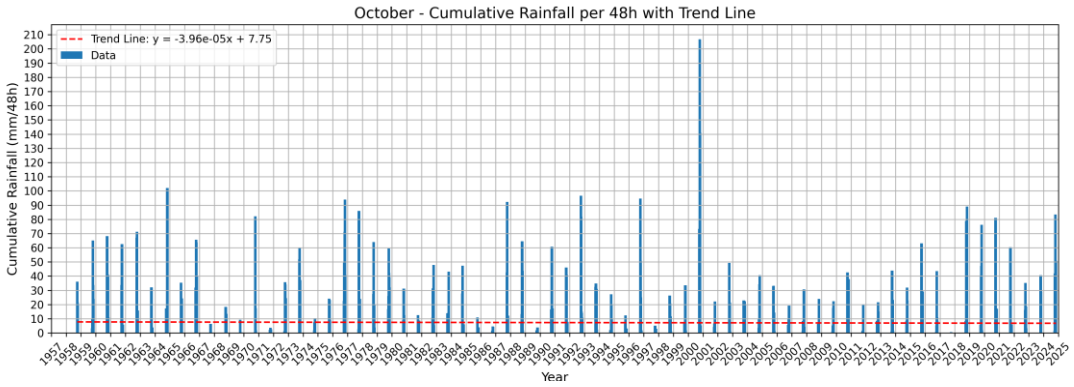

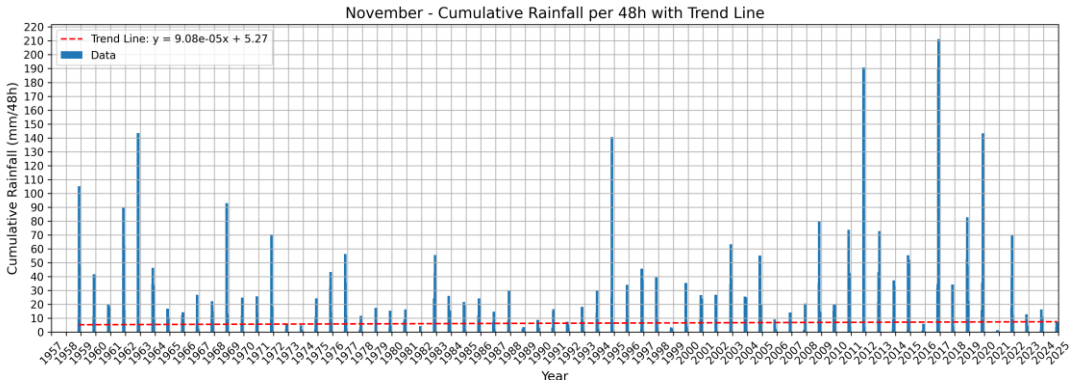

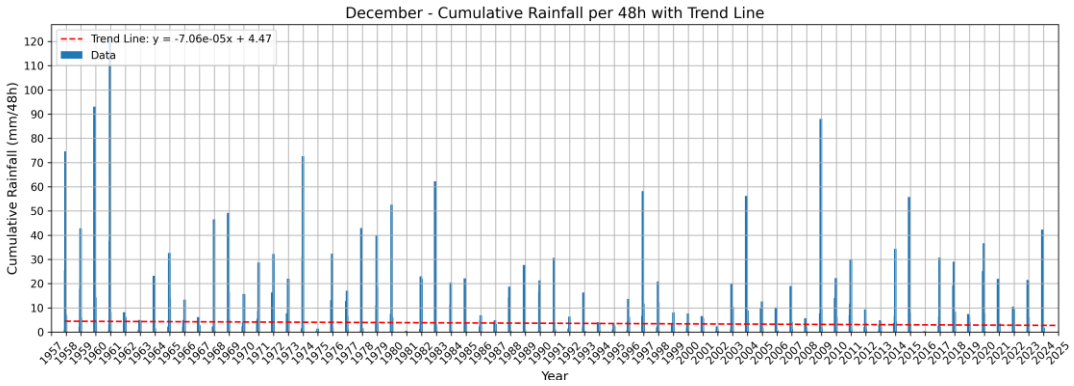

Figure 42_Cumulative Rainfall per 48 hours from 1957 to 2024_ Sep to Dec

Seasonal differences in rainfall extremes are clearly visible in the monthly trend analysis of 48-hour cumulative rainfall from 1957 to 2025 (Figure 40,41,42). The slight negative trends observed in the majority of winter months, such as January, February, and December, point to a long-term decline in medium-duration rainfall events during colder seasons. Although less noticeable, March and April also show negative slopes, suggesting either slight decline or relative stability. May, on the other hand, is significant for having a distinctly rising trend, which indicates a change toward heavier rainfall in the late spring. The summer months exhibit a range of behavior: August is largely stable, while June and July show slight upward trends. Over time, September and October show erratic trends with slight variations. Interestingly, November exhibits the strongest upward trend, pointing to a remarkable rise in the intensity of 48-hour rainfall in late autumn. These monthly differences offer important insight into seasonal hazard dynamics by illuminating the evolution of rainfall distribution over multi-day periods.

4.3.3 Return Period Analysis of Extreme Events

The statistical probability and recurrence of high-intensity precipitation events were evaluated using the return period concept. This approach provides important information about how climate variability affects slope instability and flood risk by estimating the average time between two events of comparable magnitude.

The ARPA Piemonte platform provided the return period data used in this analysis, which included recurrence intervals ranging from 2 to 200 years and durations ranging from 10 minutes to 24 hours. 24-hour cumulative rainfall was the main focus in order to meet the goals of the study. In order to determine whether recent extremes are consistent with historically uncommon events, historical summer precipitation data (1957–2024) was examined to identify maximum events and compare them with return period thresholds. The results provide important information for risk assessment and long-term adaptation planning in mountainous regions and aid in determining whether climate change has affected regional precipitation patterns.

Given the increased likelihood of convective storms and short-duration extreme rainfall during the summer season, the months of June, July, and August were selected for focused analysis. In the following section, the 24-hour cumulative rainfall charts for these months are presented, along with the corresponding 24-hour return period thresholds for 2-, 5-, 10-, 50-, 100-, and 200-year intervals (Figure 43).

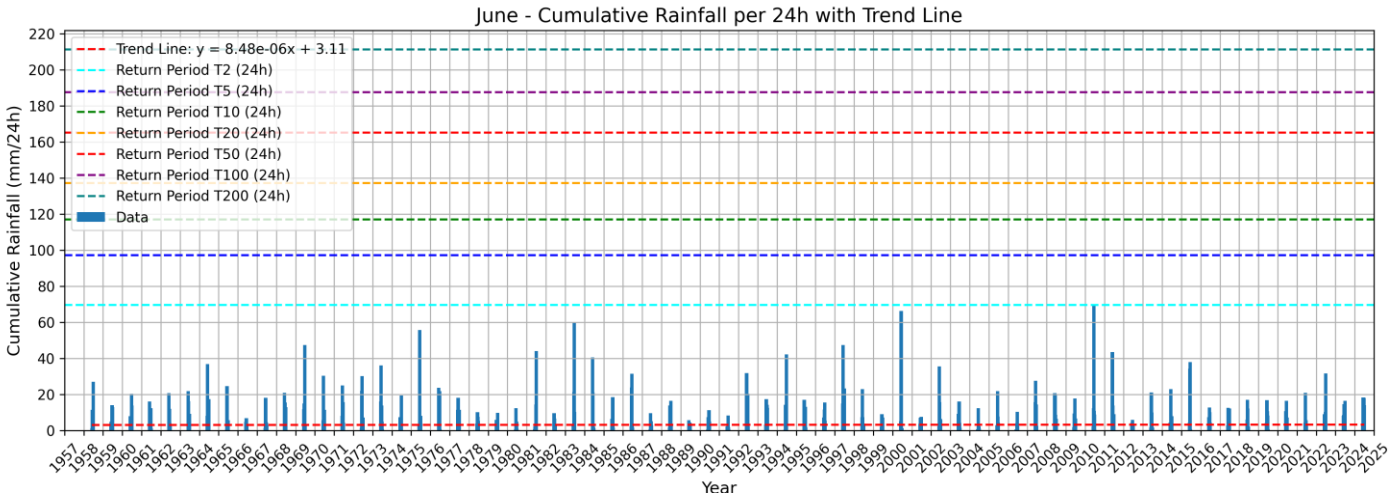

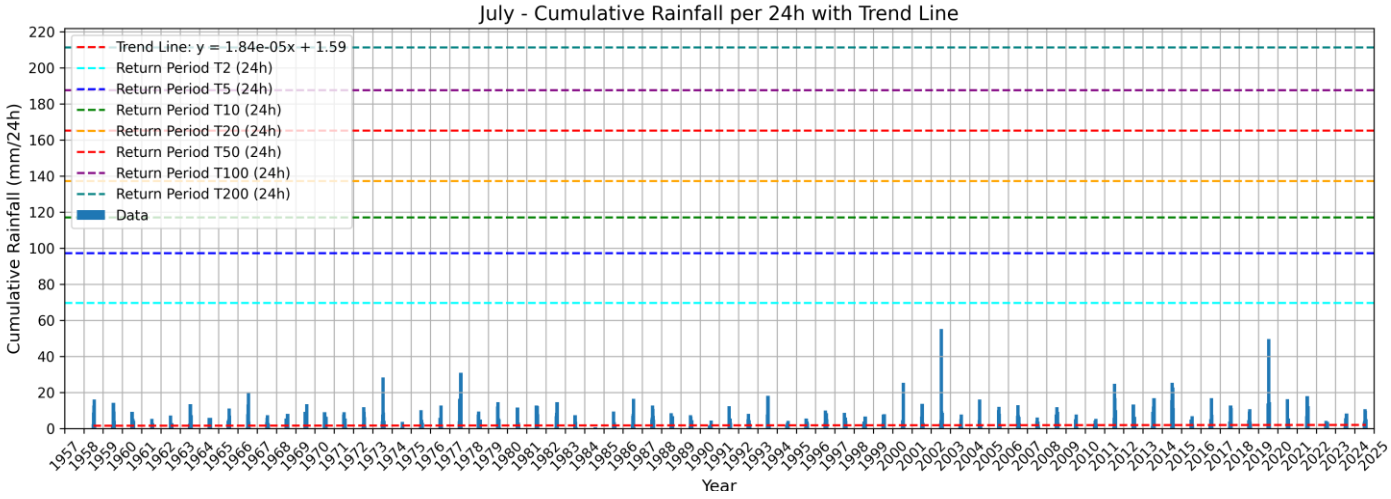

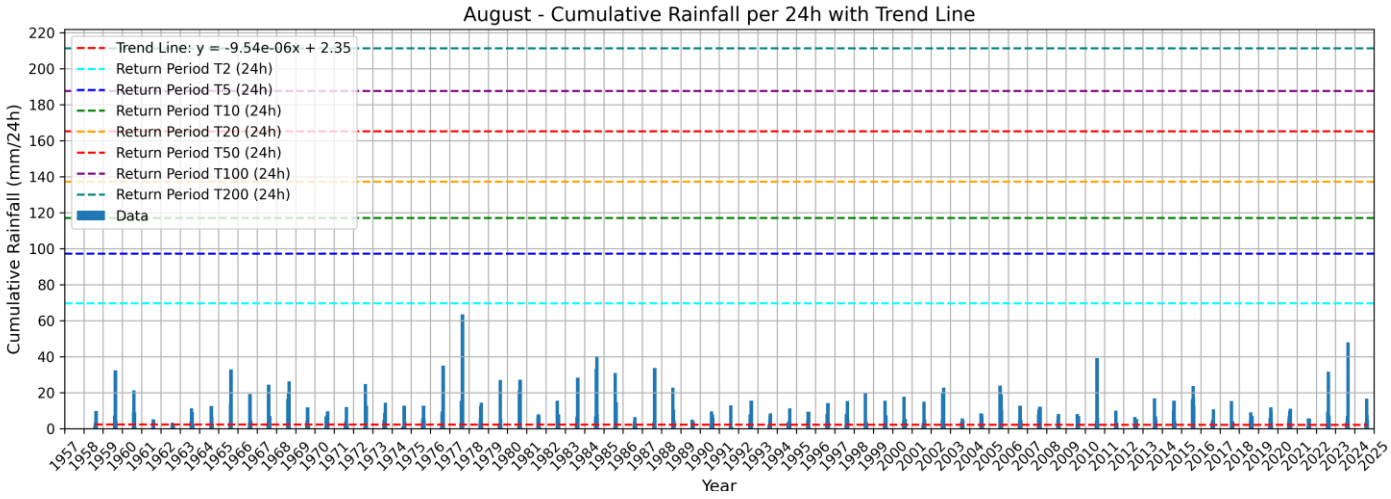

Figure 43_Return Period of Cumulative Rainfall per 24 hours with Trend Line from 1957 to 2024_ Jun to Aug

Figure 43 summarizes summer 24-hour rainfall extremes with trend lines and return period thresholds for key recurrence intervals. In all three months, the annual rainfall peaks consistently remain below the 2-year return period threshold. The observed trends are slightly increasing in June and July, and slightly decreasing in August. The graphs indicate limited interannual variability and no occurrences of high-intensity events exceeding the defined return thresholds during the summer period.

4.4 Analysis of Historical Susceptibility Classes under Climatic Conditions

The relationship between topographic susceptibility to three types of slope failure (debris flows, shallow landslides, and rockfall) and historical temperature and precipitation patterns is examined in this section. Hazard-prone areas throughout the Susa Valley were identified and examined using high-resolution geospatial datasets, such as susceptibility maps and a 10-meter DEM.

Three classified susceptibility maps were considered:

- **Rockfall susceptibility** was assessed in relation to both temperature (Delta T 5–8°C) and precipitation thresholds (120 mm/24h and 170 mm/48h), with five classes.
- **Shallow landslide susceptibility** was evaluated using the same precipitation thresholds, with three classes.
- **Debris flow susceptibility** was analyzed using intensity-based rainfall thresholds of 20, 30, and 50 mm/h, with(three classes: ECM, GCM, BCM).

All susceptibility layers were spatially aligned with climate data to investigate how different types of slope instabilities respond to environmental triggers.

4.4.1 Rockfall Susceptibility under Temperature and Precipitation Conditions

This part of the analysis focuses on the role of daily temperature fluctuations (ΔT = Tmax − Tmin) in influencing rockfall susceptibility across the Susa Valley during the historical period from 1957 to 2024. The analysis builds upon the susceptibility classification developed by Tiranti et al. (2023), which defines five susceptibility levels ranging from very low (Class 1) to very high (Class 5).

A Python-based workflow was developed to calculate daily temperature fluctuations (ΔT) across the study area, enabling analysis of their spatial and

temporal distribution. Mean ΔT values were computed for each susceptibility class and month using a spatial mask derived from the rockfall susceptibility map. These monthly averages were stored in structured CSV files to support long-term comparisons.

Elevation was added as a second spatial variable in the following step. The 10-meter-resolution DEM of the Susa Valley was divided into five elevation bands in accordance with earlier analyses. A 5 × 5 matrix was produced by calculating the monthly and annual averages of ΔT for every combination of susceptibility class and elevation band. Additionally, for each class combination, the percentage of area within three ΔT thresholds—below 5°C, between 5°C and 8°C, and above 8°C—was estimated. The 8°C threshold is especially crucial because, as Tiranti et al. (2023) and other Alpine studies have shown, high temperatures above this point are known to dramatically speed up rockface failure and degradation.

Long-term averages of ΔT (1957–2024) were calculated for each month across the 5 × 5 class matrix to make interpretation easier and give a better picture of the relationship between elevation, topographic sensitivity, and temperature variability. The original raster resolution of 10 meters was used for all spatial analyses, guaranteeing that thermal patterns across intricate mountainous terrain were represented in detail.

The results are visualized in Figure 44 to 48, which was generated using Python code and presents a comparative matrix of rockfall susceptibility classes and elevation bands with respect to the defined ΔT thresholds. This figure highlights the spatial overlap between susceptibility levels and elevation zones, specifically showing the distribution of areas falling below 5°C, between 5°C and 8°C, and above the 8°C critical threshold.

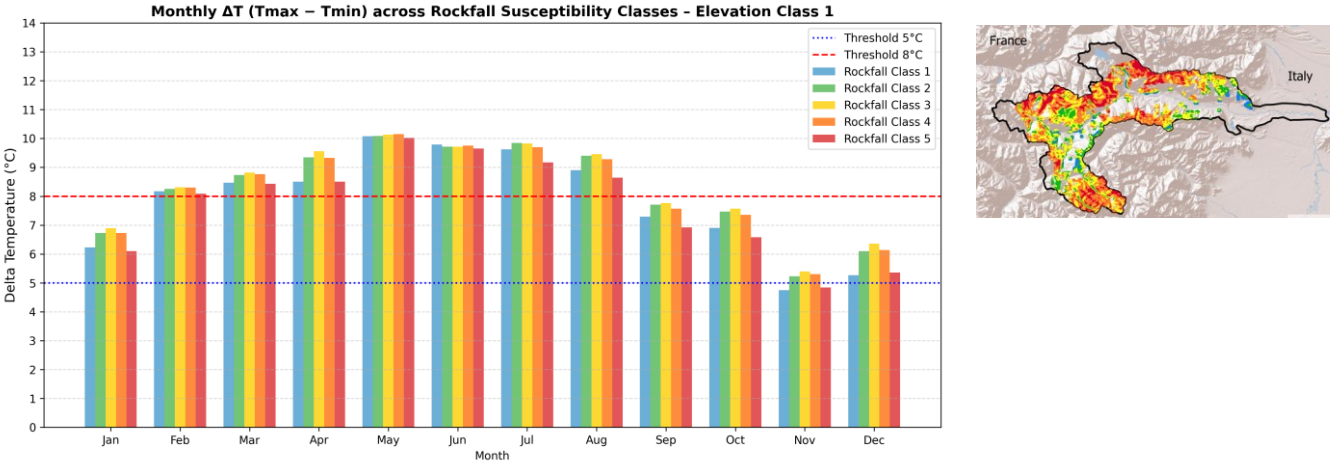

Figure 44_ Monthly ΔT across rockfall susceptibility classes in Elevation Class 1, between 5 °C and 8 °C thresholds

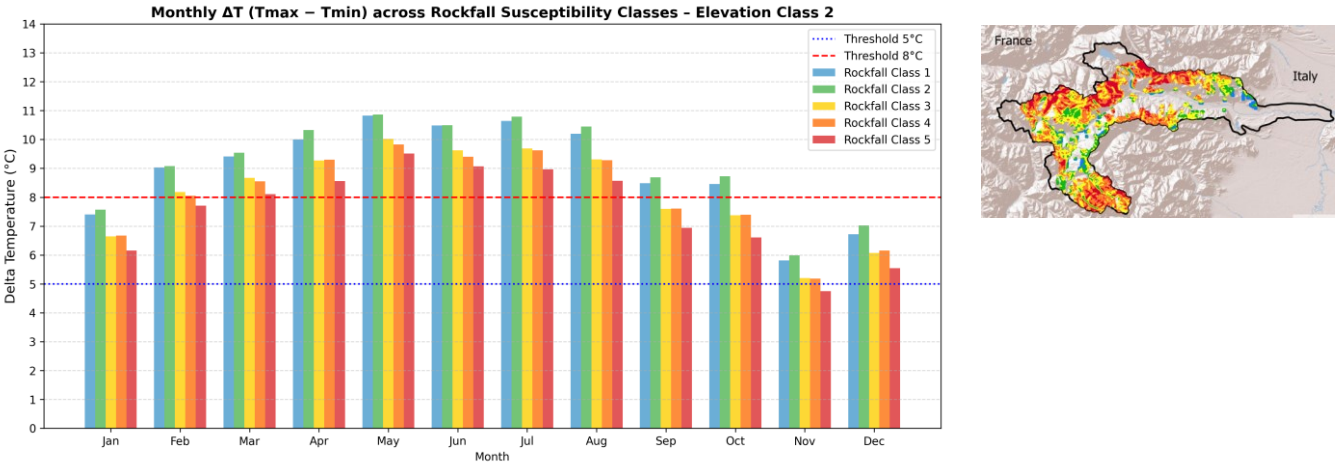

Figure 45_Monthly ΔT across rockfall susceptibility classes in Elevation Class 2, between 5 °C and 8 °C thresholds

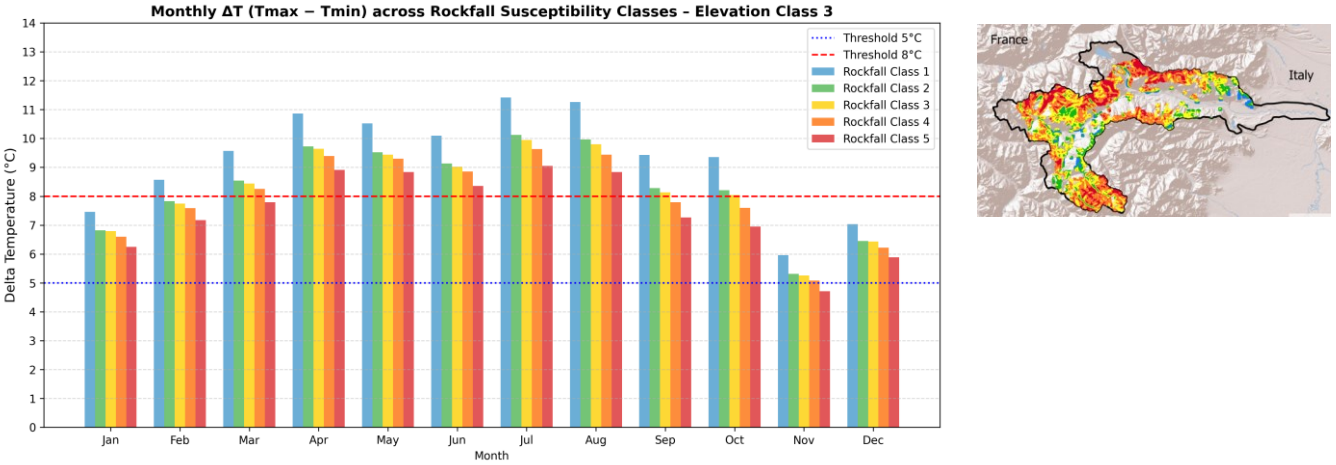

Figure 46 _Monthly ΔT across rockfall susceptibility classes in Elevation Class 4, between 5 °C and 8 °C thresholds

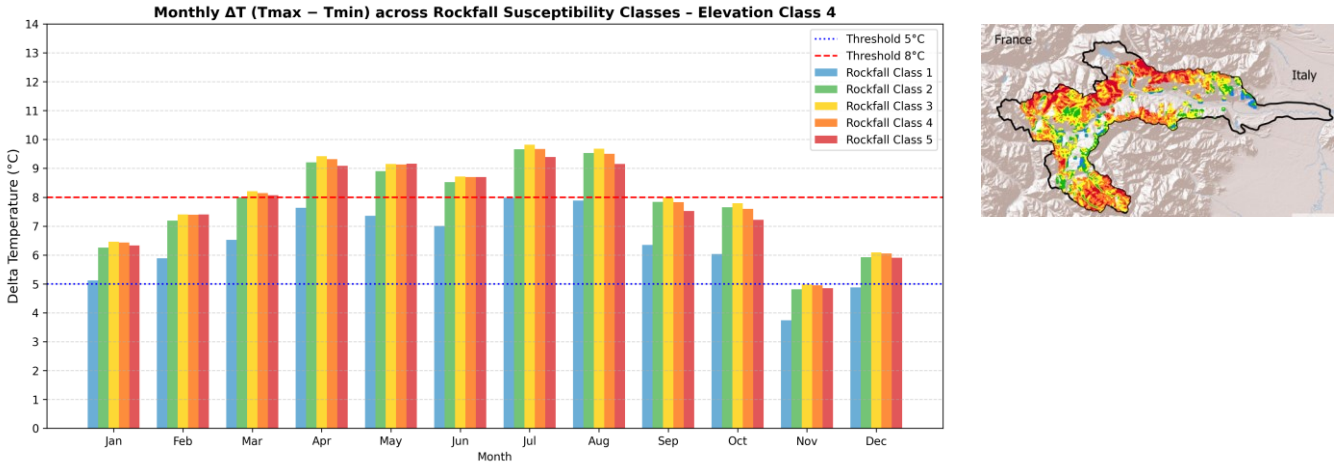

Figure 47 _Monthly ΔT across rockfall susceptibility classes in Elevation Class 4, between 5 °C and 8 °C thresholds

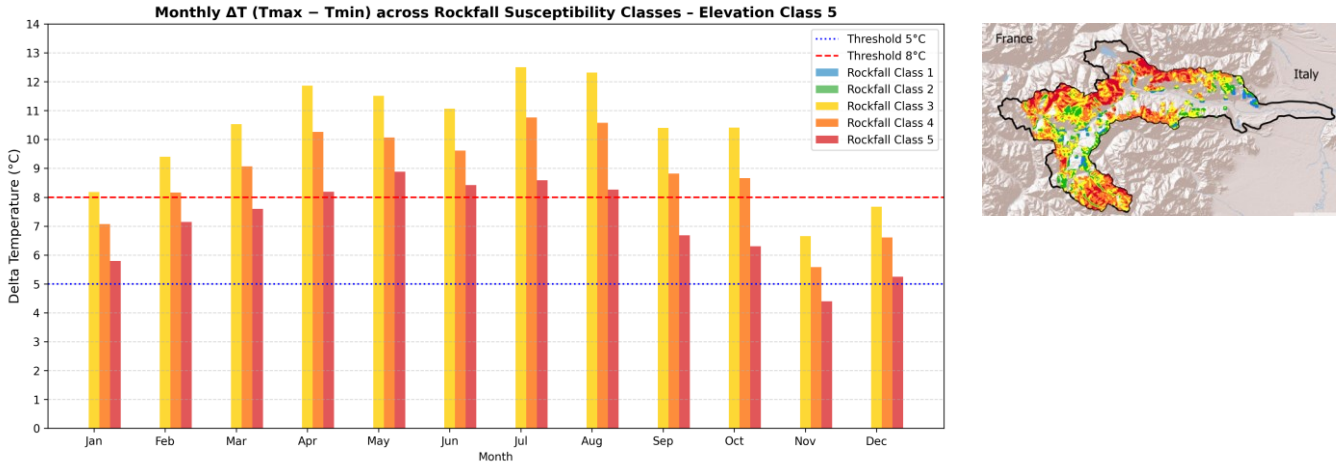

Figure 48 _Monthly ΔT across rockfall susceptibility classes in Elevation Class 5, between 5 °C and 8 °C thresholds

Based on the bar charts (Figure44 to 48), for the five elevation classes, the following patterns are observed in the monthly distribution of ΔT across rockfall susceptibility classes: In most elevation classes, the months of May, June, July, and August show the highest average ΔT values, often exceeding the 8 °C threshold. In Elevation Classes 3 and 4, Susceptibility Classes 3, 4, and 5 frequently record ΔT values above 8 °C during the warmer months. In Elevation Class 5, ΔT values in Susceptibility Classes 3 to 5 occasionally exceed 10 °C in summer. In lower elevation classes (1 and 2), ΔT values are generally lower and only approach higher thresholds during the central months of the year. During colder months (November to February), ΔT values across all classes remain mostly below 5 °C. Susceptibility Class 3 consistently shows the highest ΔT values in most months, particularly in mid- and high-elevation bands. In some months such as June and July, the difference in ΔT between susceptibility classes is more pronounced, with values decreasing progressively from Class 3 to Class 1.

In the following section, the effect of precipitation on rockfall susceptibility has been examined.

Building on earlier analyses, established rainfall thresholds were used to identify extreme events potentially triggering rockfall. The research examines how rainfall events exceeding these thresholds distribute across the five-class rockfall susceptibility map. The analysis of precipitation exceedance patterns used a classified Digital Elevation Model (DEM) to compare different altitude ranges while incorporating elevation as a secondary factor for more detailed analysis.

A workflow based on Python was used for all spatial operations, including the extraction of precipitation thresholds and intersection with susceptibility and

elevation layers. The frequency and distribution of exceedance events across elevation bands and susceptibility classes are depicted in Figure 49, which summarizes the final results. Every point plotted represents an event that has been classified by its elevation class and related rockfall susceptibility class.

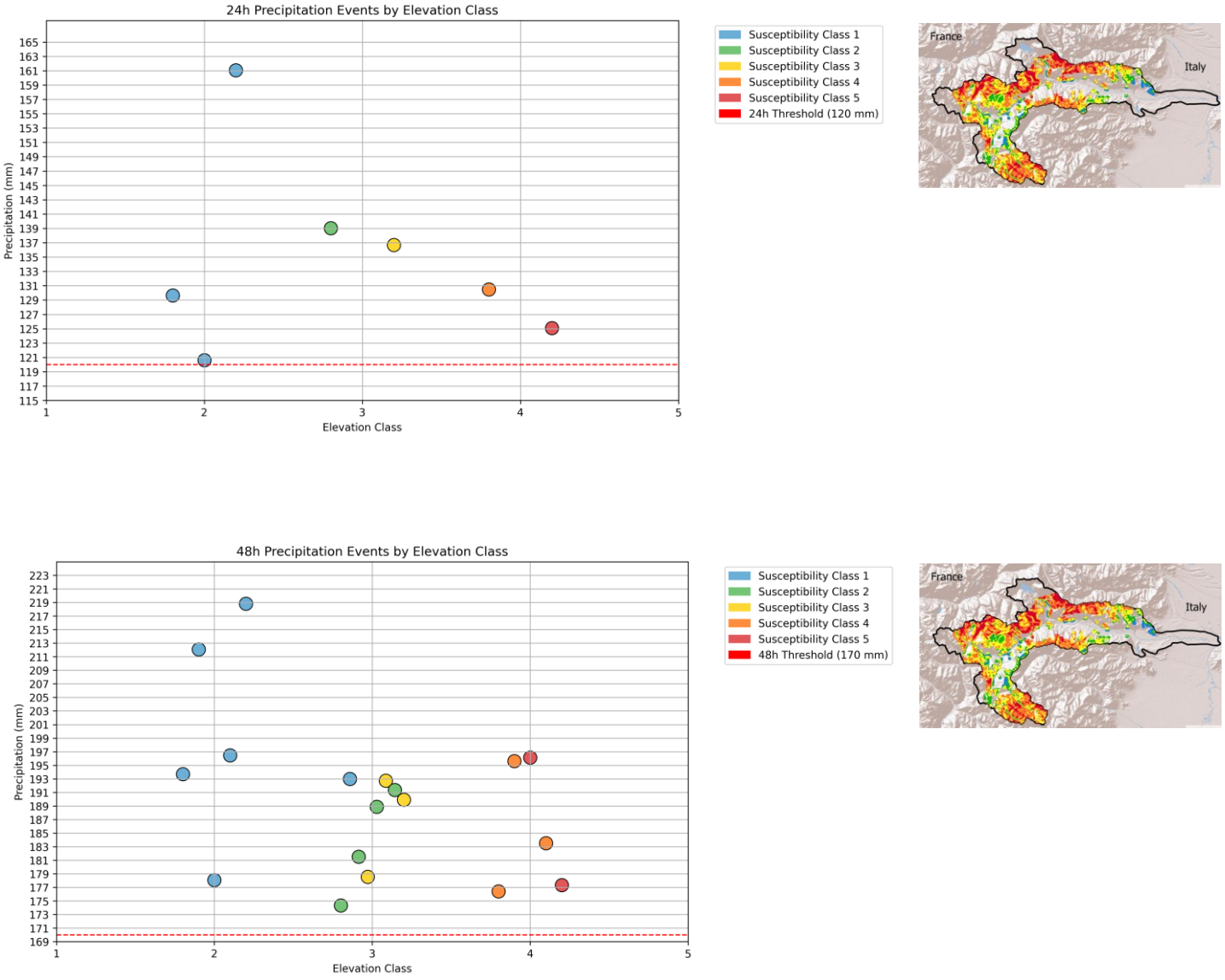

Figure 49_24 and 48 hours Rainfall Events by Elevation Class and Rockfall Susceptibility

Data points from all five susceptibility classes are distributed throughout the 24-hour precipitation plot, which displays a small number of threshold-exceeding events (≥120 mm). Importantly, Classes 2 through 5 exhibit fewer events, all of which are marginally above the threshold, while Class 1 has the most intense 24-hour event (over 160 mm). Since the majority of these exceedances are

concentrated in the lower to mid-elevation classes (roughly Classes 2 and 3), it is possible that these elevations are more vulnerable to intense rainfall that occurs for brief periods of time (Figure 49).

With a more extensive and evenly distributed throughout across susceptibility classes, the 48-hour precipitation plot shows a greater number of exceedance events (≥170 mm). A number of high-intensity events are present in Class 1 once more, and frequent exceedances are also seen in Classes 3 and 4. Despite being less frequent, Class 5 events still exceed the crucial 48-hour mark. Overall, Figure 49 shows that, in contrast to 24-hour events, intense rainfall over 48 hours has historically impacted a wider elevation and susceptibility range.

4.4.2 Debris Flow Susceptibility under Precipitation Conditions

To evaluate the role of precipitation in triggering debris flow events, daily rainfall data from December 1957 to December 2024 were analyzed. Given that debris flows are primarily influenced by short-duration rainfall intensity, 12-hour precipitation values were estimated from the daily records to approximate high-intensity episodes. These estimates were then compared against the predefined susceptibility thresholds for the three debris flow classes—ECM, GCM, and BCM—corresponding to 20 mm/h, 30 mm/h, and 50 mm/h, respectively. The susceptibility classes were defined based on lithological characteristics and their clay-forming potential. A spatial overlay was conducted between the debris flow susceptibility map and the precipitation intensity data to determine how many events exceeded the thresholds in each class. The results allow for a historical overview of where and how often critical rainfall conditions have coincided with topographic susceptibility.

Figure 50, presented below illustrates the distribution of threshold-exceeding rainfall events across the three susceptibility categories, providing a spatial summary of potential debris flow triggers throughout the study period (1957 to 2024).

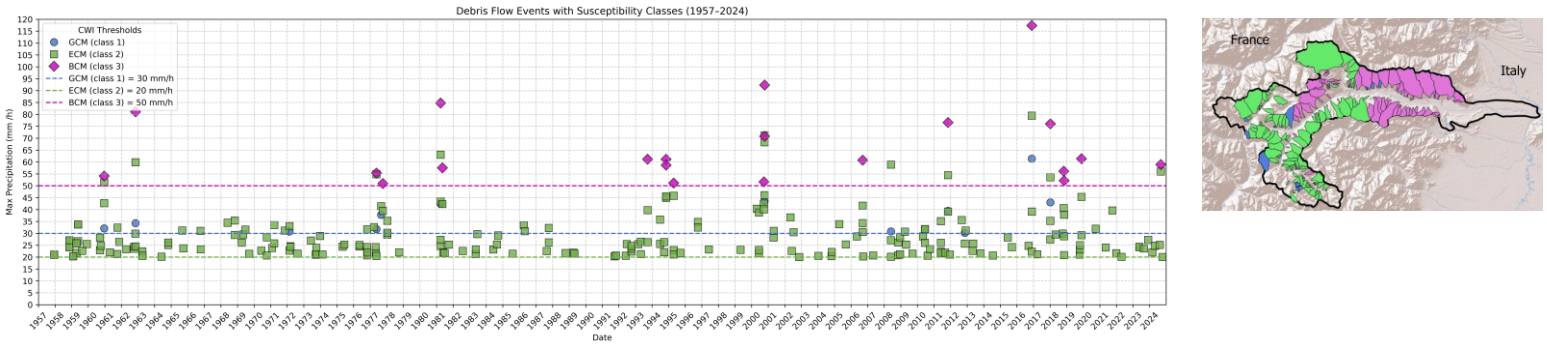

Figure 50_24 and 48 hours Rainfall Events by Elevation Class and Debris Flow Susceptibility from 1957 to 2024

Figure 50 shows the temporal distribution of debris flow events that exceeded class-specific rainfall thresholds between 1957 and 2024, categorized by susceptibility class. Each point on the plot represents a single summer rainfall event surpassing the threshold of its respective class. The chart clearly indicates that ECM-class (Class 2) events dominate the historical record, both in frequency and temporal spread, consistently exceeding their 20 mm/h threshold. BCM-class (Class 3) events, though less frequent, display particularly intense rainfall values, often well above the 50 mm/h mark and mainly clustered in the more recent decades (post-1980), hinting at a possible intensification over time. GCM-class (Class 1) events are the least common, scattered across the timeline and showing limited exceedances beyond their 30 mm/h threshold.

The following Python-based analysis evaluated elevation's impact on debris flow occurrence in the next step. The predefined elevation bands from this study were merged with debris flow susceptibility classes to analyze how rainfall intensity interacts with topographic variation. The analysis combined predicted hourly precipitation data with these classifications to determine which elevation bands experience debris flow events most often within each susceptibility class. The spatial comparison reveals how terrain altitude affects debris flow potential when rainfall intensities vary (Figure 51)

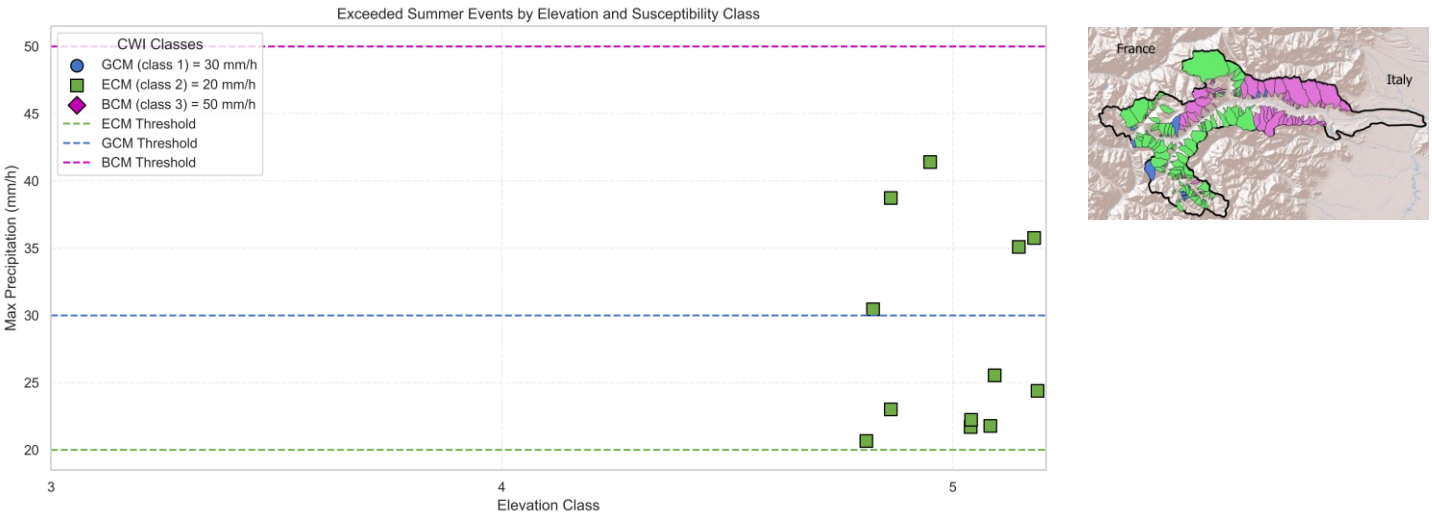

Figure 51_ Rainfall Events by Elevation Class and Debris Flow Susceptibility Summer

Figure 51 shows between the summer months of 1957 and 2024, all recorded debris flow events that exceeded critical rainfall thresholds occurred exclusively within Elevation Class 5 (above 3000 meters). No threshold-exceeding events were observed in lower elevation classes, underscoring the dominant role of high-altitude terrain in triggering debris flows during warm-season periods. Moreover, all these events belonged to the ECM susceptibility category (Class 2), which has a threshold of 20 mm/h. The data indicate that a significant portion of these events fell within the 20 to 40 mm/h range, with no occurrences recorded for either the GCM (Class 1) or BCM (Class 3) categories, as no GCM or BCM catchments are present at this elevation class.

4.4.3 Shallow Landslide Susceptibility under Precipitation Conditions

In this phase of the analysis, the methodology applied for rockfall threshold assessment under 24-hour and 48-hour rainfall conditions was similarly adopted to evaluate shallow landslide susceptibility. However, the focus here is specifically on shallow landslides, utilizing the dedicated susceptibility map provided by ARPA Piemonte. This map categorizes the study area into three susceptibility classes: Class 2 (moderate), Class 3 (high), and Class 4 (very high), which also indicate the expected number of shallow landslides when critical rainfall thresholds are exceeded, see(Tiranti et al., 2019).

The Python-based method from previous sections was used to determine average rainfall values for each susceptibility class. The following analysis examined the relationships between elevation and susceptibility and rainfall intensity. The research combined these parameters to establish a better understanding of shallow landslide susceptibility patterns across space and time under rainfall conditions. The analysis results appear in Figure 52.

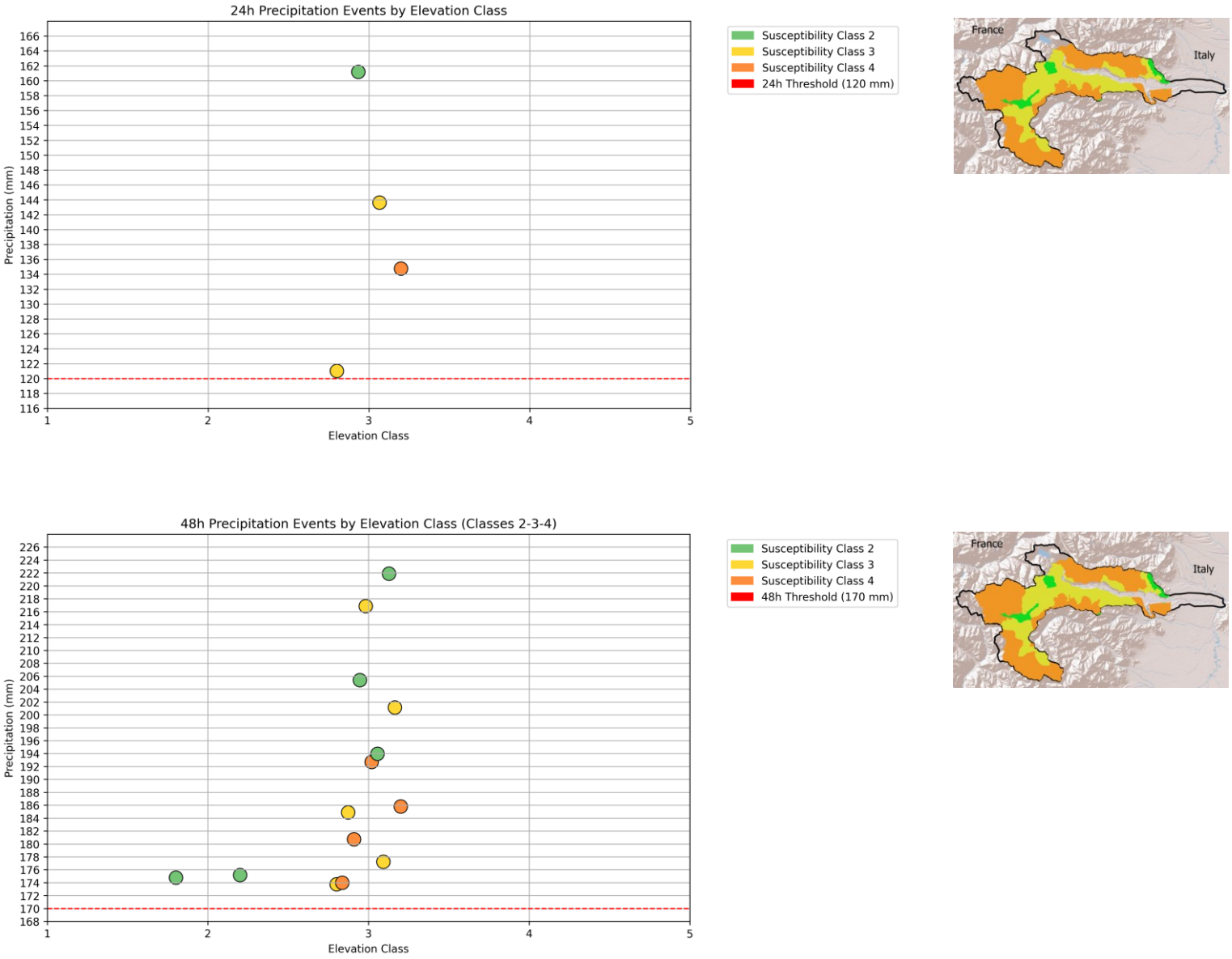

Figure 52_24 and 48 hours Rainfall Events by Elevation Class and Shallow Landslides Susceptibility Summer

Susceptibility Classes 2, 3, and 4 are represented by the distribution of events in the first chart (24-hour precipitation). Precipitation amounts range from roughly 121 mm to over 160 mm, with all recorded values exceeding the critical threshold of 120 mm. Since every event is classified as belonging to Elevation Class 3, the dataset's occurrences are restricted to a particular elevation band.In the second chart (48-hour precipitation), a larger number of extreme events is visible, all exceeding the threshold of 170 mm. Recorded precipitation values reach above 220 mm, with data points present across all three susceptibility classes. Most of the events are again concentrated in Elevation Class 3, with a few extending into lower elevation classes (around Class 2).

4.5 Future Temperature Projections Under RCP 4.5

In order to evaluate the potential impact on the Susa Valley's susceptibility to geohazards, this section looks at future temperature trends under the RCP 4.5 scenario. High-resolution raster datasets (.tif format) from ARPA Piemonte that span the years 2025–2100 serve as the basis for the analysis. The projections are based on these datasets, which include daily minimum, maximum, and delta temperatures (ΔT = Tmax − Tmin).

RCP 4.5 represents a moderate emission scenario in which greenhouse gas emissions peak around 2040 and gradually decline. Under this pathway, global temperatures are expected to rise by approximately 1.8 to 2.4°C by the end of the century (IPCC, 2014).

Due to the limitations of QGIS in handling large raster datasets efficiently, the analysis was performed in Python. This allowed for more precise computation of daily and monthly temperature indicators and their distribution across elevation bands. The following sections present the spatial and temporal trends of these variables under RCP 4.5, with a focus on identifying thermal thresholds related to slope instability processes.

4.5.1 Monthly and Daily Average Delta Temperatures

In contrast to the historical dataset, which included daily maximum and minimum temperatures allowing for detailed daily ΔT calculations, the future projections provided in .tif format under the RCP 4.5 scenario contain only monthly data. Therefore, the analysis of delta temperature in this case was limited to monthly average values.

To compute the Monthly Average Delta Temperature, maximum and minimum values were extracted from the raster files using Python-based geospatial tools. These values were then used to calculate ΔT (Tmax − Tmin) on a monthly basis across the study period from 2025 to 2100.

The results are presented in Figures 53, which display the temporal evolution of Monthly Average ΔT under the RCP 4.5 scenario.

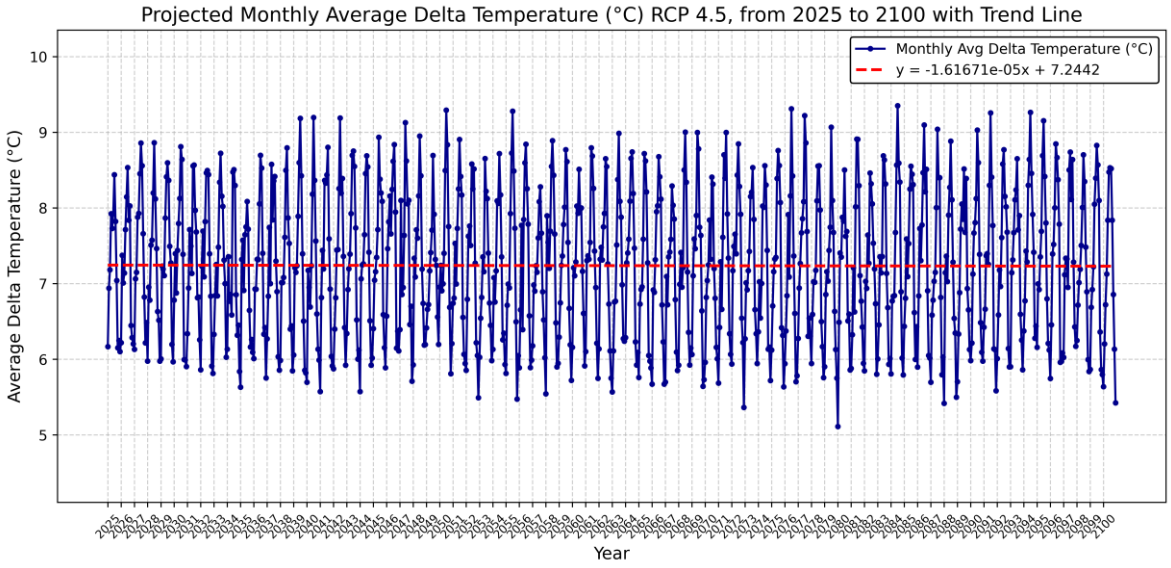

Figure 53_Monthly Average Delta Temperature (°C) from 2025 to 2100 with Trend Line, RCP 4.5

As demonstrated, ΔT values fluctuate seasonally and annually, typically falling between roughly 6°C and 9°C. Over time, these variations recur regularly, creating a discernible monthly pattern. The graph now has a trend line that indicates a very slight negative slope of about -0.000016. This suggests a slow, essentially insignificant drop in delta temperature over time. In other words, it is anticipated that the daily maximum and minimum temperature difference will decrease very gradually, but the change will be so small that the trend as a whole will be regarded as stable. As a result, daily temperature variations are predicted to stay constant under RCP 4.5, and the thermal regime of the area is probably going to continue to follow a largely stable pattern.

To provide a clearer understanding of average temperature variability, the following Figures 54 to 57, present both monthly trend analyses and corresponding daily data.

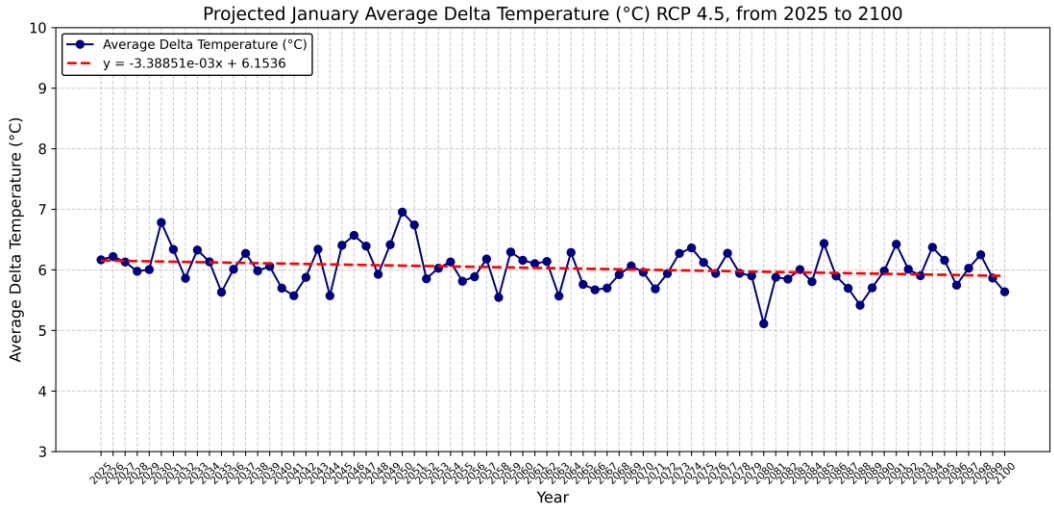

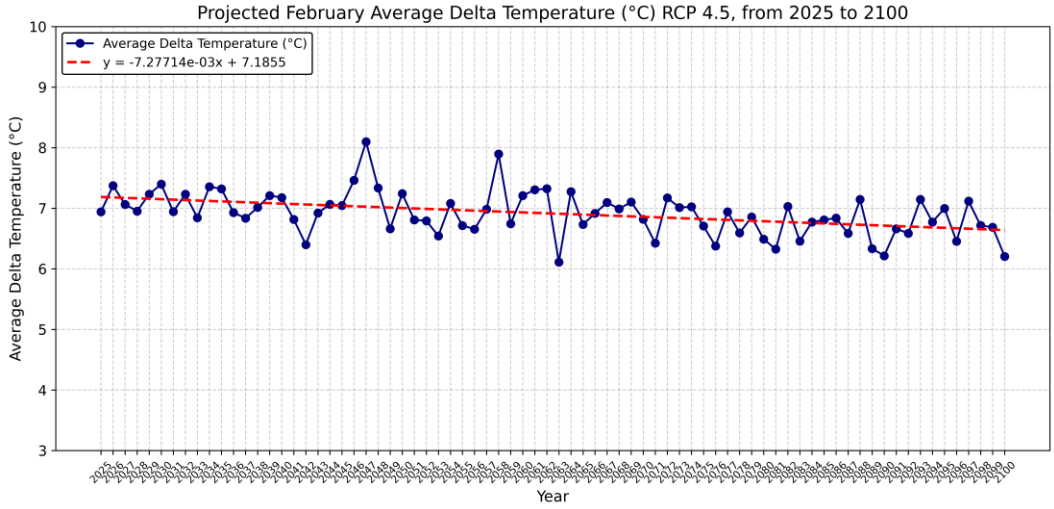

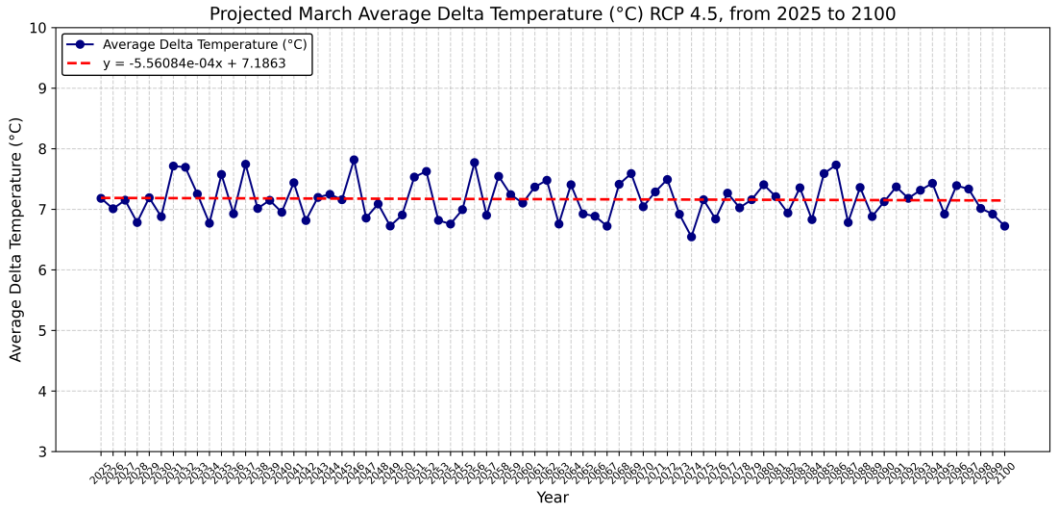

Figure 54_Monthly Average Delta Temperature (°C) from 2025 to 2100 with Trend Line, RCP 4.5_ Jan to Mar

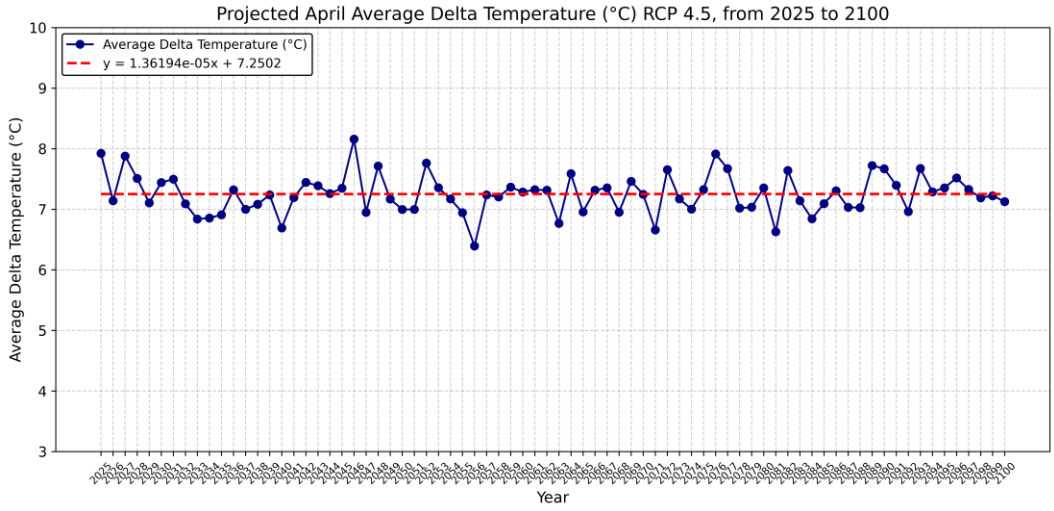

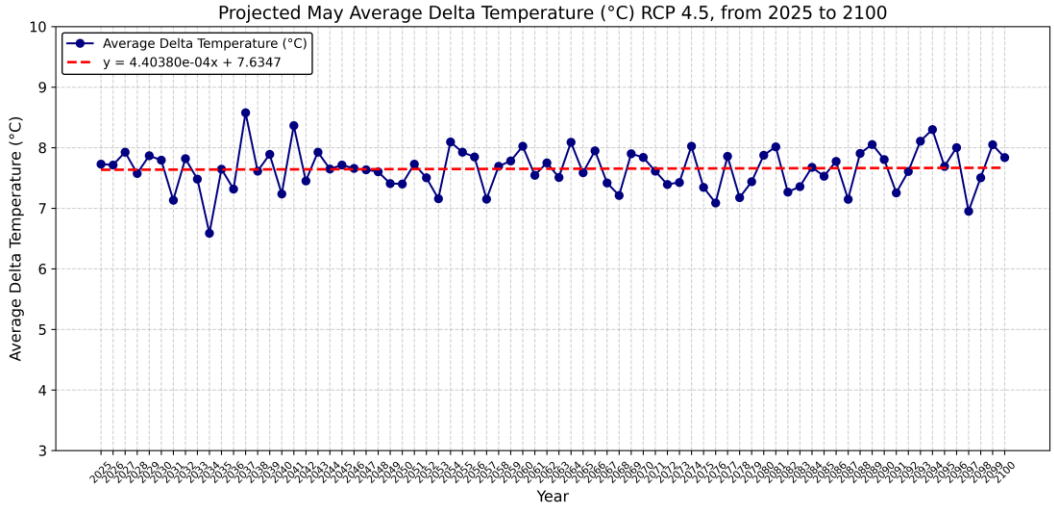

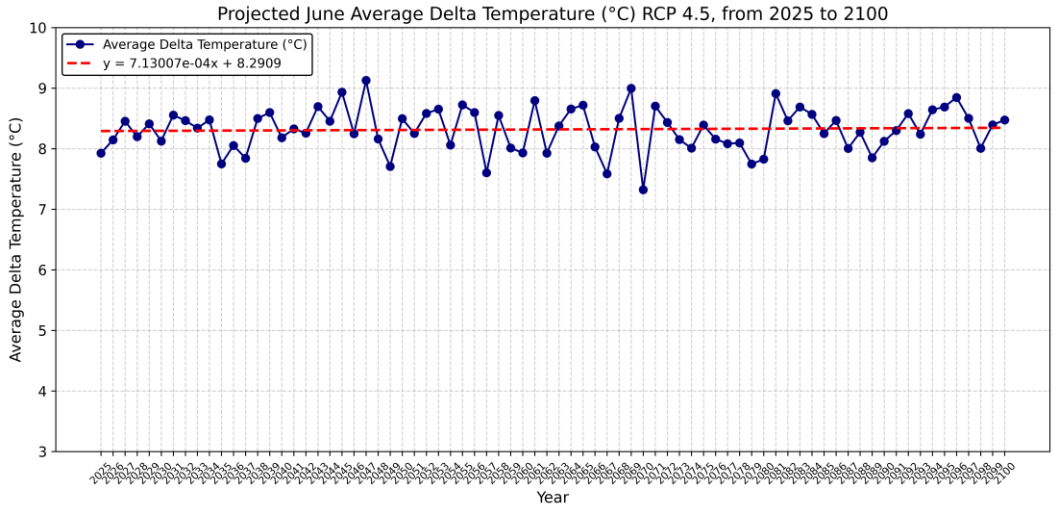

Figure 55_Monthly Average Delta Temperature (°C) from 2025 to 2100 with Trend Line, RCP 4.5_ Apr to Jun

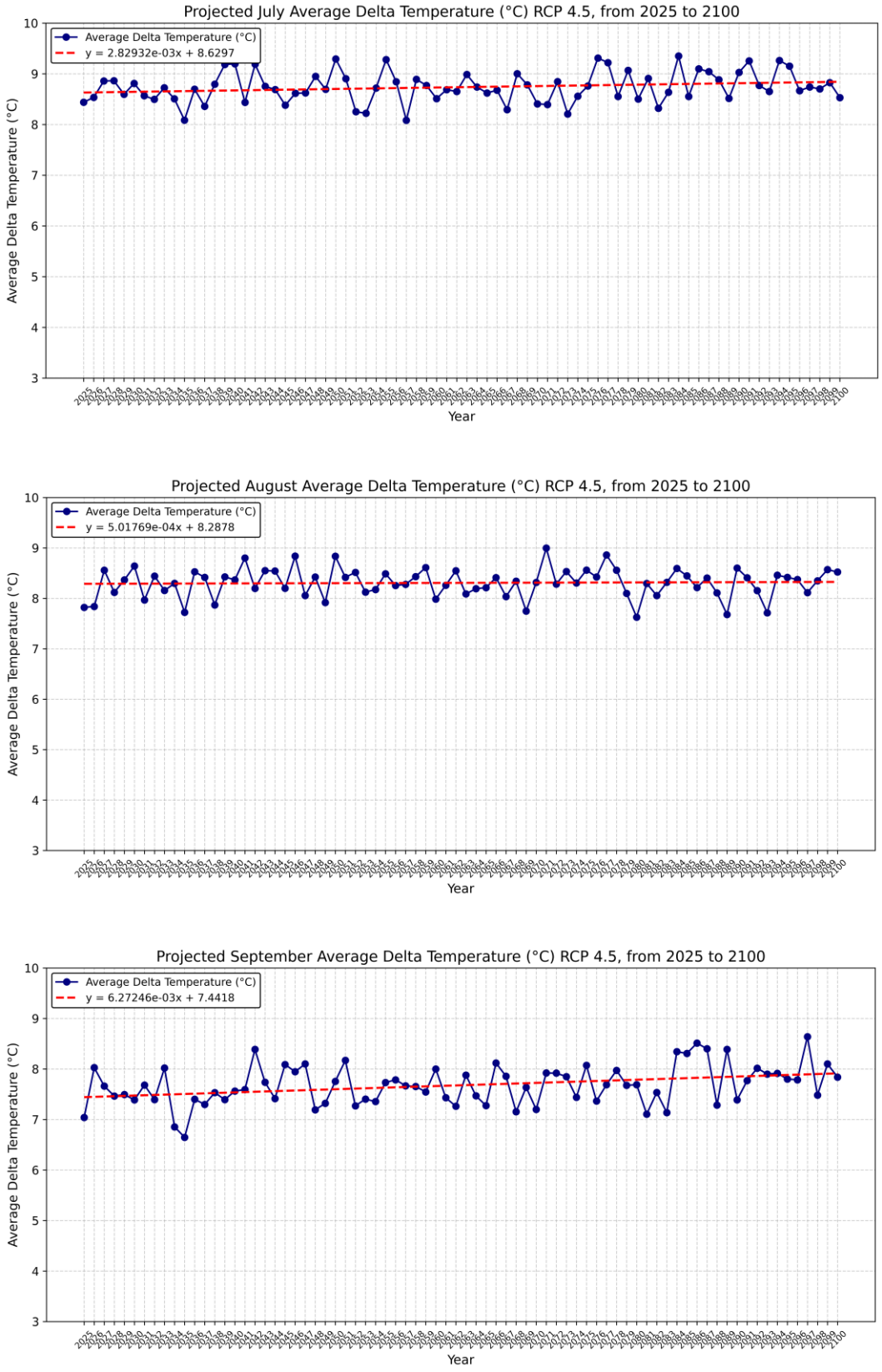

Figure 56_Monthly Average Delta Temperature (°C) from 2025 to 2100 with Trend Line, RCP 4.5_ Jul to Sep

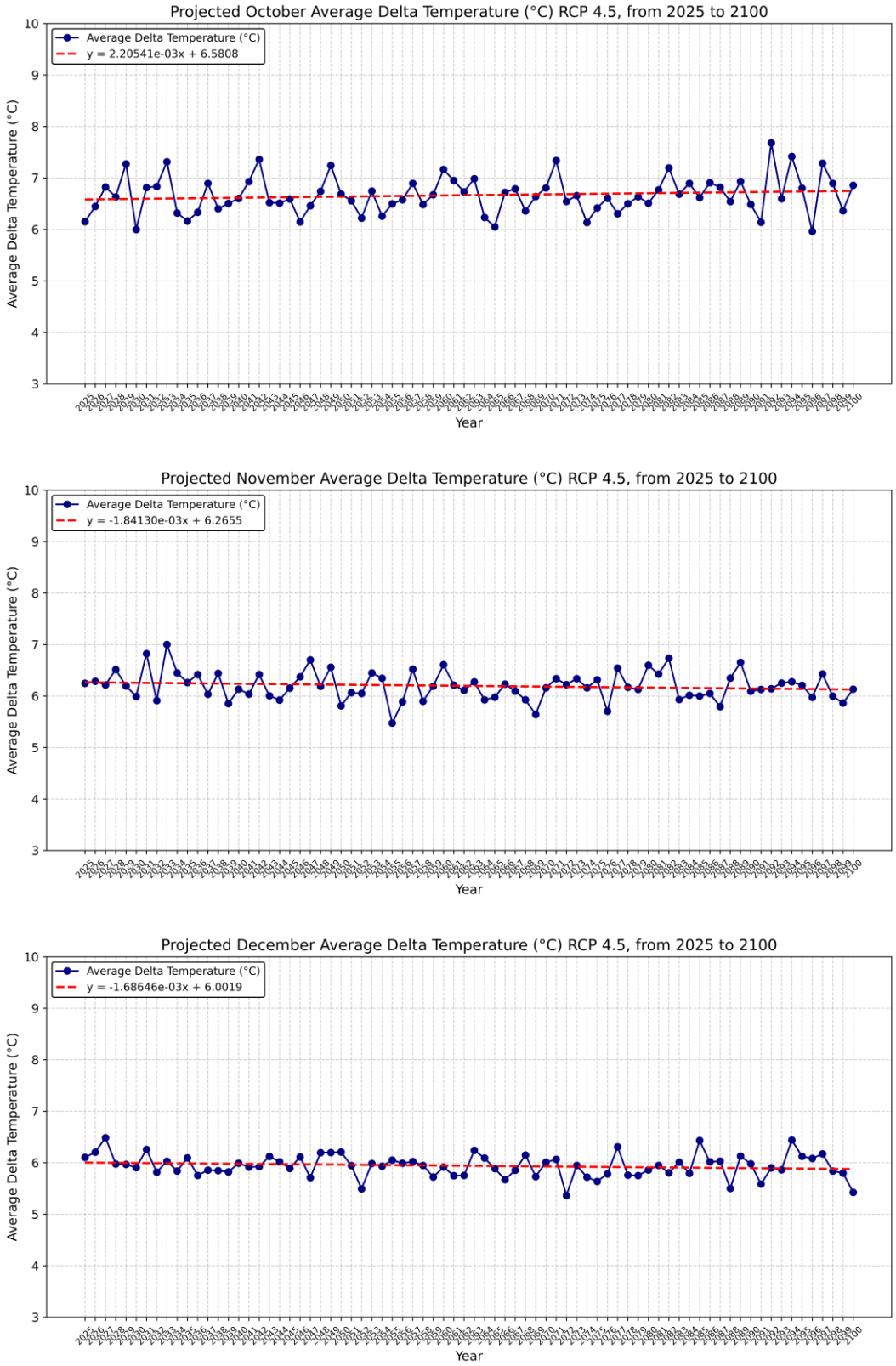

Figure 57_Monthly Average Delta Temperature (°C) from 2025 to 2100 with Trend Line, RCP 4.5_ Oct to Dec

To gain a clearer understanding of seasonal patterns in daily temperature variation, the average delta temperature (ΔT) was analyzed month by month over the period 2025 to 2100 under the RCP 4.5 scenario (Figure 54 to 57). The projection period shows stable monthly Average ΔT values according to the results. Trend lines in January, February and December show a slight downward direction, but the changes remain minimal. The summer months of June, July and September show upward trends, indicating a small rise in day-night temperature differences. Overall, these monthly variations are consistent with the general pattern of thermal stability observed across the entire projection period.

4.5.2 Monthly Delta Temperature (ΔT)

Delta temperature (ΔT), was taken from RCP 4.5 scenario data for the years 2025 to 2100 in order to examine future monthly temperature variations. Using the same methodology as for historical data, this analysis was performed on Excel files created in Python. The difference in temperature between day and night is indicated by ΔT. The overall monthly ΔT trend under the RCP 4.5 scenario is displayed for the anticipated period in Figure 58.

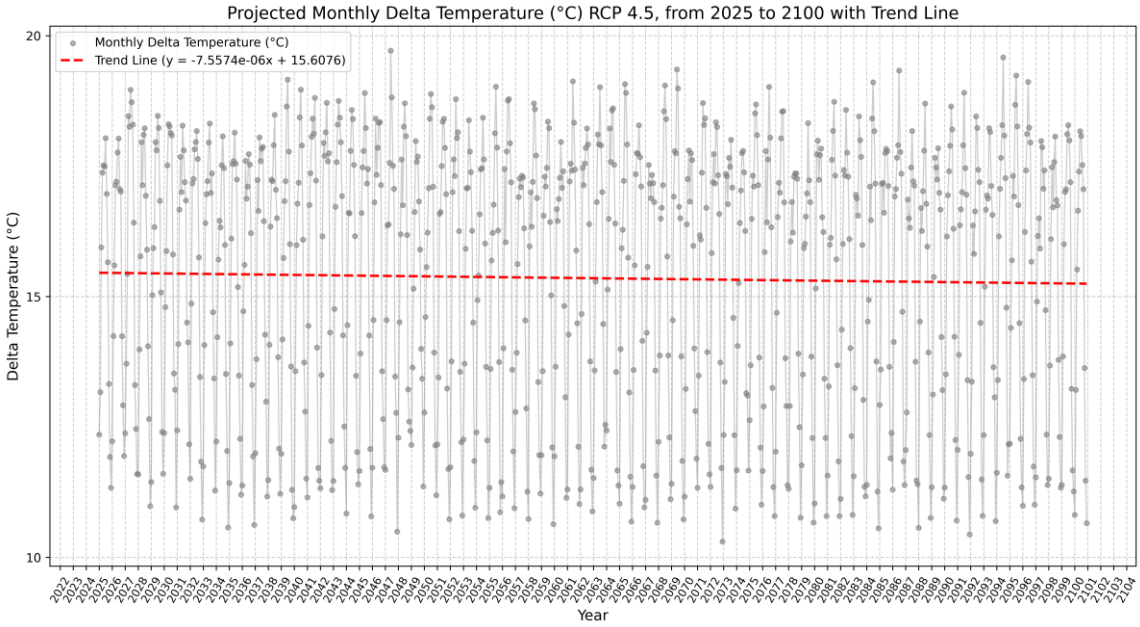

Figure 58_Monthly Delta Temperature (°C) from 2025 to 2100 with Trend Line, RCP 4.5

The estimated monthly delta temperature (ΔT) values for the years 2025–2100 under the RCP 4.5 scenario are shown in Figure 58. Every monthly ΔT data point is shown on the chart as a grey marker, and the general direction is indicated by a red trend line. The trend line's slope is very near zero, but slightly negative (about -0.0000076).

The ΔT values show natural yearly variations but stay between 13°C and 18°C throughout the entire period. The temperature difference between day and night shows no noticeable upward or downward trend throughout this period which indicates stable monthly temperature variability. The flat trend line indicates that RCP 4.5 conditions will not lead to significant long-term changes in monthly temperature variability.

The ΔT for each month over this future period was then looked at in order to further elucidate the conditions (Figure 59 to 62).

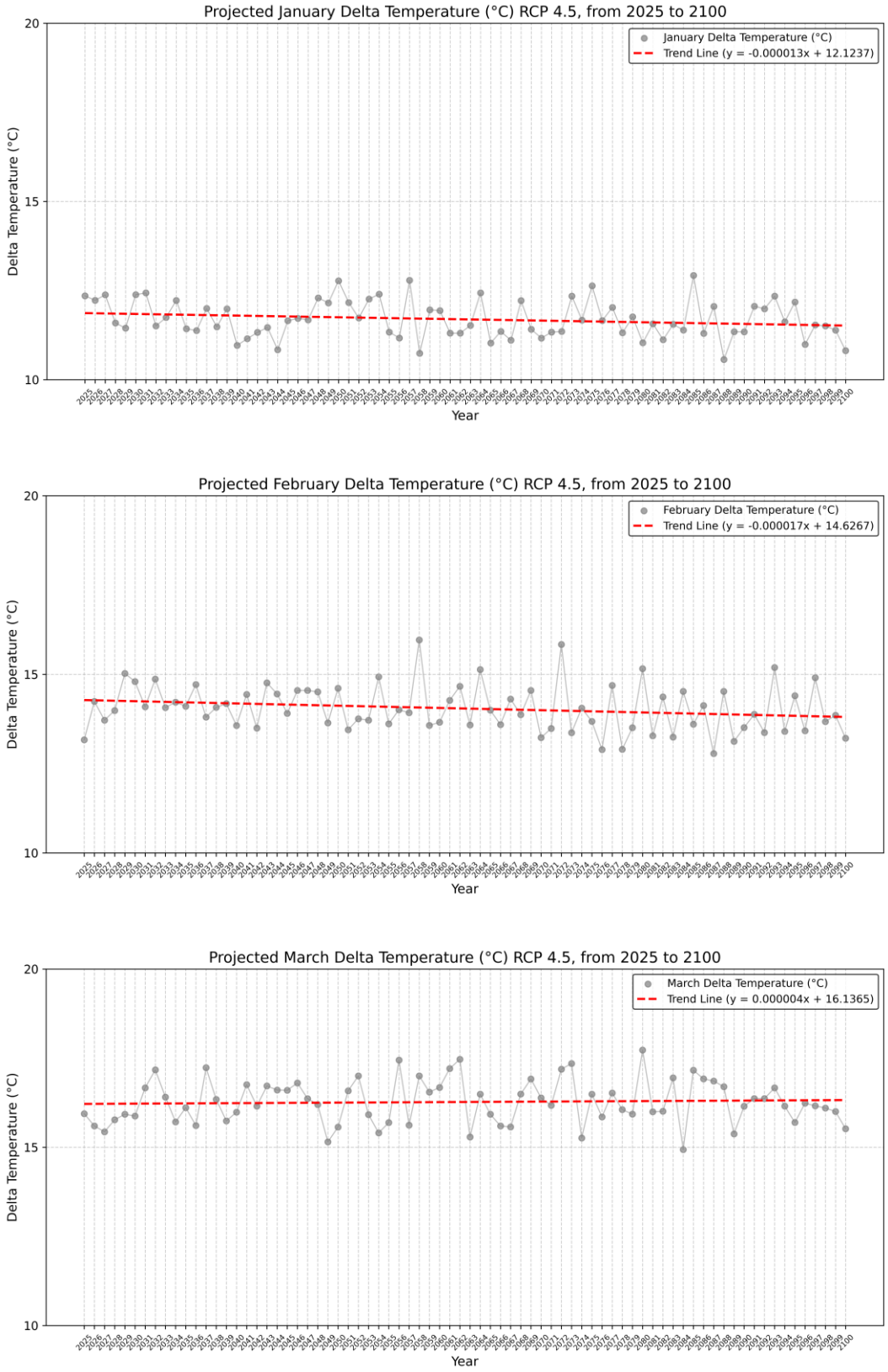

Figure 59_Monthly Delta Temperature (°C) from 2025 to 2100 with Trend Line, RCP 4.5_ Jan to Mar

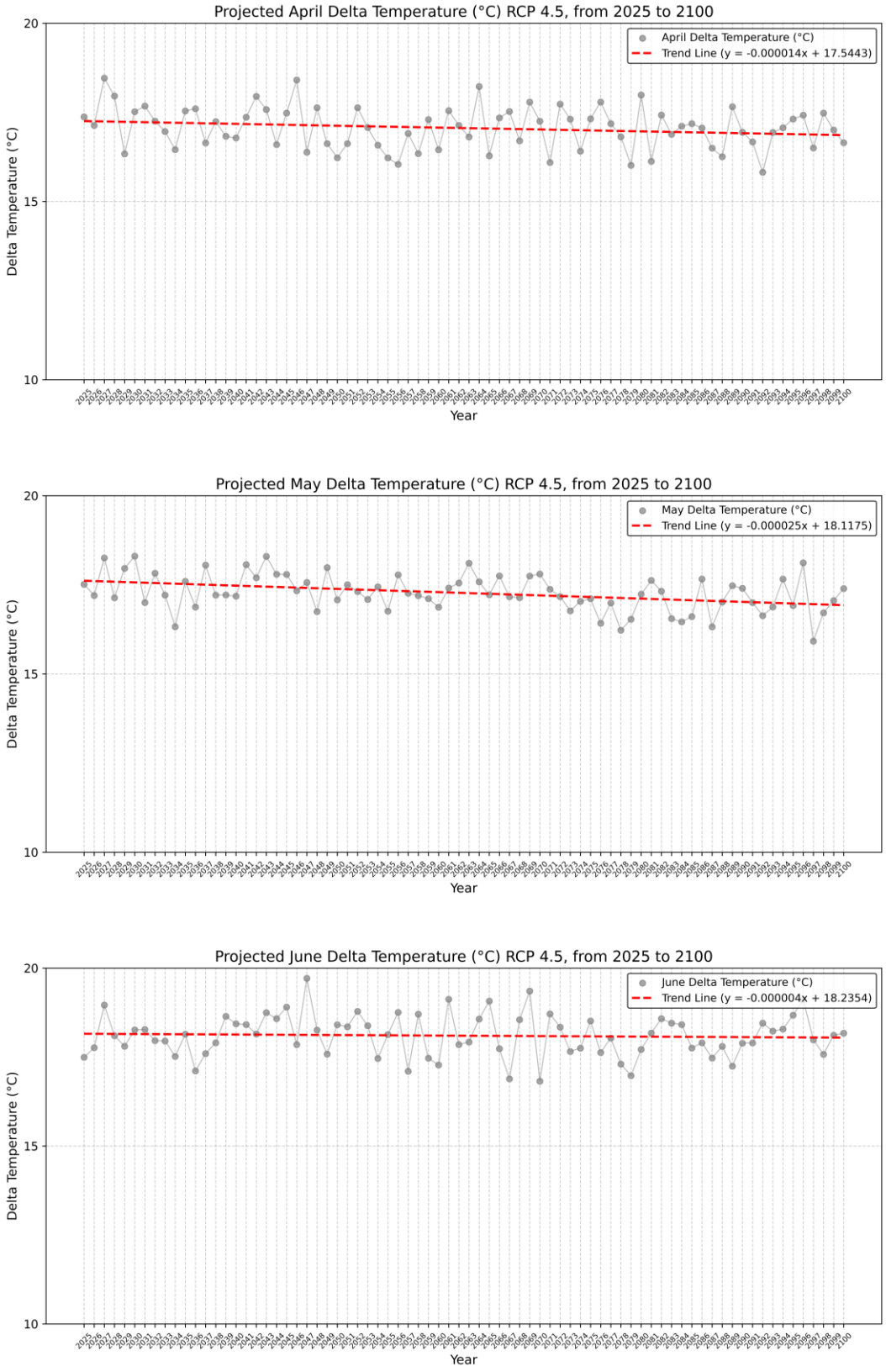

Figure 60_Monthly Delta Temperature (°C) from 2025 to 2100 with Trend Line, RCP 4.5_ Apr to Jun

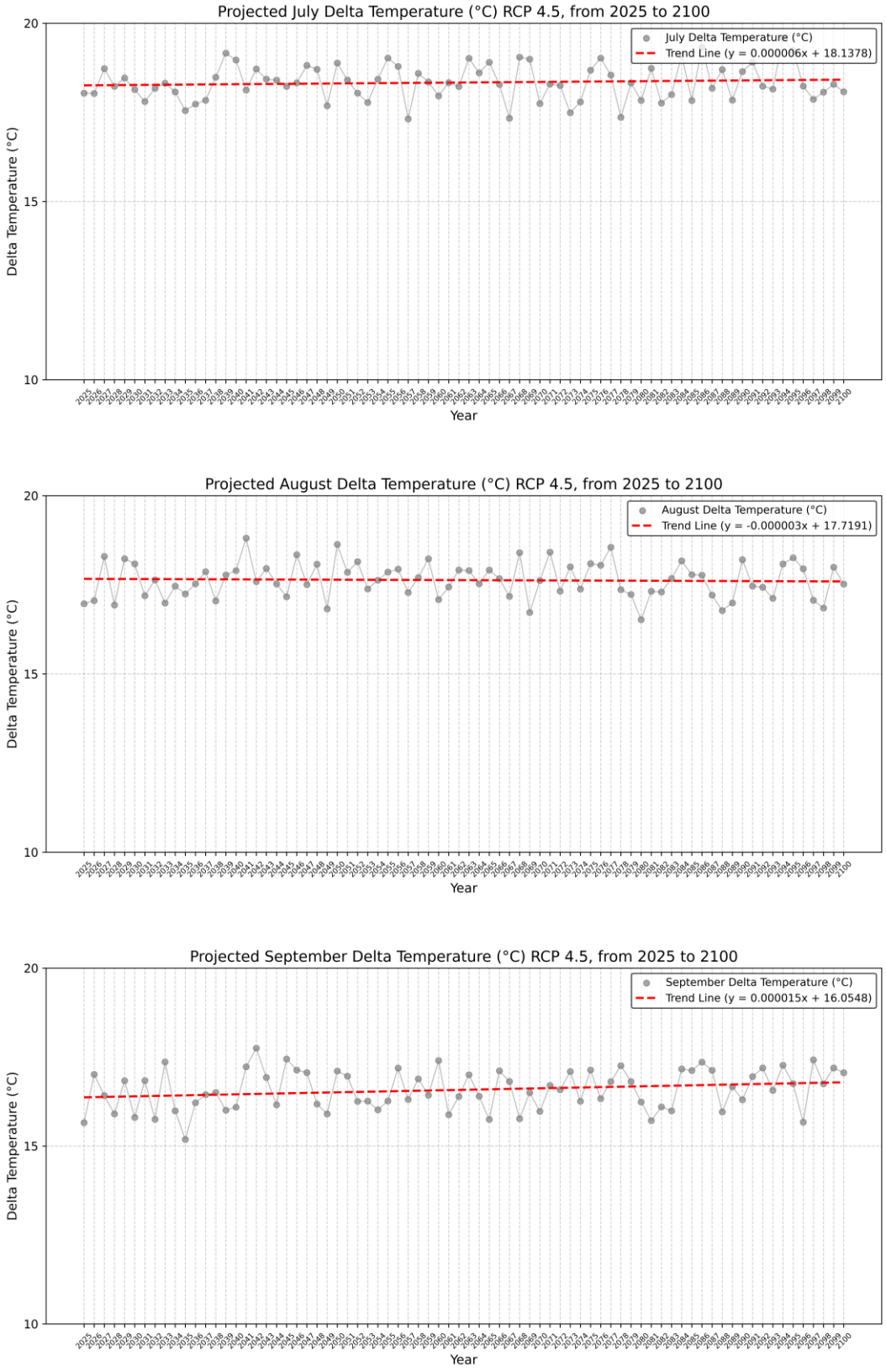

Figure 61_Monthly Delta Temperature (°C) from 2025 to 2100 with Trend Line, RCP 4.5_ Jul to Sep

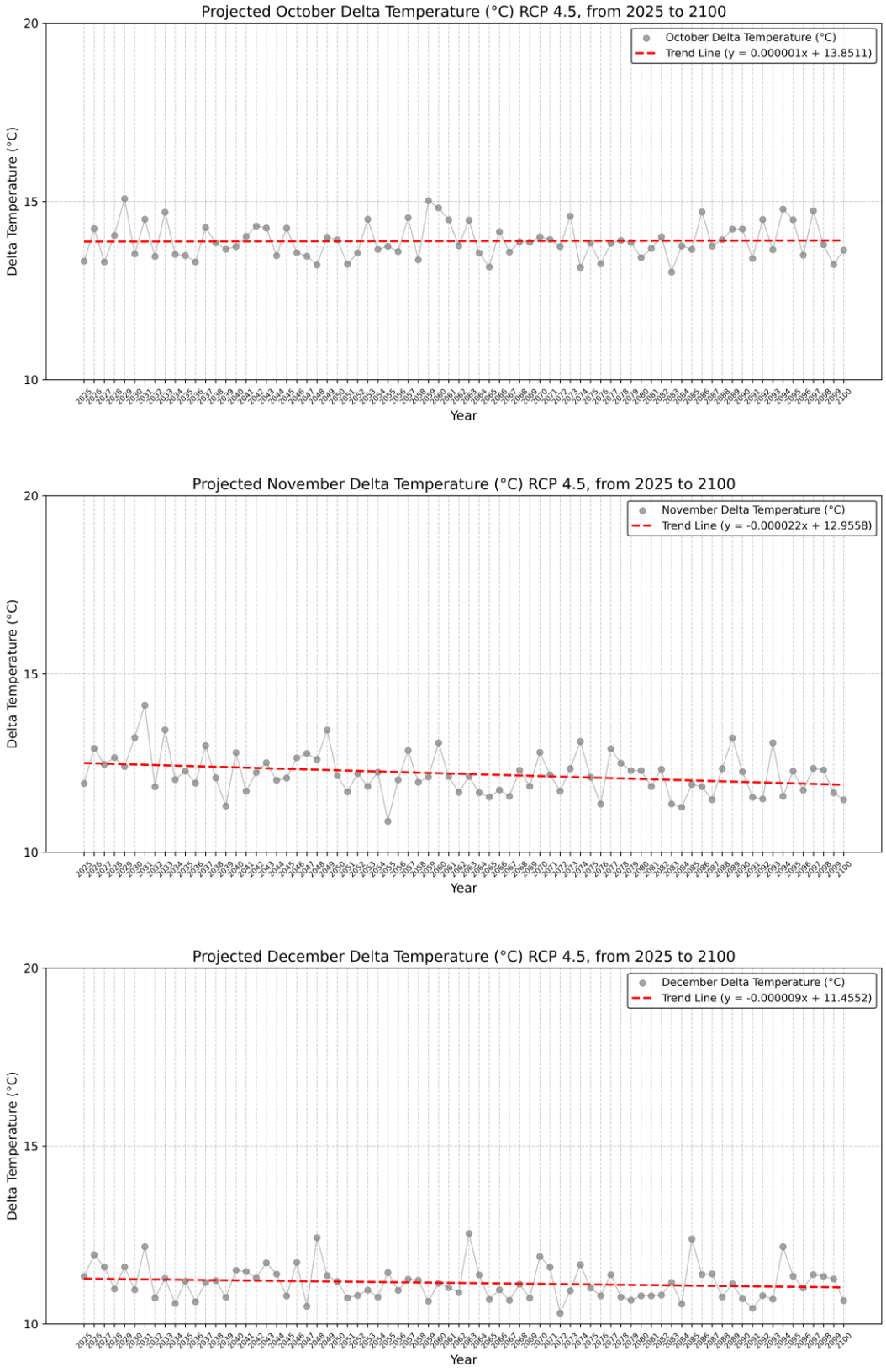

Figure 62_Monthly Delta Temperature (°C) from 2025 to 2100 with Trend Line, RCP 4.5_ Oct to Dec

According to a large analysis of the graphs, the majority of the months show comparatively constant annual variability over the course of the anticipated period, with no notable fluctuations. The trend lines of the colder months (January, February, November, and December) usually slope downward and exhibit lower ΔT values. The rate of decline, though, is slow and does not portend a significant shift. On the other hand, higher ΔT values are found in warmer months like June, July, August, and September. A slight increase in day-night temperature differences during the summer is indicated by trend lines that slope slightly upward in some of these months. These upward trends, however, are extremely slow and do not signify significant departures. The trend lines for each month are generally flat, suggesting that under the RCP 4.5 scenario, ΔT will be mostly stable between 2025 and 2100, with only slight seasonal variations.

4.5.3 Monthly Maximum and Minimum Temperatures

In this section, projected monthly Tmax and Tmin under the RCP 4.5 scenario were analyzed for the period from 2025 to 2100. The goal is to examine long-term trends in temperature extremes and seasonal dynamics that may indicate future thermal risks in the Susa Valley.

For each month, projected Tmax and Tmin values were obtained from monthly GeoTIFF datasets and processed using Python to create time series of monthly temperatures. These values were then visualized along with fitted trend lines to highlight the overall evolution of Tmax and Tmin over the 21st century.

In the following section, an overall view of the increasing and decreasing temperature trends from 1957 to 2024 is first presented (Figure 63).

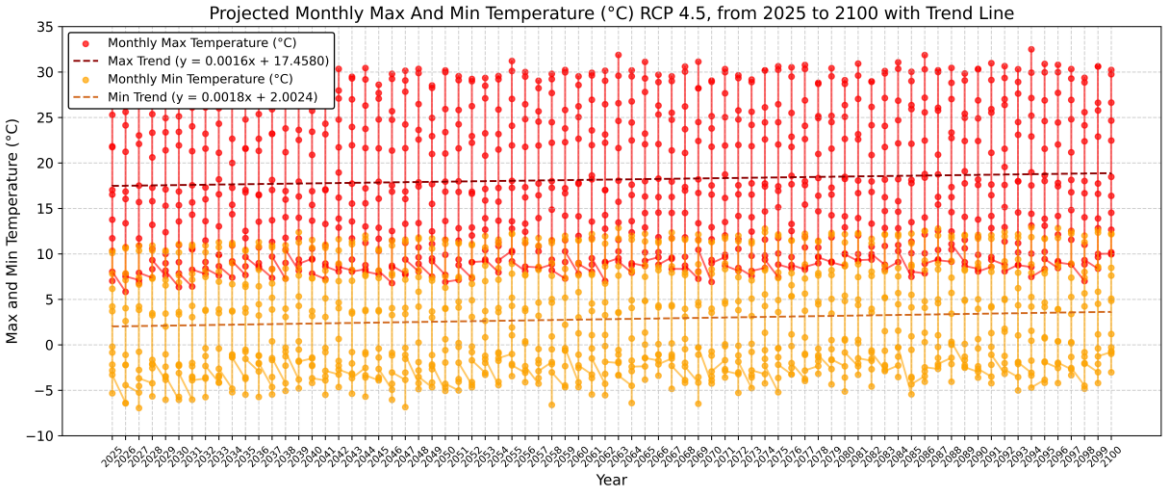

Figure 63_Monthly Max and Min Temperature (°C) from 2025 to 2100 with Trend Line, RCP 4.5

The presented chart illustrates that based on the added trend lines, Tmax shows a gradual increase with a slope of approximately 0.0016 °C per year. In

comparison, Tmin also follows an upward trend, but with a slightly steeper slope of about 0.0018 °C per year, indicating that nighttime temperatures are rising faster than daytime temperatures.

The Tmax and Tmin temperature difference shows an increasing trend which indicates a reduction in the delta temperature (ΔT) throughout the study period. To explore this further, the maximum and minimum temperatures were calculated and analyzed separately for each month over the last six decades (Figures 64 to 67).

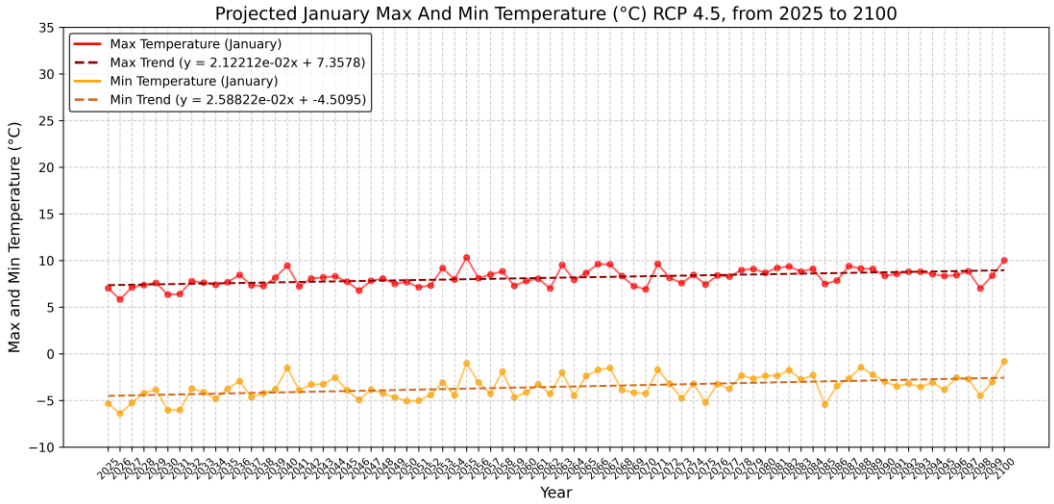

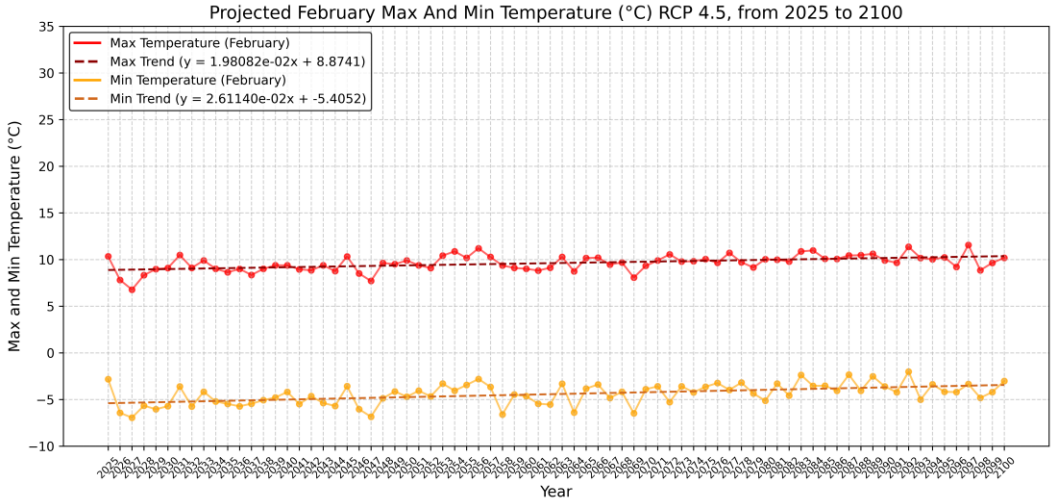

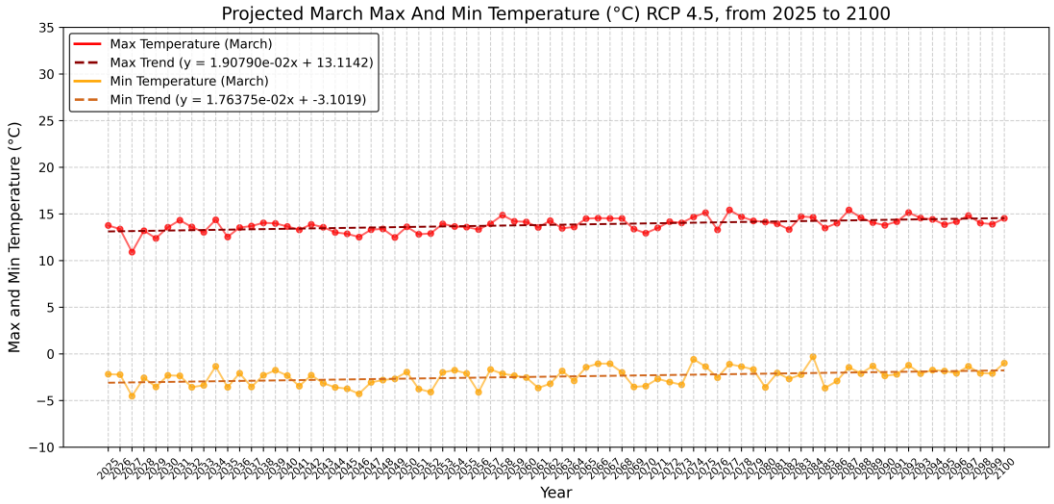

Figure 64_Monthly Max and Min Temperature (°C) from 2025 to 2100 with Trend Line, RCP 4.5_ Jan to Mar

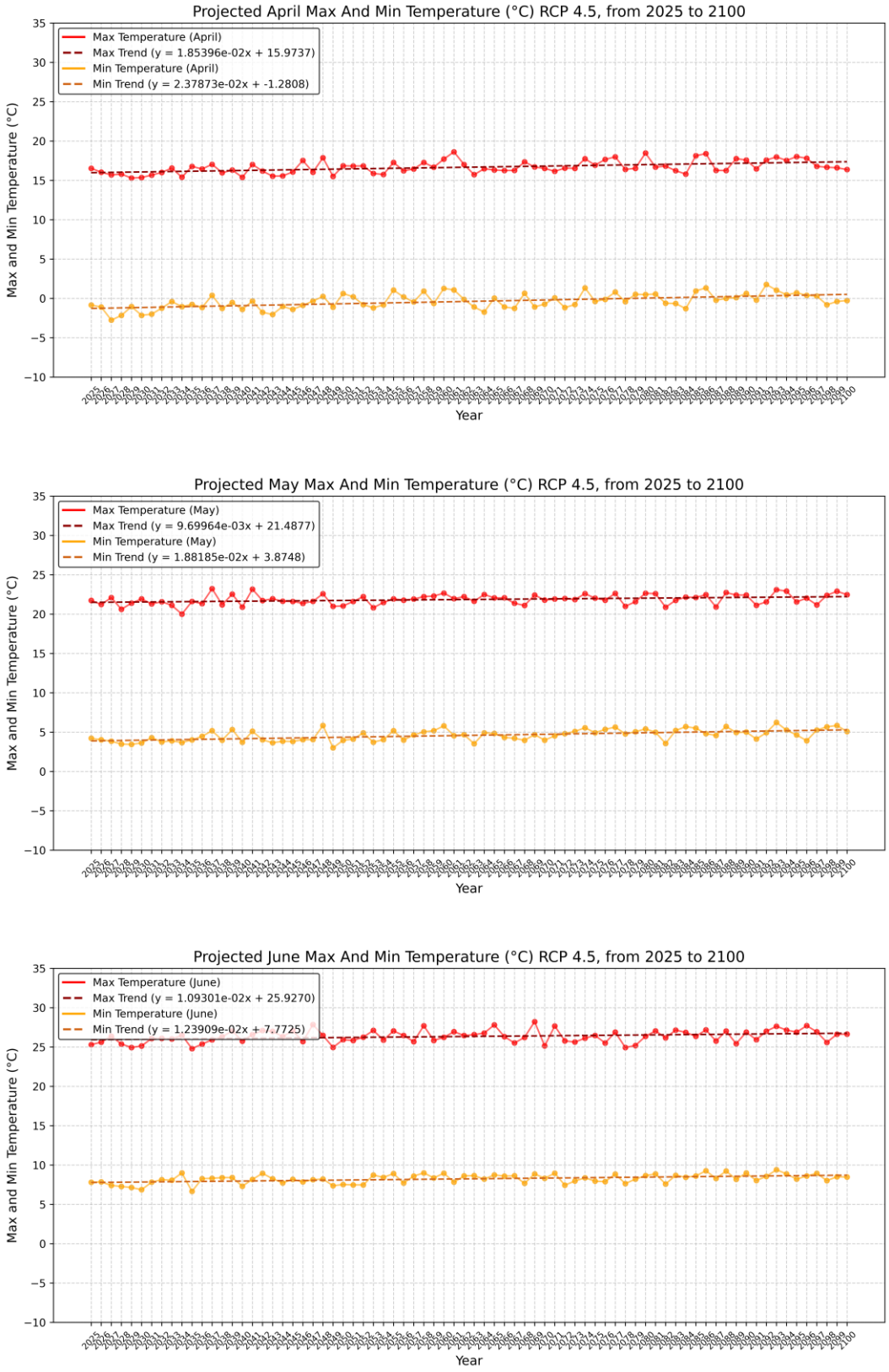

Figure 65_Monthly Max and Min Temperature (°C) from 2025 to 2100 with Trend Line, RCP 4.5_ Apr to Jun

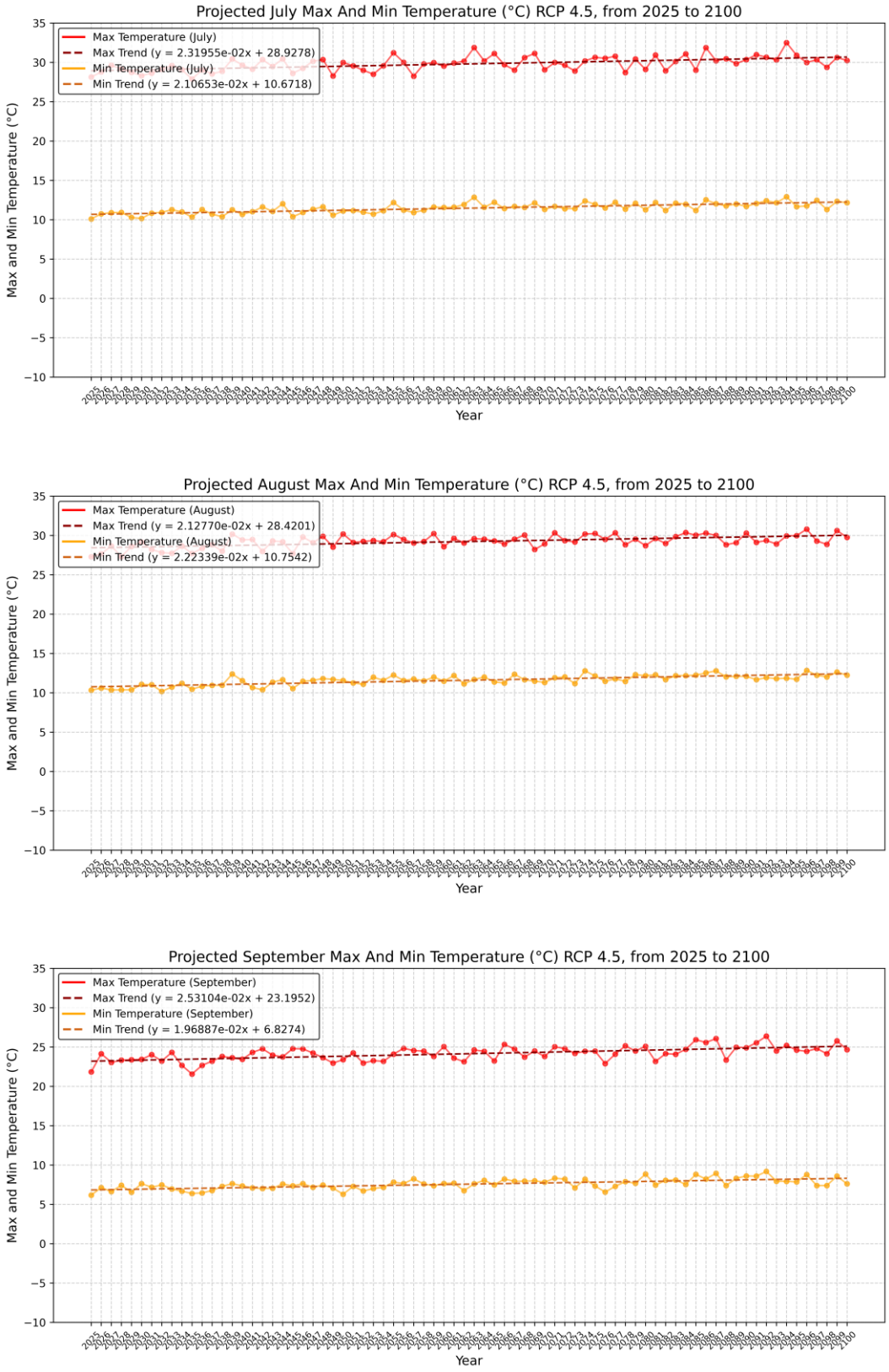

Figure 66_Monthly Max and Min Temperature (°C) from 2025 to 2100 with Trend Line, RCP 4.5_ Jul to Sep

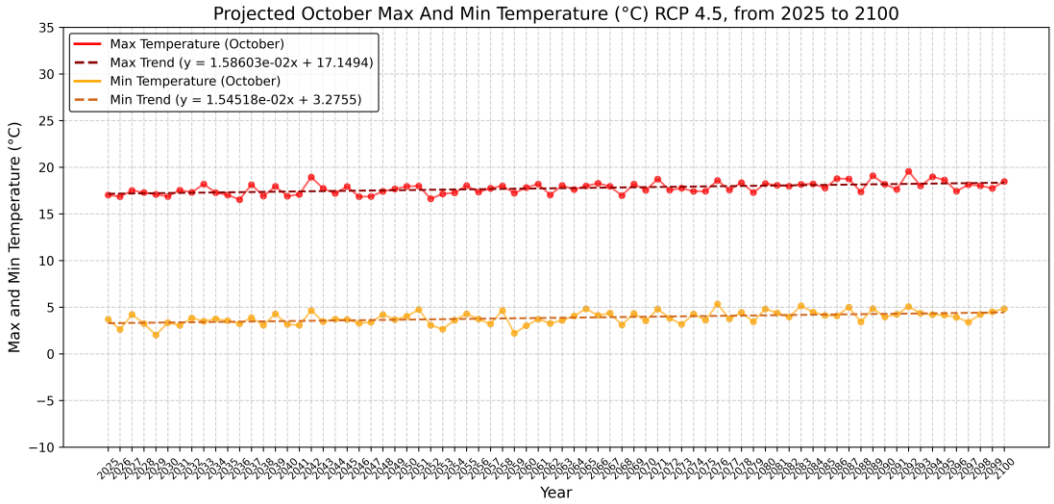

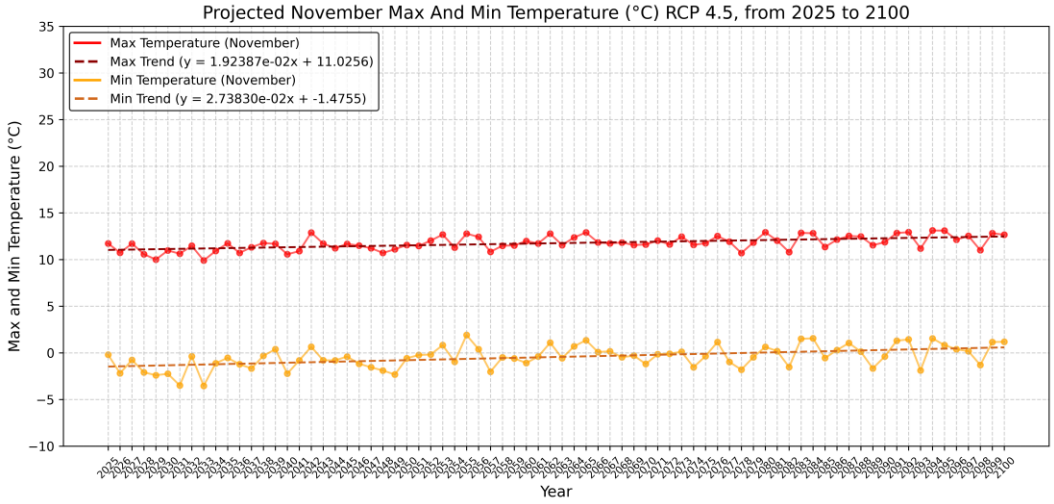

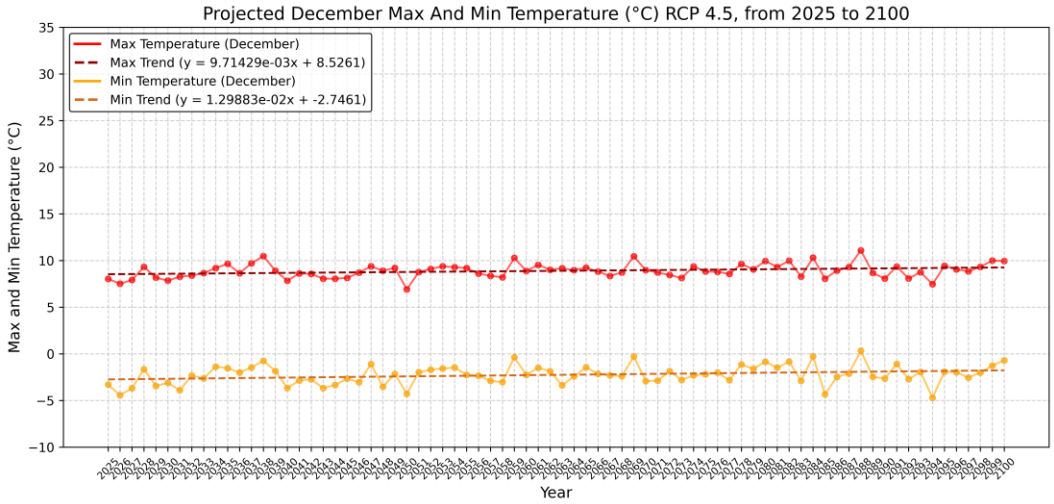

Figure 67 Monthly Max and Min Temperature (°C) from 2025 to 2100 with Trend Line, RCP 4.5_ Oct to Dec

According to an overall examination of the charts, all months exhibit an increasing trend in both the Tmax and Tmin. The trend slope for minimum temperature (Tmin) is steeper than that for maximum temperature (Tmax) in the majority of months. Maximum temperatures stay higher and continue to rise gradually during the warmer months of June, July, August, and September. The colder months of January, February, and December also gradually warm, though their lowest temperatures typically stay below freezing.

4.5.4 Elevation-Based Temperature Analysis

For the future projections under RCP 4.5, the same elevation classification proposed by Tiranti et al. (2023) was applied to evaluate temperature behavior across altitudinal zones in the Susa Valley. Using monthly GeoTIFF datasets and the regional DEM, average Tmax and Tmin values were extracted for each of the five elevation classes. Temperature trends were then analyzed separately for each class from 2025 to 2100 using Python-based geoprocessing. The aim was to observe how warming patterns vary with elevation under projected climate conditions. Figures 68 and 69, present the results, while the following section summarizes the trends for each elevation band.

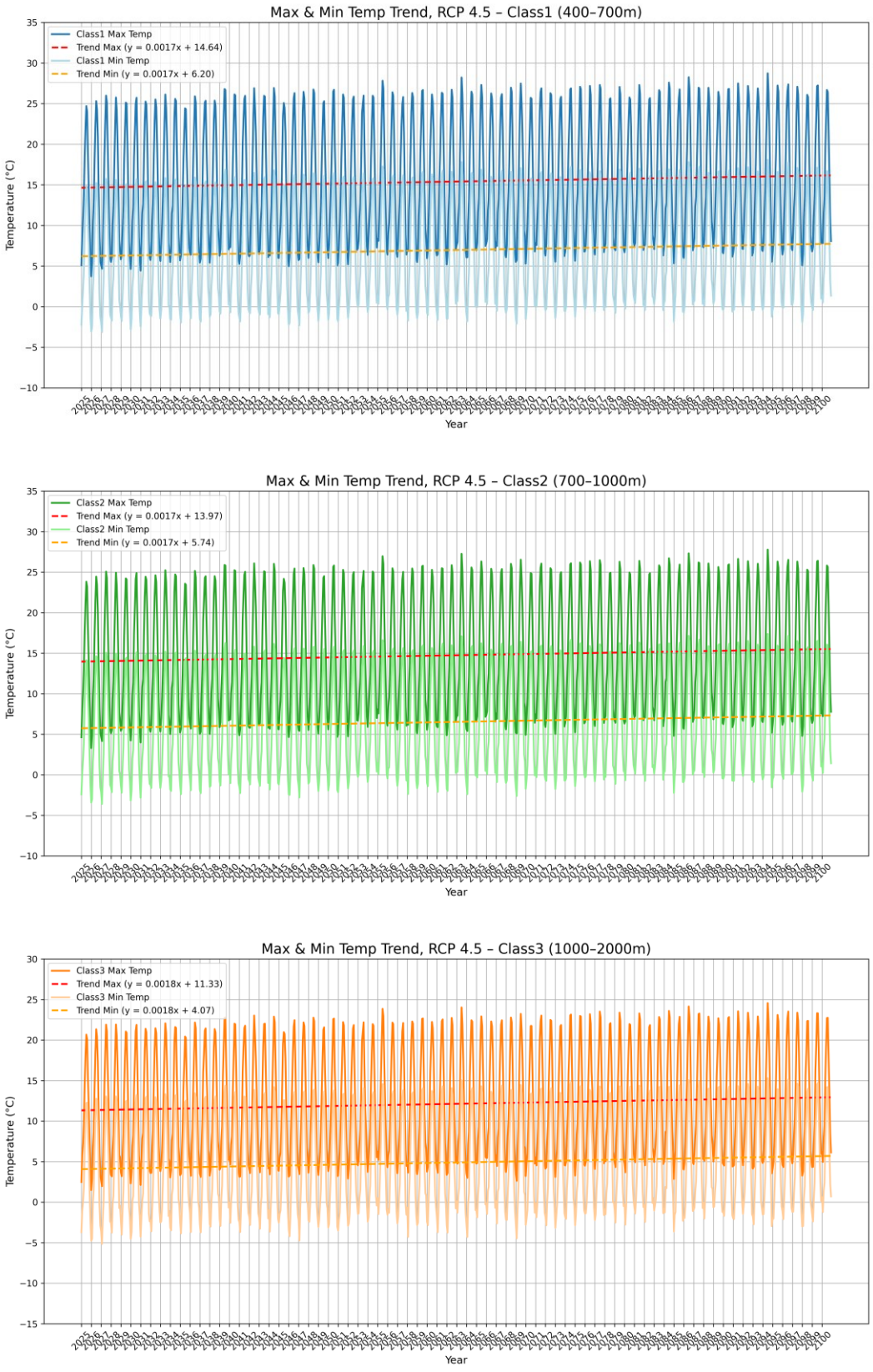

Figure 68 _Max and Min Temperature Trend with Elevation Classes 1,2,3, RCP 4.5

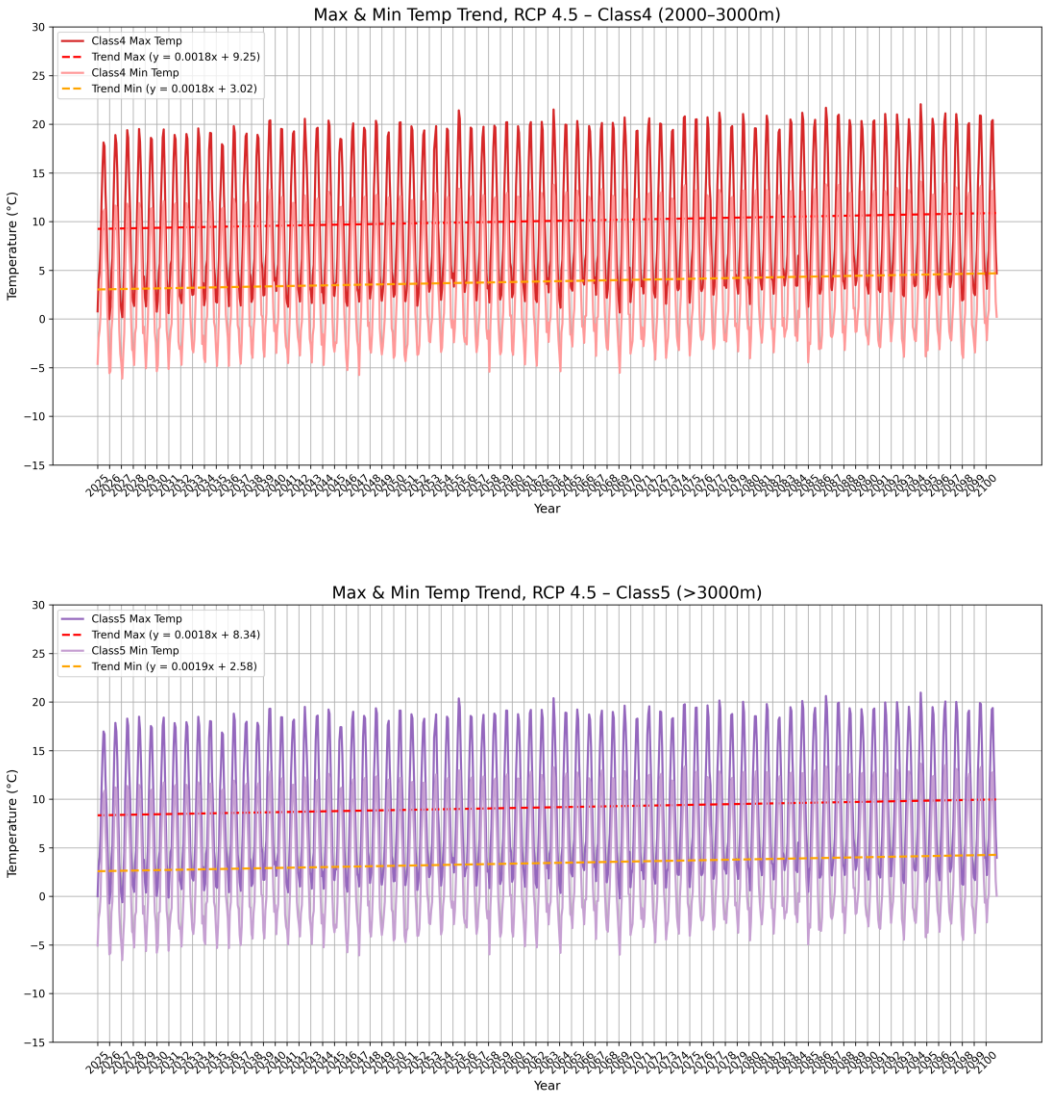

Figure 69_Max and Min Temperature Trend with Elevation Classes 4,5, RCP 4.5

Based on the projected temperature data under RCP 4.5, the linear trends of monthly maximum and minimum temperatures across the five elevation classes in the Susa Valley from 2025 to 2100 reveal a consistent pattern of warming. The results show positive slopes for both Tmax and Tmin in all altitudinal bands, confirming a persistent warming signal across the entire elevation gradient.

In Class 1 (400–700 m), Tmax and Tmin are increasing at a rate of +0.0017 °C/year, showing balanced warming at lower elevations. With slightly lower depending temperatures, Class 2 (700–1000 m) shows a similar warming pace to Class 1, with both Tmax and Tmin rising at +0.0017 °C/year. Class 3 (1000–2000 m) shows steady warming in the mid-altitude Alpine environment, alongside Tmax increasing at a rate of +0.0018 °C/year and Tmin complying with closely behind at the same rate (0.0018 °C/year). Class 4 (2000-3000 m): Tmax and Tmin both

suggest an upward trend at +0.0018 °C/year, continuing the general pattern seen in Class 3 but beginning with lower baseline values.Class 5 (>3000 m): Tmax shows a trend of +0.0018 °C/year, and Tmin exhibits the steepest increase among all classes at +0.0019 °C/year, pointing to slightly accelerated nocturnal warming at the highest elevations.With little difference between Tmax and Tmin trends, the predicted data under RCP 4.5 show a consistent warming pattern across elevation bands overall.

For clearer comparison, Figure 70 presents bar charts showing the average Tmax and Tmin for each elevation class.

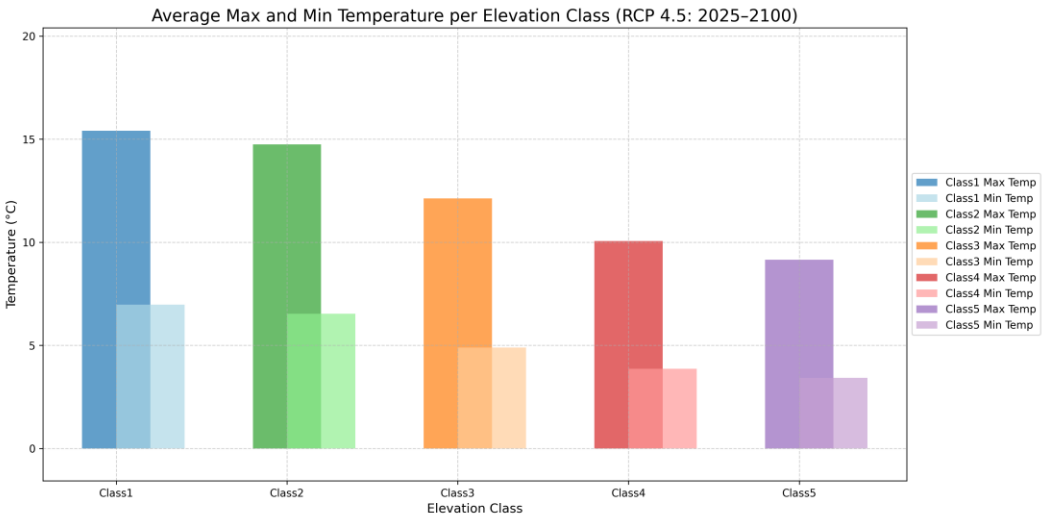

Figure 70_Average Max and Min Temperature per Elevation Class from 2025 to 2100, RCP 4.5

Figure 70, shows the average Tmax and Tmin, projected for the period 2025–2100 across the five elevation classes in the Susa Valley. The data confirm a consistent altitudinal temperature gradient, with both Tmax and Tmin decreasing as elevation increases.

The highest average Tmax (about 15.4°C) and Tmin (~7.1°C) are recorded in Class 1 (400–700 m), which is closely followed by Class 2 (700–1000 m), which has Tmax of about 14.7°C and Tmin of about 6.5°C. Average Tmax and Tmin decrease to roughly 12.1°C and 4.9°C, respectively, in Class 3 (1000–2000 m). Tmax is close to 10°C and Tmin is around 3.9°C in Class 4 (2000–3000 m), indicating a further decline. The lowest average temperatures are found in Class 5 (>3000 m), where Tmax is slightly less than 9°C and Tmin is nearly 3.3°C.

4.5.5 Critical Elevation Identification

In the future scenario under RCP 4.5, the identification of critical elevation thresholds was performed using pre-processed monthly GeoTIFF datasets for Tmax. Unlike the historical analysis, no data format conversions were needed, allowing the workflow to be fully executed within QGIS using consistent geospatial tools. Functions such as r.series were applied for temporal aggregation, followed by Raster Calculator, Raster pixels to points, and the Point Sampling Tool to extract Tmax values at varying altitudes throughout the Susa Valley. The resulting dataset was organized into an Excel table and analyzed to assess the elevation at which Tmax values approach or drop below the freezing point.

A scatter plot was generated to illustrate the correlation between elevation and projected average Tmax from 2025 to 2100 (Figure 71).

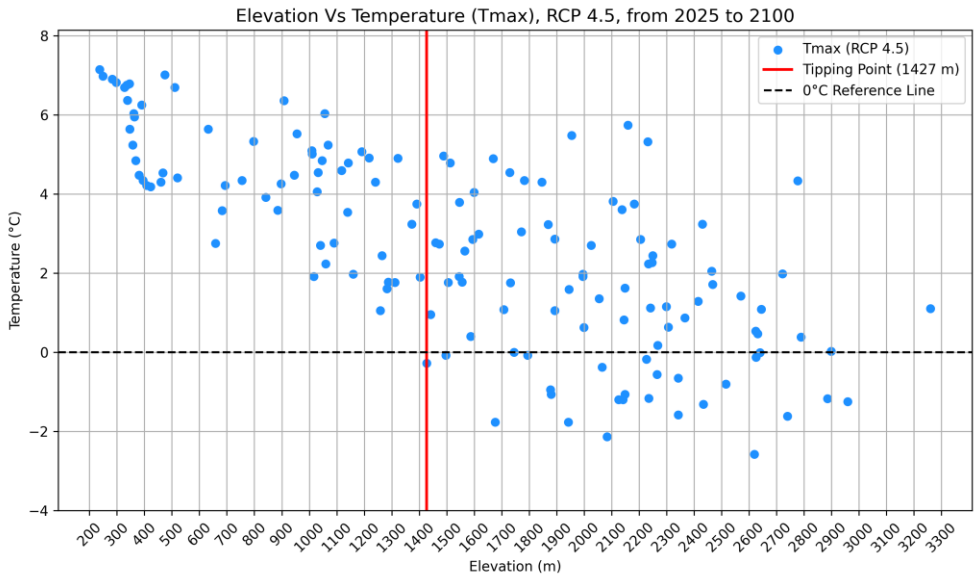

Figure 71_Elevation Vs Max Temperature, from 2025 to 2100, RCP 4.5

Under the RCP 4.5 scenario for the period 2025–2100, the plot shows a clear inverse pattern between Tmax and elevation. A distinct threshold appears at approximately 1427 meters, above which a large portion of Tmax values fall below 0 °C. This elevation is identified as the projected thermal tipping point, separating areas with predominantly sub-freezing conditions from those that generally remain above freezing (Figure 71).

4.6 Future Precipitation Projections Under RCP 4.5

This section analyzes projected precipitation trends in the Susa Valley under the RCP 4.5 scenario. The dataset, provided by ARPA Piemonte, consists of GeoTIFF raster files where each band represents the modeled mean daily

precipitation for a specific month in future climate conditions. To focus the analysis on the Susa Valley, all raster layers were spatially masked using the valley's boundaries. It is important to clarify that although the data are organized monthly, the values refer to the mean daily precipitation—that is, the average amount of rainfall per day throughout each month. For instance, a reported value of 45.89 mm indicates that each day in that month received, on average, 45.89 mm of rainfall, assuming a uniform distribution.

Only mean daily precipitation values were used in this analysis to align with the 24-hour time scale of return period thresholds. This approach allows a consistent and meaningful comparison between projected rainfall and historically defined extreme precipitation events.

4.6.1 Cumulative 24-Hour Rainfall

This section examines the Susa Valley's expected 24-hour cumulative rainfall under the RCP 4.5 scenario in order to evaluate short-duration rainfall patterns that may be connected to hydrogeological hazards. The long-term trend of the Susa Valley's anticipated 24-hour average monthly rainfall is depicted in Figure 72.

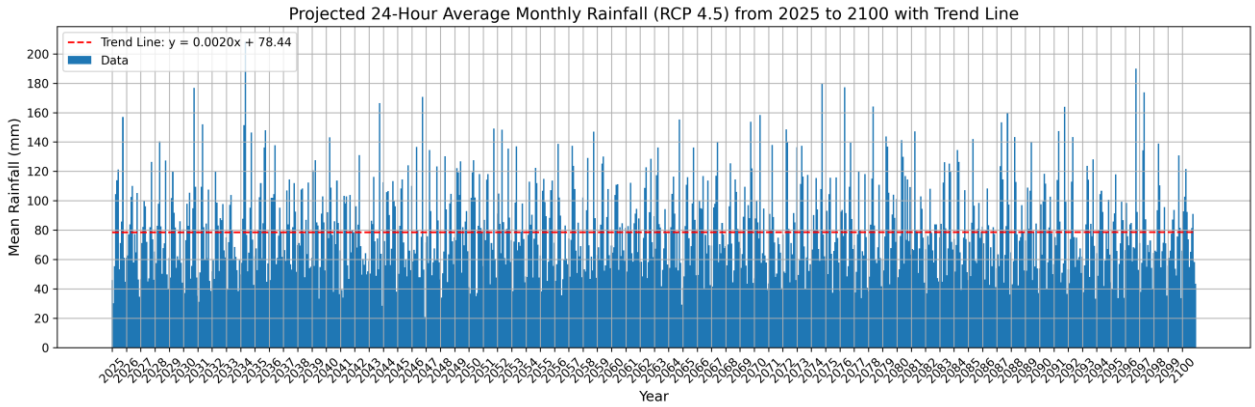

Figure 72_Cumulative Rainfall per 24 hour from 2025 to 2100, RCP 4.5

The 2025–2100 period shows multiple distinct peaks which represent sporadic intense precipitation events according to Figure 72. The red trend line shows a very slight upward trajectory in long-term rainfall intensity with a slope of +0.0020 mm/year. The small slope value indicates that daily rainfall amounts might rise gradually during RCP 4.5 conditions. This method reveals climate changes while enhancing seasonal hazard evaluation (Figures 73 to 75).

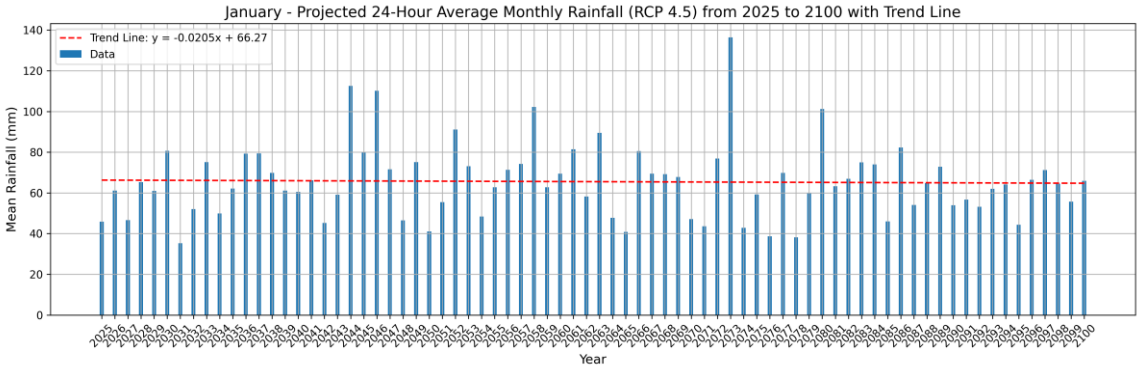

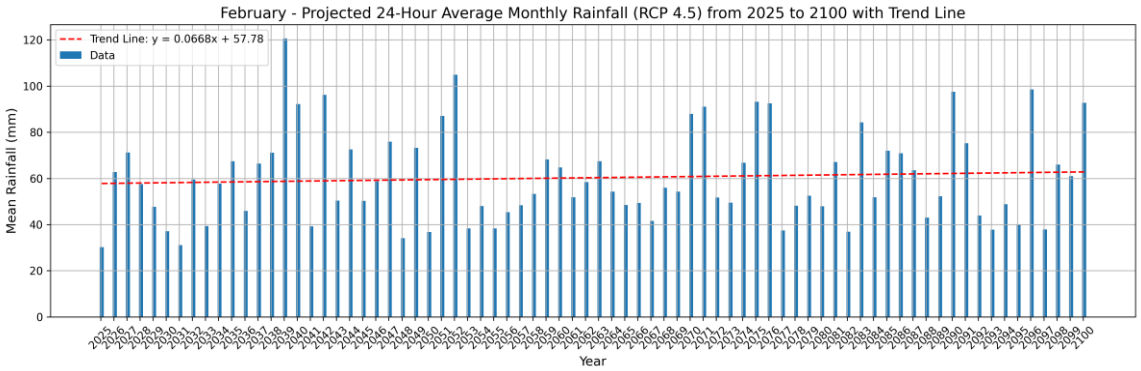

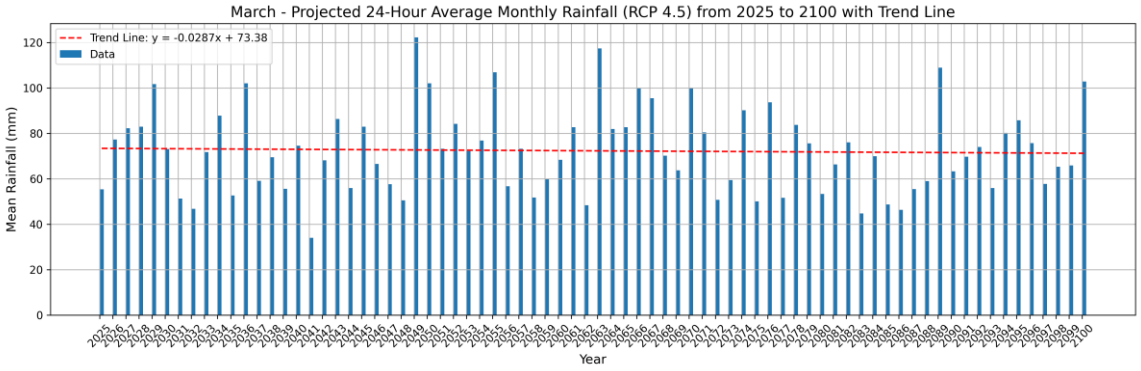

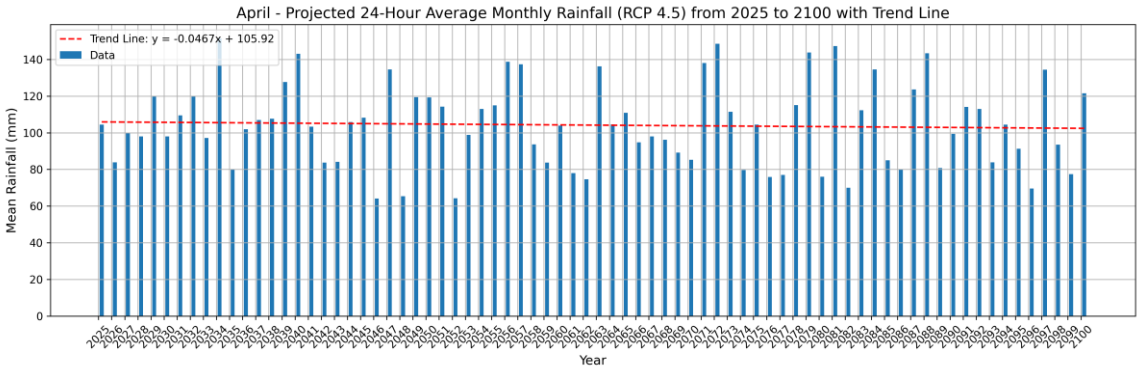

Figure 73_Cumulative Rainfall per 24 hours from 2025 to 2100, RCP 4.5_ Jan to Apr

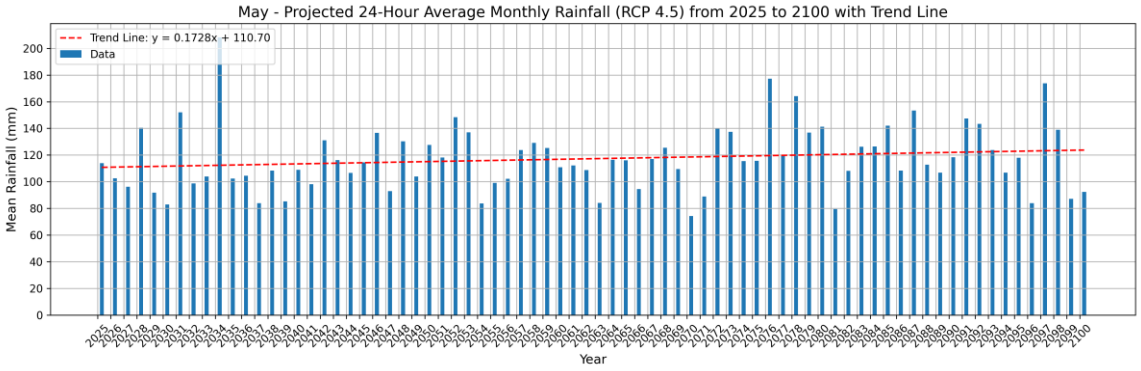

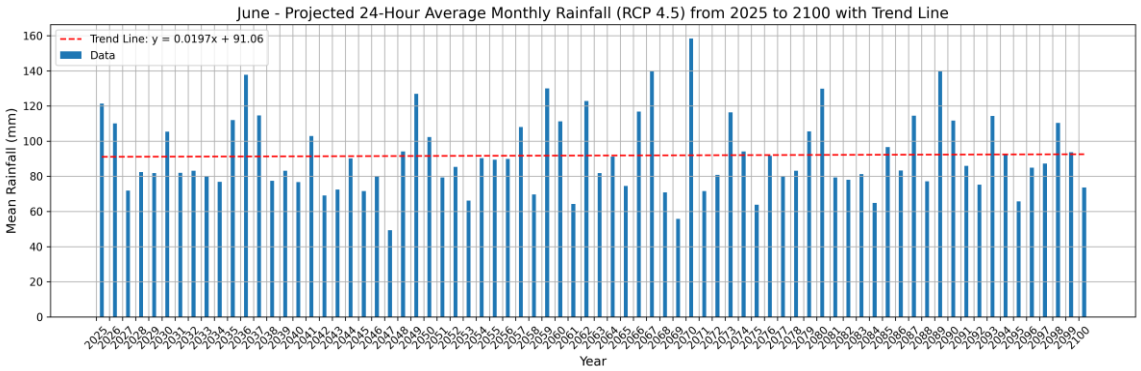

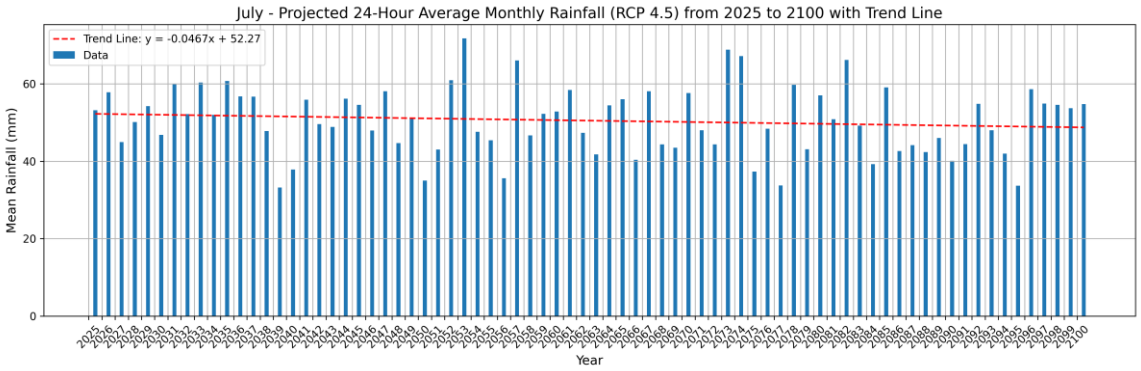

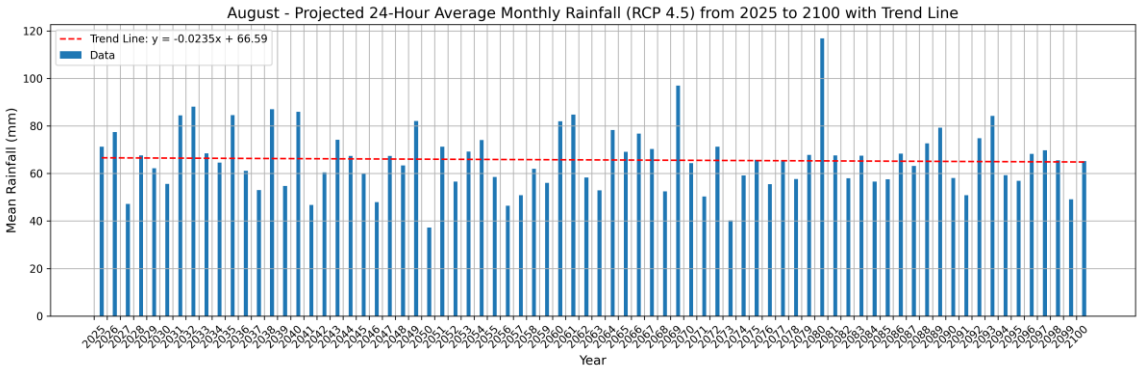

Figure 74_Cumulative Rainfall per 24 hours from 2025 to 2100, RCP 4.5_ May to Aug

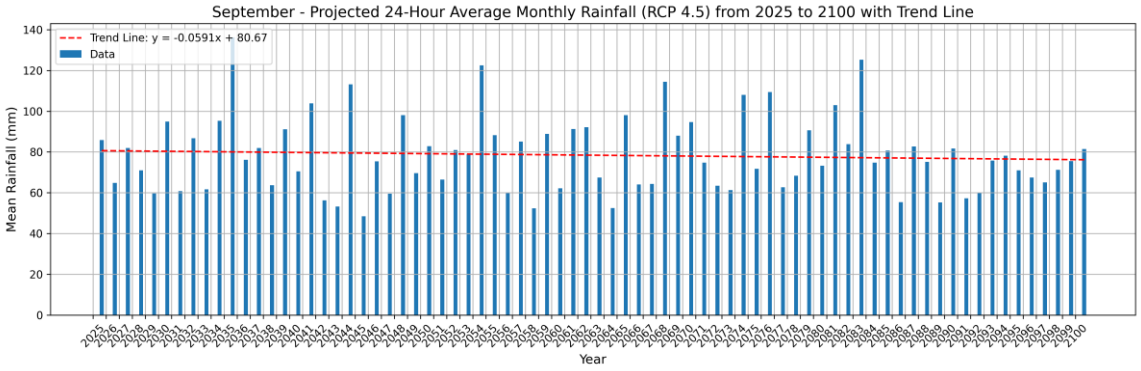

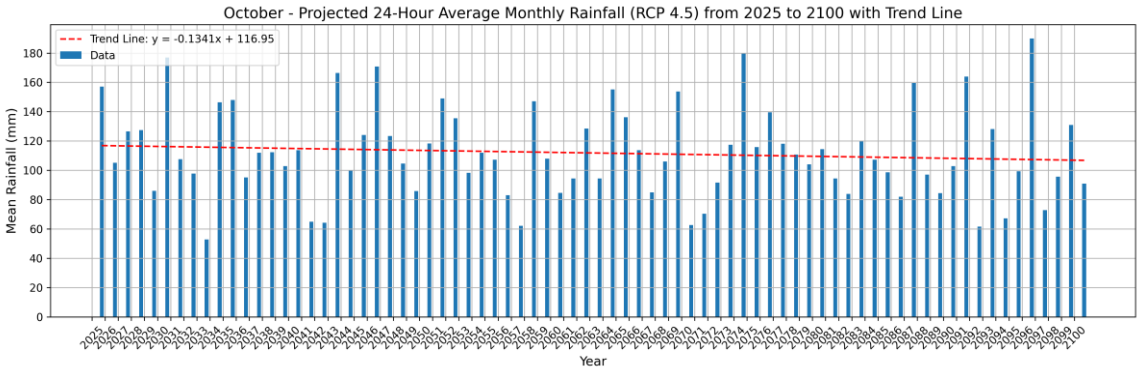

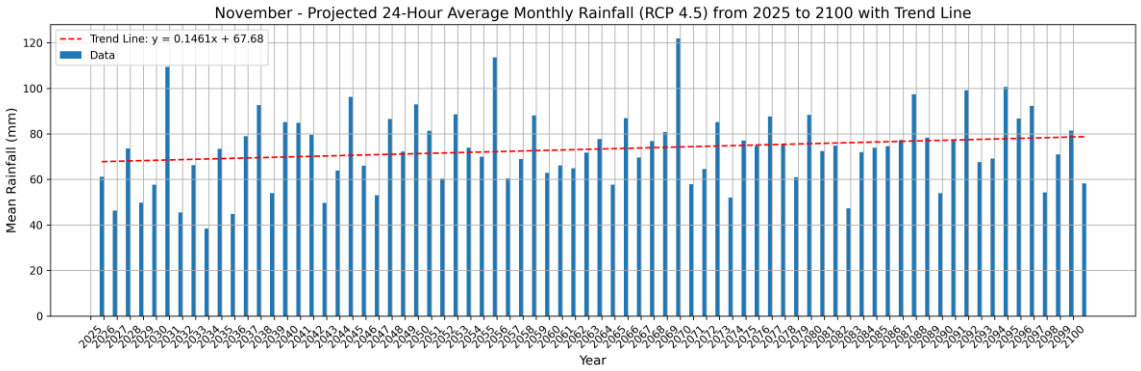

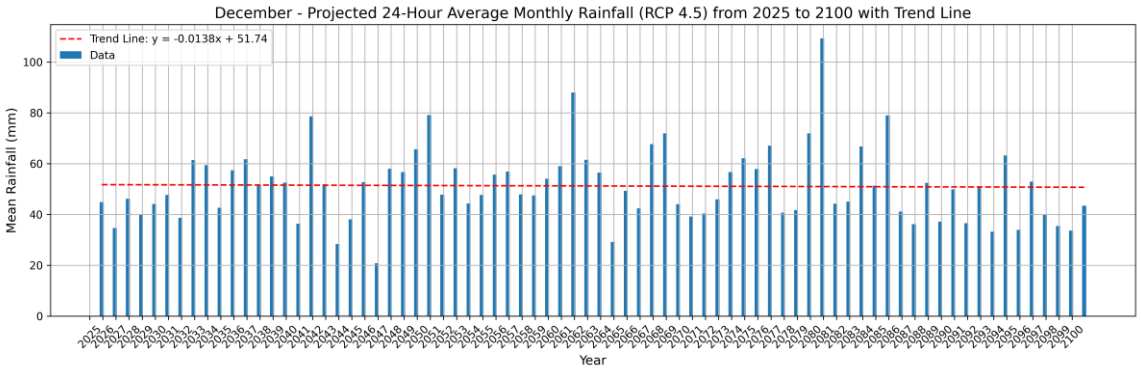

Figure 75_Cumulative Rainfall per 24 hours from 2025 to 2100, RCP 4.5_ Sep to Dec

There are clear seasonal patterns in the Susa Valley's 24-hour cumulative rainfall trends for the years 2025–2100 (RCP 4.5). Particularly in winter (January, December) and early spring (March, April), the majority of the months exhibit steady or somewhat decreasing trends. May (+0.1728) displays the most significant increase, indicating enhancing rainfall intensity in late spring, whereas February and May remain toward with positive slopes. In the summer, July and August observe a slight decline, while June demonstrates a mild upward trend. Autumn exhibits contrasting trends, with the highest negative trend (–0.1341) occurring in October and a strong positive trend (+0.1461) in November, suggesting an increase in late-autumn rainfall. These differences point to possible seasonal changes in rainfall intensity that could affect the region's future risks of landslides and floods.

4.6.2 Return Period Analysis of Extreme Events

This section examines projected summer rainfall intensities (June, July, August) under RCP 4.5 against 24-hour return period thresholds.

The 24-hour cumulative rainfall charts for these months are presented, along with the corresponding 24-hour return period thresholds for 2-, 5-, 10-, 50-, 100-, and 200-year intervals (Figure 76).

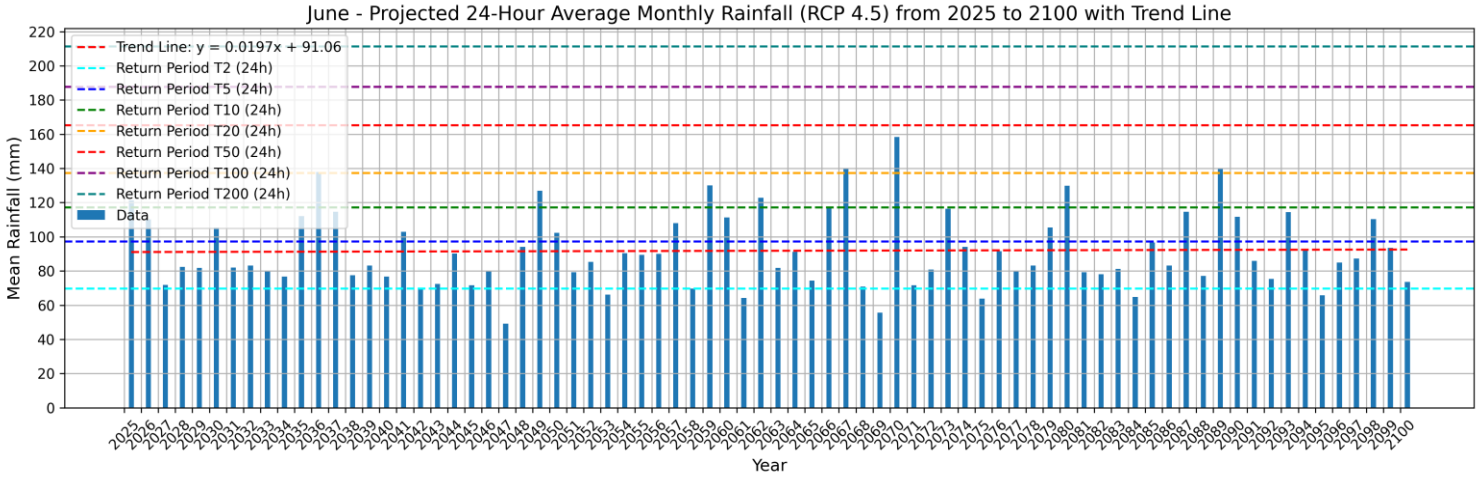

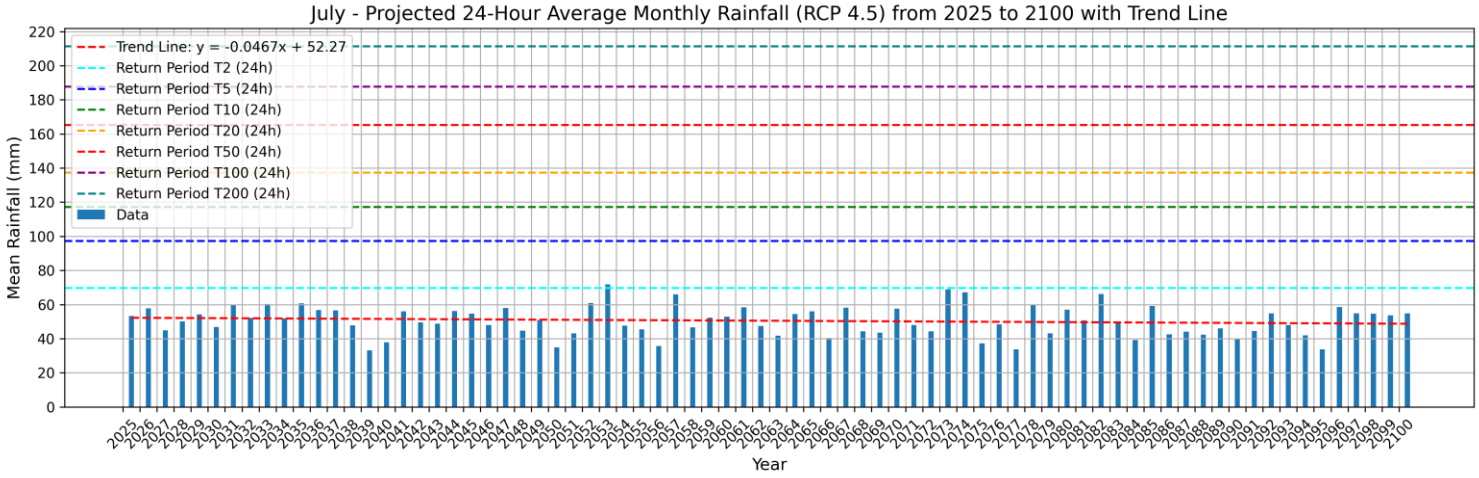

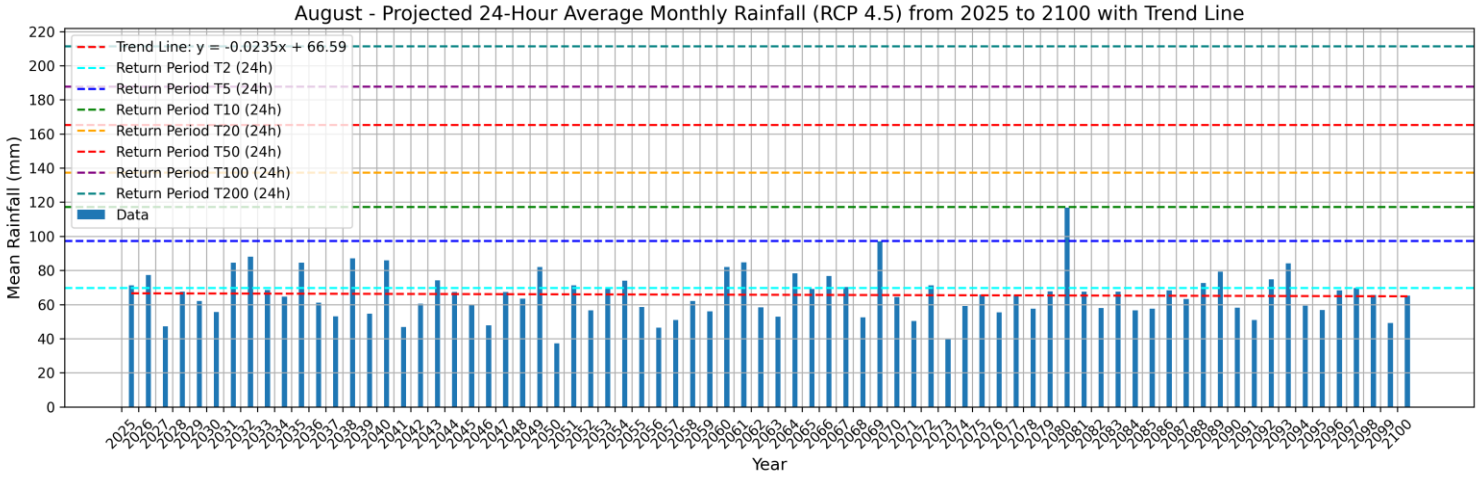

Figure 76_Return Period of Cumulative Rainfall per 24 hours with Trend Line from 2025 to 2100, RCP 4.5_ Jun to Aug

Based on the projected data for the summer months under the RCP 4.5 scenario, Figures 76, illustrate the evolution of 24-hour average monthly rainfall from 2025 to 2100 for summer monthes, overlaid with return period thresholds (T2 to T200). In June, several rainfall peaks exceed the T10 and even T20 thresholds, with a slight upward trend (slope ≈ +0.0197). July shows moderate variability with most values remaining below T10, and a mild decreasing trend (slope ≈ –0.0467). August presents a similar pattern, with occasional exceedances of T5 and T10, and a gentle downward trend (slope ≈ –0.0235).

4.7 Analysis of Future Susceptibility Classes under Climatic Conditions Under RCP 4.5

This section provides a brief overview of how climate data were integrated with susceptibility maps for rockfall, shallow landslides, and debris flows in the Susa Valley. Specifically:

- **Rockfall susceptibility** was evaluated using Delta temperature (5–8°C) and 24/48-hour precipitation threshold, with five classes.
- **Shallow landslide** susceptibility was analyzed based on 24-hour rainfall thresholds, with three classes.
- **Debris flow** susceptibility was assessed using rainfall intensity thresholds (20, 30, and 50 mm/h).
  All susceptibility layers were spatially aligned with climate projections to assess the influence of environmental triggers on slope instability, with three classes: ECM, GCM, BCM.

4.7.1 Rockfall Susceptibility under Temperature and Precipitation Conditions

A targeted analysis was carried out under the RCP 4.5 scenario to evaluate the potential impact of projected temperature fluctuations (ΔT = Tmax − Tmin) on future rockfall susceptibility in the Susa Valley. Using future Tmax and Tmin raster datasets in GeoTIFF format, monthly ΔT values for the years 2025–2100 were obtained, building on the historical methodology. Using the framework developed by Tiranti et al. (2023), these values were calculated and examined across five predetermined elevation bands and five rockfall susceptibility classes.

Long-term monthly averages were calculated for each elevation and susceptibility class combination, and the proportion of values falling within three important ΔT thresholds (<5°C, 5–8°C, and >8°C) was determined. The three temperature thresholds serve as essential indicators to detect thermal fatigue which speeds up rockface instability in Alpine environments. The study provides

spatial and seasonal insights about thermal variability under RCP 4.5 warming conditions while pinpointing areas where future ΔT values will surpass critical limits. The analysis creates a uniform framework to evaluate past and projected thermal stress exposure which enables better assessments of changing rockfall hazard patterns in mountainous areas.

The results are summarized in Figures 77 to 81, which display the distribution of ΔT values across rockfall susceptibility classes and elevation bands, highlighting the proportion of areas falling within key air thermal thresholds (<5°C, 5–8°C, and >8°C).

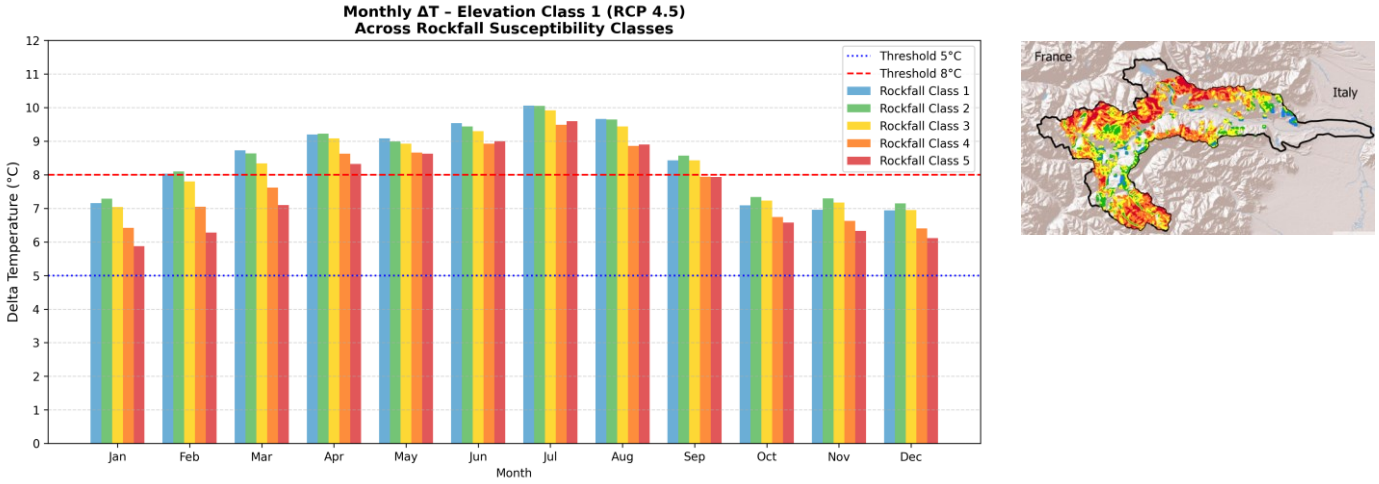

Figure 77_Monthly ΔT across rockfall susceptibility classes in Elevation Class 1, RCP 4.5, between 5 °C and 8 °C thresholds

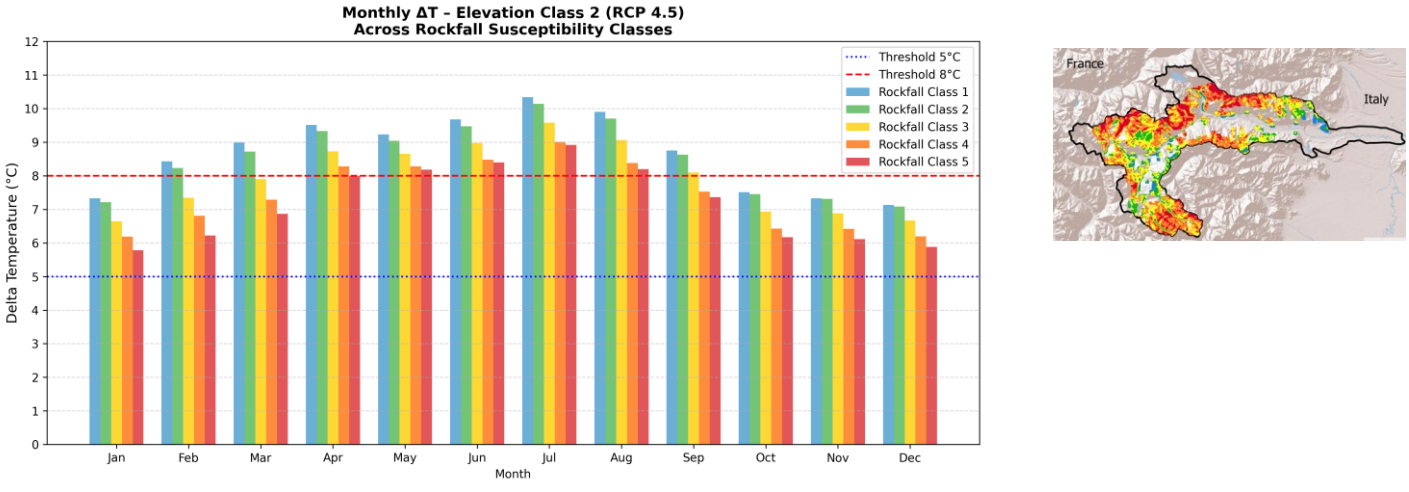

Figure 78_Monthly ΔT across rockfall susceptibility classes in Elevation Class 2, RCP 4.5, between 5 °C and 8 °C thresholds

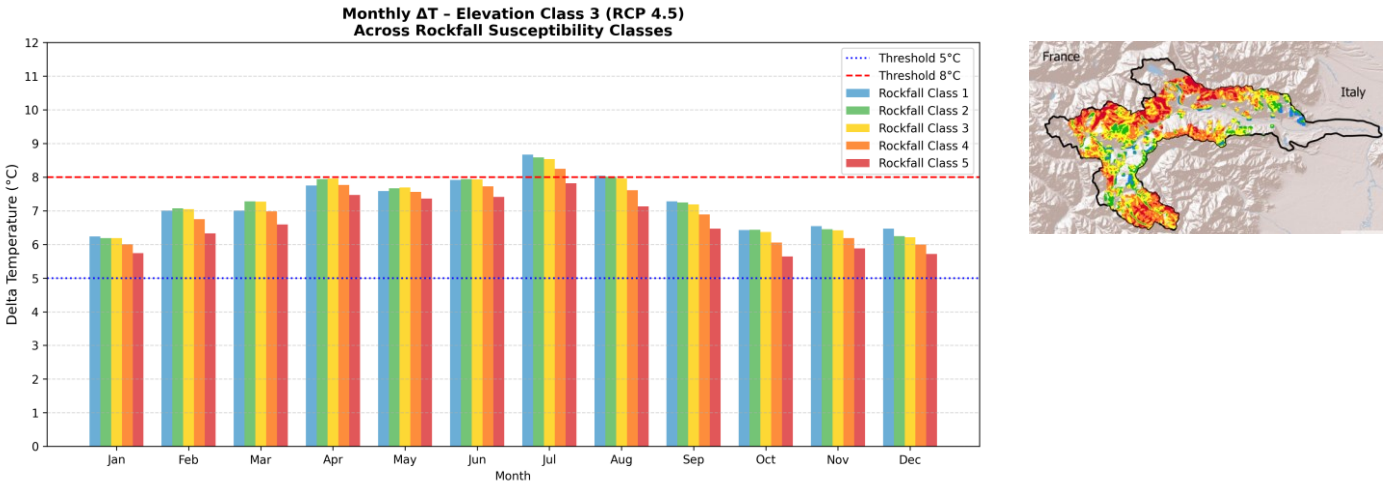

Figure 79_Monthly ΔT across rockfall susceptibility classes in Elevation Class 3, RCP 4.5, between 5 °C and 8 °C thresholds

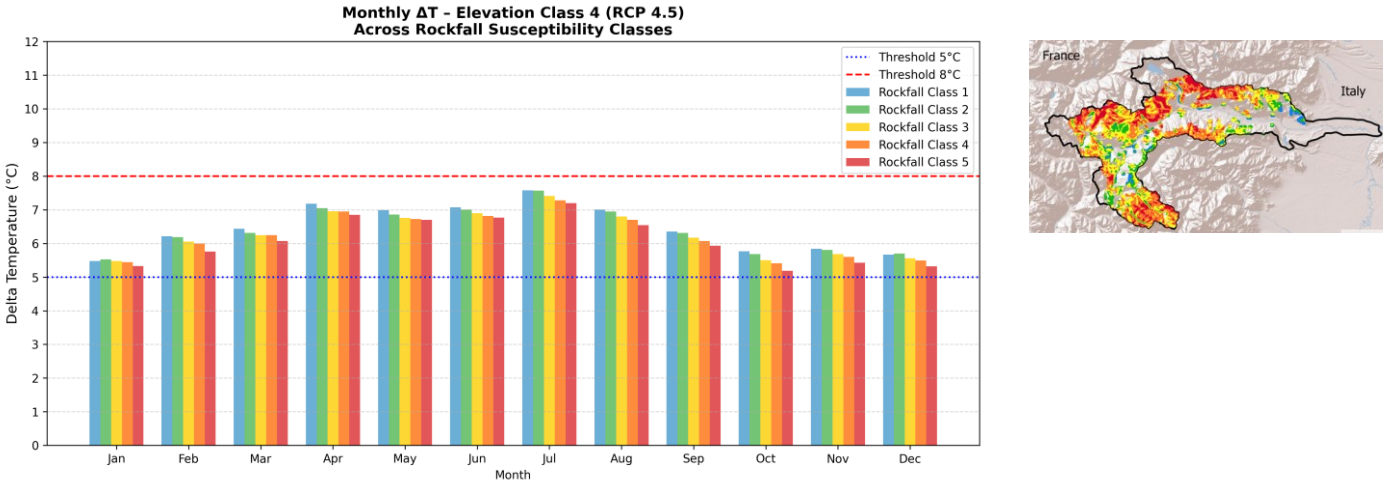

Figure 80_Monthly ΔT across rockfall susceptibility classes in Elevation Class 4, RCP 4.5, between 5 °C and 8 °C thresholds

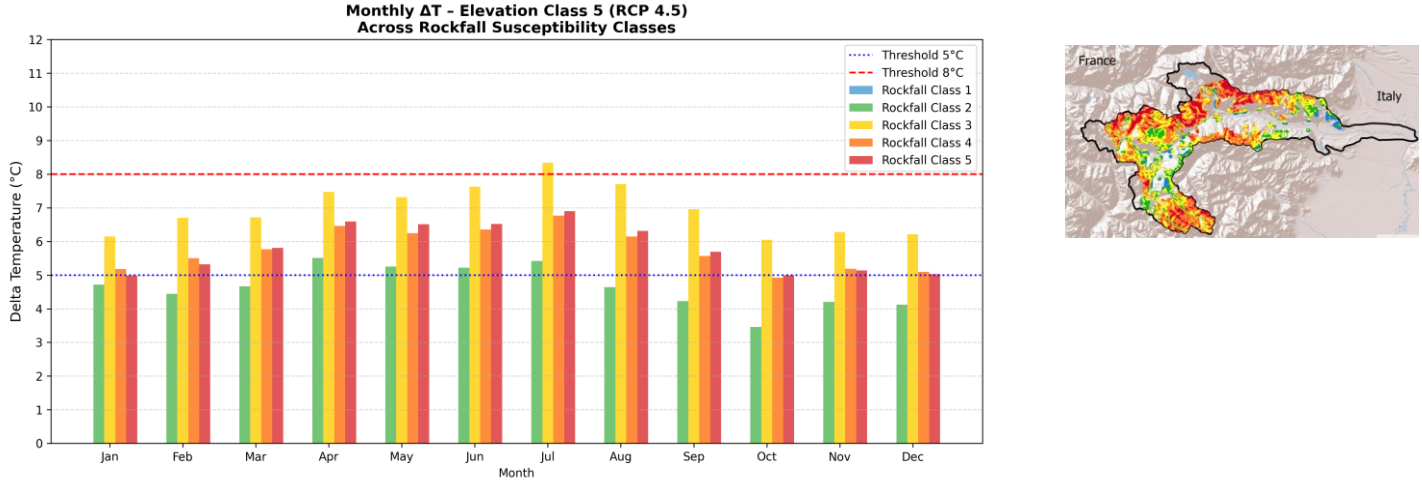

Figure 81_Monthly ΔT across rockfall susceptibility classes in Elevation Class 5, RCP 4.5, between 5 °C and 8 °C thresholds

The projected ΔT charts for the period 2025–2100 (Figures77-81) reveal consistent seasonal patterns across all five elevation classes. ΔT values peak during the warmer months—particularly from May to August—where values often exceed the 8 °C threshold, especially in lower elevation bands (Classes 1 and 2). In these zones, Susceptibility Classes 1 to 3 consistently register ΔT values above 8 °C during summer, indicating increased thermal stress exposure. In mid-elevation bands (Classes 3 and 4), ΔT values remain relatively high during summer, though exceedance of the 8 °C threshold is more limited to Susceptibility Classes 1 to 3. While Susceptibility Class 3 continues to exhibit elevated ΔT during July and August, the highest elevation band (Class 5) exhibits more moderate ΔT values, typically staying below 8 °C across all susceptibility classes. With very few exceptions, ΔT values for all elevation and susceptibility classes decrease dramatically during the colder months of November through February, usually staying between 5°C and 7°C. In line with past patterns, Susceptibility Class 3 generally maintains higher ΔT values throughout the majority of months and elevations.

In the following section, the effect of precipitation on rockfall susceptibility has been examined.

As outlined in previous sections, projected daily precipitation data for the period 2025–2100 under the RCP 4.5 scenario were analyzed to assess the potential occurrence of rainfall-induced rockfall events. Two critical thresholds were considered for identifying extreme events: 120 mm within 24 hours and 170 mm within 48 hours, both of which are commonly referenced in the literature as triggering conditions for rockfall activity.

In order to investigate the spatial distribution of these extreme events, each event's geographic coordinates were taken out, and a Digital Elevation Model (DEM) was used to calculate the associated elevation.

Five predetermined altitude classes were created from these elevation values. An aligned susceptibility raster map was then used to spatially match each event to a rockfall susceptibility class. Python was used to programmatically carry out every analytical step, guaranteeing accuracy, consistency, and reproducibility. This included threshold-based filtering and spatial overlay with susceptibility and elevation layers. The distribution of extreme precipitation events (based on both 24-hour and 48-hour thresholds) across susceptibility and elevation classes under the RCP 4.5 scenario is depicted in Figure 82, which displays the final classified results. This future-focused analysis offers valuable insight into how changing

climate conditions may influence the spatial dynamics of rockfall hazards in mountainous regions.

Figure 82_ 24 and 48 hours Rainfall Events by Elevation Class and Rockfall Susceptibility, RCP 4.5

In the 24-hour precipitation chart (≥120 mm), a significant number of extreme events are observed, predominantly concentrated within Elevation Classes 3 and 4. These events are mostly associated with higher susceptibility levels—specifically Susceptibility Classes 3, 4, and 5—indicating an elevated potential for future rockfall occurrences in mid-to-high elevation zones with moderate to very high susceptibility (Figure 82).

In the 48-hour precipitation chart (≥170 mm), the number of extreme events is lower, but they are still present within Elevation Classes 3 and 4. These longer-duration events are also more commonly linked to Susceptibility Classes 3 through

5, though their distribution is more limited in comparison to the 24-hour events (Figure 82).

4.7.2 Debris Flow Susceptibility under Precipitation Conditions

Daily rainfall data from 2025 to 2100 was analyzed and transformed into roughly 12-hour intensity values in order to assess the risk of debris flow in the future under the RCP 4.5 scenario. Class-specific thresholds of 20 mm/h (ECM), 30 mm/h (GCM), and 50 mm/h (BCM) were contrasted with these. The analysis determines where and how frequently critical rainfall intensities may occur in susceptible areas by superimposing these data with the debris flow susceptibility map. A spatial summary of potential debris flow triggers during the study period (2025 to 2100) is provided by Figure 83, which shows the distribution of threshold-exceeding rainfall events in the summer months across the three susceptibility categories.

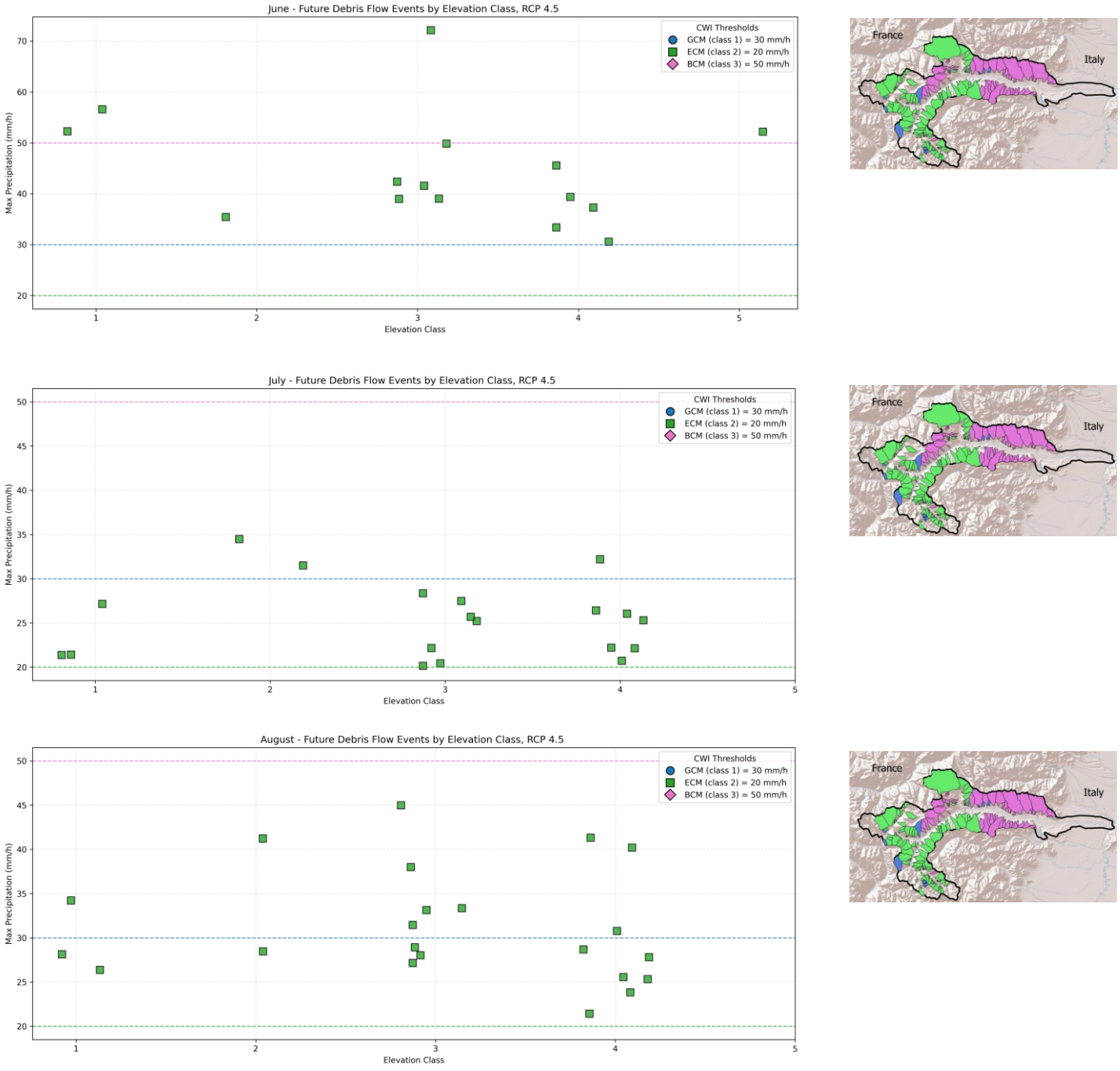

Figure 83_ Rainfall Events by Elevation Class and Debris Flow Susceptibility Summer, RCP 4.5

Under the future RCP 4.5 scenario, the spatial distribution of summer debris flow events across June, July, and August reveals a notable shift toward lower elevation classes (Figure 83). In June, high-intensity rainfall events are recorded even in Elevation Class 1, with some exceeding the critical BCM threshold of 50 mm per hour. During July, events are primarily concentrated within Elevation Classes 2 to 4, while Class 1 also shows instances of rainfall approaching critical

levels. In August, a high density of intense rainfall events is observed mainly in mid-elevation classes (3 and 4), with most cases exceeding the ECM threshold of 20 mm/h. Overall, the data suggest that critical debris flow–triggering rainfall events are distributed across a wider range of elevations during the summer months, each month exhibiting its own unique pattern of concentration and exceedance.

4.7.3 Shallow Landslide Susceptibility under Precipitation Conditions

This analysis evaluates the potential occurrence of shallow landslides under future precipitation extremes projected by the RCP 4.5 scenario. Precipitation data were clipped and resampled to match the ARPA Piemonte susceptibility map, which includes three classes: moderate (Class 2), high (Class 3), and very high (Class 4). Using Python, events exceeding 120 mm (24h) and 170 mm (48h) were extracted and associated with their corresponding elevation and susceptibility classes. This spatial comparison highlights where future extreme rainfall may align with vulnerable areas. The results are shown in Figure 84.

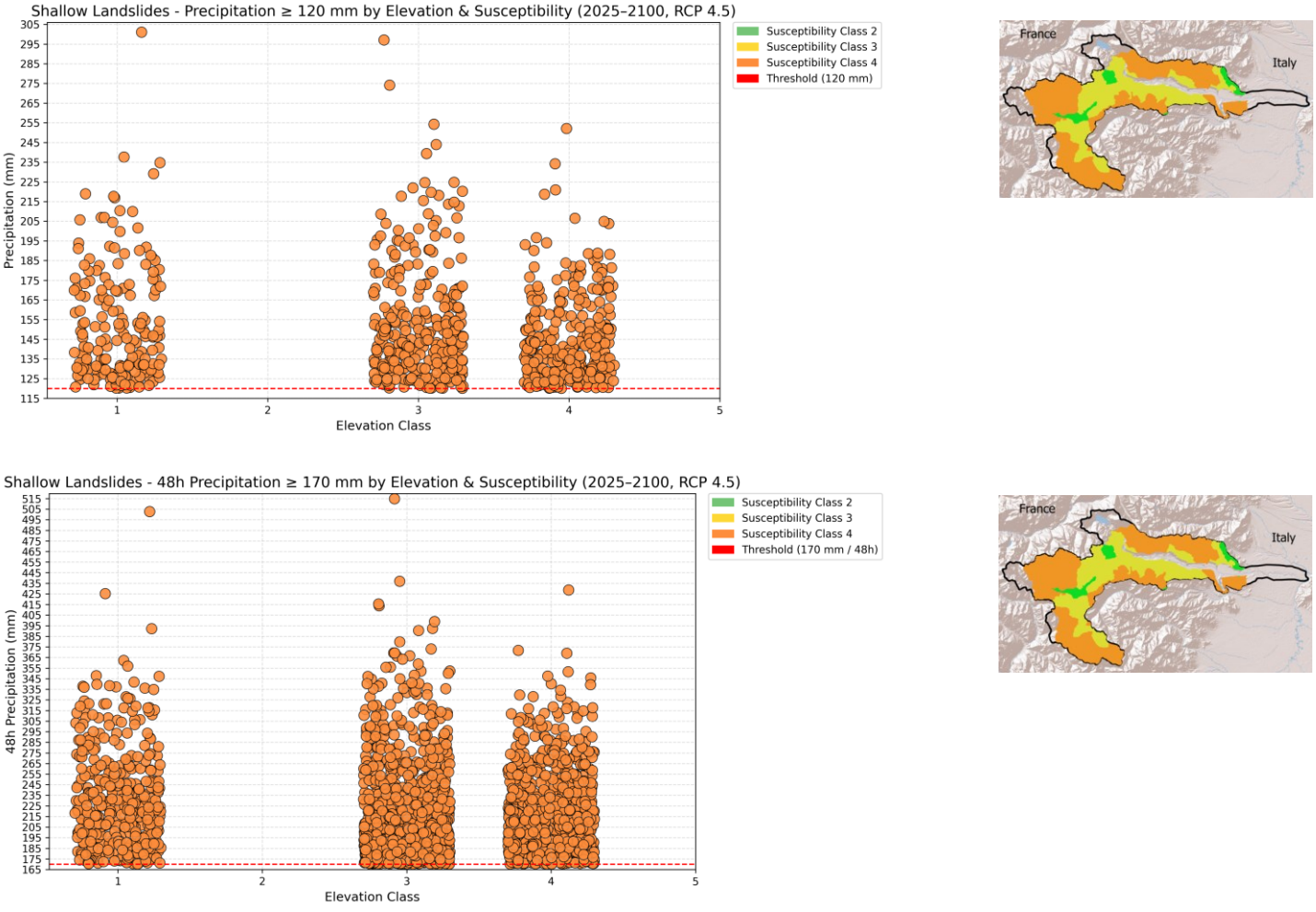

Figure 84_ 24 and 48 hours Rainfall Events by Elevation Class and Shallow Landslides Susceptibility Summer, RCP 4.5

In the 24-hour precipitation window, the majority of intense rainfall events occur within Elevation Classes 1, 3, and 4, all of which are associated with Susceptibility Class 4 (very high). For the 48-hour precipitation window, a similar pattern is observed, but with higher frequency and intensity. Rainfall events exceeding 500 mm are predominantly concentrated in the same elevation classes (1, 3, and 4), again falling entirely within Susceptibility Class 4.

4.8 Future Temperature Projections Under RCP 8.5

This section analyzes projected temperature patterns under the RCP 8.5 scenario to evaluate their influence on geo-hazard susceptibility in the Susa Valley. Using ARPA Piemonte's high-resolution raster data (2025–2100), daily and monthly ΔT (Tmax − Tmin) values were calculated in Python to overcome QGIS processing limitations. RCP 8.5 represents a high-emission pathway, with global temperatures projected to rise by over 3°C by 2100. The analysis focuses on spatial and temporal ΔT trends across elevation bands to identify thermal stress levels relevant to slope instability.

4.8.1 Monthly and Daily Average Delta Temperatures

Unlike the historical dataset, which enabled daily ΔT calculations, the RCP 8.5 projections include only monthly temperature layers. Thus, the delta temperature analysis was based on monthly average values computed from Tmax and Tmin raster files using Python tools. The results, covering the period 2025–2100, are shown in Figure 85.

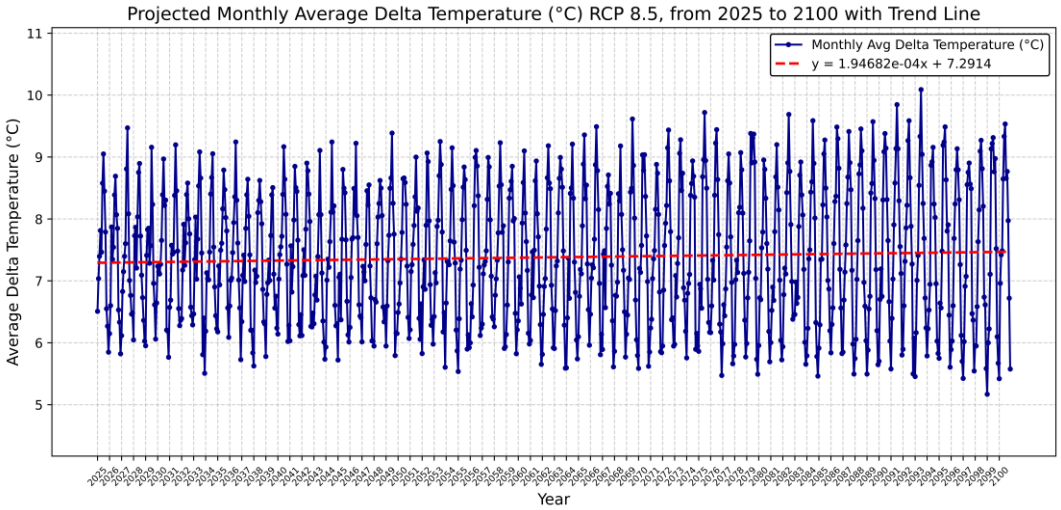

Figure 85_ Monthly Average Delta Temperature (°C) from 2025 to 2100 with Trend Line ,RCP 8.5

Figure 85 shows the difference between daily Tmax and Tmin, or ΔT values, show distinct seasonal and annual fluctuations, typically falling between 6°C and

9°C, according to the updated chart for the RCP 8.5 scenario, which spans the years 2025 to 2100. These fluctuations create a discernible monthly pattern that is consistent with an annual cycle. The trend line added to the graph shows a very slight positive slope of approximately +0.00019, indicating a minor and gradual increase in ΔT over time. In other words, under the RCP 8.5 scenario, the difference between daytime and nighttime temperatures is projected to increase slightly.

The following Figures 86 to 89 show monthly trend analyses along with corresponding daily data to give a better picture of average temperature variability.

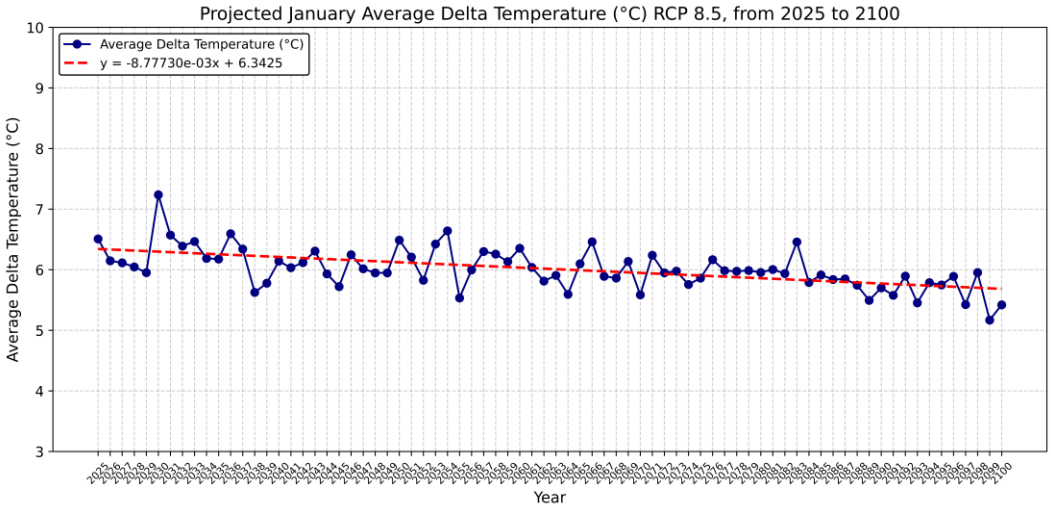

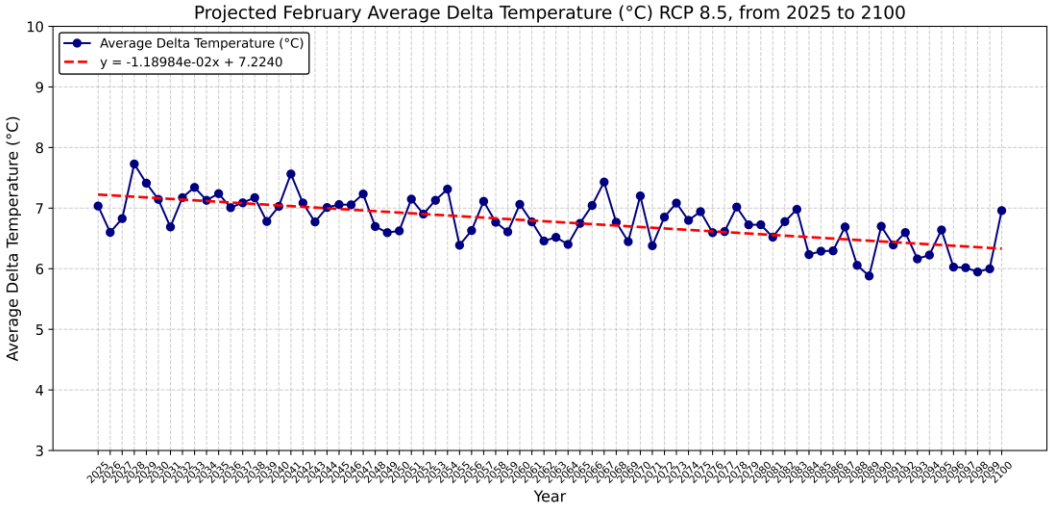

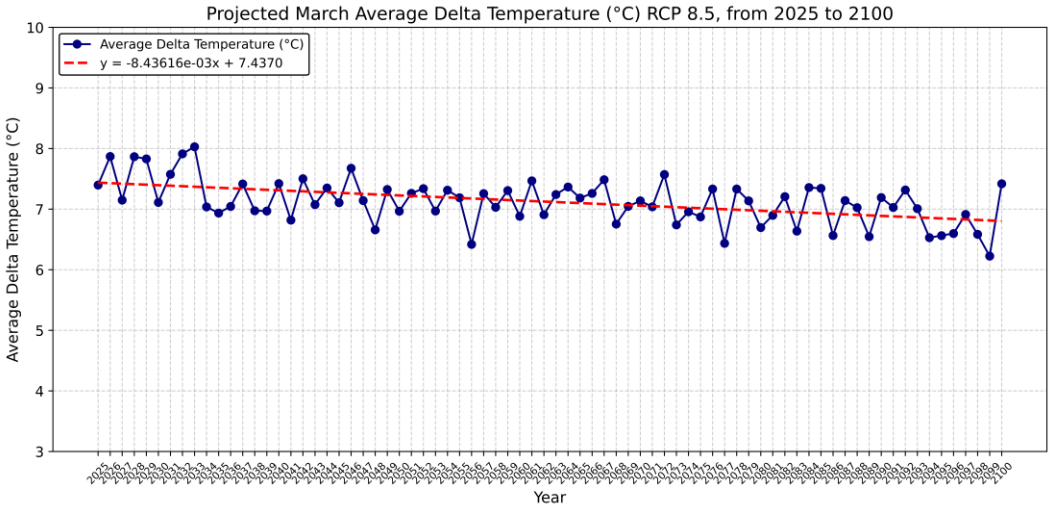

Figure 86_ Monthly Average Delta Temperature (°C) from 2025 to 2100 with Trend Line, RCP 8.5_ Jan to Mar

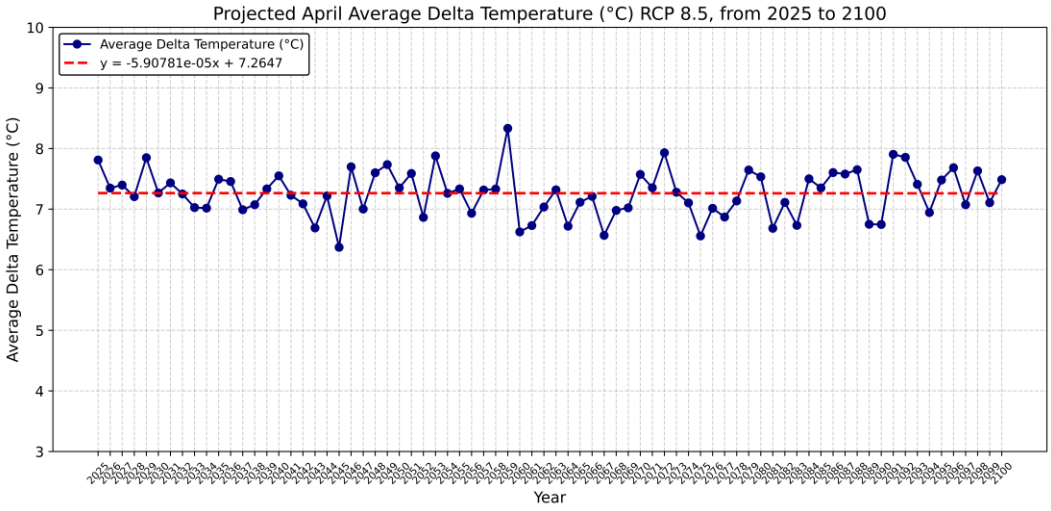

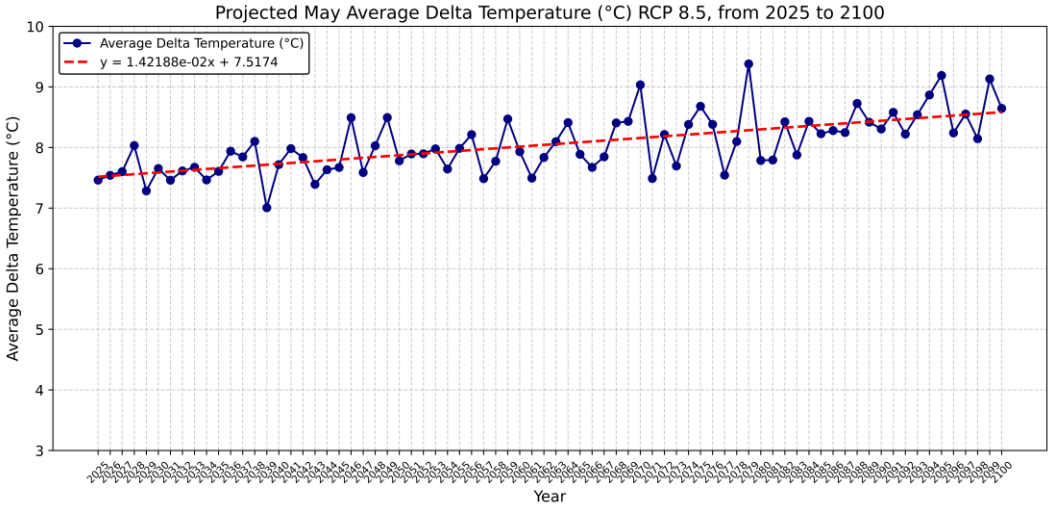

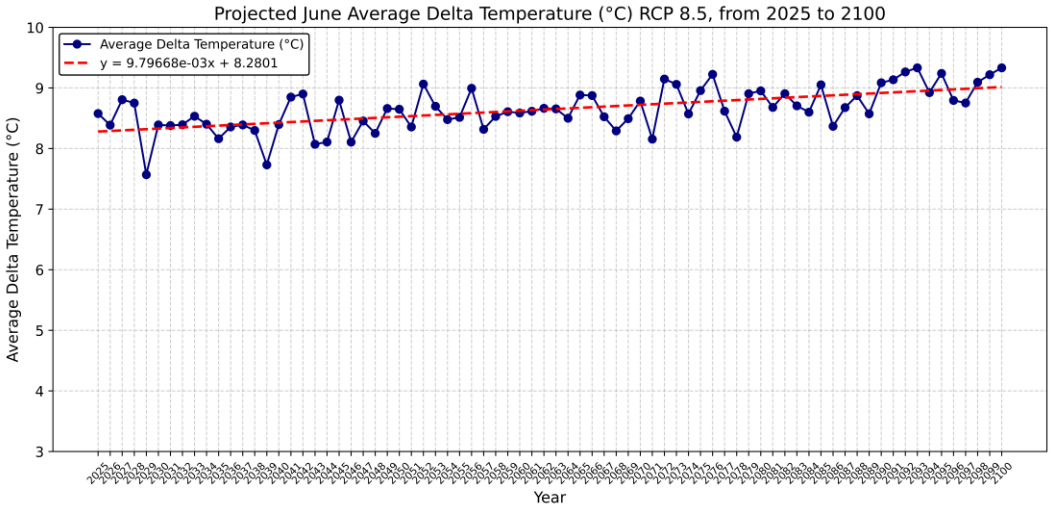

Figure 87_ Monthly Average Delta Temperature (°C) from 2025 to 2100 with Trend Line, RCP 8.5_ Apr to Jun

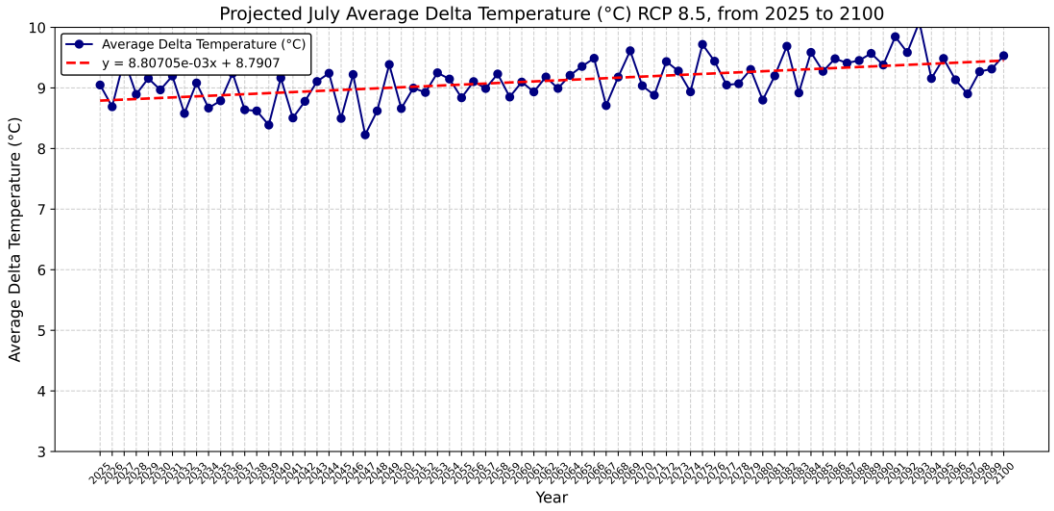

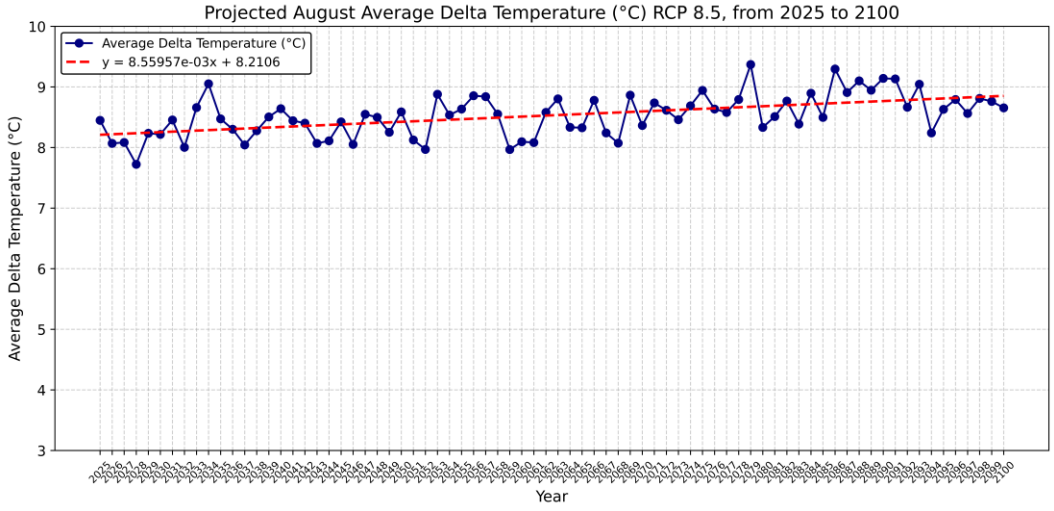

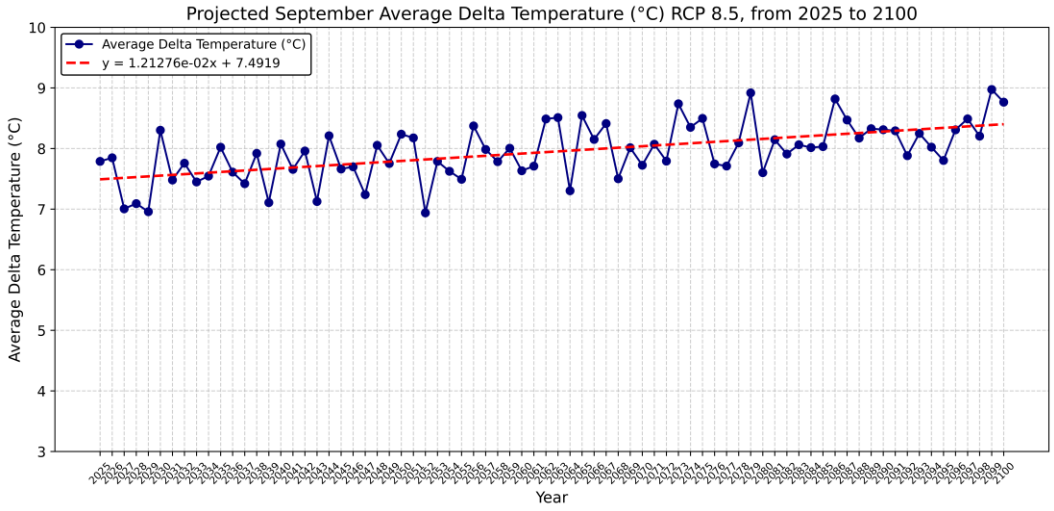

Figure 88_ Monthly Average Delta Temperature (°C) from 2025 to 2100 with Trend Line, RCP 8.5_ Jul to Sep

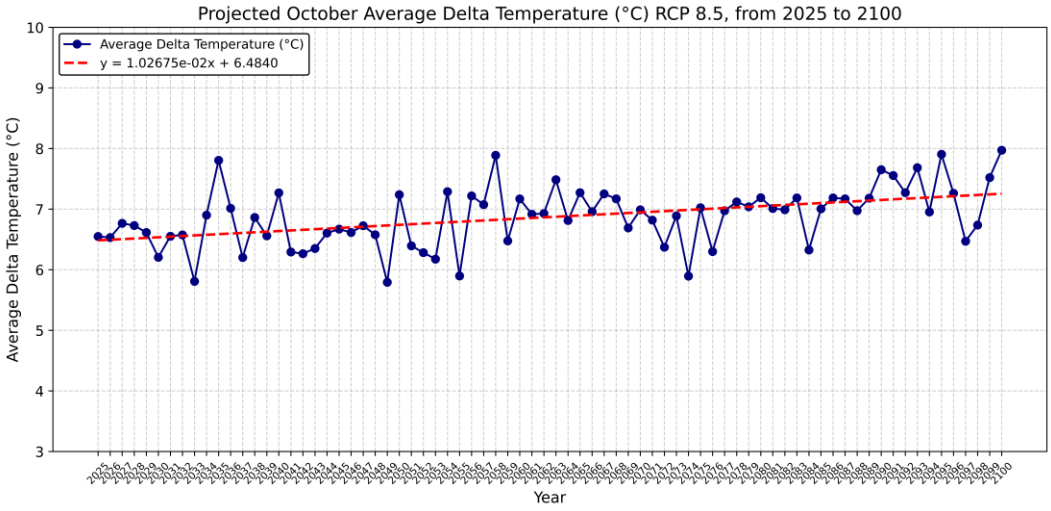

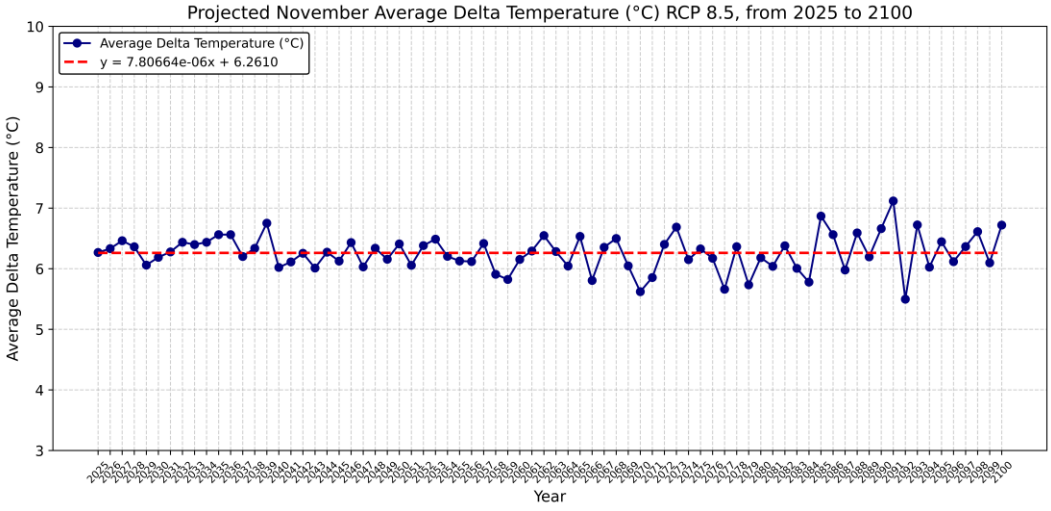

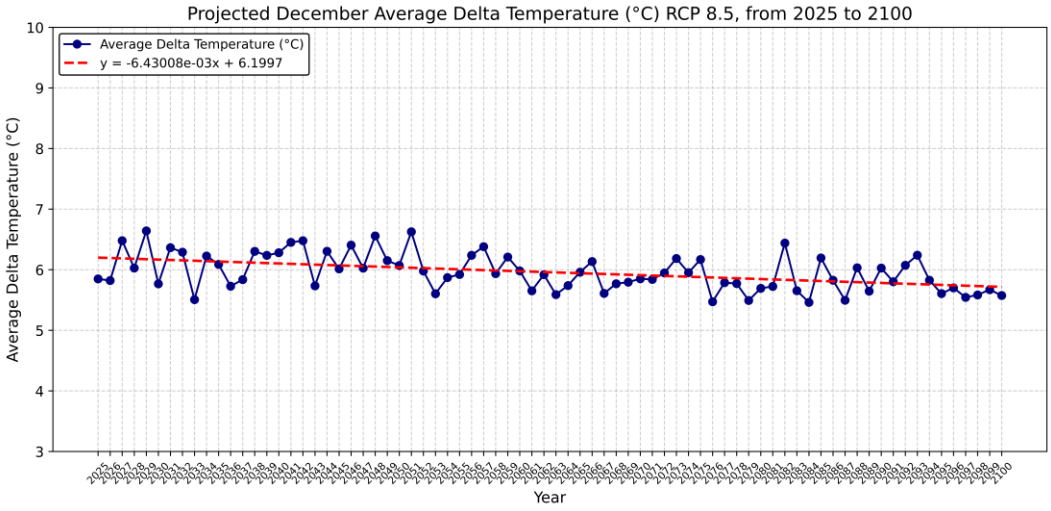

Figure 89_ Monthly Average Delta Temperature (°C) from 2025 to 2100 with Trend Line, RCP 8.5_ Oct to Dec

The following is a summary of the trends in monthly ΔT, plots under the RCP 8.5 scenario for the years 2025 to 2100: The trend lines exhibit a distinctly positive slope during the warmer months of May, June, July, August, and September, suggesting a slow rise in the delta temperature throughout the summer. On the other hand, ΔT gradually decreases during the colder months of January, February, and December, indicating a decrease in day-night temperature differences during the winter. More diverse patterns are seen for the spring and fall transitional seasons: While October exhibits a noticeably rising slope, which may indicate an extension of summer-like conditions into the autumn season, March and April show steady or slightly declining trends.

4.8.2 Monthly Delta Temperature (ΔT)

Using Excel files created with Python, delta temperature (ΔT), was computed in order to examine future monthly temperature variability under the RCP 8.5 scenario (2025–2100). The same methodology used for historical data is used here. Figure 90, presents the projected monthly delta temperature (ΔT) values under the RCP 8.5 scenario for the period 2025 to 2100. The

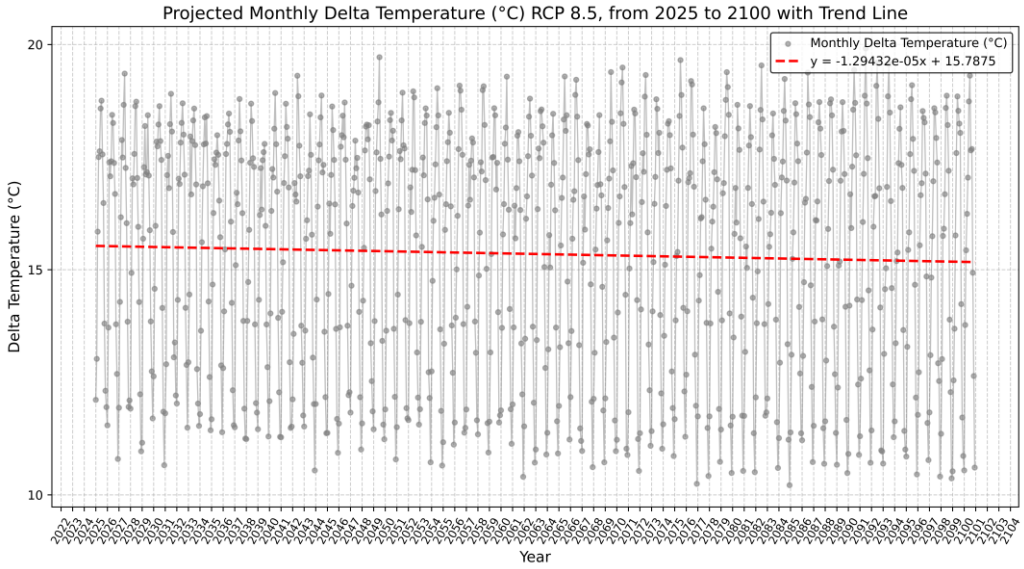

Figure 90_ Monthly Delta Temperature (°C) from 2025 to 2100 with Trend Line, RCP 8.5

chart shows all monthly ΔT data points as grey markers, with a red dashed trend line representing the overall direction. The slope of the trend line is slightly negative (approximately −0.0000129), but remains very close to zero. Despite evident seasonal and interannual fluctuations, the ΔT values generally range between 12°C and 18°C throughout the study period.

The Delta Temperature for each month over this future period was then looked at in order to further elucidate the conditions (Figure 91 to 94).

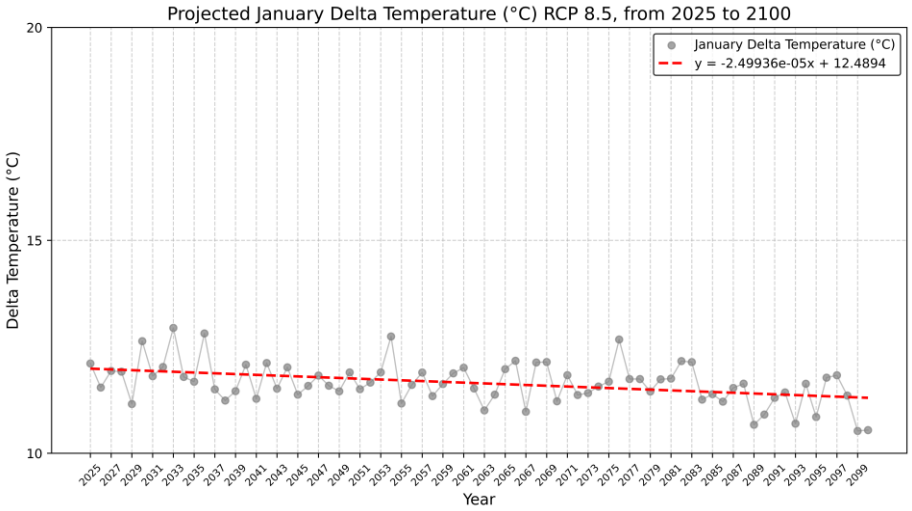

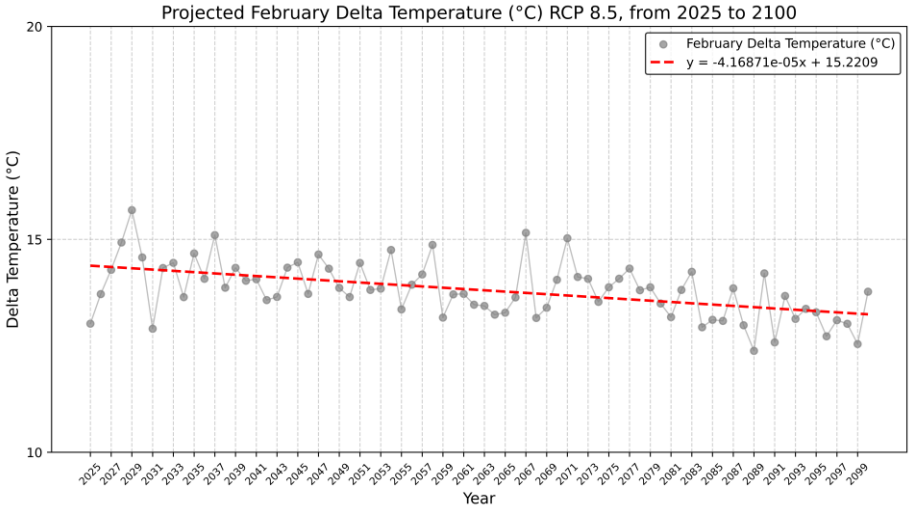

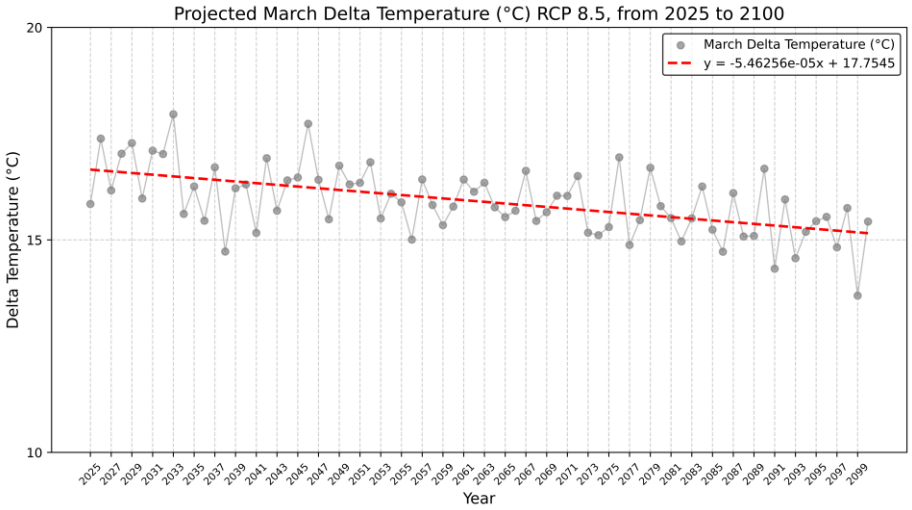

Figure 91_ Monthly Delta Temperature (°C) from 2025 to 2100 with Trend Line, RCP 4.5_ Jan to Mar

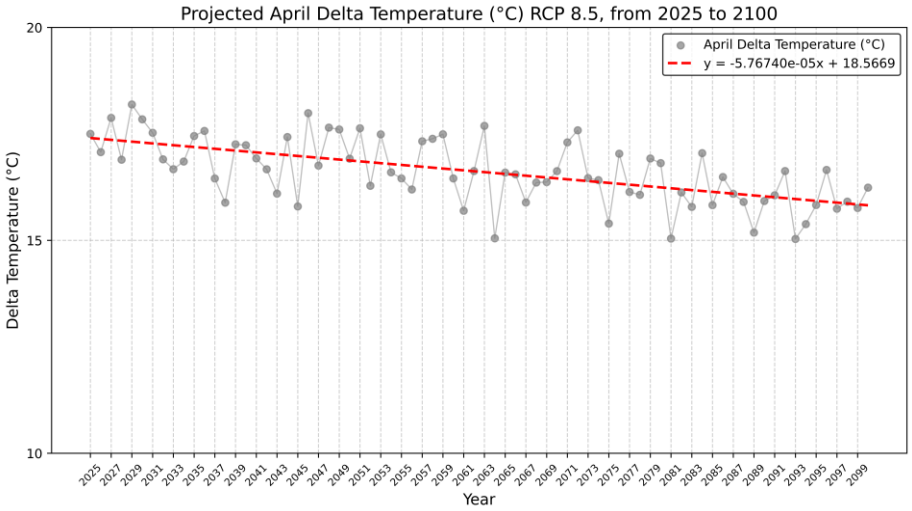

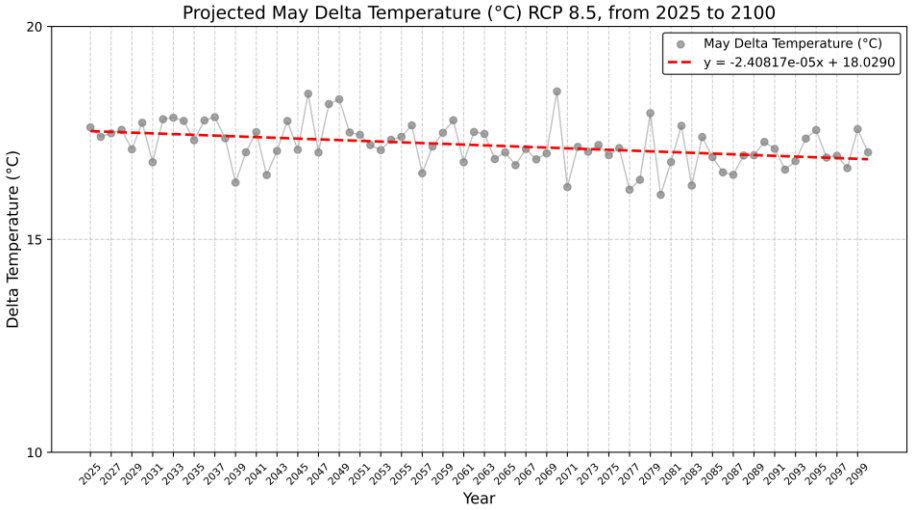

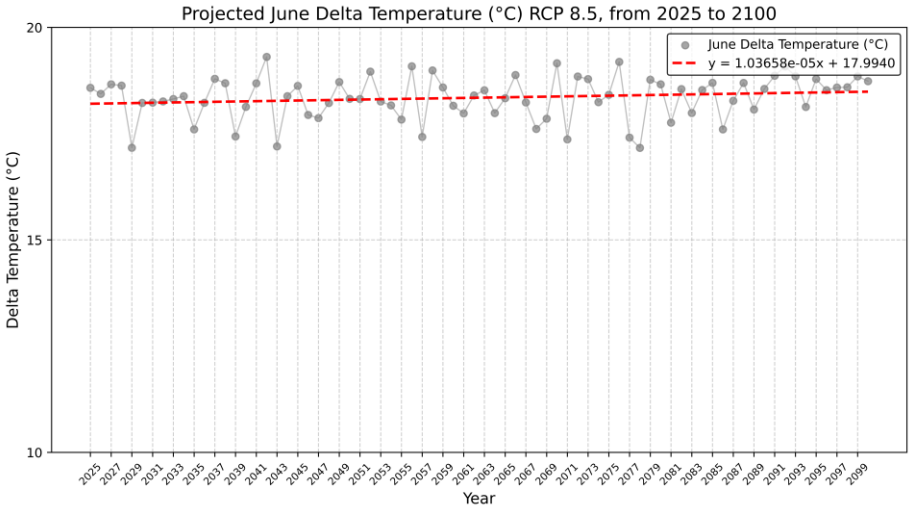

Figure 92_ Monthly Delta Temperature (°C) from 2025 to 2100 with Trend Line, RCP 8.5_ Apr to Jun

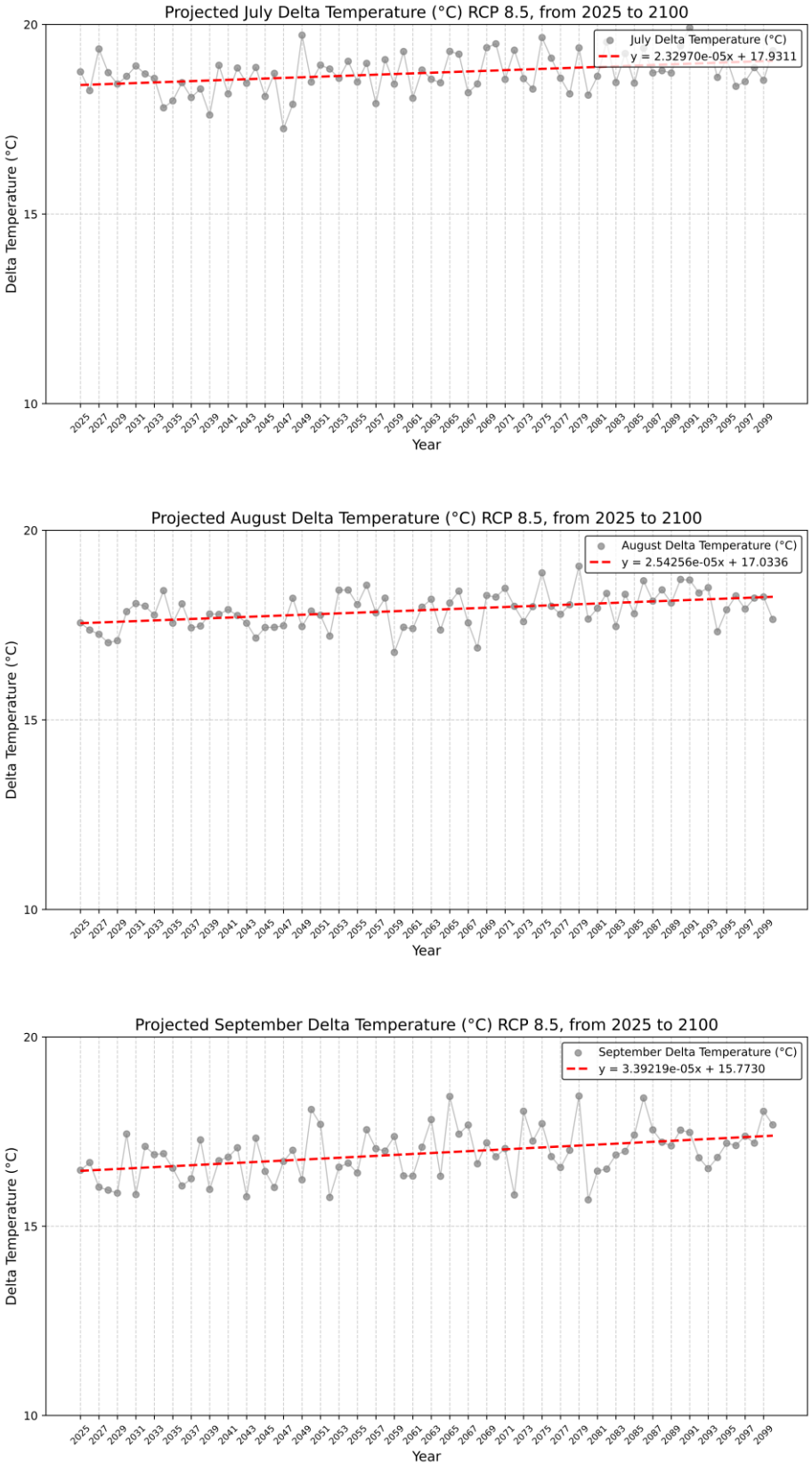

Figure 93_ Monthly Delta Temperature (°C) from 2025 to 2100 with Trend Line, RCP 8.5_ Jul to Sep

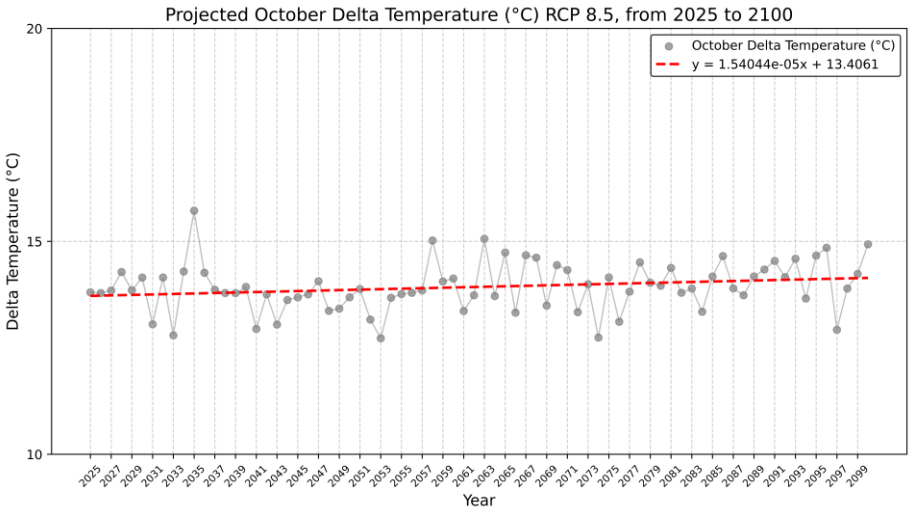

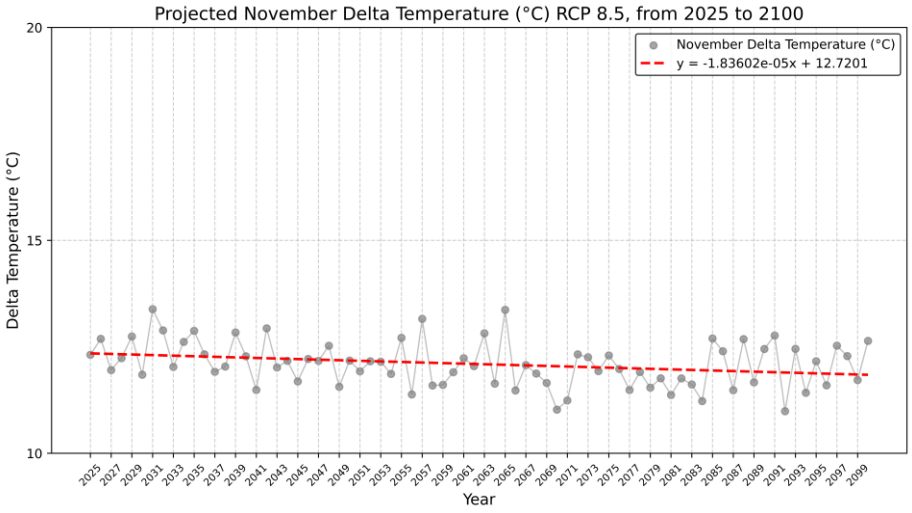

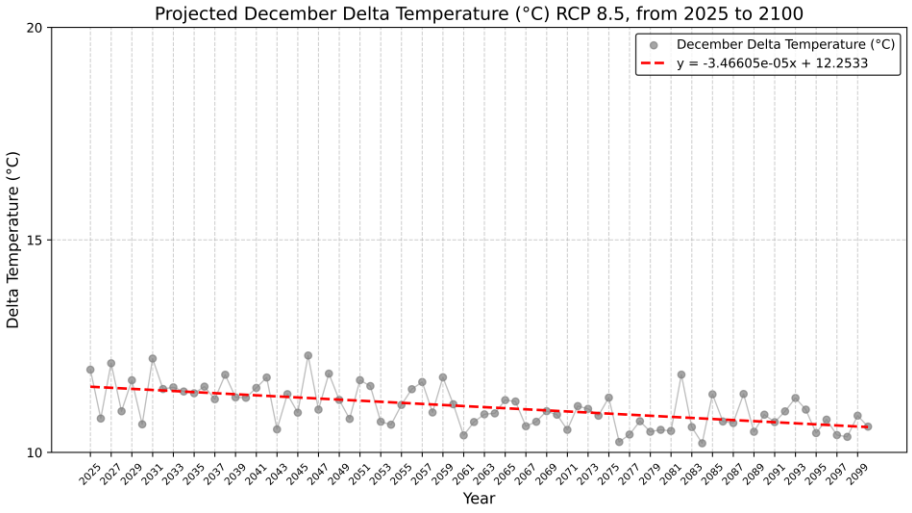

Figure 94_ Monthly Delta Temperature (°C) from 2025 to 2100 with Trend Line, RCP 8.5_ Oct to Dec

Most months exhibit relatively stable year-to-year variability; however, unlike the RCP 4.5 scenario, the trend lines in several months under RCP 8.5 are more pronounced. Notably, in the warmer months—June, July, August, and September—there is a gradual increase in ΔT, indicating an expanding difference between daytime and nighttime temperatures during the summer. On the other hand, ΔT typically shows a decreasing trend during the colder months of January, February, November, and December. In line with more general trends of global climate change. While October exhibits a noticeably positive slope, spring months like March and April also exhibit a clear downward trend.

4.8.3 Monthly Maximum and Minimum Temperatures

In this section, projected monthly Tmax and Tmin values under the RCP 8.5 scenario (2025–2100) were analyzed to assess long-term trends in temperature extremes. Data were extracted from GeoTIFF files and processed in Python to generate time series and trend lines for each month, highlighting seasonal thermal shifts and potential future risks.

In the following section, an overall view of the increasing and decreasing temperature trends from 2025 to 2100 is first presented (Figure 95).

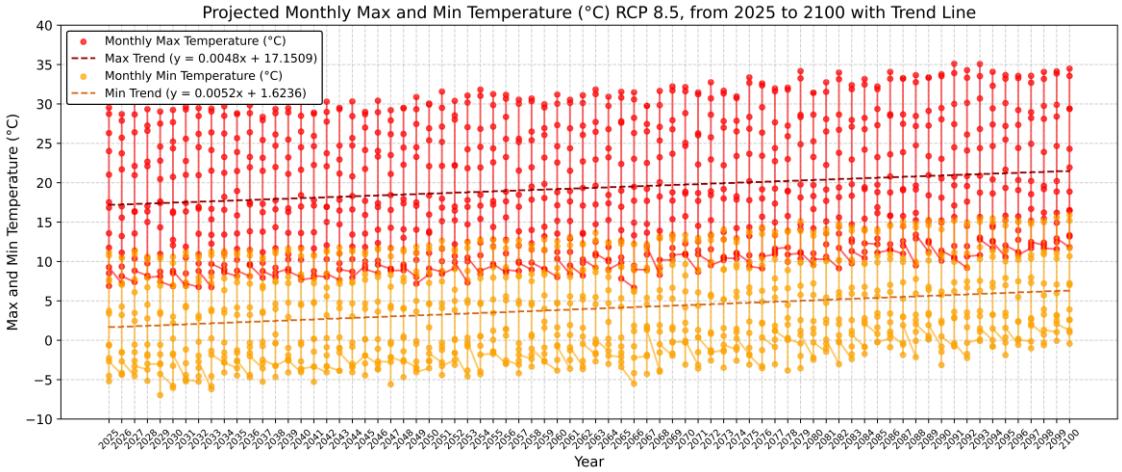

Figure 95_Monthly Max and Min Temperature (°C) from 2025 to 2100 with Trend Line, RCP 8.5

The presented chart illustrates the projected trends in monthly Tmax and Tmin, from 2025 to 2100 under the RCP 8.5 scenario. According to the fitted trend lines, both Tmax and Tmin show clear upward trends. The slope for Tmin is approximately 0.0052 °C per year—significantly steeper than that of Tmax, which increases by around 0.0048 °C per year. The figure also highlights persistent seasonal temperature cycles, with summer months recording higher temperatures and winter months lower ones, consistent across the projected period. To explore this further, the Tmax and Tmin were calculated and analyzed separately for each month over the last six decades (Figure 96 to 99).

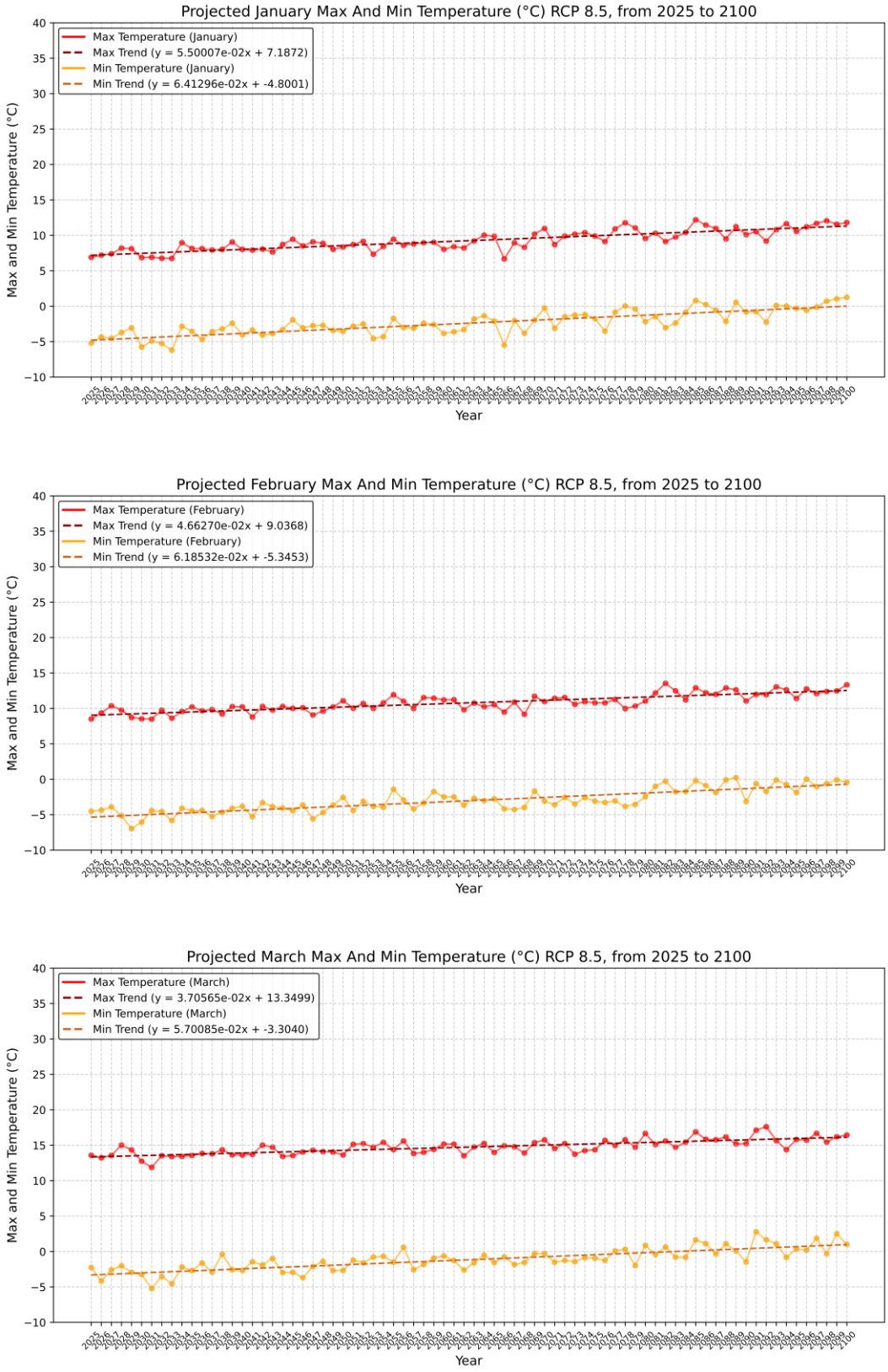

Figure 96_ Monthly Max and Min Temperature (°C) from 2025 to 2100 with Trend Line, RCP 8.5_ Jan to Mar

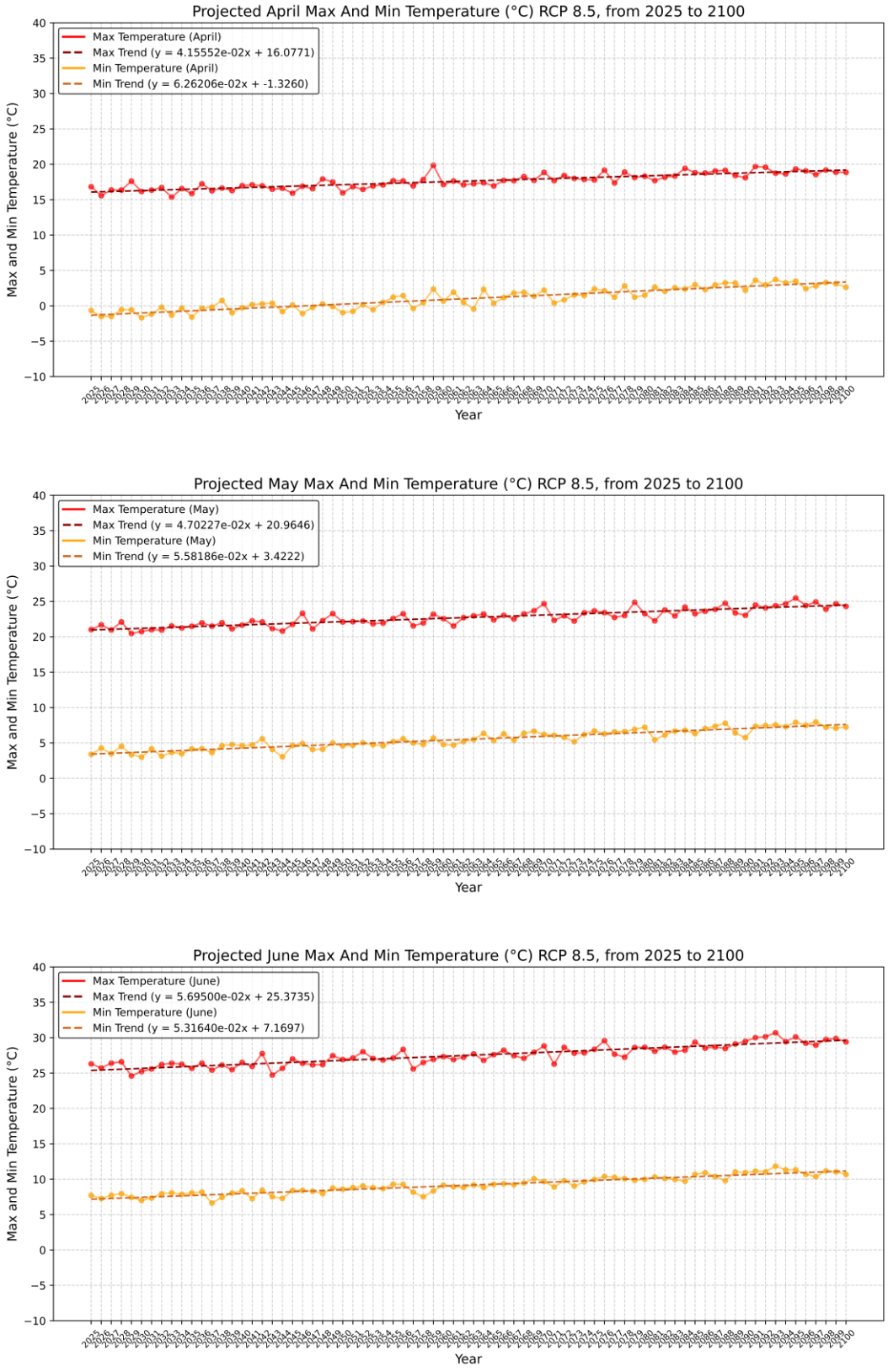

Figure 97_Monthly Max and Min Temperature (°C) from 2025 to 2100 with Trend Line, RCP 8.5_ Apr to Jun

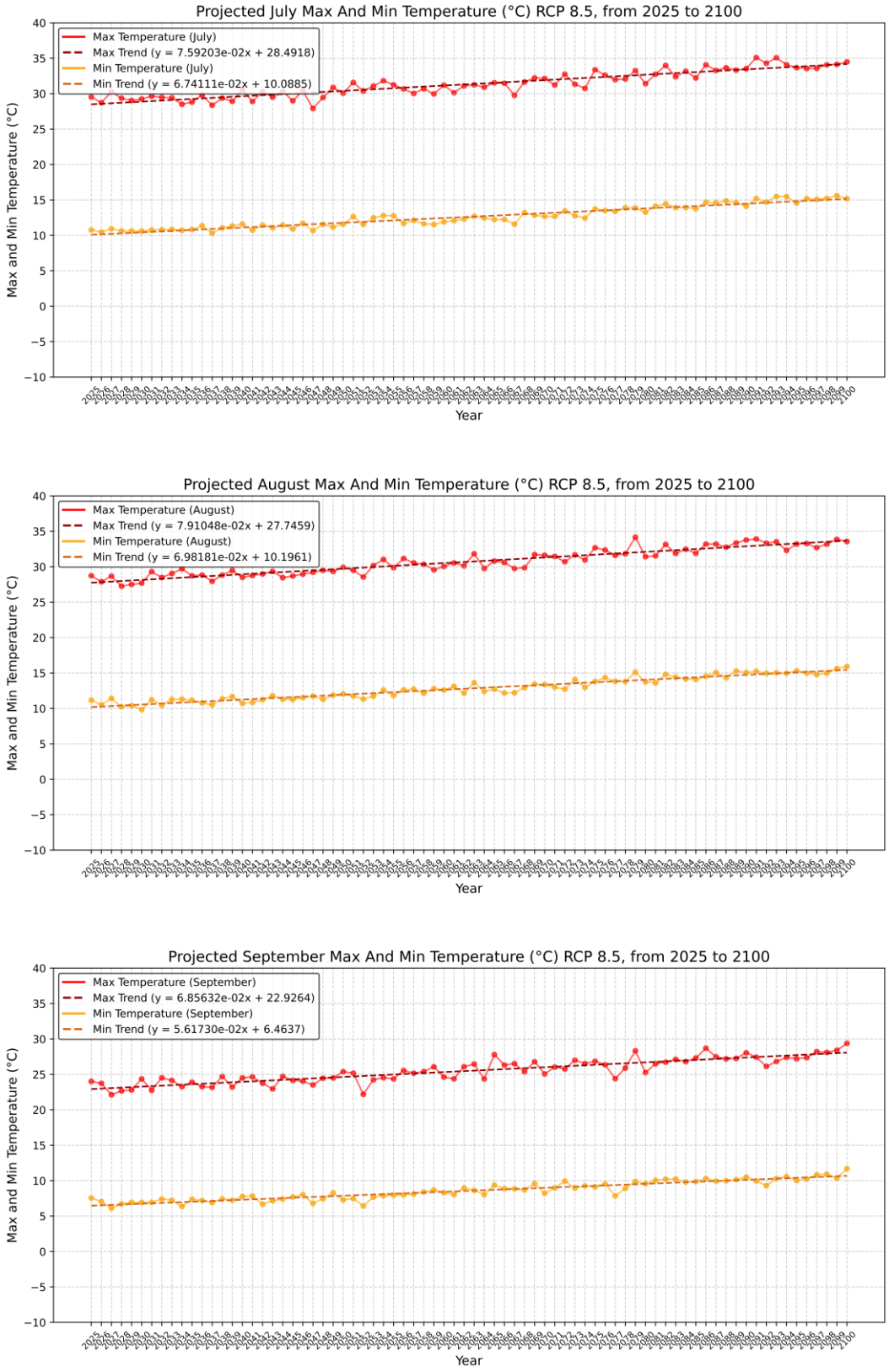

Figure 98_ Monthly Max and Min Temperature (°C) from 2025 to 2100 with Trend Line, RCP 8.5_ Jul to Sep

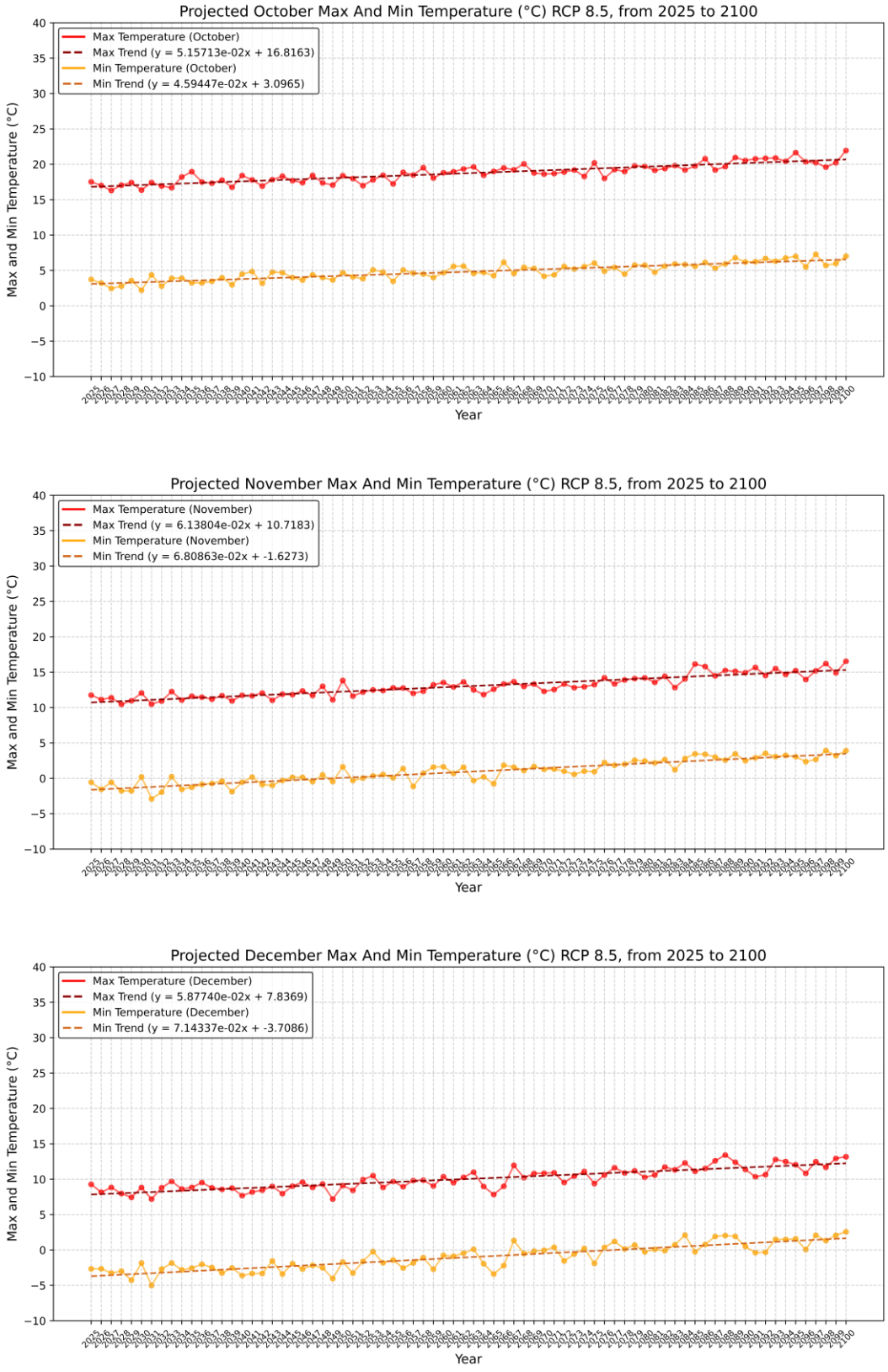

Figure 99_ Monthly Max and Min Temperature (°C) from 2025 to 2100 with Trend Line, RCP 8.5_ Oct to Dec

A comprehensive analysis of the monthly forecasts under the RCP 8.5 scenario shows that Tmax and Tmin, are consistently rising throughout the year. Summer months (June, July, August, and September) show steeper positive slopes for Tmax values. Winter months (January, February, and December) exhibit noticeable warming trends, with Tmin rising more rapidly. Spring months (March, April, and May) show modest increases in both Tmax and Tmin, while fall months (particularly September and October) demonstrate dramatic and sustained warming for both parameters. The minimum temperature trend lines are consistently steeper than the maximum ones across most months.

4.8.4 Elevation-Based Temperature Analysis

For the RCP 8.5 scenario, the elevation classification by Tiranti et al. (2023) was also used to assess future temperature trends across different altitudinal zones in the Susa Valley. By integrating monthly GeoTIFF projections with the regional DEM, average Tmax and Tmin values were extracted for each elevation class. The data were then analyzed using Python to identify how warming evolves from lowlands to highlands under more extreme climate forcing. The resulting trends are visualized in Figures 100 and 101, with a detailed interpretation provided in the following section.

Figure 100_ Max and Min Temperature Trend with Elevation Classes 1,2,3, RCP 8.5

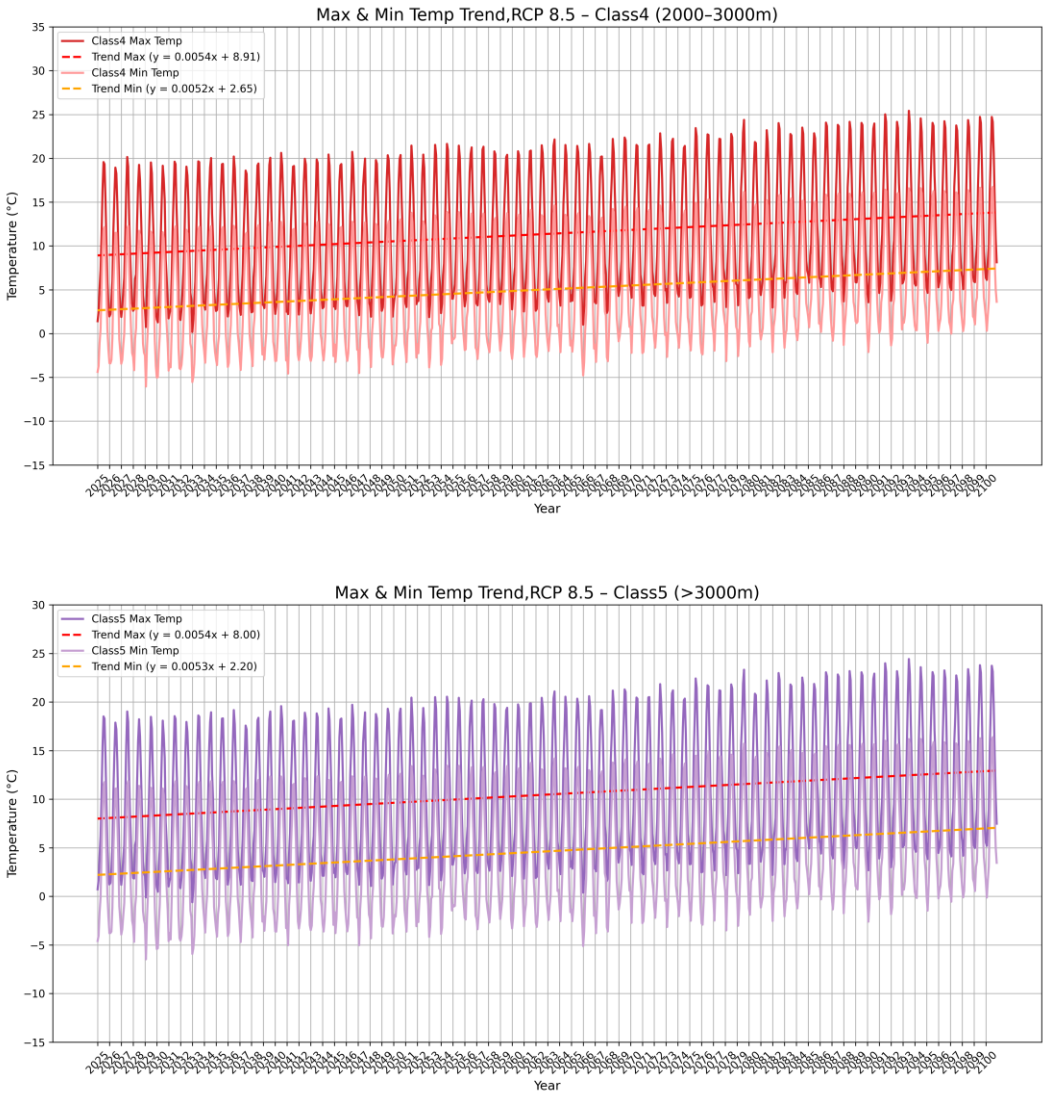

Figure 101_ Max and Min Temperature Trend with Elevation Classes 4,5, RCP 8.5

Under the RCP 8.5 scenario, a consistent upward trend in both Tmax and Tmin, is observed across all elevation classes in the Susa Valley.

In class 1 (400–700 m), Tmax and Tmin increase at nearly identical rates of +0.0049 and +0.0047 °C/year, respectively, showing uniform warming at lower elevations. Class 2 (700–1000 m), Tmax and Tmin both increase at +0.0050 and +0.0048 °C/year, respectively, following comparable paths. Class 3 (1000–2000 m), Tmax and Tmin increase at +0.0053 and +0.0051 °C/year, respectively, maintaining the pattern of closely correlated warming. Class 4 (2000–3000 m), Tmax and Tmin show consistent warming at higher elevations, growing at +0.0054 and +0.0052 °C/year, respectively. Class 5 (>3000 m), There is no indication of decreased warming even at very high elevations, with Tmax increasing at a rate of +0.0054 °C/year and Tmin showing a similar rate of +0.0053 °C/year.

For clearer comparison, Figure 102 presents bar charts showing the average Tmax and Tmin for each elevation class.

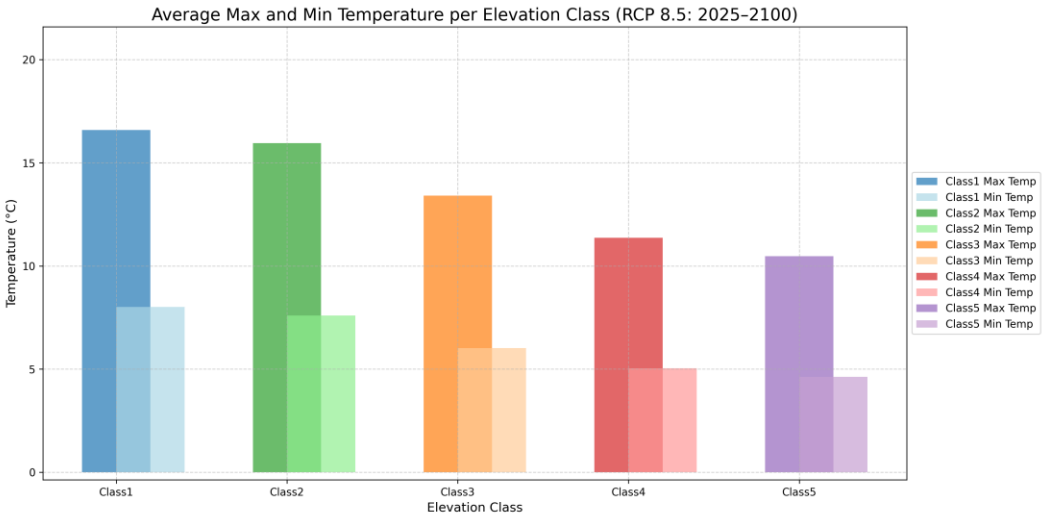

Figure 102_ Average Max and Min Temperature per Elevation Class from 2025 to 2100, RCP 8.5

Figure 102 that shows a clear altitudinal temperature gradient is evident, where both Tmax and Tmin systematically decrease with increasing elevation.

Class 1 (400–700 m) records the highest averages, with Tmax close to 16.7°C and Tmin around 8.1°C. Class 2 (700–1000 m) follows with a slightly lower Tmax of approximately 16.0°C and Tmin of 7.6°C. Class 3 (1000–2000 m) shows a further decline, averaging around 13.4°C (Tmax) and 6.1°C (Tmin). Class 4 (2000–3000 m) exhibits Tmax near 11.3°C and Tmin about 5.1°C. Class 5 (>3000 m) records the lowest values, with average Tmax around 10.5°C and Tmin close to 4.6°C.

4.8.5 Critical Elevation Identification

For the RCP 8.5 scenario, critical elevation thresholds were identified using monthly Tmax GeoTIFF datasets directly within QGIS. Temporal aggregation was conducted using r.series, followed by spatial extraction with Raster Calculator and the Point Sampling Tool. This process enabled efficient retrieval of Tmax values across elevation gradients without data format conversions. The compiled data was analyzed in Excel to determine the altitudes where Tmax values fall near or below 0°C.

A scatter plot was generated to illustrate the correlation between elevation and projected average Tmax from 2025 to 2100 (Figure 103).

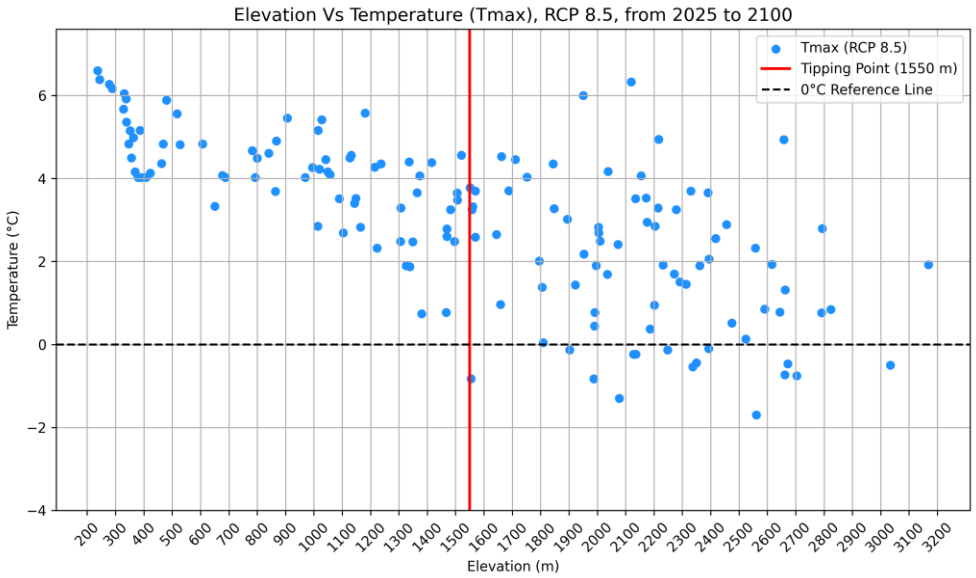

Figure 103_ Elevation Vs Max Temperature, from 2025 to 2100, RCP 8.5

The scatter plot clearly shows an inverse relationship between elevation and Tmax, under the RCP 8.5 scenario for the years 2025–2100. Above about 1550 meters, a noticeable thermal threshold is seen, and many Tmax values drop below 0 °C. The projected tipping point is indicated by this elevation, which separates areas with primarily freezing or sub-freezing maximum temperatures from those with warmer temperatures (Figure 103).

4.9 Future Precipitation Projections Under RCP 8.5

This section examines projected precipitation patterns in the Susa Valley under the RCP 8.5 scenario using monthly GeoTIFF data from ARPA Piemonte. The raster layers, each representing modeled mean daily precipitation for a given month, were spatially masked to the Susa Valley extent. All analyses focused on average daily values to maintain consistency with 24-hour threshold standards used in return period assessments. This ensures a meaningful comparison with historical extreme rainfall events under future climate projections.

4.9.1 Cumulative 24-Hour Rainfall

This section examines the Susa Valley's expected 24-hour cumulative rainfall under the RCP 8.5 scenario in order to evaluate short-duration rainfall patterns that may be connected to hydrogeological hazards.

The long-term trend of the Susa Valley's anticipated 24-hour average monthly rainfall is shown in Figure 104. This summary aids in spotting possible long-term changes in hydrogeological hazard patterns as well as slow variations in rainfall intensity.

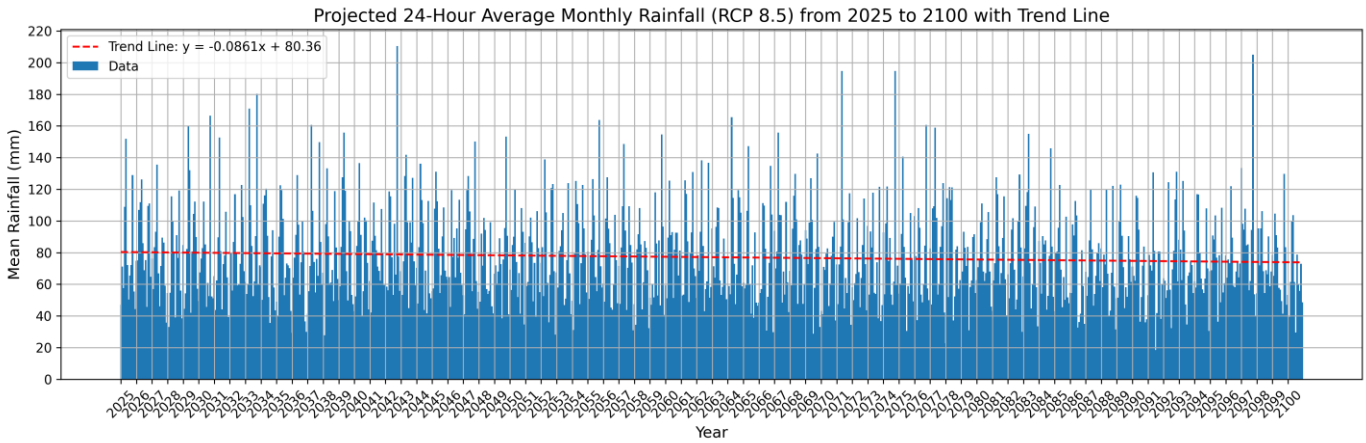

Figure 104_ Cumulative Rainfall per 24 hour from 2025 to 2100, RCP 8.5

The RCP 8.5 scenario shows in Figure 104 that the projected 24-hour average monthly rainfall for the period 2025–2100 has a lot of interannual variability with many sharp peaks indicating extreme precipitation events. The trend line here shows a slightly negative gradient (−0.0861 mm/year), suggesting a gradual decrease in overall mean daily rainfall levels over time. While sporadic high-rainfall events still occur, this downward trend could imply a shift toward drier baseline conditions in the long term. These findings warrant further examination of seasonal rainfall behavior and its implications for future hydrological risks in the Susa Valley.

approach highlights climate-driven changes and improves seasonal hazard assessment (Figures 105 to 107).

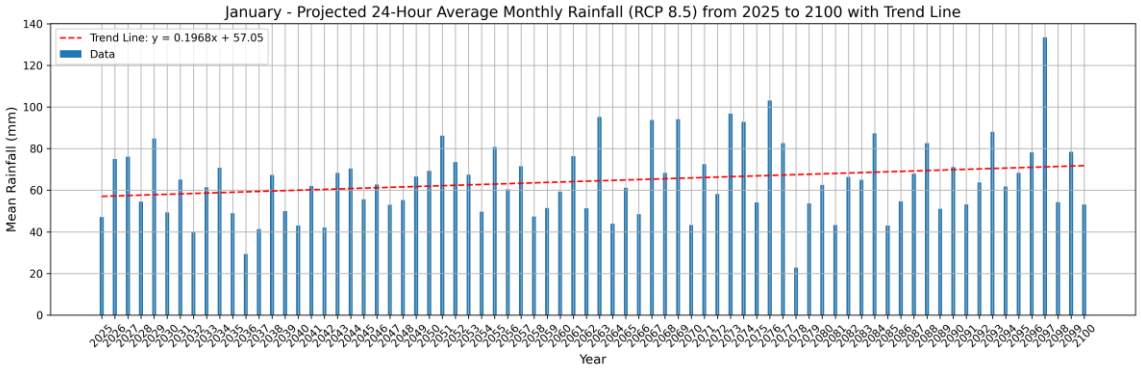

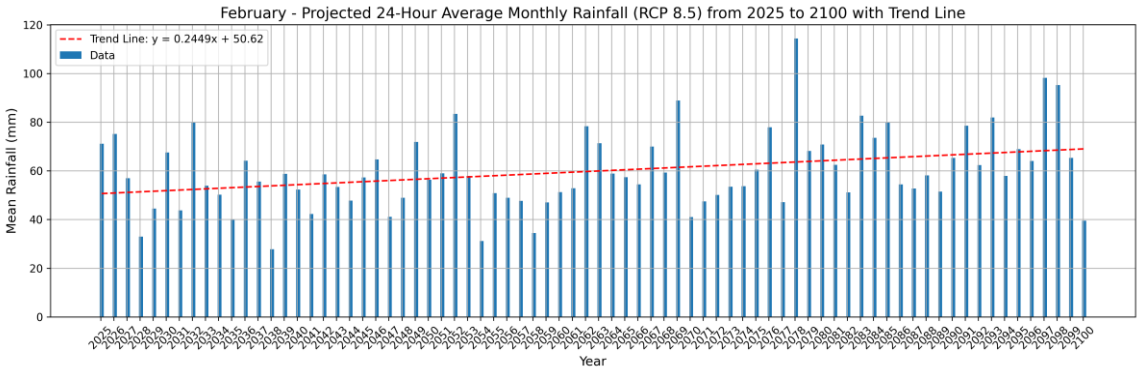

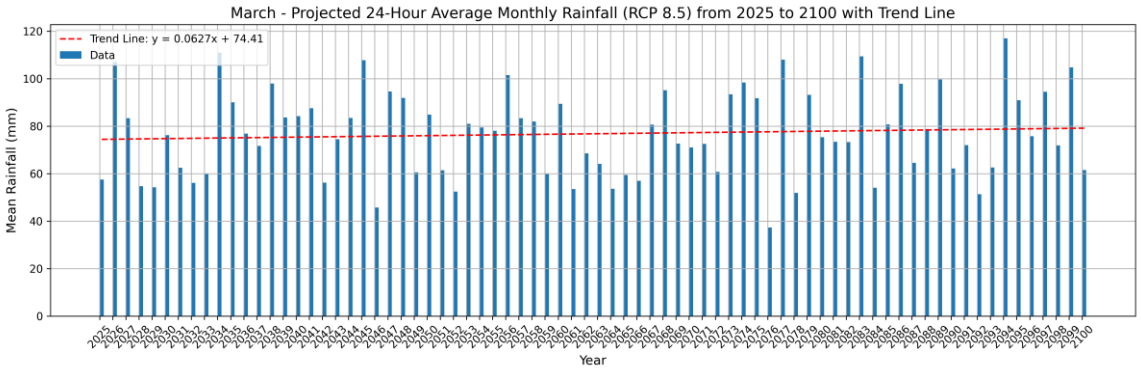

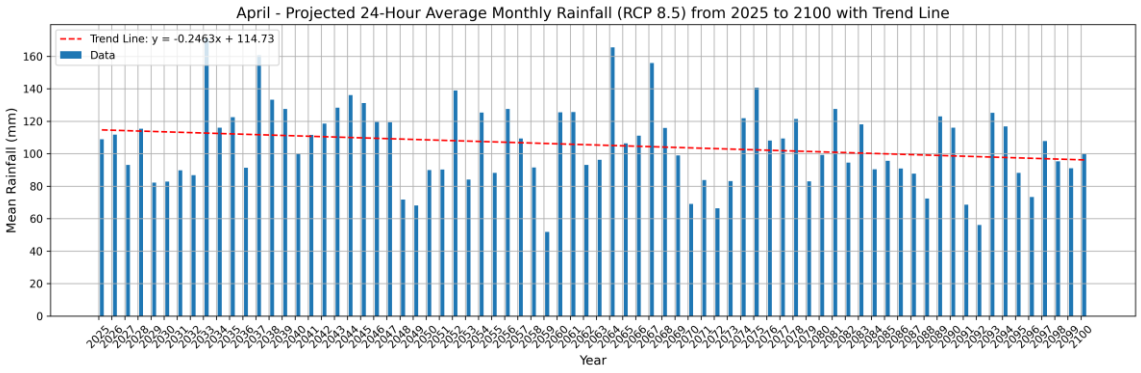

Figure 105_ Cumulative Rainfall per 24 hours from 2025 to 2100, RCP 8.5_ Jan to Apr

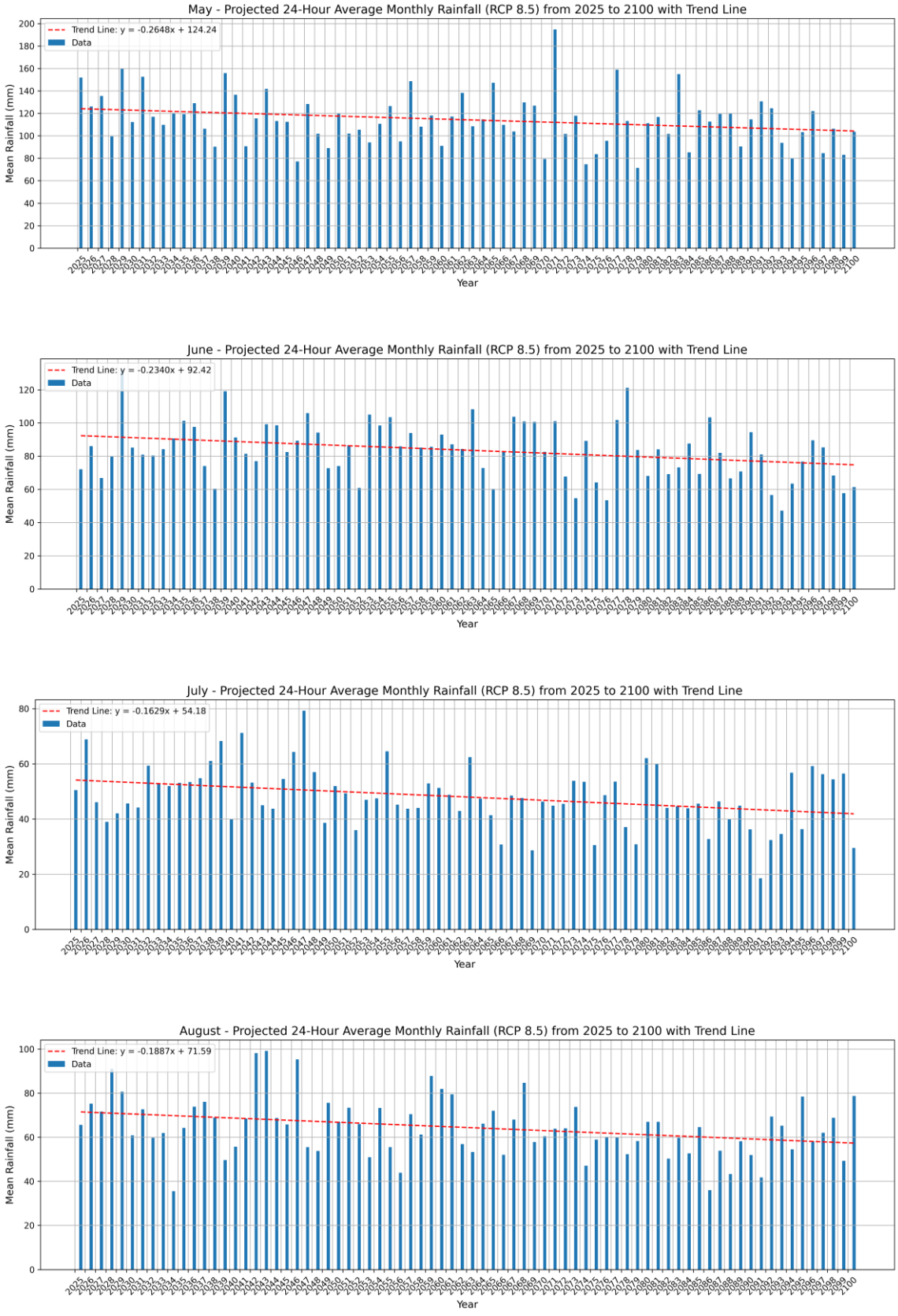

Figure 106_ Cumulative Rainfall per 24 hours from 2025 to 2100, RCP 8.5_ May to Aug

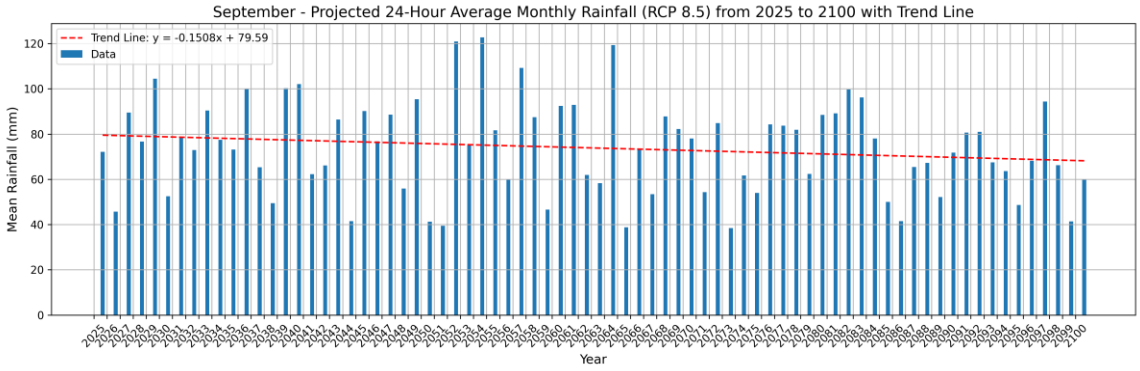

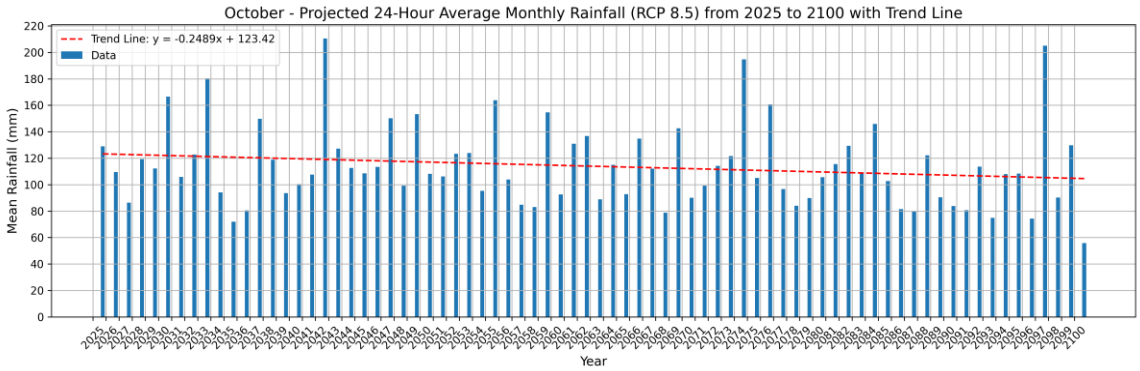

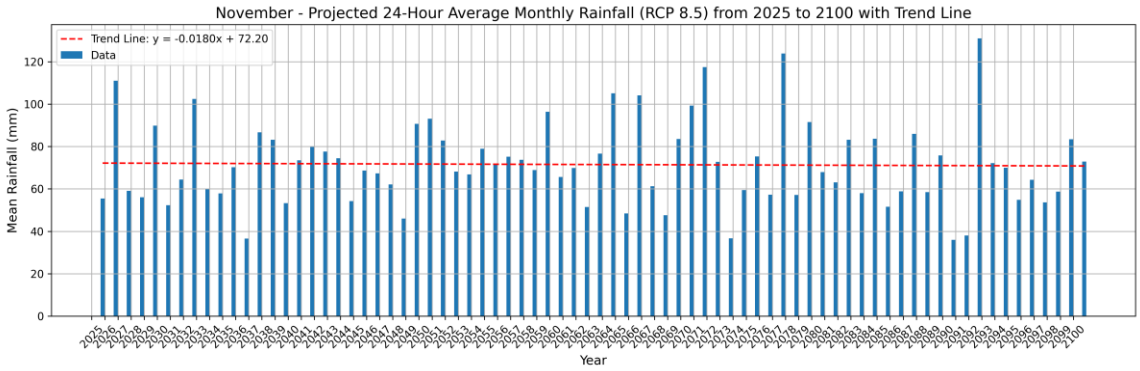

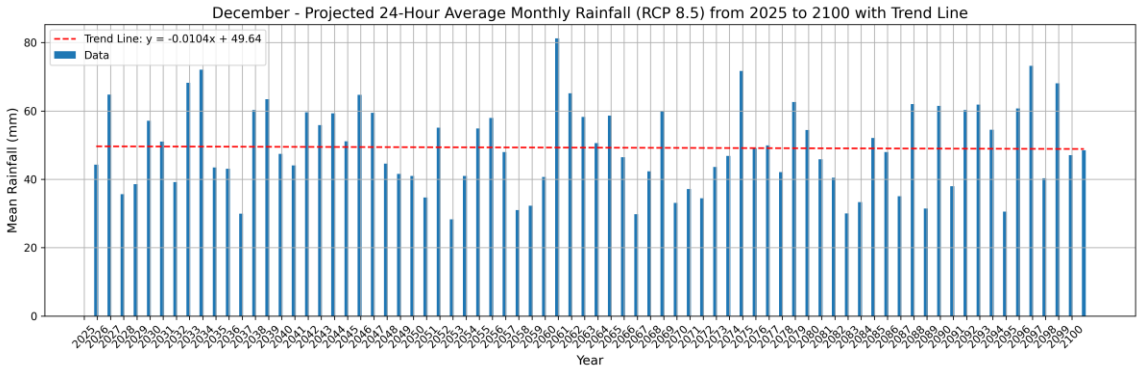

Figure 107_ Cumulative Rainfall per 24 hours from 2025 to 2100, RCP 8.5_ Sep to Dec

Under the RCP 8.5 scenario, most months in the Susa Valley show a declining trend in 24-hour average rainfall, especially in May, April, October, June, and July, indicating reduced precipitation in spring and summer. August and September also follow this downward pattern. In contrast, February, March, and January display positive trends, suggesting a slight increase in winter and early spring rainfall. December remains relatively stable. These trends highlight a possible seasonal shift, with drier warm months and wetter cold months, potentially affecting flood and drought risks in the region.

4.9.2 Return Period Analysis of Extreme Events

This section examines projected summer rainfall intensities (June, July, August) under RCP 8.5 against 24-hour return period thresholds.

The 24-hour cumulative rainfall charts for these months are presented, along with the corresponding 24-hour return period thresholds for 2-, 5-, 10-, 50-, 100-, and 200-year intervals (Figure 108).

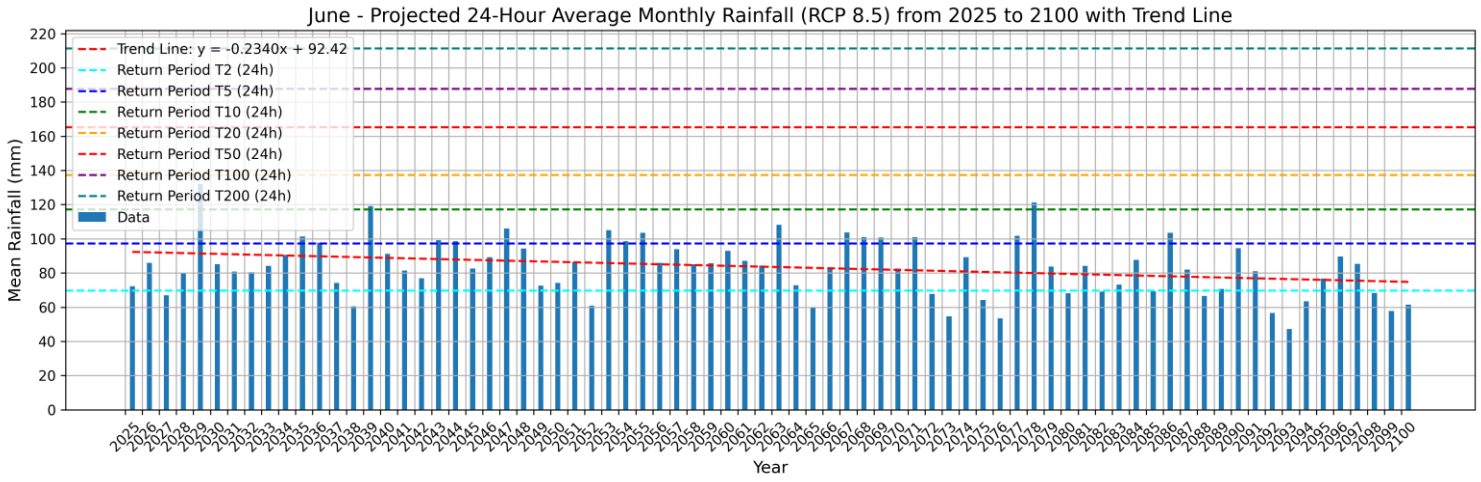

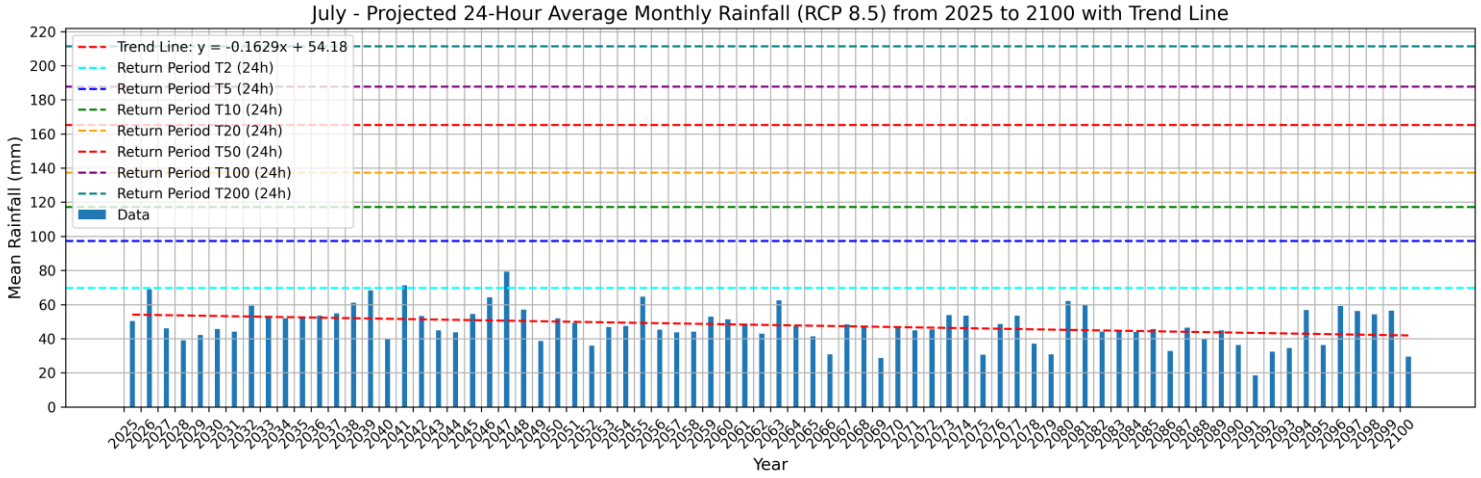

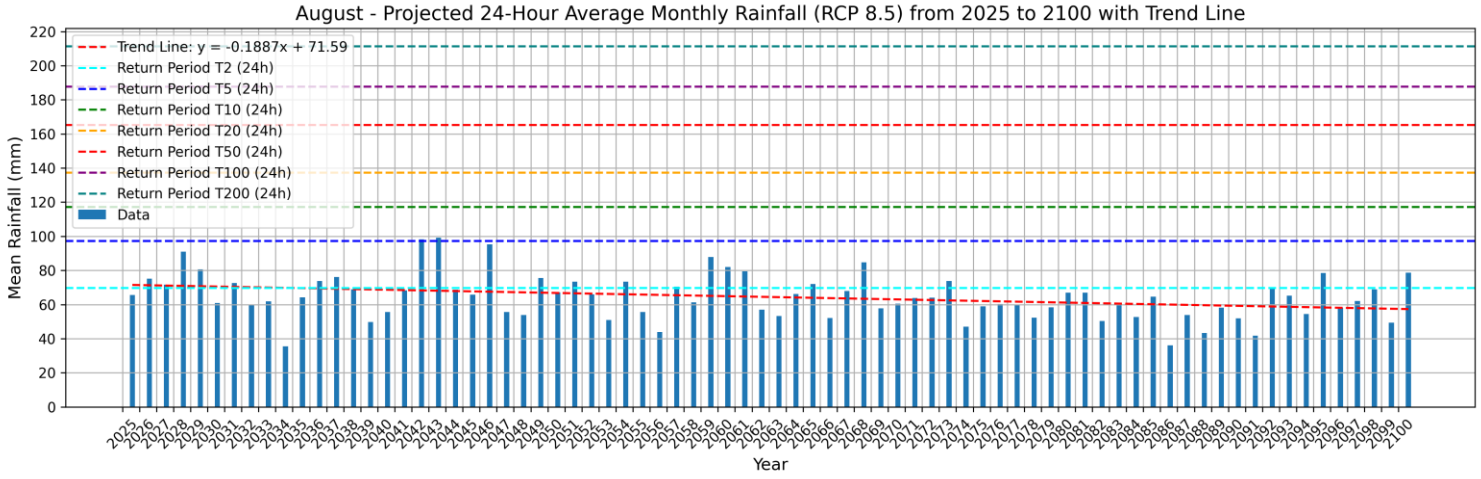

Figure 108_ Return Period of Cumulative Rainfall per 24 hours with Trend Line from 2025 to 2100, RCP 8.5_ Jun to Aug

Based on the projected data for the summer months under the RCP 8.5 scenario, the charts for June, July, and August illustrate the evolution of 24-hour average monthly rainfall from 2025 to 2100, overlaid with return period thresholds (T2 to T200). In June, several rainfall values approach or exceed the T10 and T20 thresholds. However, the overall trend is negative (slope ≈ –0.2340), indicating a gradual decline in summer rainfall intensity during this month. In July, the data show relatively stable variability, with most values remaining below the T10 threshold. The trend is also mildly negative (slope ≈ –0.1629), suggesting a slight decrease in rainfall intensity over the century. In August, a more pronounced downward trend is observed (slope ≈ –0.1887). Although some years record rainfall above the T2 and T5 thresholds, the majority of values remain below the T10 level.

4.10 Analysis of Future Susceptibility Classes under Climatic Conditions Under RCP 8.5

This section provides a brief overview of how climate data were integrated with susceptibility maps for rockfall, shallow landslides, and debris flows in the Susa Valley. Specifically:

- **Rockfall susceptibility** was evaluated using Delta temperature (5–8°C) and 24/48-hour precipitation thresholds, with five classes.
- **Shallow landslide** susceptibility was analyzed based on 24-hour rainfall thresholds, with three classes.
- **Debris flow** susceptibility was assessed using rainfall intensity thresholds (20, 30, and 50 mm/h). All susceptibility layers were spatially aligned with climate projections to assess the influence of environmental triggers on slope instability, with three classes: ECM, GCM, BCM.

4.10.1 Rockfall Susceptibility under Temperature and Precipitation Conditions

A monthly analysis was conducted for the 2025–2100 period in order to assess the effect of projected temperature fluctuations (ΔT = Tmax − Tmin) on future rockfall susceptibility in the Susa Valley under the RCP 8.5 scenario. In accordance with Tiranti et al. (2023), ΔT values were obtained from GeoTIFF datasets of future Tmax and Tmin and examined across five elevation bands and susceptibility classes. Key ΔT thresholds (<5°C, 5–8°C, >8°C) were used to group the data. These thresholds show different levels of thermal stress and possible rockface degradation. This assessment helps identify regions where increased

thermal fatigue may increase future rockfall hazards by highlighting seasonal and spatial trends in thermal variability under high-emission conditions. The results are summarized in Figures 109 to 113, which display the distribution of ΔT values across rockfall susceptibility classes and elevation bands, highlighting the proportion of areas falling within key thermal thresholds (<5°C, 5–8°C, and >8°C).

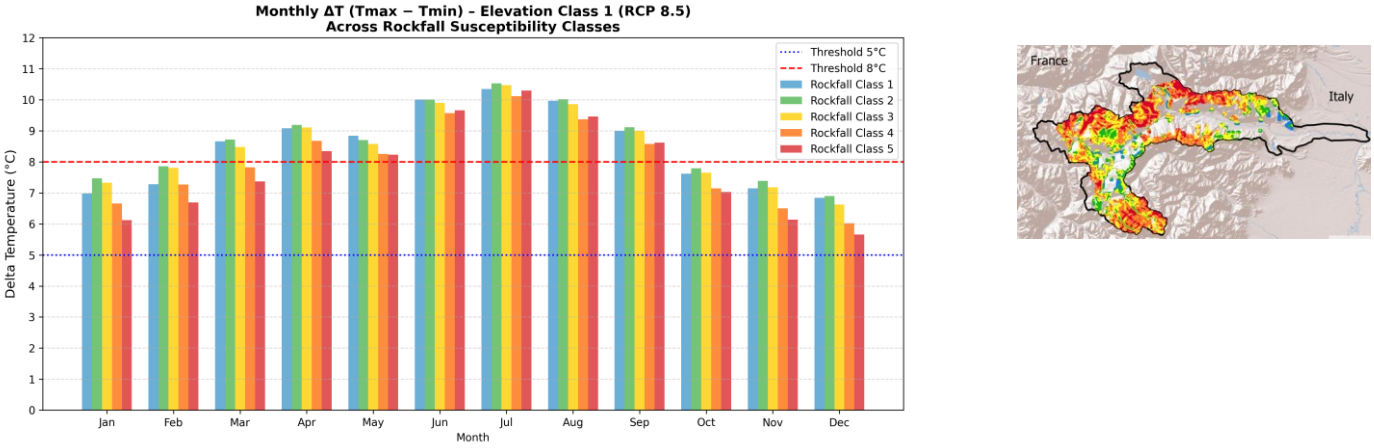

Figure 109_ Monthly ΔT across rockfall susceptibility classes in Elevation Class 1, RCP 8.5, between 5 °C and 8 °C thresholds

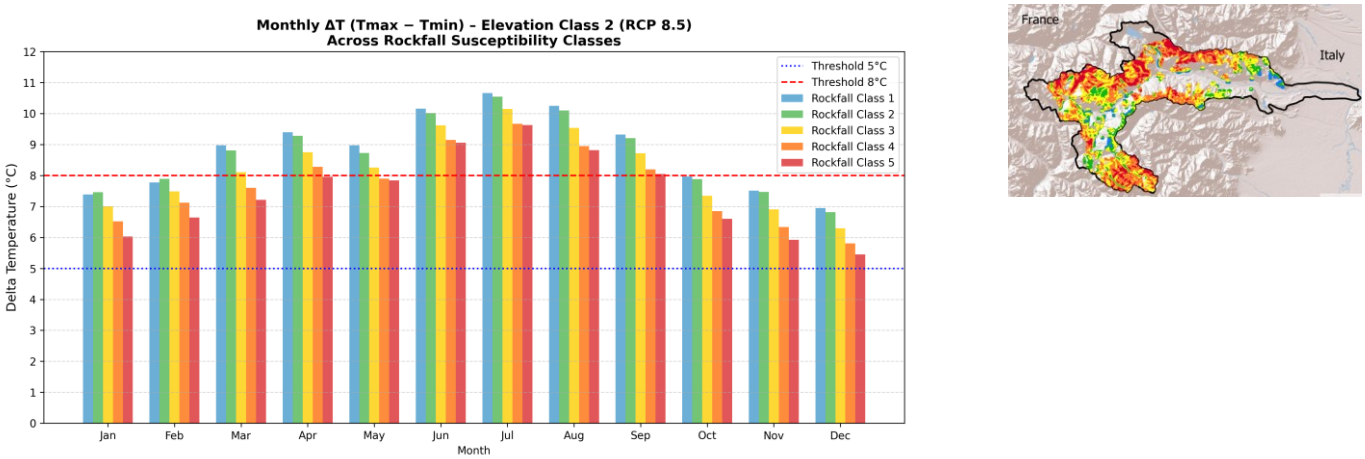

Figure 110_ Monthly ΔT across rockfall susceptibility classes in Elevation Class 2, RCP 8.5, between 5 °C and 8 °C thresholds

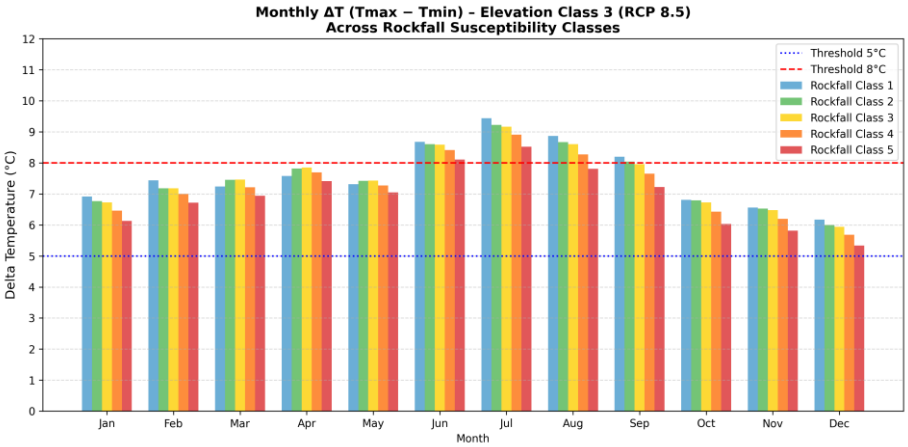

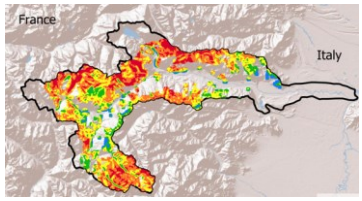

Figure 111_ Monthly ΔT across rockfall susceptibility classes in Elevation Class 3, RCP 8.5, between 5 °C and 8 °C thresholds

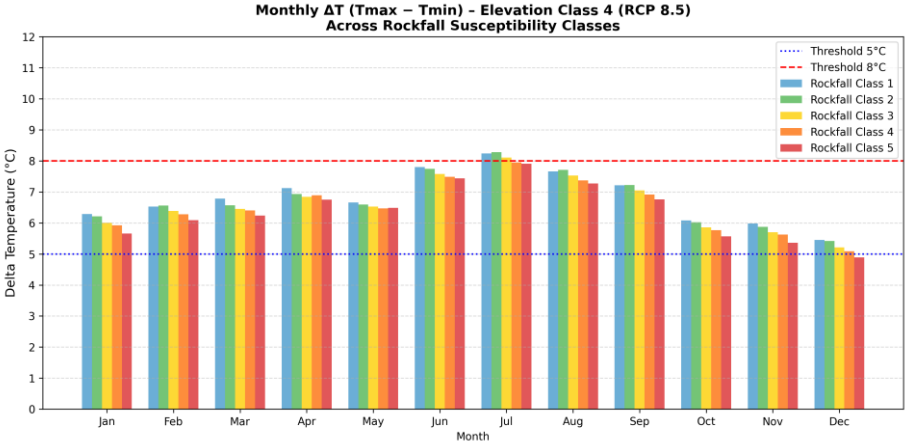

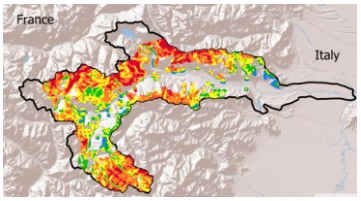

Figure 112_ Monthly ΔT across rockfall susceptibility classes in Elevation Class 4, RCP 8.5, between 5 °C and 8 °C thresholds

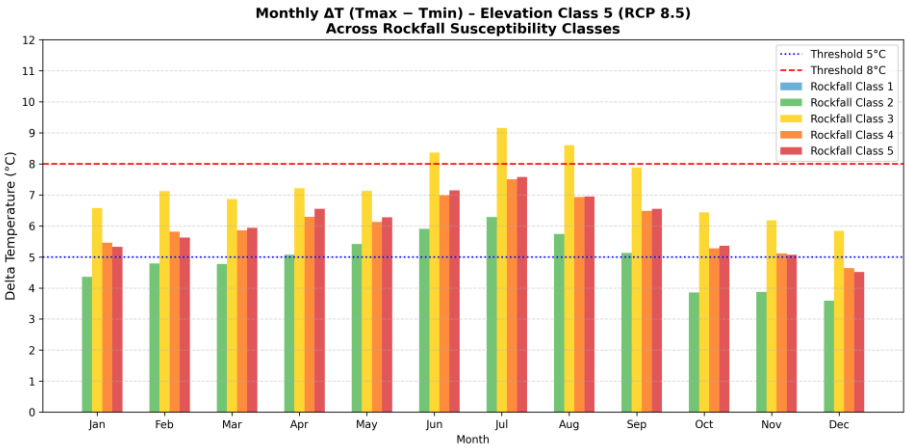

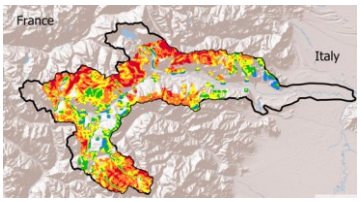

Figure 113_ Monthly ΔT across rockfall susceptibility classes in Elevation Class 5, RCP 8.5, between 5 °C and 8 °C thresholds

All five elevation classes exhibit distinct seasonal variability in the projected ΔT trends under the RCP 8.5 scenario (2025–2100). Peak ΔT values are consistently

found in warmer months (May to August), and the most frequent exceedances of the critical 8°C threshold occur at lower elevations (Classes 1 and 2), especially in Susceptibility Classes 1 to 3. These circumstances point to increased heat stress, which could quicken the weathering process. During the summer, ΔT values in mid-elevation bands (Classes 3 and 4) continue to be high, occasionally exceeding 8 °C, most notably in Susceptibility Class 3.Although Class 3 still records peaks in July and August, the highest elevation band (Class 5) generally maintains more moderate ΔT levels, with values typically below 8 °C. All zones see a decrease in ΔT values during the colder months of November through February, typically falling between 5°C and 7°C while remaining within moderate thermal stress thresholds. Class 3 exhibits the highest ΔT values consistently across the majority of elevations and months among all susceptibility classes, suggesting a possible vulnerability to long-term thermal fatigue effects. These trends suggest that the risk of thermally induced rockface instability may increase under RCP 8.5, particularly in zones with moderate to high rockfall susceptibility that are lower to mid-elevation.

In the following section, the effect of precipitation on rockfall susceptibility has been examined. Event-based data surpassing the specified 24-hour (≥120 mm) and 48-hour (≥170 mm) thresholds were examined in order to investigate the spatial distribution of future extreme precipitation events under the RCP 8.5 scenario (Figure 114). In order to classify each event into five predetermined elevation classes, the geographic coordinates were extracted, and a Digital Elevation Model (DEM) was used to determine the corresponding elevation. At the same time, a spatially aligned susceptibility raster was used to assign a rockfall susceptibility level to each event. To guarantee consistency and reproducibility, automated Python scripts were used for every processing step, including threshold filtering, spatial joining, and classification.

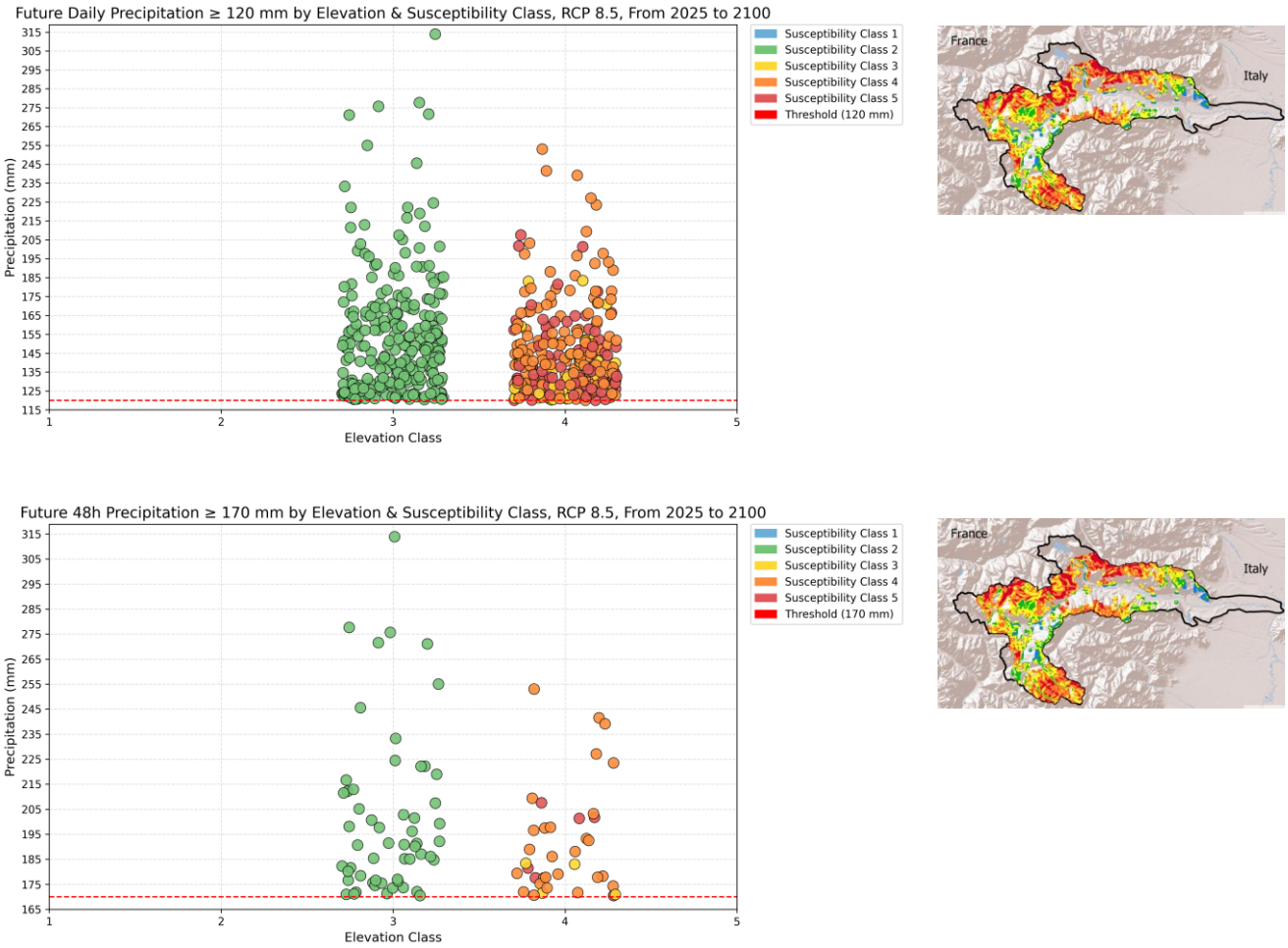

Figure 114_24 and 48 hours Rainfall Events by Elevation Class and Rockfall Susceptibility, RCP 8.5

In the 24-hour precipitation chart (≥120 mm), a substantial number of extreme events are recorded, primarily clustered within Elevation Classes 3 and 4. These events are strongly associated with higher susceptibility levels—particularly Susceptibility Classes 3, 4, and 5. No threshold-exceeding events are observed in Elevation Classes 1 and 2 (Figure 114).

In the 48-hour precipitation chart (≥170 mm), the frequency of extreme events is lower, yet they continue to occur within Elevation Classes 3 and 4. These longer-duration events are also mostly linked to Susceptibility Classes 3 to 5, although their spatial distribution appears more limited than the 24-hour events (Figure 114).

4.10.2 Debris Flow Susceptibility under Precipitation Conditions

Daily rainfall data from 2025 to 2100 was analyzed and converted into roughly 12-hour intensities in order to evaluate the risk of debris flow in the future under

the RCP 8.5 scenario. These were contrasted with susceptibility class-specific critical thresholds of 20 mm/h, 30 mm/h, and 50 mm/h. The analysis illustrates the frequency and spatial distribution of threshold-exceeding summer events in vulnerable areas over the course of the study period by superimposing the results with the debris flow susceptibility map (Figure 115).

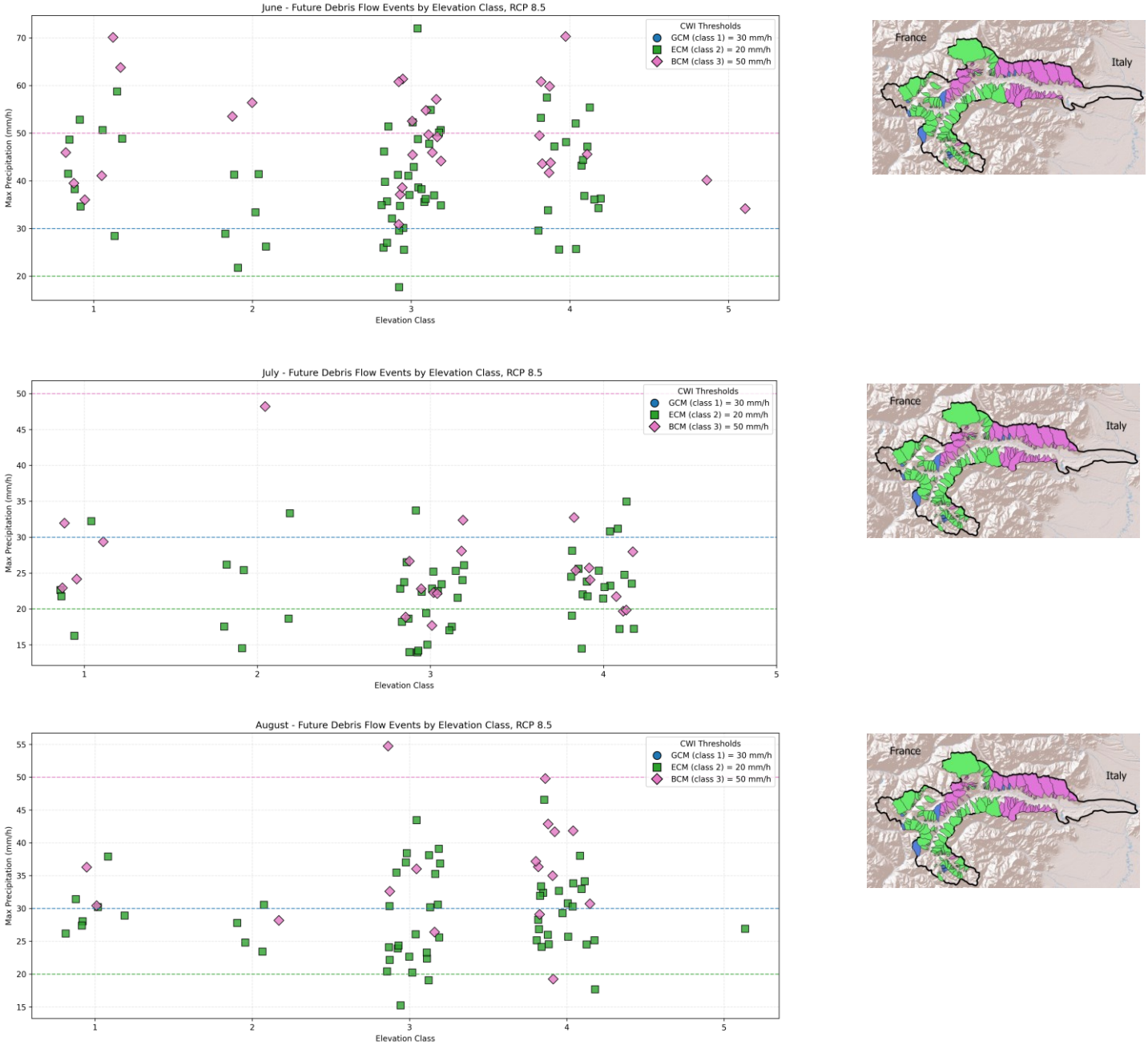

Figure 115_ Rainfall Events by Elevation Class and Debris Flow Susceptibility Summer, RCP 8.5

Under the RCP 8.5 future scenario, the spatial distribution of summer debris flow events across June, July, and August reveals notable variability across both elevation and susceptibility classes (Figure 115). In June, threshold-exceeding

events are widespread, occurring across all elevation classes (1 to 5), with multiple instances surpassing the BCM threshold of 50 mm. July shows a slight reduction in frequency, yet events are still observed across lower to mid-elevation classes (particularly Classes 2 to 4), with exceedances of both ECM and GCM thresholds, and occasional BCM-level events. In August, event density increases, especially within Elevation Classes 3 and 4, with many occurrences exceeding the 30 mm threshold. Across all three months, BCM-class events are prominently represented, indicating more intense rainfall and a higher potential for debris flow activity under future climate conditions.

4.10.3 Shallow Landslide Susceptibility under Precipitation Conditions

This study examines the possibility of shallow landslides in the future during periods of extreme precipitation predicted by the RCP 8.5 scenario. The ARPA Piemonte map was used to identify and spatially match events that exceeded 120 mm (24 hours) and 170 mm (48 hours) with elevation and susceptibility classes. The findings point to areas where high landslide vulnerability may coexist with heavy rainfall (Figure 116).

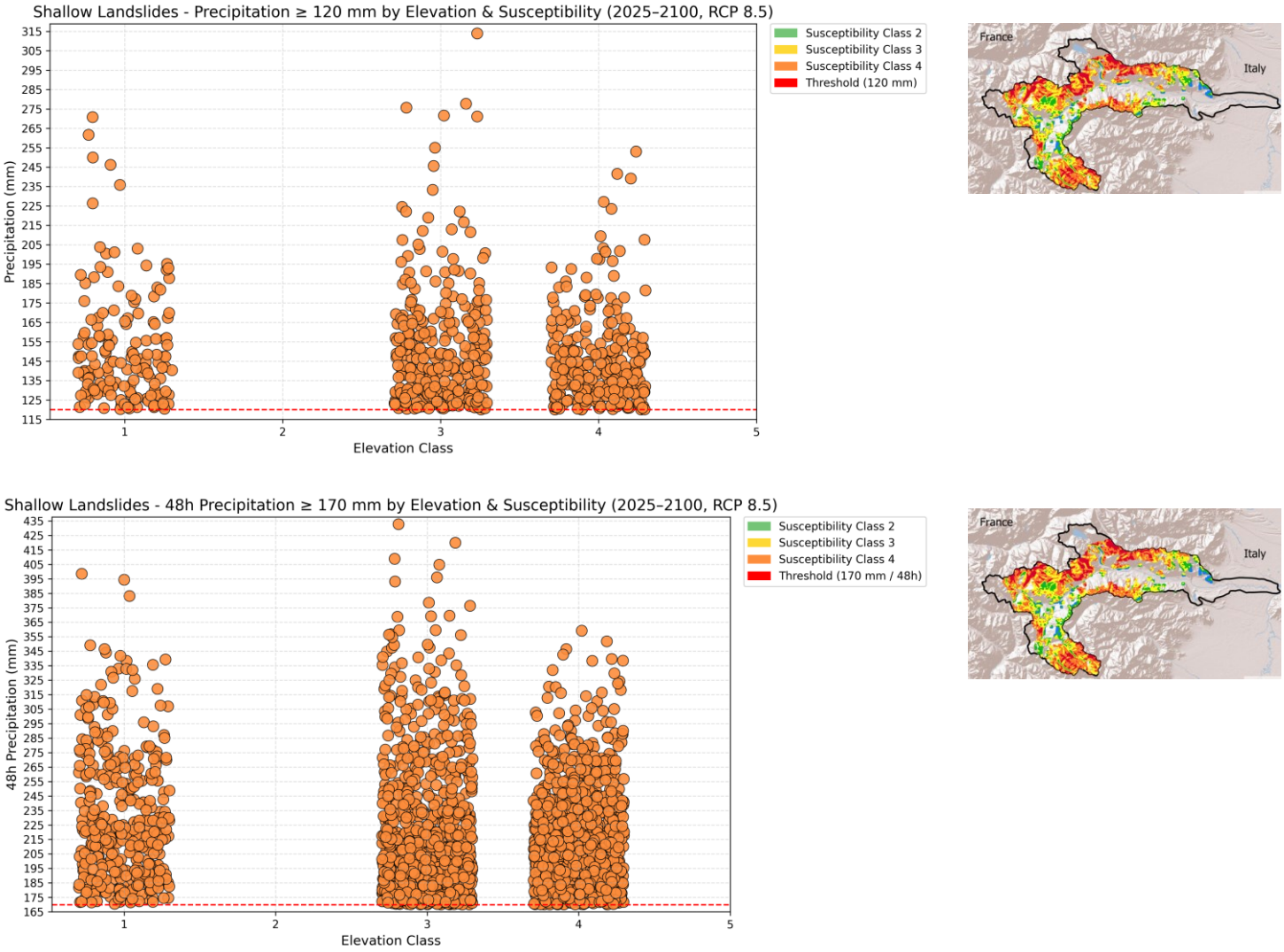

Figure 116_ 24 and 48 hours Rainfall Events by Elevation Class and Shallow Landslides Susceptibility Summer, RCP 4.5

In the 24-hour precipitation dataset (≥120 mm), intense rainfall events are primarily concentrated in Elevation Classes 1, 3, and 4. Notably, all of these events are associated with Susceptibility Class 4. Similarly, in the 48-hour precipitation chart (≥170 mm), the same elevation bands (Classes 1, 3, and 4) exhibit the greatest frequency and magnitude of events. All threshold-exceeding occurrences are again tied to Susceptibility Class 4, with multiple events surpassing 400 mm.

Chapter 5

Discussion

5.1 Overview of Key Findings

The primary findings are organized and thematically presented in this section. To show how historical data (1957-2024) and future climate projections under RCP 4.5 and RCP 8.5 scenarios have been analyzed, the key climatic and geohazard trends are described. Examined are variations in temperature and precipitation patterns, elevation-dependent reactions, and their effects on geohazards, particularly rockfalls, debris flows, and shallow landslides. In order to facilitate a comparison of past and future dynamics and to identify emerging spatial vulnerabilities throughout the Susa Valley, each topic is succinctly summarized to highlight both observed patterns and anticipated developments.

5.2 Interpretation of Historical Climate Trends

Tmax and Tmin increased in all months, but especially in autumn and winter, according to historical climate analysis (1957–2024), which showed consistent seasonal warming. Tmin frequently increased more quickly than Tmax, which resulted in a smaller delta temperature (ΔT), suggesting less daily variability and thermally stable nights.

Since even high-altitude zones (Class 5, >3000 m) demonstrated annual increases of +0.0038 °C (Tmax) and +0.0027 °C (Tmin), elevation-dependent warming (EDW) was verified. Permafrost stability is at risk, snow cover duration is shortened, and hydrological regimes are changed by this warming.

A seasonal shift in hazard exposure was suggested by precipitation patterns, which showed slight decreases in winter and increased rainfall in transitional months (May, November). The need for updated risk frameworks is highlighted by the fact that extreme 24- and 48-hour rainfall events happened in both moderately susceptible zones and high-risk areas.

Surface cohesion, vegetation, and slope stability are all impacted by these climatic trends, which include decreased ΔT, changed rainfall timing, and continuous warming. Rockfalls, shallow landslides, and debris flows are more likely to occur during spring and fall when rainfall intensity is higher. This emphasizes the necessity of location-specific assessments and seasonally adaptive hazard monitoring.

5.3 Historical Geo-Hazard Sensitivity Analysis

The analysis of Chapter 4 spatial and temporal patterns leads to this section which investigates how climatic factors affect the three main geohazards of rockfalls debris flows and shallow landslides in the Susa Valley. The research uses ARPA Piemonte susceptibility maps as the baseline to analyze the relationship between geohazards and their sensitivity to precipitation intensity and daily temperature fluctuations and elevation bands and seasonal dynamics.

5.3.1 Rockfall Susceptibility under Climatic Conditions

The findings show that one of the main factors influencing rockfall activity in the study area is the delta temperature (ΔT = Tmax − Tmin). The highest ΔT values were recorded in high susceptibility classes (3 to 5), especially in elevation bands 3 to 5, during the warmer months (May to August), according to an analysis of average ΔT across susceptibility and elevation classes. Increased rockface instability was indicated by ΔT exceeding 11°C in certain cases.

Even though ΔT tends to decrease during the colder months of November through February, the simultaneous drop in Tmin toward the freezing point makes conditions for freeze-thaw cycles more favorable. Notable ΔT values (between 5°C and 8°C) are still recorded by Susceptibility Classes 3 and 4, which are adequate to trigger mechanical weathering and the start of rockfall. These findings highlight how crucial it is to take into account both ΔT and Tmin when determining when rockfall activity is most likely to occur.

Additionally, the impact of extreme 24-hour and 48-hour rainfall events was assessed. For 24-hour totals, several intense episodes (above 120 mm) were recorded across susceptibility Classes 2 , 3 and 4, with one extreme event exceeding 160 mm even in Class 2. For 48-hour rainfall, more widespread

exceedances above 170 mm occurred, including events in Classes 2, 3, and 4. This suggests that prolonged heavy rainfall contributes significantly to rockfall hazards across a broader range of zones.

5.3.2 Debris Flow Susceptibility under Precipitation

Spatial features and short-duration intense rainfall are strongly associated with debris flow sensitivity, according to historical analysis. Estimated 12-hour precipitation values were compared to class-specific thresholds (ECM = 20 mm/h, GCM = 30 mm/h, and BCM = 50 mm/h) using daily records from 1957 to 2024. Whereas GCM and BCM regions saw fewer but sometimes more intense events, ECM zones saw the majority of threshold-exceeding rainfall events.

Subsequent analysis focused on summer months (June, July, August), incorporating elevation bands. The spatial-seasonal distribution shows that all threshold-exceeding events during this period occurred exclusively in Elevation Class 5 (above 3000 meters) and within the ECM susceptibility category. No critical exceedance was detected for GCM or BCM during this warm-season window.

The research shows that debris flow hazards primarily occur in high-altitude regions during summer months even though geomorphological sensitivity remains moderate in these areas. The results show that elevated zones need specific early warning systems and continuous monitoring during warmer months.

5.3.3 Shallow Landslide Susceptibility under Precipitation

Shallow landslides are typically caused by cumulative rainfall that surpasses critical thresholds (120 mm and 170 mm, respectively), according to analysis of 24- and 48-hour precipitation events. All recorded events in the 24-hour dataset were above the 120 mm threshold and were mostly found in Elevation Class 3, spanning susceptibility Classes 2 through 4. This demonstrates that under enough rainfall accumulation, even areas that are moderately sensitive become vulnerable.

Rainfall intensity and spatial spread both increased during the 48-hour analysis. In addition to Class 3, some events extended to lower elevation bands and exceeded 220 mm. These trends support the idea that the antecedent soil moisture, saturation levels, and slope morphology are important factors in the initiation of shallow landslides.

5.3.4 Spatiotemporal Overlap of Hazards

Several sites in the Susa Valley showed concurrent or sequential occurrences of various geohazards, including shallow landslides or rockfalls followed by debris flows. The elevation bands 3 and 4, which are characterized by steep slopes, dynamic climate conditions, and high runoff potential, were where these overlaps were most common.

The sequence of events started with temperature-induced stress which led to heavy summer rainfall. The sequential nature of these events demonstrates why multi-hazard assessment methods are crucial for protecting residential and infrastructure areas that face vulnerability.

5.4 Interpretation of Future Climate Projections

The Susa Valley's climate is projected under two Representative Concentration Pathways (RCPs) in this section: the high-emissions RCP 8.5 and the moderate-emissions RCP 4.5, for the years 2025–2100. While RCP 8.5 depicts a continuous, unabated increase in radiative forcing over the course of the twenty-first century, RCP 4.5 assumes emissions stabilize around the middle of the century. These scenarios represent divergent greenhouse gas trajectories. With significant ramifications for seasonal regimes, altitudinal gradients, and geomorphological hazard processes, both pathways lead to persistent—and frequently accelerated—climate trends when compared to the historical baseline (1957–2024).

According to RCP 4.5, Tmax and Tmin will warm by +0.0017 °C per year in the 400–700 m lower elevation band, for a total increase of roughly +1.3 °C by 2100. This gradual warming has an impact on vegetation dynamics, snowmelt timing, and freeze-thaw cycles. However, compared to RCP 4.5, RCP 8.5 forecasts a much faster rate of warming of +0.0049°C/year (Tmax) and +0.0047°C/year (Tmin), or +3.7°C over the same time period. The faster warming under RCP 8.5 is linked to stronger atmospheric water vapor retention, increased radiative forcing, and intensified positive feedback loops (e.g., reduced albedo from snow/ice loss).

In both scenarios, Elevation-Dependent Warming (EDW) persists across all bands but is more pronounced in RCP 8.5 due to combined thermal amplification

at high altitudes and snow-albedo feedback. As a result, the elevation at which Tmax remains below freezing (0°C)—a proxy for freeze–thaw zone boundaries—shifts from 795 m (historical) to 1427 m in RCP 4.5 and up to 1550 m in RCP 8.5. This vertical displacement of ~755 m under high emissions alters the distribution of thermally sensitive geomorphic processes such as frost weathering, ice lens formation, and permafrost degradation.

24-hour rainfall forecasts for the Susa Valley under RCP 4.5 indicate a noticeable seasonal intensification, especially in May, June, and November, but comparatively stable annual totals. The positive trends in these months (e.g., +0.0294 mm/year in May, +0.0586 mm/year in June) frequently surpass the 120 mm (24h) and 170 mm (48h) thresholds, which are crucial for causing debris flows and shallow landslides. The higher atmospheric moisture capacity and increased convective instability are the main causes of this.Conversely, RCP 8.5 shows an overall negative annual trend (−0.0861 mm/year), especially in spring and summer months like May (−0.2664 mm/year) and June (−0.2310 mm/year), yet still features sporadic high-intensity peaks, occasionally surpassing T10–T20 thresholds. These differences suggest that while RCP 4.5 may lead to clustered seasonal risks, RCP 8.5 introduces a more irregular and spatially dispersed hazard regime, requiring adaptive, threshold-based hazard management frameworks.

5.5 Future Hazard Susceptibility

This section evaluates how future temperature and precipitation changes may affect the Susa Valley's susceptibility to three main geohazards: rockfalls, debris flows, and shallow landslides. It builds on the climate projections discussed in Section 5.4. Seasonal and altitudinal trends are combined with ARPA Piemonte's susceptibility classification to assess potential spatial and temporal shifts in hazard exposure under RCP 4.5 and RCP 8.5 scenarios.

5.5.1 Rockfall Susceptibility under Future Thermal Conditions

Rockfall susceptibility in the Susa Valley is largely determined by the delta temperature (ΔT) in the RCP 4.5 scenario, particularly during the warm season (May to September). Mid- and lower-elevation classes (Classes 2 and 3) more consistently surpass the 8°C threshold, whereas ΔT increases in higher elevation zones (Classes 4 and 5) are moderate. Rockfall susceptibility in the Susa Valley is

largely determined by the delta temperature (ΔT) in the RCP 4.5 scenario, particularly during the warm season (May to September). Mid- and lower-elevation classes (Classes 2 and 3) more consistently surpass the 8°C threshold, whereas ΔT increases in higher elevation zones (Classes 4 and 5) are moderate. The daily freezing elevation reaches 1427 meters which reduces freeze-thaw action at lower elevations yet higher Tmin values in higher zones maintain a favorable environment for thermal fatigue. Slopes with moderate vulnerability to instability will become unstable when heavy rainfall occurs (e.g., ≥120 mm in 24 hours and ≥170 mm in 48 hours). The convergence of thermal stress and hydrological triggers requires hazard monitoring to extend beyond traditional high-risk areas into lateral terrain and mid-slope corridors where future rockfall activity is expected to rise.

The amount of freeze-thaw action at lower elevations may be lessened by higher Tmin values in higher zones, which maintain conditions favorable to thermal fatigue even though the daily freezing elevation rises to about 1427 m. Even moderately susceptible slopes can become unstable when combined with periods of heavy rainfall (e.g., ≥120 mm in 24 hours and ≥170 mm in 48 hours). It is recommended that hazard monitoring be expanded beyond conventional high-risk areas to include mid-slope corridors and lateral terrain, where future rockfall activity is anticipated to increase, due to the convergence of hydrological triggers and thermal stress.

Extreme rainfall events are less common but noticeably more intense in RCP 8.5, especially during June and August. These high-magnitude events may exacerbate rock detachment on thermally weakened slopes. Compared to RCP 4.5, RCP 8.5 has a longer, more intense, and wider risk window. These trends highlight the need for long-term, threshold-based early warning systems that operate across elevation gradients and seasonal intervals.

5.5.2 Debris Flow Susceptibility under Future Rainfall Events

Debris flow susceptibility in the Susa Valley is influenced by the temporal and spatial distribution of high-intensity summer rainfall under both climate scenarios. A number of events in high elevation classes surpass the GCM and BCM thresholds in June, while some events in Class 1 surpass even the 50 mm/h threshold, indicating an upward expansion of hazard in RCP 4.5. Even though they are not as

severe, July and August frequently surpass ECM-level rainfall in Classes 2 through 4, indicating a developing lateral extension of risk into lower elevations. Focused monitoring is necessary in the early and late summer months due to the hazard's spatial dispersion and continued relative moderateness.

This pattern becomes more pronounced in RCP 8.5. All elevation classes are impacted by June events, which frequently surpass the GCM and BCM thresholds, particularly in Classes 3 and 4. While August becomes the most critical month with a dense concentration of events in Classes 3 and 4, many of which surpass the 50 mm/h mark, July maintains mid-elevation risk despite slightly fewer events. The RCP 8.5 scenario exhibits increased frequency, wider elevation reach, and higher rainfall intensities in comparison to RCP 4.5, suggesting a shift toward more aggressive and spatially extensive hazard conditions. These modifications highlight how urgent it is to create threshold-based early warning systems and revise susceptibility classifications to incorporate zones that were previously thought to be only moderately at risk.

5.5.3 Shallow Landslide Susceptibility under Future Cumulative Rainfall

Initial findings under both RCP 4.5 and RCP 8.5 scenarios indicate that shallow landslide events are predominantly concentrated in Susceptibility Class 4 and Elevation Classes 1, 3, and 4. These events frequently exceed the critical thresholds of 120 mm (24-hour) and 170 mm (48-hour) rainfall, with some extreme cases recording more than 500 mm in 48 hours, suggesting significant instability in certain high-risk zones. However, the absence of recorded exceedance events in Elevation Class 2 under both scenarios should not be interpreted as a definitive result. Given the geomorphological context of the Susa Valley—particularly the transitional slopes and human-modified terrains—one would reasonably expect at least some threshold-crossing events in this class. The lack of data here is likely not due to an actual absence of hazard, but rather the result of analytical limitations stemming from the high data volume and limited computational capacity. Because the rainfall simulations and exceedance analyses were carried out on a personal computer with restricted processing power, it was not possible to fully process all raster points at high resolution across the entire 2025–2100 period. Because of this, it is possible that some events were inadvertently excluded during the data extraction or filtering stages, particularly

in mid-elevation classes with moderate event density. The conclusions derived from this section should therefore be interpreted with some caution. The assessment of susceptibility in Elevation Class 2 would benefit from additional research using cloud-based processing or HPC clusters for more precise results which could validate or improve the current findings. Risk management strategies and early warning system designs need improvement especially in transitional elevation zones.

5.5.4 Spatial and Temporal Overlap of Future Hazards

A growing propensity for spatiotemporal overlap among geohazards in the Susa Valley is indicated by future climate projections under both RCP 4.5 and RCP 8.5. This is most noticeable in Elevation Classes 3 and 4, where climate variability and steep slopes meet. Many times, early summer thermal stress (high ΔT) can serve as a prelude to heavy rainfall events, causing rockfalls, debris flows, and shallow landslides to occur quickly after. Even though this pattern is already apparent under RCP 4.5, under RCP 8.5 it becomes more widespread and spatially expansive, with hazard cascades increasingly impacting areas that were previously thought to be moderately sensitive. These characteristics highlight the necessity of adaptive response systems and multi-hazard monitoring across interconnected elevation bands.

Chapter 6

Conclusion

To investigate how climate change is affecting three major geomorphological hazards in the Susa Valley—rockfalls, debris flows, and shallow landslides—this study merged historical climate data (1957–2024) with future climate projections (2025–2100) under two greenhouse gas scenarios (RCP 4.5 and RCP 8.5). The research offered a comprehensive understanding of past and projected hazard patterns through a multi-dimensional approach that included elevation zoning, ARPA Piemonte's susceptibility maps, and thermal (Tmax, Tmin, ΔT) and precipitation (24-hour and 48-hour cumulative rainfall, hourly intensity) indices.

The research data showed that temperature increase exists throughout all elevation zones with the most significant changes observed above 1000 meters. The elevation-dependent warming (EDW) effect caused by increasing nighttime minimum temperatures (Tmin) has resulted in a decrease of delta temperature (ΔT) which intensifies thermal stress during warmer months. The thermal dynamic shows a direct relationship with increased rockfall susceptibility when the ΔT exceeds 8 °C. The summer threshold exceeded frequently in mid- and high-susceptibility zones which indicates that thermally driven rockfall will become a seasonal threat in Alpine environments in the future.

Specifically under RCP 4.5, rainfall analysis showed notable increases in transitional periods like May, June, and November, but stable or declining annual totals in the majority of months. Shallow landslides and debris flows are more likely as a result of this seasonal intensification, antecedent soil saturation, and compromised surface cohesiveness. Events involving debris flows were more common in lithological units with a high potential for clay formation, particularly in the ECM class. During summer storms, critical short-duration rainfall thresholds (20, 30, and 50 mm/h) were most frequently exceeded in these higher elevation zones.

In the case of shallow landslides, nearly all recorded 24-hour events exceeded the 120 mm threshold and were concentrated in Elevation above 1000 m under Susceptibility Class 4. Some 48-hour totals surpassed 220 mm, indicating instability even in moderately sensitive zones. Although no exceedance was recorded in Elevation Class 2 (400-700 m) , this absence may be due to data processing constraints rather than a lack of hazard. Overall, patterns observed across both scenarios suggest that higher-elevation, high-susceptibility areas will continue to face elevated landslide risks in the future.

Summer was found to be the most crucial season for climate-related risks out of all of them. ΔT regularly surpassed 8°C from May to August, raising the risk of rockfall and thermal fatigue. Debris flow and shallow landslide activity were accelerated concurrently by intense short-duration rainfall events, particularly in June and August, which frequently surpassed the 24- and 48-hour thresholds. The necessity of hazard calendars and seasonal early warning systems specific to mountainous areas is highlighted by this seasonal concentration.

Another important finding was the overlap in space and time between hazards. Thermal stress, followed by heavy rainfall and cascading hazards, was a recurrent pattern in Elevation Classes 3 and 4 (a, especially during warm months. Under RCP 8.5, these patterns were more pronounced and widespread in space, progressively impacting regions that had previously been categorized as moderately susceptible. The critical freezing elevation, for instance, which was previously around 795 meters, is predicted to increase by more than 750 meters vertically to roughly 1427 meters under RCP 4.5 and 1550 meters under RCP 8.5. The thermally vulnerable zone is widened by this upward migration, which also exposes higher terrain to increased slope instability and rockface degradation.

The historical period featured episodic hazards which were primarily elevation-class and threshold-based whereas future projections under RCP 8.5 show a shift toward more frequent and widespread compound hazard interactions. The risk landscape has evolved from sporadic geohazard activity to a more persistent and systemic risk landscape.

References

Allen, S., & Huggel, C. (2013). Extremely warm temperatures as a potential cause of recent high mountain rockfall. *Global and Planetary Change*, *107*, 59–69. https://doi.org/10.1016/j.gloplacha.2013.04.007

Booth, A. M., & Pétursson, H. G. (2025). Permafrost and Structural Controls on Holocene Bedrock Landslide Occurrence Around Eyjafjörður, North-Central Iceland. *Journal of Geophysical Research: Earth Surface*, *130*(1), e2024JF007933. https://doi.org/10.1029/2024JF007933

Borgogno Mondino, E., Giardino, M., & Perotti, L. (2009). A neural network method for analysis of hyperspectral imagery with application to the Cassas landslide (Susa Valley, NW-Italy). *Geomorphology*, *110*(1–2), 20–27. https://doi.org/10.1016/j.geomorph.2008.12.023

Bračko, T., Jelušič, P., & Žlender, B. (2025). Geotechnical Aspects of N(H)bSs for Enhancing Sub-Alpine Mountain Climate Resilience. *Land*, *14*(3), 512. https://doi.org/10.3390/land14030512

Bračko, T., Žlender, B., & Jelušič, P. (2022). Implementation of Climate Change Effects on Slope Stability Analysis. *Applied Sciences*, *12*(16), 8171. https://doi.org/10.3390/app12168171

Cadoppi, P., Giardino, M., Perrone, G., & Tallone, S. (2007). Litho-structural control, morphotectonics, and deep-seated gravitational deformations in the evolution of Alpine relief: A case study in the lower Susa Valley (Italian Western Alps). *Quaternary International*, *171–172*, 143–159. https://doi.org/10.1016/j.quaint.2006.10.015

Calamita, G., Gallipoli, M. R., Gueguen, E., Sinisi, R., Summa, V., Vignola, L., Stabile, T. A., Bellanova, J., Piscitelli, S., & Perrone, A. (2023). Integrated geophysical and geological surveys reveal new details of the large Montescaglioso (southern Italy) landslide of December 2013. *Engineering Geology*, *313*, 106984. https://doi.org/10.1016/j.enggeo.2023.106984

Castellazzi, G., & Previtali, M. (2024). A Multi-Criteria GIS-Based Approach for Risk Assessment of Slope Instability Driven by Glacier Melting in the Alpine Area. *Applied Sciences*, *14*(24), 11524. https://doi.org/10.3390/app142411524

Chiarle, M., Iannotti, S., Mortara, G., & Deline, P. (2007). Recent debris flow occurrences associated with glaciers in the Alps. *Global and Planetary Change*, *56*(1–2), 123–136. https://doi.org/10.1016/j.gloplacha.2006.07.003

Chien-Yuan, C., Tien-Chien, C., Fan-Chieh, Y., Wen-Hui, Y., & Chun-Chieh, T. (2005). Rainfall duration and debris-flow initiated studies for real-time monitoring. *Environmental Geology*, *47*(5), 715–724. https://doi.org/10.1007/s00254-004-1203-0

Cremonini, R. (2023). *RAPPORTO PRELIMINARE D'EVENTO*. ARPA Piemonte. https://www.arpa.piemonte.it/sites/default/files/media/2023-12/Rapporto__colata_detritica_Bardonecchia_2023.pdf

Cremonini, R., & Tiranti, D. (2018). The Weather Radar Observations Applied to Shallow Landslides Prediction: A Case Study From North-Western Italy. *Frontiers in Earth Science*, *6*, 134. https://doi.org/10.3389/feart.2018.00134

Deangeli, C. (2008). Laboratory Granular Flows generated by Slope Failures. *Rock Mechanics and Rock Engineering*, *41*(1), 199–217. https://doi.org/10.1007/s00603-007-0131-1

Dussauge, C., Grasso, J., & Helmstetter, A. (2003). Statistical analysis of rockfall volume distributions: Implications for rockfall dynamics. *Journal of Geophysical Research: Solid Earth*, *108*(B6), 2001JB000650. https://doi.org/10.1029/2001JB000650

Fratianni, S., Cassardo, C., & Cremonin, R. (2009). *CLIMATIC CHARACTERIZATION OF FOEHN EPISODES IN PIEDMONT, ITALY*.

Ghignone, S., Gilio, M., Borghini, A., Boero, F., Bruno, M., & Scaramuzzo, E. (2024). Mineralogical and petrological constraints and tectonic implications of a new coesite-bearing unit from the Alpine Tethys oceanic slab (Susa Valley, Western Alps). *Lithos*, *472–473*, 107575. https://doi.org/10.1016/j.lithos.2024.107575

Gunzburger, Y., Merrien-Soukatchoff, V., & Guglielmi, Y. (2005). Influence of daily surface temperature fluctuations on rock slope stability: Case study of the Rochers de Valabres slope (France). *International Journal of Rock Mechanics and Mining Sciences*, *42*(3), 331–349. https://doi.org/10.1016/j.ijrmms.2004.11.003

Guo, Z., Ferrer, J. V., Hürlimann, M., Medina, V., Puig-Polo, C., Yin, K., & Huang, D. (2023). Shallow landslide susceptibility assessment under future climate and land cover changes: A case study from southwest China. *Geoscience Frontiers*, *14*(4), 101542. https://doi.org/10.1016/j.gsf.2023.101542

Hübl, J., Suda, J., Proske, D., Kaitna, R., & Scheidl, C. (n.d.). *Debris Flow Impact Estimation*.

Iadanza, C., Trigila, A., & Napolitano, F. (2016). Identification and characterization of rainfall events responsible for triggering of debris flows and shallow landslides. *Journal of Hydrology*, *541*, 230–245. https://doi.org/10.1016/j.jhydrol.2016.01.018

Jomelli, V., Pech, V. P., Chochillon, C., & Brunstein, D. (2004). Geomorphic Variations of Debris Flows and Recent Climatic Change in the French Alps. *Climatic Change*, *64*(1/2), 77–102. https://doi.org/10.1023/B:CLIM.0000024700.35154.44

Kandalai, S., John, N. J., & Patel, A. (2023). Effects of Climate Change on Geotechnical Infrastructures—State of the art. *Environmental Science and Pollution Research*, *30*(7), 16878–16904. https://doi.org/10.1007/s11356-022-24788-7

Krautblatter, M., & Moser, M. (2009). A nonlinear model coupling rockfall and rainfall intensity based on a four year measurement in a high Alpine rock wall (Reintal, German Alps). *Natural Hazards and Earth System Sciences*, *9*(4), 1425–1432. https://doi.org/10.5194/nhess-9-1425-2009

Lan, H., Derek Martin, C., & Lim, C. H. (2007). RockFall analyst: A GIS extension for three-dimensional and spatially distributed rockfall hazard modeling. *Computers & Geosciences*, *33*(2), 262–279. https://doi.org/10.1016/j.cageo.2006.05.013

Loche, M., & Scaringi, G. (2025). Assessing the influence of temperature on slope stability in a temperate climate: A nationwide spatial probability analysis in Italy. *Environmental Modelling & Software*, *183*, 106217. https://doi.org/10.1016/j.envsoft.2024.106217

Lopez-Saez, J., Corona, C., Eckert, N., Stoffel, M., Bourrier, F., & Berger, F. (2016). Impacts of land-use and land-cover changes on rockfall propagation: Insights from the Grenoble conurbation. *Science of The Total Environment*, *547*, 345–355. https://doi.org/10.1016/j.scitotenv.2015.12.148

Magnin, F., Pohl, B., Josnin, J.-Y., Pergaud, J., Deline, P., & Ravanel, L. (n.d.). *Permafrost Degradation Pathways during the 21 st Century of High-elevated Rock Ridge in the Mont Blanc Massif*.

Marchelli, M., & Deangeli, C. (2022). Towards a codified design procedure for rockfall reinforced earth embankments. *Towards a Codified Design Procedure for Rockfall Reinforced Earth Embankments*, *1233*(165), 50–59. https://doi.org/10.19199/2022.165.1121-9041.050

Mazzoglio, P., Viglione, A., Ganora, D., & Claps, P. (2025). Mapping the uneven temporal changes in ordinary and extraordinary rainfall extremes in Italy. *Journal of Hydrology: Regional Studies*, *58*, 102287. https://doi.org/10.1016/j.ejrh.2025.102287

Melillo, M., Gariano, S. L., Peruccacci, S., Sarro, R., Mateos, R. M., & Brunetti, M. T. (2020). Rainfall and rockfalls in the Canary Islands: Assessing a seasonal link. *Natural Hazards and Earth System Sciences*, *20*(8), 2307–2317. https://doi.org/10.5194/nhess-20-2307-2020

Mirhadi, N., & Macciotta, R. (2023). Quantitative correlation between rock fall and weather seasonality to predict changes in rock fall hazard with climate change. *Landslides*, *20*(10), 2227–2241. https://doi.org/10.1007/s10346-023-02105-8

Moos, C., Guisan, A., Randin, C. F., & Lischke, H. (2021). Climate Change Impacts the Protective Effect of Forests: A Case Study in Switzerland. *Frontiers in Forests and Global Change*, *4*, 682923. https://doi.org/10.3389/ffgc.2021.682923

Ponziani, M., Pogliotti, P., Stevenin, H., & Ratto, S. M. (2020). Debris-flow Indicator for an early warning system in the Aosta valley region. *Natural Hazards*, *104*(2), 1819–1839. https://doi.org/10.1007/s11069-020-04249-5

Psarropoulos, P. N., Makrakis, N., & Tsompanakis, Y. (2024). Climate Change Impact on the Stability of Soil Slopes from a Hydrological and Geotechnical Perspective. *GeoHazards*, *5*(4), 1190–1206. https://doi.org/10.3390/geohazards5040056

Pudasaini, S. P. (2012). A general two-phase debris flow model. *Journal of Geophysical Research: Earth Surface*, *117*(F3), 2011JF002186. https://doi.org/10.1029/2011JF002186

Rianna, G., Comegna, L., Gariano, S. L., Guzzetti, F., Mercogliano, P., Picarelli, L., & Tommasi, P. (2017). Potential Effects of Climate Changes on Landslide Activity in Different Geomorphological Contexts. In M. Mikoš, N. Casagli, Y. Yin, & K. Sassa (Eds.), *Advancing Culture of Living with Landslides* (pp. 243–249). Springer International Publishing. https://doi.org/10.1007/978-3-319-53485-5_28

Shibasaki, T., Matsuura, S., & Okamoto, T. (2016). Experimental evidence for shallow, slow-moving landslides activated by a decrease in ground temperature. *Geophysical Research Letters*, *43*(13), 6975–6984. https://doi.org/10.1002/2016GL069604

Stoffel, M., Tiranti, D., & Huggel, C. (2014). Climate change impacts on mass movements—Case studies from the European Alps. *Science of The Total Environment*, *493*, 1255–1266. https://doi.org/10.1016/j.scitotenv.2014.02.102

Tiranti, D., Cremonini, R., Marco, F., Gaeta, A. R., & Barbero, S. (2014). The DEFENSE (debris Flows triggEred by storms – nowcasting system): An early warning system for torrential processes by radar storm tracking using a Geographic Information System (GIS). *Computers & Geosciences*, *70*, 96–109. https://doi.org/10.1016/j.cageo.2014.05.004

Tiranti, D., Cremonini, R., & Sanmartino, D. (2021). Wildfires Effect on Debris Flow Occurrence in Italian Western Alps: Preliminary Considerations to Refine Debris Flow Early Warnings System Criteria. *Geosciences*, *11*(10), 422. https://doi.org/10.3390/geosciences11100422

Tiranti, D., & Deangeli, C. (2015). Modeling of debris flow depositional patterns according to the catchment and sediment source area characteristics. *Frontiers in Earth Science*, *3*. https://doi.org/10.3389/feart.2015.00008

Tiranti, D., Mallen, L., & Nicolò, G. (2023). Rockfall hazard estimation and related applications for a preliminary risk assessment at regional scale: An example from northwestern Italian Alps. *Landslides*, *20*(8), 1691–1704. https://doi.org/10.1007/s10346-023-02060-4

Tiranti, D., Nicolò, G., & Gaeta, A. R. (2019). Shallow landslides predisposing and triggering factors in developing a regional early warning system. *Landslides*, *16*(2), 235–251. https://doi.org/10.1007/s10346-018-1096-8

Varnes, D. J. (1978). *Slope movement types and processes* (Schuster, R. L.; Krizek, R. J.). Transportation Research Board, National Academy of Sciences.

Walker, C., Heitor, A., & Clarke, B. (2022). Influence of Weather-Driven Processes on the Performance of UK Transport Infrastructure with Reference to Historic Geostructures. *Applied Sciences*, *12*(15), 7461. https://doi.org/10.3390/app12157461

Yavari, N., Tang, A. M., Pereira, J.-M., & Hassen, G. (2016). Effect of temperature on the shear strength of soils and the soil–structure interface. *Canadian Geotechnical Journal*, *53*(7), 1186–1194. https://doi.org/10.1139/cgj-2015-0355